

Horizontal Coupling in Continuum Atomistics

vom Fachbereich Maschinenbau und Verfahrenstechnik
der Technischen Universität Kaiserslautern
zur Verleihung des akademischen Grades
Doktor-Ingenieur (Dr.-Ing.)
genehmigte Dissertation

von
Dipl.-Ing. Aitor Elizondo Sanchis
aus Stuttgart

Hauptreferent: Prof. Dr.-Ing. P. Steinmann
Korreferenten: Prof. E.C. Aifantis
Prof. Dr. rer. nat. H.M. Urbassek
Prof. Dr.-Ing. A. Menzel
Vorsitzende: J.P. Dr.-Ing. J. Mergheim
Dekan: Prof. Dr.-Ing. J.C. Aurich

Tag der Einreichung: 21. März 2007
Tag der mündlichen Prüfung: 22. Oktober 2007

Kaiserslautern, August 2008
D 386

Preface

The research presented in this thesis was carried out during the period 2003–2007 at the Chair of Applied Mechanics at the Technical University of Kaiserslautern (Germany). The work was financed through the EU-RTN (Research Training Network) within the project HPRN-CT-2002-00198 entitled D.E.F.I.N.O. (Deformation and Fracture Instabilities in Novel Materials and Processes), the support of which is gratefully acknowledged.

First of all, I would like to thank Professor Paul Steinmann for giving me the opportunity to work in the fascinating field of continuum–atomistic multiscale method, for his supervision and continuous support, not only in the course of my PhD, but also during my whole period at the Chair. Moreover, I want to express my gratitude to Professor Andreas Menzel, whom I consider more than just a scientific advisor, for his help and many friendly conversations. Furthermore, special acknowledgement is due to JP Julia Mergheim for representing the head of the committee and her interest in my work. In addition, I want to thank Professor H.M. Urbassek and Professor E.C. Aifantis for kindly accepting to act as referees of this thesis.

Finally, I thank all my colleagues at the LTM in Kaiserslautern, who have contributed to this research and made this period in Kaiserslautern one which I will not forget for the rest of my life. Special thanks go first to Jürgen Glaser, who convinced Professor Steinmann to involve me in this European project, and to Ralf Denzer and Alexandru Constantiniu for creating a stimulating environment and providing friendly conversations. In particular, I thank Dr. Franz Josef Barth, Natalia Kondratieva and Frau Christa Edeltraut Jeblick for their support. I do not want to forget Florian Theil, Sarah Ricker, Britta Hirschberger, Grieta Himpel, Rouven Mohr, Johannes Utzinger, Markus Klassen, Holger Meier and Patrick Schmitt. Also many thanks to my friends Alex Will, Max Wilking, Björn Schmitt and Renato Sessa for making me feel at home during my time in Germany.

Last but not least, I would like to express my gratitude to my wife and parents for their continuous support, patience and love.

Contents

Preface	i
Nomenclature	v
Abstract	1
Zusammenfassung	5
1 The Molecular Dynamics Method	9
1.1 Introduction	9
1.2 Fundamental Theoretical Foundations of Classical Molecular Dynamics Method	10
1.3 Initialisation	12
1.4 The Potential Energy Function	14
1.4.1 The Pair Potentials	15
1.4.2 Many-Body Potentials	20
1.5 Integrator	22
1.6 Choice of the Micro Molecular Dynamics Time-Step	26
1.7 Boundary Conditions	29
1.8 Errors in Molecular Dynamics	30
1.9 Molecular Dynamics at Constant Temperature	30
1.10 Evaluation of Physical Properties	31
1.10.1 Thermodynamical Properties	32
1.10.2 Structural Properties	32
1.10.3 Dynamical Properties	34
1.11 Visualization Methods	35
2 On Aspects of the Cauchy-Born rule and Atomistics	37
2.1 Introduction	37
2.2 The First-Order Cauchy-Born Rule.	38
2.3 Atomistic Failure Criteria	40
2.4 On the Validity of the Cauchy-Born Rule in the Two Dimensional Case. Numerical Results.	43
2.4.1 Simple Shear Deformation	46
2.4.2 Uniaxial Extension	52
2.4.3 Pure Shear Deformation	58
2.4.4 Dilatation Deformation	64
2.5 Summary	70

3	Horizontal Coupling in Continuum Atomistics	73
3.1	Introduction	73
3.2	Short Overview over the Atomistic/Continuum Coupling Techniques	76
3.3	Essentials of Continuum Mechanics Framework. The First–Order Cauchy–Born Rule.	77
3.3.1	Kinematics of Continuum Mechanics	77
3.3.2	Atomistic Constitutive Modelling	80
3.3.3	Continuum–Atomistic Constitutive Modelling	82
3.3.4	The Finite Element Simulation Structure	84
3.4	Coupling Algorithm in Continuum Atomistics	88
3.5	Some Numerical Results and Analysis	93
3.6	Summary	104
4	Wave Reflections at the Atomistic/Continuum Interface	105
4.1	Introduction	105
4.2	Current State of Research	105
4.3	Theoretical Foundations of the Damping Zone	106
4.4	The Cauchy–Born Rule. Numerical Results Using a Damping Zone.	109
4.4.1	Simple Shear Deformation	110
4.4.2	Uniaxial Extension Deformation	111
4.4.3	Pure Shear Deformation	112
4.4.4	Dilatation Deformation	113
4.5	The Horizontal Coupling Algorithm. Numerical Results Using a Damping Zone	114
5	Conclusions and Outlook	117
A	The Standard Deviation	121
B	Atomistic Stress	127
C	Continuum Failure Criteria	129
D	Miscellaneous	133
	Bibliography	134
	Curriculum Vitae	145

Nomenclature

Molecular Dynamics features

\mathbf{f}_i	Force acting on the atom i due to all other atoms
m_i	Mass atom i
\mathbf{a}_i	Acceleration of atom i
\mathbf{r}_i	Vector position of atom i
\mathbf{r}_j	Vector position of atom j
\mathbf{r}_{ij}	Relative position vector of atom i
\mathbf{v}_i	Vector velocity of atom i
U	Potential energy function
r_0	Lattice constant. Equilibrium position
r_c	Cut-off radius
ϕ_{LJ}	Lennard–Jones potential
ε, σ	Parameters of the Lennard–Jones pair potential
ϕ_{Morse}	Morse potential
ε, α	Parameters of the Morse pair potential
ϕ_{Buck}	Buckingham potential
σ, A, B	Parameters of the Buckingham pair potential
ϕ_{LJSH}	Lennard–Jones shifted potential
α, β	Additional parameters of the Lennard–Jones shifted pair potential
ϕ_{HA}	Harmonic potential
k	Constant parameter for Harmonic potential
$\varepsilon, r_0, \alpha, \beta^{(0)}, Z, A$	Parameters of the EAM potential
k_B	Boltzmann constant
Δt	Micro molecular dynamics time step
$\langle W \rangle$	Virial
$g(r)$	Radial distribution function
ω_D	Debye frequency
$(\Delta r)^2$	Mean-square displacement
c_i	Centrosymmetry parameter
\mathbf{s}_i	Slip vector
ρ	Density
T	Temperature
P	Pressure

Atomistic features

\mathcal{C}_0	Material lattice configuration
\mathcal{C}_t	Spatial lattice configuration
\mathbf{R}_i	Site vector of the atom i in \mathcal{C}_0
\mathbf{R}_j	Site vector of the atom j in \mathcal{C}_0
\mathbf{R}_{ij}	Relative vector position of the atom i in \mathcal{C}_0
\mathbf{r}_i	Placement vector of the atom i in \mathcal{C}_t
\mathbf{r}_j	Placement vector of the atom j in \mathcal{C}_t
\mathbf{r}_{ij}	Relative vector position of the atom i in \mathcal{C}_t
E_0	Sublimation energy
E_i	Contribution of the atom i to the total internal energy E^{int}
\mathbf{f}_i	Force acting on the atom i due to all other atoms
\mathbf{f}_{ij}	Interactive forces acting on i due to the atom j
\mathbf{k}_{ij}	Atomic level stiffness
V_i	Volume of the Voronoi cell in the material configuration
σ_i	Atomistic stress
γ	Shear number
λ	Stretch
\mathbf{e}_i	Cartesian basis vectors

Continuum features

φ	Non-linear deformation map
\mathbf{F}	Deformation gradient
\mathcal{B}_0	Material body configuration
\mathcal{B}_t	Spatial body configuration
\mathbf{X}	Material position vector in \mathcal{B}_0
\mathbf{x}	Spatial position vector in \mathcal{B}_t
\mathbf{I}	Identity tensor
J	Jacobian
$d\mathbf{X}$	Infinitesimal line elements in \mathcal{B}_0
$d\mathbf{x}$	Infinitesimal line elements in \mathcal{B}_t
dV	Volume element in \mathcal{B}_0
dv	Volume element in \mathcal{B}_t
dA	Area element in \mathcal{B}_0
da	Area element in \mathcal{B}_t
\mathbf{N}	Material normal vector
\mathbf{n}	Spatial normal vector
\mathbf{C}	Right Cauchy–Green tensor

\mathbf{b}	Left Cauchy–Green tensor
W_0	Strain energy density
\mathbf{P}	Piola stress tensor
\mathbf{S}	Piola–Kirchhoff stress tensor
$\boldsymbol{\sigma}$	Cauchy stress tensor
\mathbb{L}	4 th -order two–point tangent operator (linearization of \mathbf{P})

Damping Parameters

γ_0	Maximum damping coefficient
γ	Damping coefficient
ω_D	Debye frequency
χ	Random number ($-1 \leq \chi \leq 1$)
\mathbf{F}_A	Random acceleration component
w_x, w_y	Damping zone widths
T_0	Desired temperature

Statistical Features

X	Discrete random variable
$E[X]$	Expectation of a random variable X
θ	Population parameter
$\hat{\theta}$	Estimator
\bar{X}	Arithmetic average or arithmetic mean
P	Probability function
σ^2	Population variance of a random variable X
\bar{Y}_n	Mean sample
S^2	Sample variance
$\widehat{S^2}$	Sample cuasi–variance
sd	Sample cuasi–standard deviation

Abstract

One of the most important challenges in mechanics is the modelling of the phenomenological mechanical behaviour of crystals, i.e. understanding material phenomena such as the occurrence of dislocations, vacancies and micro-cracks and their propagation, in order to understand more about how and why materials fail. To provide a reasonable and comprehensive answer to these questions it is necessary to delve deep into the material taking into account the behaviour of the atoms, i.e. what happens at the nanoscale.

Thanks to the ongoing rapid increase and affordability of computer power, simulation methods have become a useful tool in the last decade. Furthermore, they have been established as a realistic computational option with a broad range of applications in many branches of science such as fluid mechanics, physics, chemistry, biology, material science and branches of engineering. Computer methods also have the ability to study the behaviour of complex systems and allow us to compute their features untractable with analytical methods. One of these methods is molecular dynamics, which provides an atomically detailed description of materials. In addition, nowadays it is routinely applied to predict their physical and chemical properties and to investigate structural, dynamical and thermodynamical features. Molecular dynamics can also shorten the gap which is generated by attempting to deduce and measure atomistic quantities directly from the experiment providing a consistent approach to reproduce microscopic behaviour using atomistic models.

The molecular dynamics method follows the trajectories of a set of atoms subjected to several restrictions involving the solution of the classical equation of motion (Newton's equations). In contrast to other simulation methods, molecular dynamics is a deterministic technique since given a set of initial parameters (positions and velocities), the subsequent time evolution is completely determined by integrating the equations of motion. However, the modelling of any realistic structure with macroscopic dimensions is not yet feasible with fully atomistic simulation. This is due to the exhaustive computational demand and the excessive and often useless data that results, since in large scale atomistic simulations only a small set of atoms does anything interesting. In addition, the results can rarely be compared with any direct experimental data since the laboratory observations of this sort of mechanical problem are usually made at different time and length scales.

The continuum mechanics approach has dominated the research activity of mechanics in order to model materials over time and space. The range of application of continuum models allows an efficient computation of large systems of material but at the expense of accuracy and including a number of defects. Moreover, physical phenomena such as

dislocations, plastic deformation or crack evolution, among others, cannot be explained in detail within the continuum mechanics framework.

Generally, the performance of materials cannot be described in a single scale. Different levels are inevitably involved. Therefore, in recent years many research groups have concentrated on developing hybrid approaches with the main objective of combining atomistic and continuum scales. On the one hand, they want to exploit the advantages of atomistic simulations to capture the dynamics at the atomistic scale and gain insight into sub-micron deformational complexity. On the other hand, continuum simulation techniques, e.g. the finite element method, are involved in capturing the smooth parts of the solution. Multiscale techniques reduce the number of degrees of freedom, i.e. the computational cost, and focus only on regions containing interesting information. The key idea is to use molecular dynamics only in localized regions where the deformation complexity is significant, while the finite elements method is applied everywhere else surrounding the atomistic domain. Therefore, the main difficulty is the interplay between accuracy and efficiency.

At the continuum scale the first-order Cauchy-Born rule, originally proposed by the French mathematician Augustin Louis Cauchy, and subsequently broaded by the mathematician and physicist Max Born, is a standard but efficient kinematic assumption to introduce atomistic information to the modelling of material behaviour. The essential postulate states that when a single crystal volume is subjected to a prescribed displacement at its boundary, all atoms of the volume follow this displacement by an affine deformation. The application of the Cauchy-Born rule is restricted to sufficiently homogeneous deformations, at least within the cut-off radius of the atomic interaction. In other words, this rule is not capable of capturing inhomogeneous deformation of the crystal.

The main motivation of this contribution is to introduce a computational laboratory to analyse defects and fractures at the sub-micro scale. To this end, we have attempted to present a continuum-atomistic multiscale algorithm for the analysis of crystalline deformation, i.e. we have combined the above-mentioned Cauchy-Born rule within a finite element approximation (FEM) on the continuum region with a molecular dynamics (MD) resolution on the atomistic domain. The aim is twofold: on the one hand the stability, i.e. validity of the Cauchy-Born rule and its transition to non-affine deformation at the micron-scale is studied with the help of molecular dynamics approach to capture fine-scales features; on the other hand a horizontal FEM/MD, i.e. continuum atomistic coupling, is envisaged in order to study representative cases of crystalline defects. To cope with the latter we have introduced a horizontal coupling method for continuum-atomistic analysis.

The key concept of a horizontal coupling algorithm is to combine an atomistic region and a continuum domain. The atomistic region capture highly inhomogeneous deformations surrounded by the continuum region in order to resolve far-field type smooth deformations. In other words, we will try to interplay accuracy and efficiency in order to study several atomistic phenomena. Unfortunately, the horizontal coupling thereby produces

a common difficulty in these hybrid multiscale models in that the correct treatment of the transition between the atomistic and the continuum regions and thus, the link of the different scales is a severe problem. This inconvenience arises due to the fundamental incompatibility of the non-local character of the atomistic description and the local continuum description.

We will seek to address and to respond to the above mentioned objectives in this dissertation. In the 1st Chapter we will review some of the standard features on the classical molecular dynamics method used for the present work. We will give a brief introduction of some traditional tools such as potentials, algorithms, boundary conditions or statistical mechanics.

The 2nd chapter will begin by focusing firstly on providing a general overview of the first-order Cauchy–Born theoretical background. However, the main purpose of this chapter is the investigation of the rule’s range of validity. We intend to find out the state when the deformation becomes inhomogeneous, i.e. when the use of this rule is inadequate. In order to achieve that, a monoatomic crystal lattice subjected to the Cauchy–Born rule is analysed in conjunction with the molecular dynamics method. Its main objective is to follow the deformation evolution, i.e. the phase-trajectories of a set of particles in a lattice in different deformation cases (simple shear, uniaxial extension, pure shear and dilatation), comparing their positions with the positions of the same atoms in an ideal homogeneous deformation, i.e. a crystal where the Cauchy–Born rule is applied.

In the 3rd chapter, we will restrict our attention to the features of the continuum–atomistic multiscale method combining the Cauchy–Born rule within a finite element method with a molecular dynamics resolution on the atomistic region. The chapter begins with a summary of the essential aspects concerning the kinematics of the continuum modelling. Later on, we will deal with the horizontal-coupling hybrid model itself providing a detailed exposition of the transition between the continuum and atomistic domains. Finally, we will present the acquired results for studying crystalline deformation.

Chapter 4 is devoted to the study of the common difficulties inherent to these hybrid methods as the spurious wave reflections which arise at the boundary due to the constrained boundary conditions. In order to overcome this drawback, a damping zone is implemented to avoid or reduce their negative influence as much as possible. Previously, this damping zone has also been applied for extending the study of the Cauchy–Born rule carried out in Chapter 2.

Finally, Chapter 5 wraps up this work in order to summarize the obtained results as well as point out possible suggestions about future lines of work. An Appendix provides a collection of relevant notation. It also briefly sketches significant material concerning the standard deviation formula devoted to the study of the Cauchy–Born rule and contains a brief explanation of the atomistic stress used within this contribution. Some notions about the acoustic tensor are also mentioned.

Zusammenfassung

Eine der wichtigsten Herausforderungen der Mechanik ist die phänomenologische Beschreibung des mechanischen Verhaltens von Kristallen, wobei insbesondere deren komplexes Versagensverhalten, wie zum Beispiel Entstehung und Kinetik von Versetzungen und Vakanzen, Mikrorissbildung und –ausbreitung von Interesse ist. Um eine angemessene Antwort auf diese Fragenstellung zu erhalten, ist es notwendig, das mechanische Verhalten von Kristallen auf der Nanoskala, d.h. unter Berücksichtigung des atomaren Verhaltens, zu beschreiben.

Aufgrund des permanenten Anstiegs der Rechenleistung moderner Computer ist die klassische Molekulardynamik eine geeignete Methode, um das komplexe Verhalten von Kristallen auf atomarer Ebene zu simulieren. Sie wird inzwischen intensiv zur Prognose von physikalischen, chemischen und thermodynamischen Eigenschaften von Kristallen und Molekülen eingesetzt. Molekulardynamik dient weiterhin dazu, experimentelle Ergebnisse auf atomarer Ebene zu interpretieren und ist daher eine konsistente Methode, um das mikroskopische Verhalten mit Hilfe atomarer Modelle zu reproduzieren.

Die klassische Molekulardynamik ist eine Methode, die unter Verwendung der Newtonschen Bewegungsgleichungen die Trajektorien eines Ensembles von Teilchen, die vorgegebenen Restriktionen (z.B. Volumen, Energie, Temperatur etc.) unterliegen, berechnet. Bei der Molekulardynamik handelt es sich um eine deterministische Methode, denn bei gegebenen Anfangsbedingungen (Positionen und Geschwindigkeiten der N Teilchen) ist das zeitliche Verhalten des betrachteten Teilchenensembles durch die Integration der Bewegungsgleichungen vollständig bestimmt. Allerdings ist es auch mit heutigen Hochleistungsrechnern bei weitem nicht möglich, makroskopische Stoffmengen, wie z.B. Strukturen im Ingenieurwesen, durch molekulardynamische Simulationen zu beschreiben. Derzeit kann mit Höchstleistungsrechnern eine Teilchenzahl von einigen 10^9 Atomen simuliert werden, was im Vergleich zur Avogadro-Zahl (Anzahl der Teilchen pro Mol Stoffmenge) noch verschwindend gering ist. Außerdem liefern entsprechende Simulationen eine kaum beherrschbare Datenmenge, da häufig nur ein kleiner Bereich des betrachteten Ensembles für meist nur kurze Zeit interessantes Verhalten zeigt.

Hingegen ist die Kontinuumsmechanik im Ingenieurwesen eine sehr erfolgreiche Methode zur Beschreibung des zeitlichen und räumlichen Deformationsverhaltens von Materialien. Die Kontinuumsmechanik erlaubt eine effiziente Berechnung von großen Ingenieurstrukturen allerdings auf Kosten der Genauigkeit. Es können viele physikalische Phänomene, die auf der Kristallebene stattfinden, wie z.B. Entstehung und Kinetik von Versetzungen bei Ermüdung, plastischem Fließen oder Ribbildung, im Rahmen der Kontinuumsmechanik nur sehr ungenau modelliert werden.

Zur allgemeinen Beschreibung des Verhaltens von Materialien ist daher eine Beschränkung auf eine Größenskala nicht sinnvoll, sondern es müssen verschiedene Größenskalen betrachtet werden. Deswegen haben sich einige Arbeitsgruppen in den letzten Jahren darauf konzentriert, gemischte Methoden zu entwickeln, die eine Kopplung zwischen atomistischer und kontinuumsmechanischer Skala als Ziel haben. Einerseits sollen Sie die Vorteile der Simulation auf atomistischer Ebene ausnutzen, um die dynamischen Effekte im Kristallgitter einzubeziehen und gleichzeitig einen Einblick in das Mikrodeformationsverhalten des Werkstoffen zu gewinnen. Andererseits werden mit Hilfe der numerischen Kontinuumsmechanik, wie z.B. der Methode der finiten Elemente, jene Bereiche des Anfangswertproblems gelöst, in denen das atomistische Verhalten nicht von Interesse ist. Die Entwicklung sogenannter Multiskalenmethoden ermöglicht somit die Anzahl der Freiheitsgrade und damit den Rechenaufwand zu reduzieren und beschränkt die Anwendung räumlich und zeitlich hochauflösender Methoden auf kleine interessante Bereiche. Die Hauptidee besteht darin, die Molekulardynamik nur auf einen kleinen Bereich mit signifikanten Deformationen anzuwenden, während mit der Methode der finiten Elemente das restliche Gebiet beschrieben wird. Somit gelingt es, Effizienz und Genauigkeit der Simulation zu verknüpfen.

Auf der Kontinuumsebene ist die Cauchy–Born Regel erster Ordnung Standard, aber auch eine effiziente kinematische Annahme um atomistische Information für die Modellierung des Materialverhalten einzusetzen. Sie wird von dem französischer Mathematiker Augustin Louis Cauchy vorgeschlagen and danach von dem deutscher Mathematiker und Physiker Max Born erweitert. Das Postulat der Cauchy–Born Regel lautet: Werden bei einen Einkristallvolumen auf dem Rand die Verschiebungen vorgegeben, dann erfahren alle Atome des Volumens eine affine Deformation. Folglich ist die Anwendung der Cauchy–Born Regel auf hinreichend homogene Deformationen, zumindest innerhalb des cut–off Radius der atomaren Interaktion, beschränkt. Anders formuliert ist diese Regel nicht in der Lage, inhomogene Deformationen von Kristallen zu beschreiben.

Die Hauptmotivation dieser Arbeit ist daher die Entwicklung einer numerischen Methode, um die Kinetik von Kristalldefekten und Reißbildung auf atomistischem Niveau zu studieren. Zu diesem Zweck wird ein neuartiger multi–kontinuumsatomistischer Algorithmus für die Simulation von Kristalldeformationen präsentiert. D.h. es wurde die oben genannte Cauchy–Born Regel mit Hilfe der Methode der finiten Elemente im Kontinuumsgebiet mit der Methode der Molekulardynamik im atomistischen Gebiet kombiniert. Hiermit werden folgende zwei Ziele verfolgt: Auf der einen Seite wurde die Stabilität, d.h. die Gültigkeit der Cauchy–Born Regel und ihr Übergang zu nicht–affinen Deformationen auf der Mikroskala mit Hilfe der Molekulardynamik untersucht, auf der anderen Seite wurde eine horizontale Kopplung zwischen FEM und MD, d.h. eine kontinuums–atomistische Kopplung, vorgenommen, um repräsentative Kristalldefekte zu analysieren. Letzteres wurde durch eine horizontale Kopplung der kontinuums–atomistischen Simulation erreicht. Das Grundkonzept einer horizontalen Kopplung ist, daß ein atomistisches Gebiet zur Erfassung der lokal stark inhomogenen Deformationen von einem Kontinuumsgebiet umgeben ist, das nur die kleinen Deformationgradienten des Fernfelds

abzubilden hat. Hierbei verursacht die horizontale Kopplung ein bekanntes Problem hybrider Multiskalenmodelle, welches sich in der schwierigen Behandlung des Übergangs zwischen atomistischer und kontinuumsmechanischer Modellierung niederschlägt. Diese Schwierigkeit entspringt der fundamentalen Inkompatibilität des nichtlokalen Charakters der atomistischen Beschreibung und der streng lokalen Beschreibung der klassischen Kontinuumsmechanik.

Oben genannte Ziele geben daher die Struktur dieser Arbeit vor. Im 1. Kapitel werden die Grundlagen und Eigenschaften der klassischen Molekulardynamik aufgezeigt. Hierbei werden einige Grundaussagen in Bezug auf Potentiale, Zeitintegrationsalgorithmen, Randbedingungen und statistische Mechanik angesprochen.

Das 2. Kapitel konzentriert sich darauf, die Cauchy–Born Regel zu diskutieren und deren Gültigkeitsbereich zu untersuchen. Ein Schwerpunkt hierbei ist die Charakterisierung des Übergangs von einer homogenen Deformation zu einer inhomogenen Deformation, d.h. jener Zustand, der zum Versagen der Cauchy-Born Regel führt. Dies geschieht anhand von molekulardynamischen Simulationen der Deformationsevolution eines monoatomaren Kristallgitters. Die Zielsetzung hierbei ist der Vergleich der Deformationsevolution einer Menge von Teilchen in einem Gitter bei verschiedenen beispielhaften Deformationen (einfacher und reiner Schub, einachsiger Zug und Dilatation) mit dem homogenen Deformationsverhalten eines Kristallgitters.

Im 3. Kapitel wird eine hybride Multiskalen–Methode vorgestellt, die die Cauchy–Born Regel mit der Methode der finiten Elemente verknüpft, um Fernfeld–Lösungen zu beschreiben, während zur Beschreibung des atomistischen Verhaltens in vergleichsweise kleinen Regionen (Nahfeld–Lösung) die Molekulardynamik Verwendung findet. Nach einer kurzen Einführung in die kontinuumsmechanischen Grundlagen, wird die horizontale Kopplung der Multiskalen–Methode vorgestellt. Dabei steht der Aspekt des Übergangs zwischen atomistischem Gebiet und Kontinuumsgebiet im Vordergrund. Schließlich werden für ausgewählte Deformationen von Kristallgittern numerische Ergebnisse vorgestellt.

Anschließend wird im 4. Kapitel auf einige häufig auftretende Schwierigkeiten eingegangen, die inhärent mit diesen hybriden Multiskalen–Methoden verbunden sind. Hierzu zählen fehlerhafte Reflexionen von Wellen am Rand des atomistischen Gebiets aufgrund der dort vorgenommenen Kopplung zum Kontinuumsgebiet über entsprechende Verschiebungszwangsbedingungen. Deren negativer Einfluß wird durch eine sogenannte Dämpfungszone so weit wie möglich reduziert. Diese zusätzliche Dämpfungszone wurde bereits eingesetzt, um den Gültigkeitsbereich der Cauchy–Born Regel untersuchen zu können.

Schließlich werden im 5. Kapitel die erzielten Ergebnisse zusammengefasst und ein Ausblick auf zukünftige Arbeiten gegeben. Im Anhang wird eine Übersicht über die verwendete Notation und die atomistische Spannung, die in dieser Arbeit Verwendung findet, gegeben. Des Weiteren wird die verwendete Definition zur Berechnung der Standardabweichung im Zusammenhang mit der Cauchy-Born Regel diskutiert.

1 The Molecular Dynamics Method

1.1 Introduction

Computer simulation techniques have widely increased their applications for solving scientific problems since the 1950's thanks to the rapid advances in computer power and accessibility [66]. Figure 1.1 ¹ displays this advancement in computer power throughout the past.

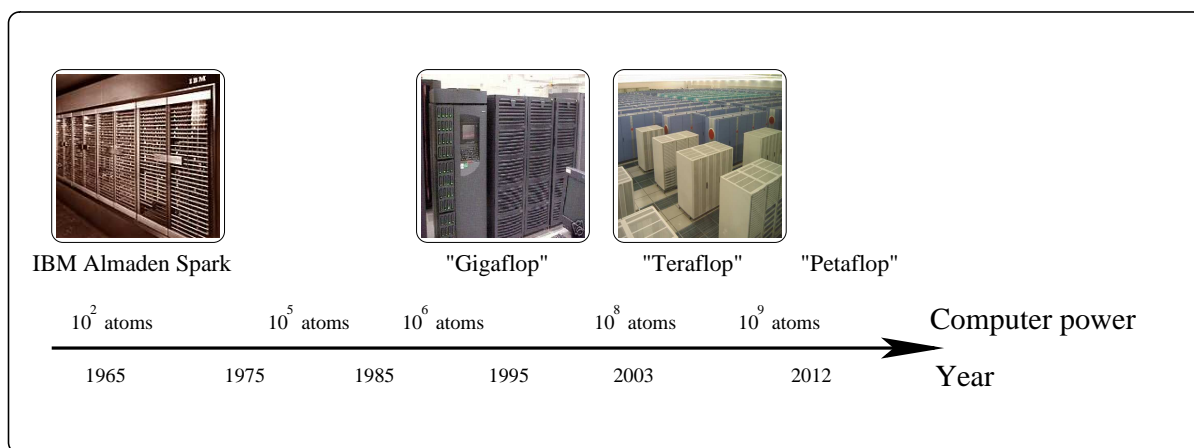


Figure 1.1: Timeline of evolution of computer power from 1960's to present.

Computers can now investigate the behavior of complex systems and calculate their properties untractable with analytical methods. Molecular dynamics belong to one of these methods. It consists of following the evolution of interacting particles in a system in order to study their structural and dynamic features.

The molecular dynamics approach was first proposed by Alder and Wainwright in 1957 [4,5]. They investigated the interactions of hard spheres in liquids. The subsequent work of Gibson et al. [60], is considered to be the first molecular dynamics computation employing finite difference time integration to investigate defects caused by radiation damage. Later, in 1964 a more realistic study of liquids was conducted by Aneesur Rahman [109]. This work contains many important properties used even today in nanofluidic molecular dynamics computations. However, the first molecular dynamics simulation applying a realistic potential appeared ten years later by Rahman together with Stillinger studying the behavior of liquid water [110]. The algorithms also improved very quickly. In 1967,

¹The idea of this figure was taken from the work pursued by Buehler [21]

Loup Verlet, a French physicist, introduced the device known as Verlet neighbour list and his Verlet time integration algorithm in the calculation of phase diagram of Argon using the Lennard–Jones potential [138, 139].

Since these first simulations, the influences and applications of molecular dynamics have rapidly increased in many different scientific fields such as biology, engineering, chemistry and physics. Specifically, since the purpose of this work focuses on solids, molecular dynamics is used to examine the dynamics of atomic-level phenomena that cannot be observed directly. Nowadays, it is widely used to provide not only structural detailed descriptions but also dynamic properties of different types of systems. In addition, macroscopic information such as pressure, energy, heat capacities, etc..., can be obtained from molecular dynamics by using statistical mechanics. However, in complex systems where molecular dynamics is not sufficiently accurate to reproduce the dynamics of molecular systems and more accurate representation is needed, we can obtain electronic behavior by using a quantum chemical method, such as Density Functional Theory (DFT approach). This is known as Ab Initio Molecular Dynamics. With this method the cost of treating the electronic degrees of freedom is much higher than in classical molecular dynamics. This implies that Ab Initio Molecular Dynamics is limited to smaller systems and shorter periods of time.

From now on the present chapter contains a brief overview on the fundamental theoretical foundations of classical molecular dynamics. In addition we will give an introduction of some traditional tools within molecular dynamics such as potentials, algorithms, boundary conditions, statistical mechanics and finally visualization methods emphasizing solids since this is the subject of this work. General references available on the subject are the classical books [7, 58, 63, 64, 66, 111]. In addition, we refer the reader to the works [6, 39, 48, 137] to complete bibliography.

1.2 Fundamental Theoretical Foundations of Classical Molecular Dynamics Method

The molecular dynamics approach is a step-by-step method which consists of solving Newton's classical equation of motion. It is done by using approximate numerical methods to predict the new atom positions and velocities. Its mathematical formula may be written for each atom i in a system constituted by N atoms as

$$m_i \ddot{\mathbf{r}}_i = \mathbf{f}_i, \tag{1.2.1}$$

where m_i is its mass and $\ddot{\mathbf{r}}_i = d_{tt}^2 \mathbf{r}_i$ its acceleration. \mathbf{f}_i represents the force on atom i due to the interactions that all other atoms of the system exert on it.

The positions of the N particles in the system are denoted by $\{\mathbf{r}_1, \mathbf{r}_2, \dots, \mathbf{r}_N\}$ and let $U(\mathbf{r}_1, \mathbf{r}_2, \dots, \mathbf{r}_N)$ define the potential energy of the particles in the system. Once the

potential energy function $U(\mathbf{r}_1, \mathbf{r}_2, \dots, \mathbf{r}_N)$ is specified, the next step is to compute the atomic forces. By definition, the total force \mathbf{f}_i upon an atom i is the negative gradient of the potential function with respect to its position \mathbf{r}_i

$$\mathbf{f}_i = -\nabla_{\mathbf{r}_i} U(\mathbf{r}_1, \mathbf{r}_2, \dots, \mathbf{r}_N) = -\frac{\partial}{\partial \mathbf{r}_i} U(\mathbf{r}_1, \mathbf{r}_2, \dots, \mathbf{r}_N). \quad (1.2.2)$$

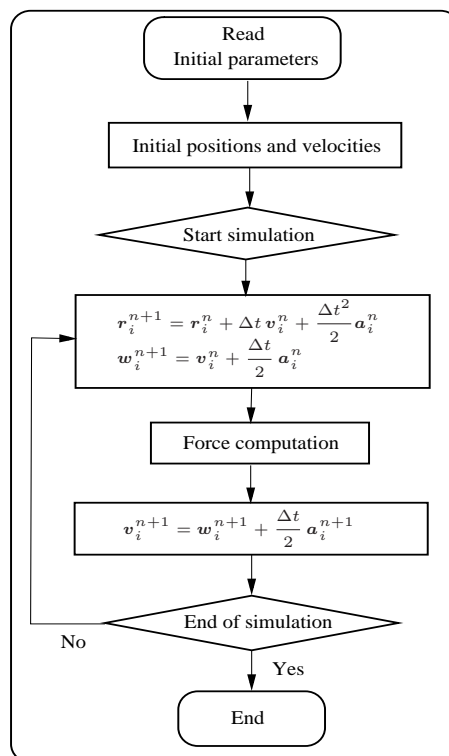
For examples related to the proper calculation of these forces, see appendix C in reference [7]. Combining 1.2.1 and 1.2.2 yields:

$$-\frac{\partial}{\partial \mathbf{r}_i} U(\mathbf{r}_1, \mathbf{r}_2, \dots, \mathbf{r}_N) = m_i \ddot{\mathbf{r}}_i, \quad (1.2.3)$$

which relates the derivative of the potential energy function to the changes in position as a function of time. At the new positions, the atomic forces are recalculated and another step in time is made. This procedure is repeated several thousand times in a typical simulation. The equation 1.2.3 governs the basis for a dynamical description of matter and provides the necessary tools to explain the chemical and physical properties.

A generic molecular dynamics scheme is shown below.

- Read the specific parameters such as temperature, number of particles, density, micro time step, number of time steps (n_{step}), etc ..., necessary to run the simulation.
- Initialize positions and velocities and compute initial forces of atoms.
- Loop $n=1,2, \dots$ until n_{step} .
 1. Integrate equation of motion for each atom.
 2. Compute force on each atom.
 3. Compute the measured quantities.
 4. Compute new time-step. Go back to 1.
- Calculation of the thermodynamical, statical and dynamical properties from atom trajectories.



The next sections will provide a closer view to each aspect of the molecular dynamics approach explained above.

1.3 Initialisation

Before starting any molecular dynamics simulation, it is necessary to assign a set of initial configurations, i.e. a starting point for each atom i in the system at time $t = 0$. It must be done carefully since this could influence the quality of the simulation. There are many ways to do this depending on the features of the simulated model. In the case of solids, they are usually taken either from experimental structures or from positions which result from a previous simulation whenever the number of atoms between simulations remains constant. However, the most common method is to simply generate the crystal lattice by placing the particles in their ideal initial positions [64].

Figure 1.2² shows three typical types of crystal structures, e.g. Simple Crystal (SC), Body-Centered Cubic (BCC) and Face-Centered Cubic (FCC) whereas Figure 1.3³ depicts the configuration of the atoms in the plane $\langle 111 \rangle$ for the same structures.

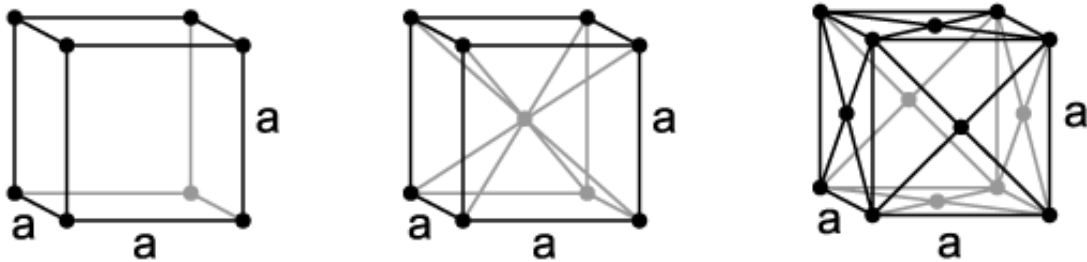


Figure 1.2: Some typical Bravais lattices structures for cubic crystals. (a) Simple Cubic (b) Body-Centered Cubic structure (c) Face-Centered Cubic structure. The lattice parameter is denoted by a which represents the length of one of the edges of the cell. It serves to define the unit cell of a crystal lattice.

The Simple Cubic Crystal (SC) consists of one particle placed on each corner of the cube, see figure 1.2 (a). Then, each particle is shared between eight adjacent cubes and hence, the unit cell (UC) contains in total one atom, i.e. $UC = (1/8) * 8 = 1$. The simple cubic system has a low density. As a consequence this is a high energy structure and therefore is rare in nature [77,96].

The Body-Centered Cubic structure (BCC) is typical in elements such as Li, Na, K, V, Cr, Rb, Fe, Nb, Mo, Cs, Ba, Eu and Ta. It has one atom in the center of the unit cell in addition to eight other atoms on each corner of the cube. It has in total two atoms per unit cell $UC = (1/8) * 8 + 1 = 2$. A primitive cell is used in solid state physics for describing the crystal structure. It is the minimum cell corresponding to a single lattice point of a structure with translational symmetry. The primitive vectors \mathbf{a}_1 , \mathbf{a}_2 and \mathbf{a}_3

²This figure was taken from the web-side http://en.wikipedia.org/wiki/Cubic_crystal_system

³This figure was taken from the web-side <http://physchem.ox.ac.uk/rkt/tutorials/surfaces/solids.html>

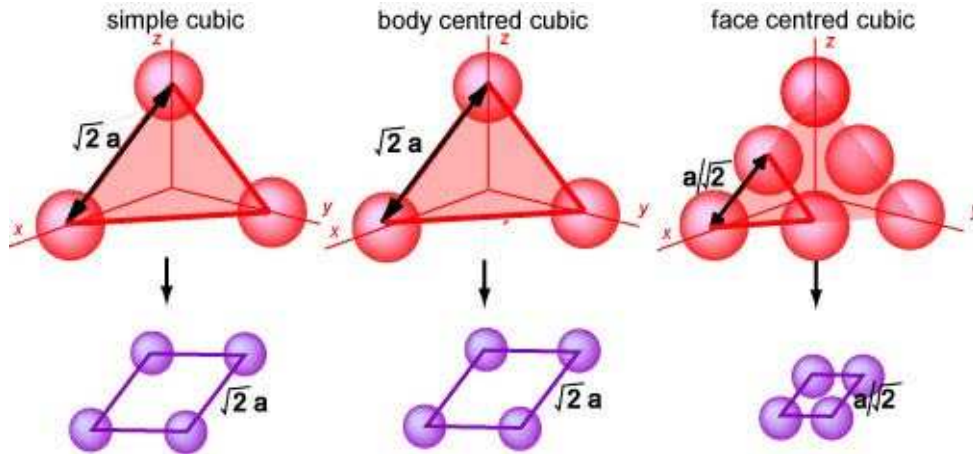


Figure 1.3: This figure illustrates again the same lattices structures as in the previous figure, i.e. Simple Cubic, Body–Centered Cubic and Face–Centered Cubic. They are depicted here in the two–dimensional case showing the plane $\langle 111 \rangle$.

are used to define the primitive cell which in the Body–Centered Cubic structure takes the format

$$\begin{aligned}
 \mathbf{a}_1 &= -\frac{a}{2}\mathbf{e}_x + \frac{a}{2}\mathbf{e}_y + \frac{a}{2}\mathbf{e}_z \\
 \mathbf{a}_2 &= \frac{a}{2}\mathbf{e}_x - \frac{a}{2}\mathbf{e}_y + \frac{a}{2}\mathbf{e}_z \\
 \mathbf{a}_3 &= \frac{a}{2}\mathbf{e}_x + \frac{a}{2}\mathbf{e}_y - \frac{a}{2}\mathbf{e}_z
 \end{aligned} \tag{1.3.1}$$

in which a is the lattice parameter and \mathbf{e}_x , \mathbf{e}_y and \mathbf{e}_z are a basis which serves to generate the lattice [77,96].

Finally, a collection of crystalline structures related to Face–Center Cubic (FCC) lattice for metals are for instance Copper (Cu), Aluminium (Al), Nickel (Ni), Cobalt (Co) and Silver (Ag). It has atoms placed on the faces of the cube in addition to eight corner atoms. Therefore, the unit cell is $UC = (1/8) * 8 + (1/2) * 6 = 4$. The lattice parameter is characterized again by a . Hence, the primitive vectors \mathbf{a}_1 , \mathbf{a}_2 and \mathbf{a}_3 depend on a as follows

$$\begin{aligned}
 \mathbf{a}_1 &= \frac{a}{2}\mathbf{e}_y + \frac{a}{2}\mathbf{e}_z \\
 \mathbf{a}_2 &= \frac{a}{2}\mathbf{e}_x + \frac{a}{2}\mathbf{e}_z \\
 \mathbf{a}_3 &= \frac{a}{2}\mathbf{e}_x + \frac{a}{2}\mathbf{e}_y
 \end{aligned} \tag{1.3.2}$$

In case of defects another possibility is to place the particles as close as possible to the equilibrium, i.e. the state which we wish to compute. Afterwards a minimization technique is applied to bring the system to an energy minimum [106].

It is necessary to assign to each atom in the system a set of initial velocities in order to start up the simulation. They are usually taken from a random function such as Maxwell–Boltzmann distribution [64], see Figure 1.5 (c).

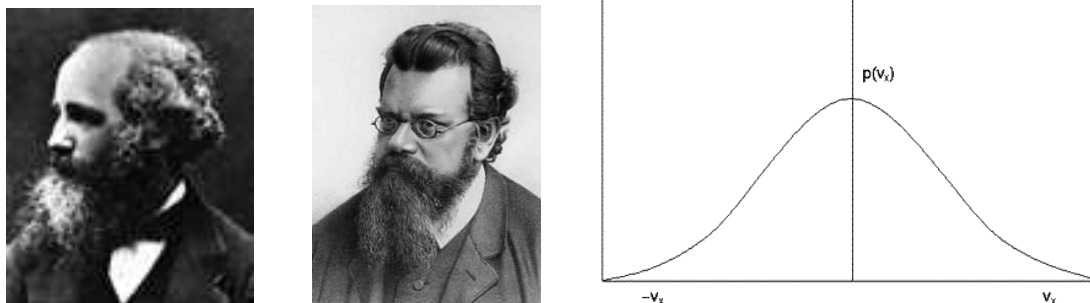


Figure 1.4: On the left, James Clerk Maxwell. (1831–1879). In the middle Ludwig Boltzmann (1844–1906). The right part of the figure shows a Maxwell–Boltzmann common distribution for initial velocities.

Thanks to the symmetry of the function, negative and positive velocities are equally probable. Later, the velocities are scaled to the desired temperature following the relation for each dimension

$$p(v_i) = e^{-\frac{mv_i^2}{2kT}}, \quad i = x, y, z \quad (1.3.3)$$

Then, the velocities are corrected in order to conserve a zero overall momentum, i.e. $\mathbf{P} = \sum m_i \mathbf{v}_i^2 = \mathbf{0}$. With that, the translation of the system is avoided [66]. For details, we refer the reader to [58].

1.4 The Potential Energy Function

Once the atomic interactions are chosen, the material behavior is determined. Therefore, the development of an accurate interatomic potential and its proper derivation for a specific material represents the central issue in molecular dynamics. Three basic questions must be answered to obtain a potential which reflects the physics of the system.

- **Computability:** how expensive this potential is to compute energies and forces. It must be as simple as possible but as complicated as it needs to be.
- **Accuracy:** how many decimal points you ought to believe.
- **Transferability:** The possibility to obtain sensible results over a range of systems, phases or configurations.

The general structure of the potential energy function for a system containing N atoms is divided into terms depending on the coordinates of individual atoms, pairs, triplets, etc, see [7]. It takes the general format

$$U(\mathbf{r}_1, \mathbf{r}_2, \dots, \mathbf{r}_N) = \sum_i V_1(\mathbf{r}_i) + \sum_{i,j>i} V_2(\mathbf{r}_i, \mathbf{r}_j) + \sum_{i,j>i,k>i} V_3(\mathbf{r}_i, \mathbf{r}_j, \mathbf{r}_k) + \dots \quad (1.4.1)$$

The function V_m , with $m = 1, 2, \dots$, is called the m -body potential and \mathbf{r}_N represents the vector position of the N th atom. The first term of the equation 1.4.1 indicates the effect of an external force field on the system where it is immersed such as gravitational or electrostatic [88]. In practice, this term is usually ignored. The second term V_2 shows pair-wise interaction depending only on the pair separation $r_{ij} = |\mathbf{r}_i - \mathbf{r}_j|$ between atoms i and j . The three-body term involves angle-dependent forces whereas four-body term includes torsion effects.

Interatomic potentials can be deduced from quantum-mechanics theory solving the Schrödinger equation keeping into account the electronic structure [121]. However, quantum-mechanics is still limited to short scales in time and length, on the order of a few Angstroms and picoseconds [27]. They obtain an expression of the energy as a function of the nuclei position. But hiding the role of electrons and assuming some empirical interactions giving maximum priority to realism rather than connections with first-principles, several interatomic potentials have been developed with different levels of accuracy during the last decade [22]. They allow us to increase the length and time scales for understanding nanoscale behaviour.

In the following parts of this section we will summarize the main features of some of the most common potentials, with their weakness and strengths. We will start with the most simple and computationally least expensive pair potentials such as Lennard-Jones, Morse or Buckingham, to the more sophisticated multi-body potentials proposed by Finnis and Sinclair [54] or Daw et al. [11,56] in order to capture the electronic structure of real solids.

1.4.1 The Pair Potentials

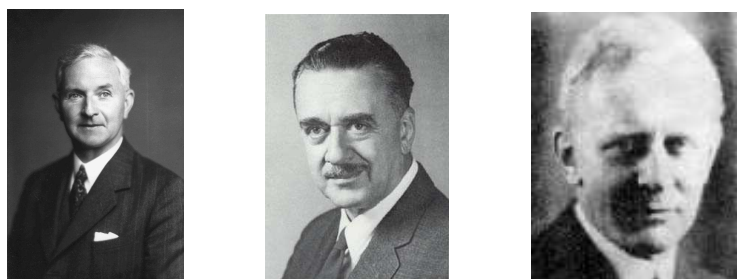


Figure 1.5: On the left Lennard Jones (1894–1954). In the middle Philip M. Morse (1903-1985). On the right Edgar Buckingham (1867–1940)

The simplest choice in order to describe the physics of a system is via pair-potentials which are represented by the second term $V_2(\mathbf{r}_i, \mathbf{r}_j)$ in the equation 1.4.1. Higher-order terms, in the same Equation 1.4.1, do not contribute much compared to pair-interactions and thus, they are usually neglected in molecular dynamics computations. However, their effects are included into an effective pair potential $V_2^{\text{effective}}$ in order to reduce computational cost, such that the potential energy reads

$$U(\mathbf{r}) \approx \sum_i V_1(\mathbf{r}_i) + \sum_{i,j>i} V_2^{\text{effective}}(r_{ij} = |\mathbf{r}_i - \mathbf{r}_j|). \quad (1.4.2)$$

As a consequence, this effective potential depends on the temperature, density and other quantities of the system. From here on, we present several popular pair-potentials. We will represent them by $\phi(r_{ij})$ where $i, j = 1, \dots, N$ with $i \neq j$. N is the number of neighbouring atoms for atom i , which are usually reduced to the second or third closest atoms thanks to the introduction of a cut-off radius. This allows us to save computational demand. A typical pair-wise potential and probably the most commonly used model is the Lennard-Jones potential. It was proposed by the mathematician Lennard Jones [82]. It is given by the expression

$$\phi(r_{ij}) = 4\epsilon \left[\left[\frac{\sigma}{r_{ij}} \right]^{12} - \left[\frac{\sigma}{r_{ij}} \right]^6 \right]. \quad (1.4.3)$$

The parameter σ scales the length and represents the distance to zero in the potential function and the parameter ϵ scales the energy of the atomic bonds and indicates the energy at the minimum in the potential, see Figure 1.6.

The dimension of σ is equal to several Angstroms (\AA), in that $1 \text{\AA} = 10^{-10} \text{ m}$, whereas the dimension of ϵ is typically equal to $10^{-19} \dots 10^{-18} \text{ Joule (J)}$. Sometimes, it is more convenient to use a smaller energy unit such as an electron volt (eV), see Appendix D. The term with power 12 in Equation 1.4.3 dominates at shorter distances and represents atomic repulsion among atoms that are close each other. When the electronic clouds that surround the atoms start to overlap, the energy of the system increases abruptly. Nevertheless, the term with power 6 dominates at large distance and represents the attractive interactions adding cohesion to the system.

The Lennard-Jones potential is derived from the Van der Waals interaction forces. Therefore, only materials that can be modelled fairly well are the weakly interacting rare gases such as Argon or Xenon. Despite this limitation, it is widely used for modelling solids, liquids or clusters when the main purpose is to study a general class of effects and not any particular potential's feature. Due to their simplicity, two body potentials provide a short computing time and the advantage of being easy to deal with them due to the few parameter involved for describing materials. The derivative of the Lennard-Jones potential $\phi(r_{ij})$ with respect to the vector distance \mathbf{r}_i of atom i provides the forces acting on i

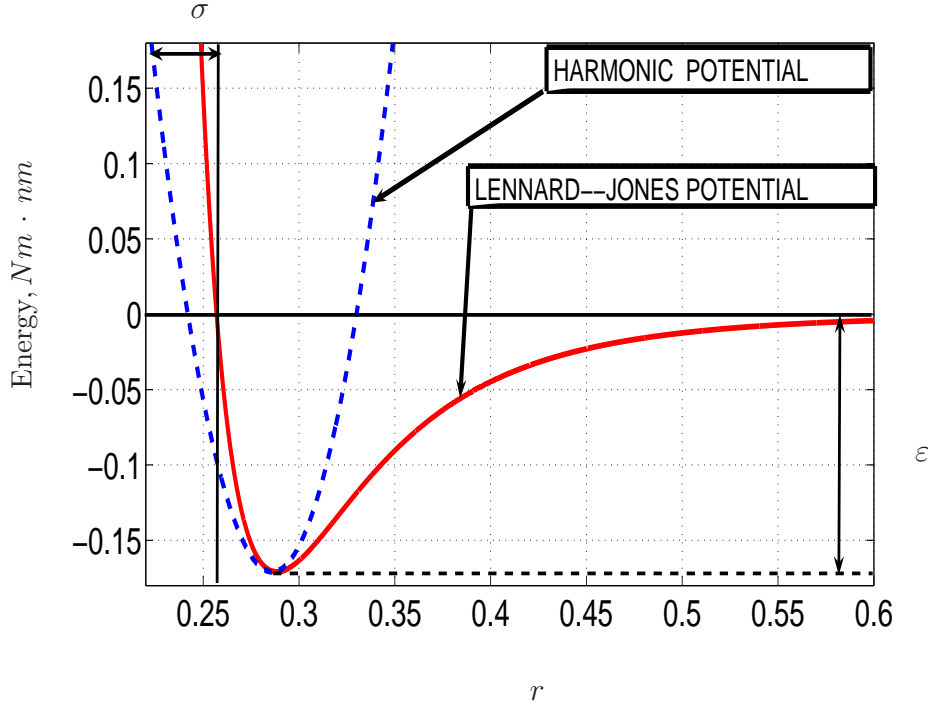


Figure 1.6: Lennard–Jones potential and Harmonic potential (dashed line). Note that the Harmonic potential is a suitable approximation when the particles are around the equilibrium position.

$$\mathbf{F}_i = -\frac{\partial\phi(r_{ij})}{\partial\mathbf{r}_i} = \frac{48\epsilon}{\sigma} \left[\left(\frac{\sigma}{r_{ij}}\right)^{13} - \left(\frac{\sigma}{r_{ij}}\right)^7 \cdot 0.5 \right] \frac{\mathbf{r}_{ij}}{r_{ij}}. \quad (1.4.4)$$

A second pair potential is the Morse potential used for describing the covalent bond proposed by Philip M. Morse in 1929, see [94]. It is given by the expression 1.4.5 in terms of the lattice parameters r and r_0 and the further fitting constants ϵ and α

$$\phi(r_{ij}) = \epsilon \left[e^{2\alpha\left(1-\frac{r_{ij}}{r_0}\right)} - 2e^{\alpha\left(1-\frac{r_{ij}}{r_0}\right)} \right]. \quad (1.4.5)$$

Again, the first term dominates the atomic repulsion at small distances between atoms and the second term governs the attraction at large distances. As can be seen in figure 1.7 the Morse potential has the same curvature as the Lennard–Jones potential at the bottom for $\alpha = 6$ but a harder repulsion at large distances [125].

From the computational viewpoint this potential is more expensive than the Lennard–Jones potential due to the exponential term but more realistic for simulating certain materials. The corresponding force can be expressed as

$$\mathbf{F}_i = -\frac{\partial\phi(r_{ij})}{\partial\mathbf{r}_i} = 2\epsilon\alpha \left[e^{2\alpha\left(1-\frac{r_{ij}}{r_0}\right)} - 2e^{\alpha\left(1-\frac{r_{ij}}{r_0}\right)} \right] \frac{\mathbf{r}_{ij}}{r_{ij}}. \quad (1.4.6)$$

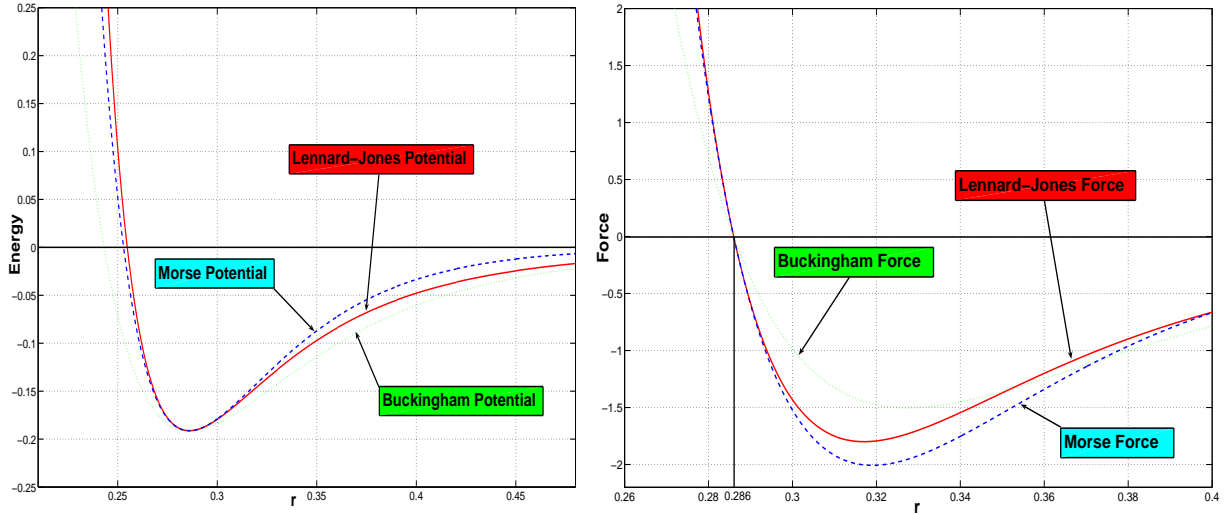


Figure 1.7: On the left, the Buckingham, Morse and Lennard–Jones potentials. The value α chosen to bring the Morse potential to the same equilibrium distance $r_0 = 0.286 \text{ nm}$ as the Lennard–Jones is $\alpha = 6$. For the Buckingham potential the corresponding parameters are $A = \frac{1}{2} - \epsilon$, $B = \sigma^6$, $\alpha = \frac{3}{\frac{1}{2} - \epsilon}$ and $\alpha = 6$. On the right the derivatives of the same potentials are displayed. Note that the minimum of the potential energy functions coincide with the state where the forces render a value equal to zero.

Another popular pair potential is the Buckingham potential, defined by the physicist Edgar Buckingham as

$$\phi(r_{ij}) = Ae^{\alpha(1-\frac{r_{ij}}{r_0})} - \frac{B}{r_{ij}^6}, \quad (1.4.7)$$

with the force acting upon i

$$\mathbf{F}_i = -\frac{\partial\phi(r_{ij})}{\partial\mathbf{r}_i} = \left[A\alpha e^{\alpha(1-\frac{r_{ij}}{r_0})} - \frac{6B}{r_{ij}^7} \right] \frac{\mathbf{r}_{ij}}{r_{ij}}. \quad (1.4.8)$$

The repulsive part of the curve comes from the exponential term in the function. The attractive part derives from the r_{ij}^6 term and is a response to the dispersion forces sometimes called Van der Waals attraction. A drawback of the Buckingham potential is that it becomes strongly attractive at short distances. Keep in mind that the parameters for pair potentials are often derived by fitting the calculated lattice energy at zero temperature to the crystal sublimation energy [116].

The above–mentioned potentials 1.4.3, 1.4.5 and 1.4.7, are nonlinear functions of the radius r_{ij} . Therefore, it is sometimes useful to use the so–called harmonic potential (refer back to Figure 1.6). The mathematical formula reads

$$\phi(r_{ij}) = a_0 + \frac{1}{2}k(r_{ij} - r_0)^2, \quad (1.4.9)$$

where a_0 is a constant parameter, r_0 is the equilibrium position and k represents the spring constant which has the following connection to the parameters ϵ and σ for the case of Lennard–Jones potential

$$k = \frac{24\epsilon}{\sigma^2} \left[26 \cdot 2^{-\frac{14}{6}} - 7 \cdot 2^{-\frac{8}{6}} \right]. \quad (1.4.10)$$

The Cut–off Radius of the Potential Function

An important issue related to compute the internal forces arises due to the imposition of the truncation in the potential functions, Equations 1.4.3, 1.4.5 or 1.4.7. Taking into account the interactions of each current atom i with all others in the system, the computational demand required is $(N^2 - N)/2$ where N is the number of atoms in the model. This can be very expensive even for systems with a small number of particles. Therefore, in practical simulations the introduction of a cut–off radius allows us to reduce significantly the computational effort. The main idea consists of imposing a maximum value of the modulus of the radius vector. Thus, the sum over all the atoms in the body is replaced by interaction only with its nearest neighbours and the number of terms involved is reduced to $nN/2$, with n being the number of atoms into the cut–off radius. The truncated potential can be written as follows

$$U(r) = \begin{cases} V(r) & r \leq r_{\text{cut-off}} \\ 0 & r > r_{\text{cut-off}} \end{cases} \quad (1.4.11)$$

In others words, if the interatomic distances are greater than a certain value, the interactions are simply set to zero. However, it produces a break in the continuity of the potential function at the cut–off separation causing a small step in the energy function as atoms move in and out of the cut–off. This has two consequences. On the one hand it can lead to large fluctuations in the energy during the simulation, i.e. a distortion could arise in the conservation energy. On the other hand, the interactive forces between the atoms are also affected producing anomalous structural features [39]. Although these effects do not cause much disturbance because the cut–off is chosen to make the jump in the energy and force extremely small, a factor f_c can be introduced to assure continuity in the truncated potential as following $V(r) = f_c(r) V(r)$. This provides a smooth transition as can be seen in Figure 1.8.

This truncation function may be applied to any potential energy function. For instance all that is required is to add two terms. See the equation 1.4.12 for the case of Lennard–Jones potential.

$$\phi(r_{ij}) = 4\epsilon \left[\left[\frac{\sigma}{r_{ij}} \right]^{12} - \left[\frac{\sigma}{r_{ij}} \right]^6 \right] + \alpha r_{ij} + \beta \quad r_{ij} < r_{\text{cut-off}}, \quad (1.4.12)$$

where α and β are the constants to be fitted. Firstly, α is derived so that the force at the cut–off radius is zero. β is then chosen so that the potential function is zero at the

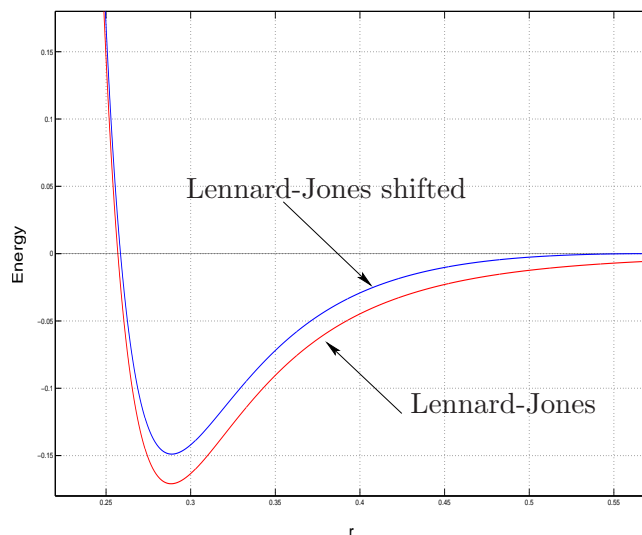


Figure 1.8: The Lennard–Jones and Lennard–Jones shifted potentials. Note how the value of shifted potential is 0 when $r = r_{cut-off}$, in this case $r_{cut-off} = 2r_0 = 0.5720$ nm, being $r_0 = 0.286$ nm fitted to Aluminium.

cut-off [39]. This is referred to the shift cut-off method, see [15]. There are many other ways to obtain a shifted force function and assure a smooth transition, but this is the simplest method. In the next section another example of truncation function f_c is shown. Another possibility is the Switch cut-off method which conserves the usual form of the potential function until a value is reached until zero. The setback to this method is that it suffers from strong forces perturbing the equilibrium.

1.4.2 Many-Body Potentials

The idea behind many-body potentials is to introduce the higher-order terms of the potential function 1.4.1 and thereby incorporate more detailed information about the bonds among atoms. Essentially, they attempt not only to consider the simple distance between two neighbour atoms, but also capture its local environment accounting for the bond formation, their topology and spatial arrangement [85]. They are typically used in simulations of solids and complex molecular structures.

Some traditional formulations to express many-body interactions have been suggested e.g. by Stillinger and Weber [124]. They provide a good description for materials in order to model covalent bonds in silicon's diamond crystal structures. They proposed a potential with two- and three-particle terms as

$$\begin{aligned}
 \phi(1 \dots N) &= \sum_{i,j} V_2(i,j) + \sum_{i,j,k} V_3(i,j,k) \\
 &= \sum_{i,j} \epsilon f_2 \left(\frac{r_{ij}}{\sigma} \right) + \sum_{i,j,k} \epsilon f_3 \left(\frac{r_i}{\sigma}, \frac{r_j}{\sigma}, \frac{r_k}{\sigma} \right),
 \end{aligned} \tag{1.4.13}$$

where ϵ and σ are introduced here to make the potential dimensionless, see also [116]. The two-body term was discussed in the previous section. The three-particle interaction are deduced from the equation

$$f_3 \left(\frac{r_i}{\sigma}, \frac{r_j}{\sigma}, \frac{r_k}{\sigma} \right) = h(r_{ij}, r_{ik}, \theta_{jik}) + h(r_{ji}, r_{jk}, \theta_{ijk}) + h(r_{ki}, r_{kj}, \theta_{ikj}), \quad (1.4.14)$$

with

$$h(r_{ij}, r_{ik}, \theta_{jik}) = \lambda e^{\left(\frac{\gamma}{r_{ij} - a} + \frac{\gamma}{r_{ik} - a} \right)} \left(\cos(\theta_{jik}) + \frac{1}{3} \right)^2. \quad (1.4.15)$$

Here, θ_{jik} represents the angle between the vectors \mathbf{r}_{ij} and \mathbf{r}_{ik} . The potential parameters are γ and λ . The function h is computed when the length of the vectors are smaller than the cut-off considered and it is zero otherwise. The drawback of this description is that it cannot be applied for non-tetrahedral crystals. Moreover, it does not provide the crystal cohesive energy [116].

Another popular many-body potential was proposed by Tersoff [132, 133]. This is also widely used for modelling silicon and other covalent materials. The potential function has the appearance as if it would be a pair potential

$$E = \sum_i E_i = \frac{1}{2} \sum_{i \neq j} V_{ij}, \quad (1.4.16)$$

where V_{ij} takes the format $V_{ij} = f_c(\mathbf{r}_{ij})a_{ij}f_r(r_{ij}) + b_{ij}f_A(r_{ij})$. E is the total energy consisting of the pair contributions. There are two parts that can be distinguished in this equation which are an attractive part described by $f_A(r_{ij})$ and a repulsive part represented by $f_r(r_{ij})$. Both forces are approximated by exponential functions as for the Morse potential equation 1.4.5.

$$\begin{aligned} f_r(r) &= Ae^{-\lambda_1 r} \\ f_A(r) &= -Be^{-\lambda_2 r} \\ f_c(r) &= \begin{cases} 1 & r < R - D \\ \frac{1}{2} - \frac{1}{2} \sin \left[\frac{\pi(r - R)}{D} \right] & R - D < r < R + D \\ 0 & r > R + D \end{cases} \end{aligned} \quad (1.4.17)$$

where $f_c(r)$ is a suitable function which confines the interaction within the cut-off radius considered. A and B are constants and a_{ij} and b_{ij} are bond order parameters, see Selezenev et al. [116]. The Tersoff potential is widely used for a wide range of models. But, it is not easy to parameterize in the angular part. A large number of empirical parameters are needed.

To complete the bibliography we refer the reader to the potential function suggested by Finnis and Sinclair [53, 54]. A review pertaining to these potential functions was done by Carlsson [25].

The Embedded Atom Method (EAM)

The embedded atom method (EAM) is currently the popular choice for modelling metallic systems. The embedded atom method overcomes the lack of information which arises by using only pair-potentials adding an extra term to embed an atom in the background electron density of its neighbours. Thus, it requires more computational work than using only a standard pair-potential function. In the embedded atom method proposed by Foiles, Baskes and Daw [10, 11, 56] the energy is typically given in the form

$$E^{tot} = \sum_i E_i = \sum_i \left[F_i(\rho_i) + \frac{1}{2} \sum_{i \neq j} \phi(r_{ij}) \right]. \quad (1.4.18)$$

Here, $F_i(\bar{\rho}_i)$ specifies the embedded energy function of atom i in the environment with the local electron density $\bar{\rho}_i = \sum_j \rho_j(r_{ij})$ created by the electrons of all other atoms of the system. The distance r_{ij} between atoms i and j and $\phi(r_{ij})$ is the pair potential function describing the short range nuclear repulsion. Again, $\phi(r_{ij})$ and $\rho_j(r_{ij})$ are a short range function with a cut-off distance limited to the first few neighbours. The EAM has performed particularly well to model phenomena such as crack growth [11], grain boundary structure and diffusivity [99].

1.5 Integrator

Due to the deterministic character of the equations of motion and the complicated nature of the potential energy since it is a function of the positions which constitute the system, no analytical solution can be found. Therefore, once the initial positions, velocities and forces at time zero are fixed it is necessary to apply approximate numerical methods. They yield the trajectories of the particles in the system and predict the new atom positions, velocities and forces at any time in the simulation and bring the system in the desired equilibrium. In this section, we will undertake this problem presenting different algorithms.

Before choosing which algorithm must be used, it should satisfy some fundamental requirements and criteria in order to be a good numerical method for the simulation of the system. One of the best general references is [58].

- Accuracy: how accurate is the description of the atomic motion.
- Stability: how well it conserves the system's energy, momentum, angular momentum and temperature while avoiding the fluctuations on them.
- Simplicity: How easy it is to write the computer code for the system.
- Speed: how fast it calculates the atomic motion and the interactive forces.
- Economy: how many computing resources, e.g. memory, are necessary to memorize positions, velocities, forces.

There are several established numeric schemes for integrating the equations of motion. The common algorithms are the Euler, the Verlet, the Leap-Frog, the velocity-Verlet and the Gear or Beeman algorithms. Several of these schemes are described here with more detail.

Verlet Algorithm

Maybe, the most commonly used group of integration algorithms among molecular dynamics programmers are the different versions of the Verlet algorithm. There are three forms, attributed to Verlet [138, 139], which differ slightly in their usefulness but are still essentially equivalent in accuracy and stability. We concentrate here only on the Verlet and the velocity-Verlet algorithm, that is used for the simulations performed in the present work. It is derived by using a Taylor expansion of the position variable \mathbf{r} of the particles around some moment in time t_n . We take the previous ($t_n - \Delta t$) and subsequent ($t_n + \Delta t$) times steps

$$\begin{aligned} \mathbf{r}(t_n + \Delta t) &= \mathbf{r}(t_n) + \Delta t \dot{\mathbf{r}}(t_n) + \frac{1}{2} \Delta t^2 \ddot{\mathbf{r}}(t_n) + \frac{1}{6} \Delta t^3 \dddot{\mathbf{r}}(t_n) + O((t_n)^4), \\ \mathbf{r}(t_n - \Delta t) &= \mathbf{r}(t_n) - \Delta t \dot{\mathbf{r}}(t_n) + \frac{1}{2} \Delta t^2 \ddot{\mathbf{r}}(t_n) - \frac{1}{6} \Delta t^3 \dddot{\mathbf{r}}(t_n) + O((t_n)^4). \end{aligned} \quad (1.5.1)$$

Here, $\dot{\mathbf{r}}$ represents the velocities of each atom in the system. $\ddot{\mathbf{r}}$ is the acceleration and $\dddot{\mathbf{r}}$ the third derivative of the position. Finally, $O((t_n)^4)$ is the error of fourth-order introduced into the integration of the equations of motion. The Δt is the length of the time step used for the numerical integration which relates two close steps in the simulation, see Figure 1.9.

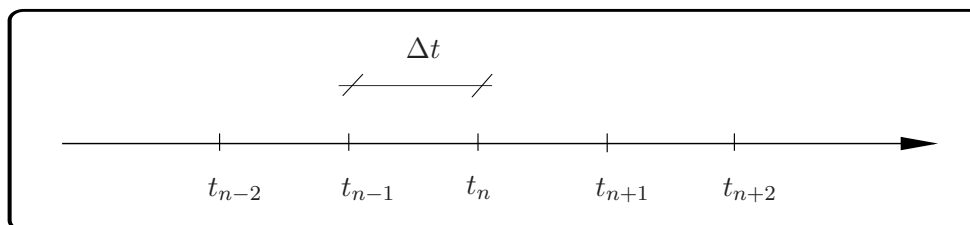


Figure 1.9: Time-step length Δt between two consecutive steps in a molecular dynamics simulation. A typical time-step size used in numerical integration is set to $10^{-14} \dots 10^{-16}$ seconds.

Adding these two equations together yields the update formula for the positions as

$$\mathbf{r}(t_n + \Delta t) + \mathbf{r}(t_n - \Delta t) = 2\mathbf{r}(t_n) + \Delta t^2 \ddot{\mathbf{r}}(t_n) + O((t_n)^4), \quad (1.5.2)$$

and arranging into a more conventional format renders

$$\mathbf{r}(t_n + \Delta t) \approx 2\mathbf{r}(t_n) - \mathbf{r}(t_n - \Delta t) + \Delta t^2 \ddot{\mathbf{r}}(t_n) + O((t_n)^4), \quad (1.5.3)$$

which is the basic form of the Verlet algorithm. The Equation 1.5.3 is correct except for errors in the order of $O((t_n)^4)$ which represents fourth-order and higher terms in the Taylor expansion. If the velocities are needed to estimate the kinetic energy, they can be derived by subtracting these two original Taylor series, i.e. Equations 1.5.1 giving

$$\dot{\mathbf{r}}(t_n) = \frac{\mathbf{r}(t_n + \Delta t) - \mathbf{r}(t_n - \Delta t)}{2\Delta t} + O((t_n)^2). \quad (1.5.4)$$

The velocities are subjected to errors of order $O((t_n)^2)$. A better way to use the Verlet scheme is to implement the velocity–Verlet variant, see examples of application in [105, 128]. Mathematically this is equivalent but from a computational viewpoint it is superior, with a higher precision. Moreover, the handling of the velocities is better than in the other forms of the Verlet algorithm. The velocity–Verlet algorithm stores particle coordinates, velocities, and accelerations at the same time. It takes the form

$$\begin{aligned} \mathbf{r}_i^{n+1} &= \mathbf{r}_i^n + \Delta t \mathbf{v}_i^n + \frac{\Delta t^2}{2} \mathbf{f}_i^n. \\ \mathbf{v}_i^{n+1} &= \mathbf{v}_i^n + \frac{\Delta t}{2} [\mathbf{f}_i^n + \mathbf{f}_i^{n+1}]. \end{aligned} \quad (1.5.5)$$

We will reiterate the sequence of the velocity–Verlet algorithm for understanding facilities, see Table 1.1.

<p>Loop over the number of total time steps</p> <ol style="list-style-type: none"> 1. Compute new positions $\mathbf{r}_i^{n+1} = \mathbf{r}_i^n + h\mathbf{v}_i^n + \frac{h^2}{2}\mathbf{f}_i^n$ $\mathbf{w}_i = \mathbf{v}_i^n + \frac{h}{2}\mathbf{f}_i^n$ 2. Compute new forces $\mathbf{f}_i^{n+1} = \sum_{j \neq i} \mathbf{f}_{ij}^{n+1}$ 3. Compute new velocities $\mathbf{v}_i^{n+1} = \mathbf{w}_i + \frac{h}{2}\mathbf{f}_i^{n+1}$ 5. Compute new time-step. Go to 1.
--



Table 1.1: Sequence of implementation of the velocity–Verlet algorithm. On the right the French physicist Loup Verlet (1931–).

Starting with the initial conditions of the positions and velocities, one can calculate the initial forces. The new positions are computed at the full step. Then, the velocities are

calculated at mid-step. The new forces are obtained thanks to the new positions. In the end, the complete computation of the velocities can be done at the full step. The implementation is also described graphically in figure 1.10⁴

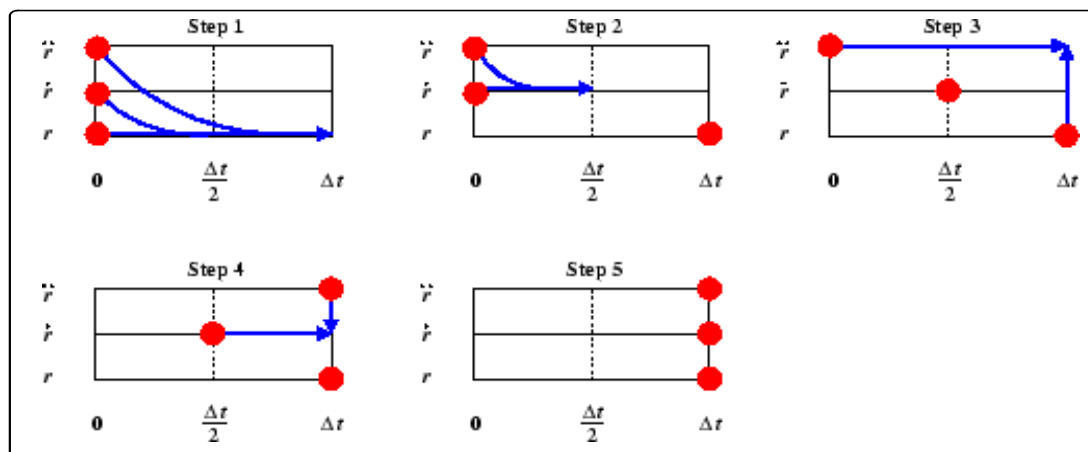


Figure 1.10: Illustration of the velocity-Verlet integration scheme. The initial conditions are given by the positions r_i , velocities \dot{r}_i and forces \ddot{r}_i at time t . In the first step the new positions at time $t + \Delta t$ are computed. In the second step at time $t + \frac{\Delta t}{2}$ the velocities are calculated. Then, the new forces acting upon the particles at their new positions are determined after a full time step $t + \Delta t$. In the closing fourth step the new velocities $\dot{r}_i(t + \Delta t)$ are realized.

This allows the calculation of coordinates and particle velocities in one time step. However, it also requires the accelerations to be stored in the computer since the velocity vector must be computed in two steps. Despite this drawback, it is a very compact algorithm and easy to program. Due to its time reversibility it conserves the energy very well avoiding excessive drift.

Alternative more sophisticated algorithms are the Beeman and the predictor-corrector Gear schemes. They are more accurate due to a higher order of Δt . Therefore, they reduce the error in the integration and present fewer fluctuations in the total energy compared to the above-mentioned algorithms. However, they require a large amount of computer memory due to the large time needed to bridge the simulation until the desired equilibrium state. For more details see for example [58, 137].

Verlet Neighbour List

In order to reduce the computational demand, Verlet conceived a technique called the Verlet neighbour list [138, 139]. This method consists of creating a list for each particle with its neighbours that are inside a radius r_{list} bigger than the $r_{cut-off}$, see Figure 1.11.

⁴This figure was taken from the work pursued by Nicholas Thomas Wilson in the web-side <http://nickwilson.co.uk/research/bham.ac.uk/PhD/node28.html1084>

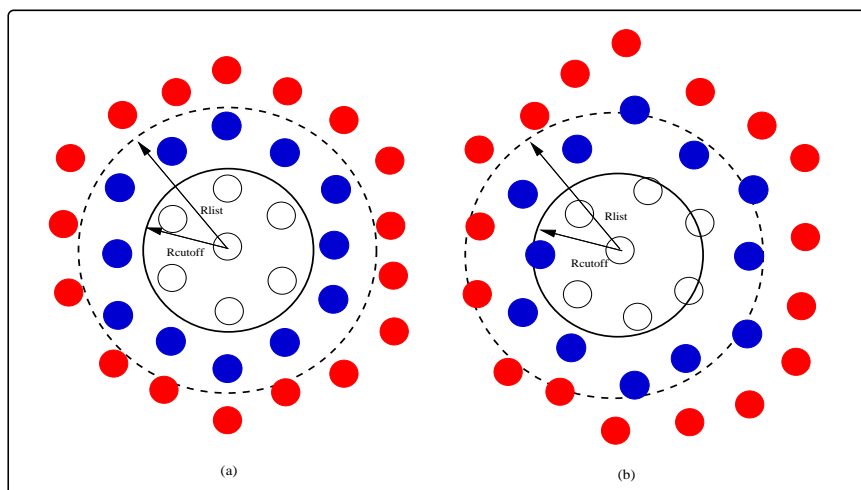


Figure 1.11: Verlet neighbour list to the force calculation in a molecular dynamics simulation. For clarity, the situation in two dimensions is shown. The white and red particles inside the dashed circle constitute the neighbours of Verlet List (figure a). The same particles after a certain number of steps (figure b). The list must be reconstructed before the particles in blue have entered in the cut-off sphere (dashed circle)

Instead of evaluating distances between each particle and the rest of $N - 1$ particles, the method checks the distances only among the particles included in this list. The neighbour list will be reconstructed after a certain number of steps. In low-temperature solids, where the particles do not move too much in two consecutive time steps, it is possible to carry out a simulation with only a few updates or even any at all. Nonetheless, simulations of liquids normally need to be updated more frequently. A typical value of Δr is set to $\Delta r = r_{list} - r_{cut-off} \approx 1.5 \text{ \AA}$ [7]. In summary, a small Δr needs frequent updates of the list. On the contrary a large Δr renders large lists and thus more computations. The time saving is significant for systems between 500 and 5000 particles. For systems with more than 5000 particles, there are other techniques as a link-cell-list which is used in conjunction with the Verlet list, see [7]. In this work, where velocities are considerably low, we will take a radius $r_{list} = 1.1 r_{cut-off}$. That allows us to perform the simulation saving computational time.

1.6 Choice of the Micro Molecular Dynamics Time-Step

The election of the optimum time step Δt in molecular dynamics is clearly one of the crucial or rather delicate tasks that can lead to the success of the simulation since the propagation of the equation of motion is calculated in discrete intervals of time. The time step affects the evolution of the errors during the simulation [48]. Two criteria must be followed, see Liu et al. [88] and Bishop et al. [15].

- The time step should be short enough relative to the time it takes for the whole simulation, so that the simulation of the system is realistic and the accuracy of the algorithm increases.

- The time step should be made as long as possible, so that increment in time permits longer simulations, increasing the efficiency.

Unfortunately, there is not a fixed criterion or equation to choose Δt . One possibility is that the time scale is normally determined by calculating the maximal oscillation frequency of the crystal, which correspond to the Debye frequency [60].

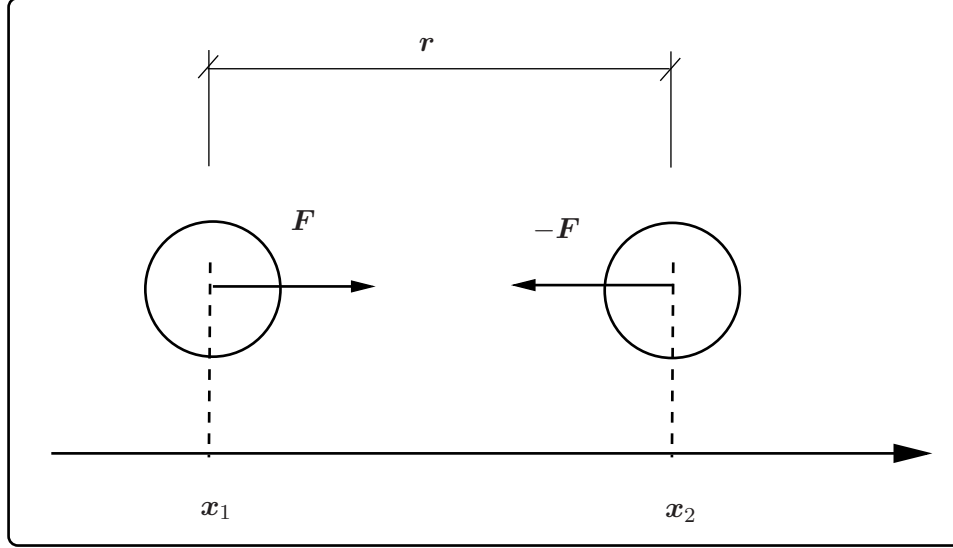


Figure 1.12: Example of interaction between two atoms described via the Lennard–Jones potential in the one–dimensional case.

Let's suppose two particles with the same mass in one–dimension, see Figure 1.12. These particles interact via the Lennard–Jones potential, equation 1.4.3 with interatomic distance r . We assume that they oscillate close to the equilibrium separation r_0 with very small amplitude. Then, the objective is to obtain the value r_0 , which results from condition $d_r \phi_{LJ} \Big|_{r=r_0} = 0$. The first derivative of the Lennard–Jones potential with respect to the separation distance r must be zero at the equilibrium position $r = r_0$. The derivative of the Lennard–Jones potential takes the format

$$\frac{d\phi_{LJ}}{dr} = -\frac{24\epsilon}{\sigma} \left[2 \left[\frac{\sigma}{r} \right]^{13} - \left[\frac{\sigma}{r} \right]^7 \right]. \quad (1.6.1)$$

We then obtain the searched value of the equilibrium distance related to the parameter σ , i.e. $r_0 = \sqrt[6]{2}\sigma$. As we have mentioned above, we suppose that the particles oscillate around r_0 , with harmonic motion. Then, the Harmonic potential energy and its first derivative can be expressed as

$$\phi_{HP} = a_0 + \frac{1}{2}k (r_{ij} - r_0)^2, \quad (1.6.2)$$

$$\frac{d\phi_{HP}}{dr} = k r_{ij}, \quad (1.6.3)$$

extending until the second derivative in the harmonic and Lennard–Jones potentials in order to calculate the parameter k results

$$\left. \begin{array}{l} \frac{d^2\phi_{HP}(r_{ij})}{d^2r} \Big|_{r_0} = k \\ \frac{d^2\phi_{LJ}(r_{ij})}{d^2r} \Big|_{r_0} \approx \frac{72\epsilon}{r_0^2} \end{array} \right\} \Rightarrow k = \frac{72\epsilon}{r_0^2}. \quad (1.6.4)$$

Here, we reiterate the equation of motion of atoms i and j using the gradient of the Harmonic potential

$$\begin{aligned} m\ddot{\mathbf{r}}_i &= -k \mathbf{r}_{ij}. \\ m\ddot{\mathbf{r}}_j &= -k \mathbf{r}_{ji}. \end{aligned} \quad (1.6.5)$$

Subtracting these two equations and taking into account that $\mathbf{r}_{ij} = -\mathbf{r}_{ji}$ yields

$$m(\ddot{\mathbf{r}}_i - \ddot{\mathbf{r}}_j) = -2k \mathbf{r}_{ij}, \quad (1.6.6)$$

which is the classical equation of the simple harmonic oscillator. The general solution is given by

$$r(t) = A \cos(\omega t + \delta), \quad (1.6.7)$$

where A is the amplitude and δ is the phase. They are determined by the initial conditions. Solving this equation results in

$$\omega = \sqrt{\frac{k}{m}} \Rightarrow \omega = \sqrt{\frac{72\epsilon}{mr_0^2}}, \quad (1.6.8)$$

where ω is the sought characteristic frequency of the oscillations that gives us a criterion for selecting the time step. ω is also called Debye frequency ω_D . The time step Δt in the Verlet algorithm is usually chosen to be 10 or 100 times shorter than the period of the highest frequency vibration in the simulation [32].

$$\Delta t = 0.1 \div 0.01 \cdot \omega_D^{-1} \quad (1.6.9)$$

In order to control the proper choice of the time step others authors, such as Heermann [66], recommends that the fluctuations in the total energy should not exceed a percentage of the fluctuations in the potential energy. On the other hand, Gibson et

al. [60] states that the forces must not vary by too large a fraction of itself in one time step. Some practical examples for choosing the time step may be found in the works pursued by Gumbsch et al. [61] and Vitek and Egami [141].

For this work a constant time step is implemented as usual in molecular dynamics but it is possible to use a variable value of the time step to improve the efficiency of the simulation adapted to the required problem as Liu and co-workers proposed, see [88].

1.7 Boundary Conditions

Due to the limitation of the speed of execution in any molecular dynamics program and the prohibitively computational demand required for a large size model, the simulations are usually performed only for a few number of atoms far away from a macroscopic piece of matter. Therefore the imposition of periodic boundary conditions is a clever trick (and also the most popular choice) which enable us to perform a finite relatively small system acting as if it would be an infinite region in size. Figure 1.13⁵ on the left illustrates the basic idea of periodic boundary conditions (PBC).

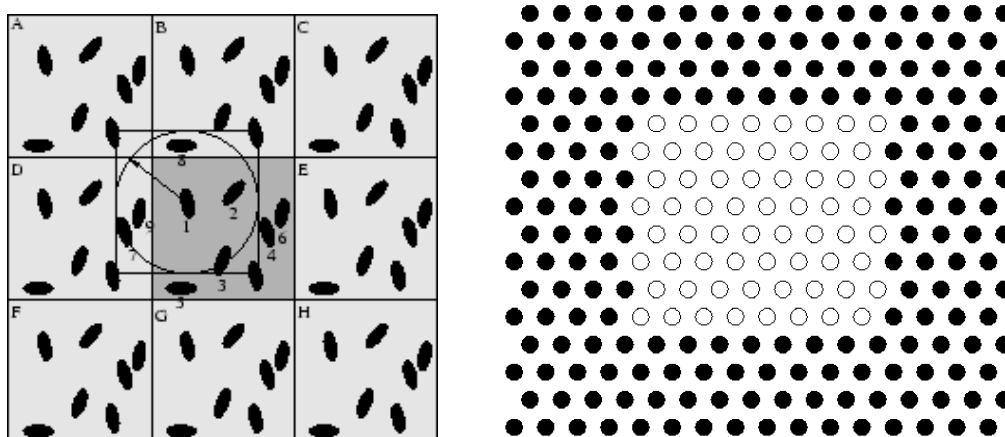


Figure 1.13: On the left the Figure shows Periodic boundary conditions. The center box is shown with its first periodic images. The circle round molecule in red is the cut-off radius. On the right the figure shows rigid boundary conditions. The black atoms are considered as constrained atoms while the white circles are considered as unconstrained particles.

With periodic boundary conditions, one removes the negative surface effects that arise. This is done because the atoms near the boundary have fewer neighbours than the atoms placed inside. The idea is to enclose the particles in a central box and replicate in all directions filling the whole space [39, 66]. Thus, every particle in the cube has a duplicate in each surrounding cell. Furthermore, if an atom leaves any face of the box, another atom immediately emerges from the opposite face replacing it. This ensures that the

⁵This figure was taken from internet under <http://www.compsoc.man.ac.uk/lucky/Democritus/Theory/pbc-mi.html>

atoms can move in all directions without encountering a fixed boundary and the number of atoms are conserved. In addition, the atoms close to the boundary not only interact with their neighbours inside, but also with their images in the nearby boxes. Surface effects have also been removed from the modelled system. This method simplifies the set up of molecular dynamics and is therefore commonly used, see [7, 48].

Other possibilities are to simulate a system without imposing any boundary conditions [137]. This kind of test is only valid for cluster simulations in which the evolution of a number atoms are followed without any surface restriction. However, we will use in our case another kind of boundary conditions, the fixed boundary conditions. This surrounds the perimeter of the cell and does not allow atoms to cross the cell. They assure that the atoms in the middle (white circles), see figure 1.13 on the right, have a complete set of interatomic neighbours. Therefore, the rigid boundary must have a width at least greater than the cut-off radius used to compute the interactive forces. Rigid boundary conditions are normally used when one wants to limit the degrees of freedom of the system.

1.8 Errors in Molecular Dynamics

The errors in a molecular dynamic simulation appear due to the propagation of the equations of motion that are calculated in discrete intervals of time Δt using finite difference [48, 64]. Two kinds of errors can be distinguished:

- Truncation errors: they are related to the accuracy of the finite difference method and how close the solution obtained by the finite difference method is to the real solution. They are associated to the first non-zero term omitted on the Taylor series necessary to deduce the finite difference. Therefore, higher order methods have smaller truncation errors.
- Round-off errors: they refer to the implementation of the algorithm and the number of digits retained in the calculations.

Both errors are related to the time step (Δt). If Δt is very large, the truncation errors dominate. Therefore, it can be reduced by decreasing Δt . On the other hand, the round-off errors also decrease with Δt but at a slower rate. Therefore, they dominate at small Δt but the problems arise because the number of calculations required to reach the desired equilibrium increase and hence, the global round-off error. A very small time step requires large simulations and long scale process although the accuracy of the integration increases. A long time step allows longer simulation time decreasing the accuracy. For this, a compromise must be found.

1.9 Molecular Dynamics at Constant Temperature

The first simulations were performed for systems where the energy is a constant in time for a given boundary conditions. This statistical ensemble is called the microcanonical ensemble (NVE) where the number of particles N , the volume V and E are kept constant.

However, to broaden the applicability of molecular dynamics it is often interesting to perform simulations for studying the behaviour of systems in other ensembles, for example systems where the temperature and/or the pressure are maintained constant [13], rather than keep constant the energy and volume.

Here we concentrate on the so-called canonical ensemble (NVT) where the number of particles N , the volume V and temperature T are maintained constant. Several methods have been proposed and applied to impose these constraints. The simplest form employed in molecular dynamics, but adequate for the purpose of obtaining the required temperature, is the temperature scaling or also called velocity scaling. The idea consists of driving the simulation towards the prescribed temperature by multiplying the velocity of every atom by a factor of $\lambda = \sqrt{\frac{T_{req}}{T(t)}}$ until the prescribed value has been achieved. T_{req} is the required temperature and $T(t)$ is the instantaneous temperature. The method usually tries to correct the temperature rescaling as infrequently as possible to minimize the influence on the trajectories of the atoms at regular intervals during the equilibration period. However, rescaling in every step in order to keep the reference temperature was carried out for instance by Woodcock [149] or Evans [50].

There are some other sophisticated approaches for controlling temperature or pressure in a simulation without having such drastic effects on the molecular motion. These methods include e.g. the Berensen thermostat [13], Andersen thermostat [8] and Nose-Hoover thermostat [72,100], where the system is coupled to a heat bath that imposes the desired temperature. For a general overview we refer here to [58].

1.10 Evaluation of Physical Properties

Molecular Dynamics generates the phase-trajectories of a set of atoms in time. In order to run a molecular dynamics simulation it is necessary to arrange a number of steps. So far we have explained how the initial coordinates and velocities were chosen. We also described several potential functions and the numerical method needed to start up the simulation. Then, during the simulation there is a period called the equilibration process in which the system is periodically scaled to reach the desired state. Afterwards, the simulation continues several times (production phase) where the coordinates and velocities of every single particle are saved. That can take several pico-seconds to nano-seconds. It is during this period where the molecular dynamics simulation provides a huge amount of data at the atomistic scale which should be extracted and interpreted. Here is where statistical mechanics comes into play [51,73]. It provides the theoretical basis to draw observable macroscopic features from microscopic information. The properties can be divided in thermodynamic, static and dynamic. Thermodynamic time dependence properties such as pressure, energy, etc. can be displayed graphically. One axis corresponds to time and the quantity of interest is monitored in the other axis. Structural properties can be evaluated using some quantities as mean-square displacement or radial distribution function. Finally, molecular dynamics allows us to directly compute dynamic properties

such as the velocity autocorrelation function, the diffusion coefficient or the vibrational state density.

1.10.1 Thermodynamical Properties

In the context of molecular dynamics, macroscopic properties are obtained as time averages of instantaneous microscopic mechanical properties. For example, the temperature of the system T , making use of the classic equipartition theorem⁶, is nothing more than a quantity of the average kinetic energy given by

$$\langle E_{kin} \rangle = \frac{1}{2} \sum_i^N m_i v_i^2 = \frac{3}{2} N k_B T. \quad (1.10.1)$$

The kinetic energy denoted by E_{kin} and $\langle E_{kin} \rangle$ represents the kinetic energy time average. N is the number of atoms included in the system and k_B is the Boltzmann constant⁷. Adding this measure to the potential energy U we may deduce the total energy $E = U + E_{kin}$.

The average pressure p is estimated by the virial theorem, which connects kinetic and potential energy by

$$pV = Nk_B T + \langle W \rangle, \quad (1.10.2)$$

where $\langle W \rangle = \frac{1}{3} \left\langle \sum_i^N \mathbf{r}_i \cdot \mathbf{F}_i \right\rangle$ is known as the virial of the system, \mathbf{r}_i being the position of particle i and \mathbf{F}_i the forces upon i . Other important Thermodynamical quantities are for instance the specific heat or entropy. We refer the reader to [58].

1.10.2 Structural Properties

Radial Distribution Function

The radial distribution function (RDF) or commonly written as $g(r)$ is a function to reveal the atomic structure of the simulated system defined by [7, 90]

$$g(r) = \frac{n(r)}{4\pi\rho r^2\Delta r}, \quad (1.10.3)$$

⁶The equipartition theorem was proposed initially by James Clerk Maxwell and broaden later by Ludwig Boltzmann. It states that in an equilibrium system, its internal kinetic energy will distribute itself evenly and each component of the average kinetic energy contribute in the same way to the temperature.

⁷The Boltzmann constant k_B , named after the physicist Ludwig Boltzmann, is a physical constant relating temperature to energy. Its value is $k_B = 1.38062 \cdot 10^{-23} \text{Joule/K} = 8.617380 \cdot 10^5 \text{eVol/K}$

in which Δr is the width of a shell at distance r and $n(r)$ is the mean number of atoms in this shell. The radial distribution function is basically a measure to describe how the atoms are packed around each other, i.e. it is proportional to find two atoms separated by distance r . The technique consists of constructing a number of concentric spheres (circles in two dimensions) with the same width Δr around a chosen atom i , see Figure 1.14.

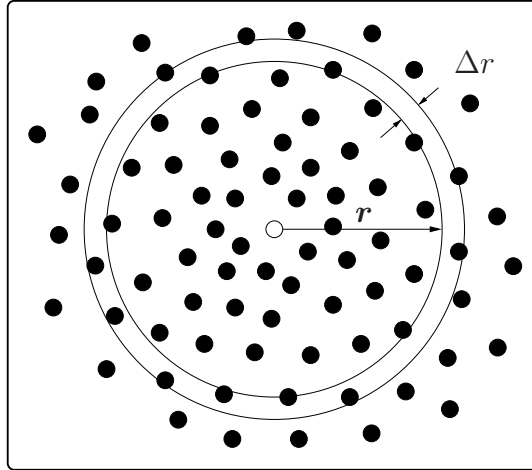


Figure 1.14: Schematic representation of constructing the radial distribution function. For the sake of representation a two dimensional case is depicted. Δr represents the width of a shell at distance r .

In each shell the number of atoms are counted and stored in the course of the computation. In the end, the average number of atoms contained in each shell is calculated according to the equation 1.10.3. The radial distribution function is usually displayed against the separation distance r . In a solid, the atoms are placed in certain cells repeated infinite times in each direction of the lattice. Then, the probability of finding an atom at these distances is very high, whereas in those distances that they do not coincide with these positions the probability is very low. Therefore, the function $g(r)$ will have narrow peaks separated by regions near zero. These peaks appear with regularity in the function of radial distribution. In liquids, $g(r)$ shows an alternation between maximum and minimum, but when the separation distance r increases $g(r)$ is getting plane and constant, more and more like a gas. In gases, the particles are dispersed and in continuous movement. Consequently, the probability of finding the particles in some place is uniform within the simulated box, i.e. is the same for any distance. Therefore the function $g(r)$ is constant. Practical examples can be found in [39].

The Mean-Square Displacement (MSD)

In order to check the behaviour of the atoms in our simulations, Haile [64] offers a tool for monitoring the evolution of a quantity, called the mean-square displacement, for distinguishing a solid from other phases. The mean-square displacement at time t is given by

$$(\Delta r)^2(t) = \frac{1}{N} \sum_i^N [\mathbf{r}_i(t) - \mathbf{r}_i(0)]^2, \quad (1.10.4)$$

where N is the total number of atoms in the system, $\mathbf{r}_i(t)$ is the position vector of the i th atom at time t and $\mathbf{r}_i(0)$ represents the position vector of the same i th atom but at time $t = 0$, i.e. the initial configuration.

A plot is constructed of the average square displacement for all particles versus time. In a solid one should expect that the mean-square displacement stays essentially constant. In a liquid the mean-square displacement versus time should show a linear increase in $(\Delta r)^2(t)$ with time.

1.10.3 Dynamical Properties

The Velocity Autocorrelation Function (VAF)

A correlation function correlates values of a property at two different points in space as well as in time [73]. If we consider the same point in space but at two different times we define that as the autocorrelation function. In summary, time correlation functions determine how the value of a property at a given time is related with its value at an earlier time.

One of the simplest known examples of a correlation function is the velocity autocorrelation function (VAF), which measures the velocity of an atom with subscript i at time t with the velocity of the same atom i at time $t = 0$. The function is defined by

$$C_{VAF}(t) = \frac{\langle \mathbf{v}_i(t) \cdot \mathbf{v}_i(0) \rangle}{\langle (\mathbf{v}_i(0))^2 \rangle}. \quad (1.10.5)$$

The velocity autocorrelation function gives us an idea about the effect of the interatomic forces on the atom's motion. The final result of the VAF is an average of all the VAF computed during the simulation. A typical plot is displayed at the final velocity autocorrelation function for all particles versus time.

If the VAF figure is almost horizontal, than this reveals that the Newton's law keeps the initial state, i.e. the atom's velocities are the same in the course the simulation. That implies that very weak forces are acting in the system. If the interactive forces are small but not negligible, one expects the VAF to decrease gradually revealing the presence of weak forces, which is typical in gases. However, the density in solids of the system increases because the atoms are packed closely together. The positions of these atoms are energetically stable and there is a balance between repulsive and attractive forces. Therefore, the atoms cannot escape easily and they oscillate around these equilibrium positions. Plotting in this case the VAF reveals a function that oscillates strongly from positive to negative decaying in time due to perturbative forces and disturbing the oscillatory motion. In liquids, the interactive forces are much weaker and therefore the VAF may show

an oscillation before decaying rapidly to zero, see for details [39]. Note there exists others parameters to study dynamical properties such as the diffusion coefficient which is deduced from the mean-square displacement using the Einstein relation. See [34, 62] for more details.

1.11 Visualization Methods

Some visualization techniques have been developed in the last years. They have the mission of filtering out the useful information from the amount of data generated during the molecular dynamics simulation. They also allow us to interpret the atomic configurations which results for the characterization of defects. These methods are an efficient tool to assist the statistical mechanics and provide help with understanding the complex phenomena such as dislocations, defects, etc... at the sub-micronscales.

In order to identify crystal defects within the molecular dynamics samples is the energy method in which the potential energy is monitored. It allows to delve into the material to discover imperfections in the lattice. This method only displays the atoms which potential energy go beyond a certain threshold. That reduces the exhibited atoms for visual facilities. That is used for example in the works done by Gumbsch and coworkers [61], Zhou et al. [155] and Gao et. al [23]. It is quite easy to implement but is distorted by the temperature, i.e. the thermal fluctuations of the particles.

Another advanced method is the centrosymmetry parameter. This construction goes back to the work of Kelchner et al. [76]. The main idea is to sum the pair opposite vectors of an atom i and then the square of this sum is added with the rest of neighbours of this atom i . The centrosymmetry parameter for each atom in the lattice is defined as

$$c_i = \sum_{i=1}^6 |\mathbf{r}_i + \mathbf{r}_{i+6}|^2, \quad (1.11.1)$$

where \mathbf{r}_i is vector position of atom i and \mathbf{r}_{i+6} is its opposite neighbour. It gives us an idea if an atom is close to a defect and can distinguish among different defects. The mayor drawback is that the centrosymmetry method can not provide information about the Burgers vector [22].

Another helpful technique is the so-called slip vector approach introduced by Zimmerman et al. [157]. It is used as a criterium to study the dislocation nucleation during the nanoindentation process of a Au crystal. The slip vector of an atom i is defined as

$$\mathbf{s}^i = -\frac{1}{n_s} \sum_{j \neq i}^n (\mathbf{r}^{ij} - \mathbf{R}^{ij}), \quad (1.11.2)$$

where n is the number of closest neighbours to atom i and n_s denotes the number of slipped neighbours. The relative vectors \mathbf{r}^{ij} and \mathbf{R}^{ij} represent the relative distances between atoms i and j in the current and initial configuration respectively. Unlike the

centrosymmetry parameter the slip vector gives information about the Burgers vector. Moreover, it is not only limited to symmetric configurations but also to any microstructure. This technique is only applicable if we have a reference configuration.

Another approach to study structural changes is the near neighbour technique or also called the common neighbor analysis developed by Honeycutt and Andersen [71]. The philosophy behind is to analyse the symmetry of the closest neighbours of a certain atom in any material in order to identify microstructural defects (cores, vacancies, dislocations,...). A similar idea was proposed by Wen et al. [148]. They studied cracking processes of *fcc* nickel and *bcc* iron in an atomistic model. In order to identify different defects during the deformation they suggested a method based on the relative movement of atoms. They introduced the deformation index (DI) defined by $u_i = \max(|\mathbf{r}_{ij} - \mathbf{r}_{ij}^0|)$, where \mathbf{r}_{ij} is the current relative position between i and j and \mathbf{r}_{ij}^0 is the initial relative position between the same atoms. The symbol j refers to the nearest neighbours of atom i .

To analyze atomic structures e.g. phase transitions, some other methods have been proposed such as the local order parameter approach due to Volkov et al. [142], the Voronoi analysis by Brostow [19] and the pair analysis method by Andersen [65, 71]. A review comparing and dealing with some of these approaches was done by Da-Qi Yu et al. [41] and Ju li [83, 84]. Finally, we report that some authors used the virial stress to display mechanical properties at the nano level, see Appendix B.

2 On Aspects of the Cauchy–Born rule and Atomistics

2.1 Introduction

It is well-known that the macroscopic mechanical deformation is a manifestation or rather a consequence of the interaction and organization of a collection of particles, e.g. atoms of crystal lattices, in the microstructure. Therefore, the main goal of many research activities has been to study the complex behaviour at the nanoscale to understand how and why materials fail. In order to investigate this subject we need an atomistic informed model for capturing fine-scale features without exhaustive computational demand. The popular Cauchy–Born rule is essentially a homogenization technique in the continuum mechanics that provides an elegant formulation to bridge atomistic processes from microscale to macroscale, see Tadmor [129]. This classical but essential rule goes back to the French mathematician Augustin Louis Cauchy and subsequently generalized by the mathematician/physicist Max Born, see photos below.



Figure 2.1: Left: Augustin–Louis Cauchy (1789–1857). Right: Max Born (1882–1970)

Cauchy expounded the hypothesis that the atoms displace according to macroscopic deformation. He assumed that atomic and continuum motion are the same [28–31,49]. Born realized that this does not always occur and modified the postulate. Born put forward that only the skeletal structure of a crystalline lattice is moving according to macroscopic deformation¹. Then, the internal atoms fit their positions in the lattice in order to reach the equilibrium [17,18].

The Cauchy–Born rule states that when subjected to a prescribed displacement of its boundary, all atoms of a single crystal volume will follow this displacement, see Milstein [93], Ericksen [49], Zanzotto [152], Sunyk and Steinmann [127]. We consider the

¹We refer here the reader for a deeply explanation of the terms skeletal vs. internal to the work [152]

Cauchy–Born prescription as a constrained atomistic deformation. The Cauchy–Born rule describes with reasonable accuracy the crystal behaviour as long as the unconstrained atomistic deformation, as predicted by an atomistic calculation, remains nearly homogeneous (even when slightly perturbed). However, this assumption fails when the deformation becomes inhomogeneous. One approach to handle the transition between the constrained Cauchy–Born rule deformation and an unconstrained lattice statics is represented by the quasicontinuum approach [118]. Different multiscale methods are compared by Curtin and Miller [40]. In the above works failure of the Cauchy–Born approximation is attributed to the magnitude of the deformation gradient.

The main objective of the present chapter focuses on investigating the stability, i.e. the range of validity of this kinematic assumption restricted to a monatomic crystal with *fcc* structure. In other words, we wish to determinate the state when a transition to non–affine deformation occurs. For this we use the advantages of the molecular dynamics method to capture instabilities.

The work presented here is organized as follows: Firstly, a short overview over the kinematics in continuum mechanics is presented for further clarity. Also the first–order Cauchy–Born rule is introduced. We will summarize the main features of the atomistic failure criteria needed for the study of the Cauchy–Born rule. Then, we will provide some numerical results to analysis its failure under different types of deformation comparing different orientations of the lattice and number of atoms.

2.2 The First–Order Cauchy–Born Rule.

This section focuses on introducing the conceptual idea of the Cauchy–Born rule. We commence with a short description of the kinematics aspects restricted to classical lattice statics. That allows us to outline the main features of this standard assumption as well as the drawbacks involved.

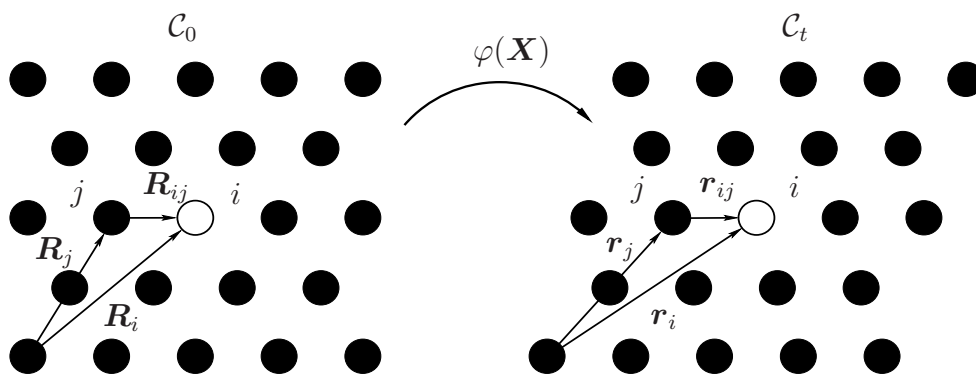


Figure 2.2: Graphical representation of a crystal lattice under homogeneous deformation. \mathcal{C}_0 and \mathcal{C}_t denote the undeformed and deformed crystal lattice configuration. \mathbf{R}_{ij} and \mathbf{r}_{ij} are the relative distance vectors between the atoms i and j in \mathcal{C}_0 and \mathcal{C}_t respectively.

Let us consider a lattice configuration consisting in N interacting particles for a monatomic crystal, see Figure 2.2. The kinematics are typically represented by the relative distance vector between two atoms labelled i and j in the crystallite body, i.e. \mathbf{R}_{ij} in the material lattice configuration \mathcal{C}_0 and \mathbf{r}_{ij} in the spatial lattice configuration \mathcal{C}_t .

$$\mathbf{R}_{ij} = \mathbf{R}_i - \mathbf{R}_j \quad \text{with} \quad R_{ij} = |\mathbf{R}_{ij}|, \quad (2.2.1)$$

$$\mathbf{r}_{ij} = \mathbf{r}_i - \mathbf{r}_j \quad \text{with} \quad r_{ij} = |\mathbf{r}_{ij}|, \quad (2.2.2)$$

where \mathbf{R}_i and \mathbf{R}_j are the position vectors of the atoms i and j in the material configuration respectively and \mathbf{r}_i and \mathbf{r}_j are the position vectors of the same atoms but in the spatial configuration.

In continuum mechanics a body is considered as a collection of material points. In this context, let $\varphi(\mathbf{X})$ denote the non–linear deformation map which relates material points \mathbf{X} in the material configuration \mathcal{B}_0 to points $\mathbf{x} = \varphi(\mathbf{X})$ in the current configuration \mathcal{B}_t , see Figure 2.3.

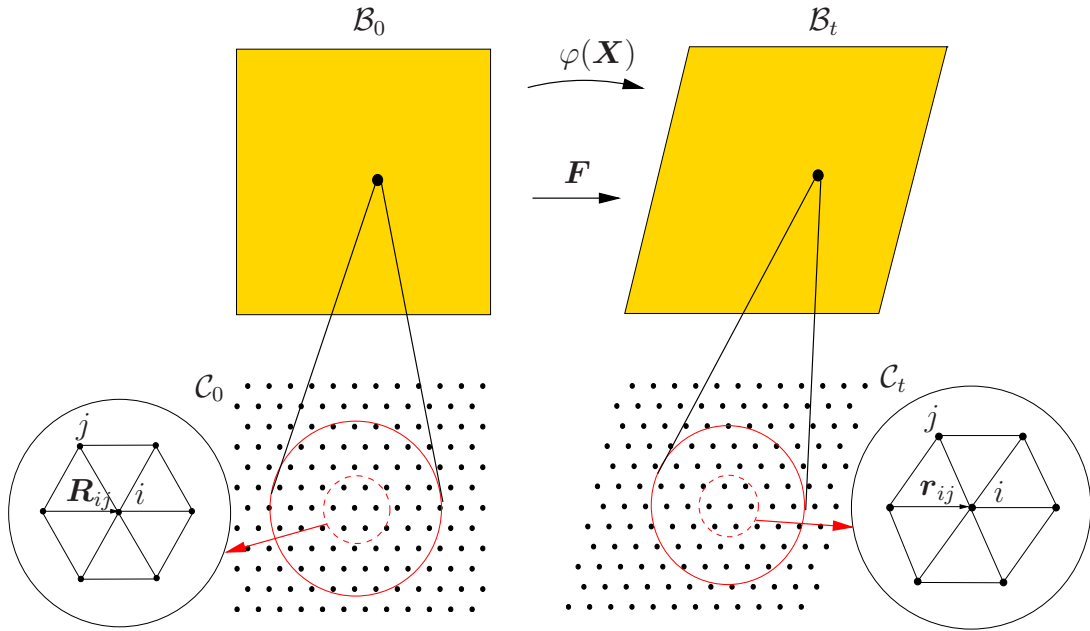


Figure 2.3: (First order) Cauchy–Born rule for the case of homogeneous deformation. \mathcal{C}_0 and \mathcal{C}_t denote the undeformed and deformed crystal lattice configuration. \mathcal{B}_0 and \mathcal{B}_t are the material and spatial configurations of continuum mechanics. The scale transition is given by the Cauchy–Born rule.

This Figure illustrates a schematic representation of the kinematics of continuum mechanics and the Cauchy–Born rule for the case of homogeneous deformation. The two–point tensor \mathbf{F} represents the local continuum deformation gradient, see upper part of Figure 2.3. It defines a linear tangent map given by

$$\mathbf{F} = \nabla_{\mathbf{X}} \varphi = \frac{\partial \varphi}{\partial \mathbf{X}}. \quad (2.2.3)$$

The key idea is to imagine an infinite defect free monatomic single crystal subjected to homogeneous deformation [102]. Under this condition, the Cauchy–Born rule postulates that the infinite crystal is deformed according to the above local deformation gradient, Equation 2.2.3. Mathematically speaking, the relative atomic distance \mathbf{r}_{ij} in the spatial configuration \mathcal{C}_t results from the corresponding relative atomic distance \mathbf{R}_{ij} in the material configuration \mathcal{C}_0 by the application of the deformation gradient \mathbf{F} . Then, the Cauchy–Born rule is defined as

$$\mathbf{r}_{ij} = \mathbf{F} \cdot \mathbf{R}_{ij}. \quad (2.2.4)$$

Thanks to the recent rapid advances in computer power and accessibility, molecular dynamics simulations have been developed very fast in the last few years. It becomes a powerful tool for exploring the features of structures, providing an atomically detailed description at the nanoscale, see [3, 98]. In order to investigate where the use of the Cauchy–Born rule becomes inadequate, we need to find out when the deformation becomes inhomogeneous. Therefore, the introduction of the molecular dynamics method is necessary for providing a detailed atomistic description. The main goal of this contribution consists of using the advantages of this numerical simulation technique to investigate the validity of the Cauchy–Born rule and its transition to inhomogeneous deformation. The validity of the Cauchy–Born rule has also been studied analytically by Friesecke and Theil [59] and using the acoustic tensor as a continuum failure criteria by Sunyk and Steinmann [126].

So far we have introduced some of the essential tools within the continuum mechanics framework. In the next section, we will focus our attention on explaining in detail the atomistic failure criterion established to the study of the Cauchy–Born rule’s validity.

2.3 Atomistic Failure Criteria

The Cauchy–Born assumption describes the behaviour of an atomic system within the range of homogeneous deformation with fair accuracy. However, its major drawback is that it fails when the deformation becomes inhomogeneous. In other words, the Cauchy–Born rule is blind to detect nano defects [130]. Therefore, the purpose of this work consists of investigating the range of its applicability, i.e. find out the state of onset of instabilities. To this end, the introduction of an atomistic failure criterion is needed. This atomistic criterion in the sense of molecular dynamics allow us to capture the deformation complexity as well as atomic displacement.

Before explaining the methodology used here for studying the Cauchy–Born rule, let us start depicting the basic geometry set up for the simulations performed with molecular dynamics approach. See figure 2.4.

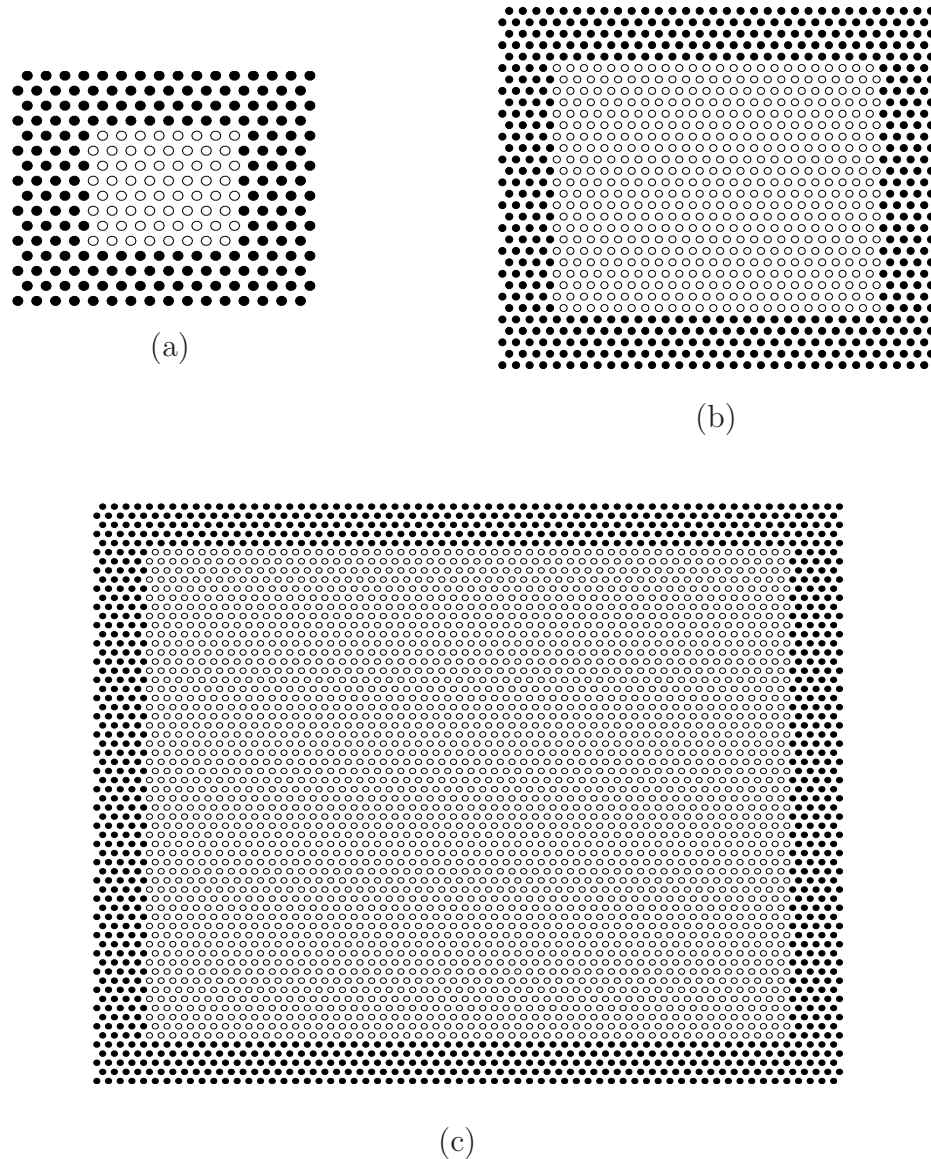


Figure 2.4: An example of the simulation models for 0 degree in the lattice orientation. The Figure (a) contains 256 atoms, the Figure (b) has 1024 atoms and the Figure (c) 4096. The black atoms are obliged to obey the Cauchy–Born rule, whereas the bright atoms are unconstrained.

Without loss of generality, we consider a two–dimensional case of a face centred cubic *fcc* crystal for the $\langle 111 \rangle$ plane of a monatomic system, see Figure 2.5. For the sake of simplicity the lattices with an orientation of 0 degree are shown. Note that the simulations were also performed to others orientations, 15 and 30 degrees, see Figure 2.6. In the physical domain two different spatial regions can be distinguished. On the boundary (black circles), the atoms are constrained and forced to follow the Cauchy–Born rule. They are also used as boundary condition for the simulation (its distance must be at least the cut–off radius considered for computing the interactive forces). On the other hand, the atoms inside

(bright circles) represent the region of interest. This region is formed by 64, 528 and 2997 atoms for the case of 256, 1024 and 4096 atoms in the respectively model.

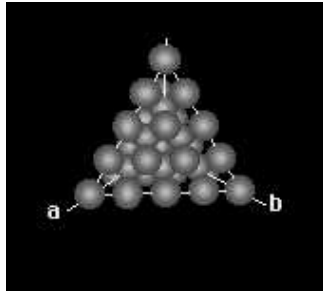


Figure 2.5: Illustrative figure of a *fcc* structure and the plane $\langle 111 \rangle$.

Two types of simulations have been performed in order to compare the accuracy of the results. They are detailed below.

1. The philosophy of the first type of computations is to study the stability against small perturbations in the sense of Lyapunov. The simulation procedure is divided in macro steps and micro iterations. In each macro step the Cauchy–Born rule is prescribed in a predictor step to the whole domain (in the constrained and unconstrained atoms). Then, a slight perturbation, this is a small initial random velocities following a Maxwell distribution is given only to the unconstrained atoms with the purpose of checking if the atoms recover the homogeneous configuration. Afterwards, a molecular dynamics simulation is performed using the velocity scaling method. It consists of rescaling the system temperature (velocities) of the unconstrained atoms in a proportional manner at regular intervals during the equilibration period until 0 K temperature [137]. If the instantaneous temperature exceeds a certain tolerance limit, then the temperature is rescaled. This part of the simulation is performed in 2000 micro steps. Once the system achieves the internal equilibrium another macro step or rather a deformation according to the Cauchy–Born rule is once again applied to the whole domain. With these macro steps and micro molecular dynamic iterations we attempt to check the stability of this assumption, i.e. find out the point in which this rule becomes inadequate due to instabilities.
2. The second type of simulations were also performed iteratively in macro steps and micro molecular dynamics simulations. The main difference to the other procedure is that in each macro step the Cauchy–Born rule is only applied on the boundary (not in the whole domain). In other words, only the constrained atoms are obliged to track the Cauchy–Born rule in order to generate deformation. After a macro step a molecular dynamics simulation is performed using again the velocity scaling method. An initial perturbation is applied to the unconstrained atoms in order to forced them to follow the deformation occurred on the boundary. Then, we relax the system temperature (velocities) in a proportional manner at regular intervals until a 0 K temperature is reached [137]. In this case the relaxation procedure takes approximately 4500 micro time steps because of the time necessary to accommodate

the atoms or rather to bring the system in a new quasistatic position. Once again a macro step is done. Only the atoms on the boundary are forced to follow the Cauchy–Born rule. The simulation continues with these macro increments and micro iterations until the prescribed deformation or the transition to non–affine deformation is achieved.

The choice of the number of macro steps is a compromise related to the choice of the total number of molecular dynamics time steps in each macro step (do not confuse with the micro–molecular dynamics time step Δt). Given a prescribed deformation, if we select a large number of macrosteps to achieve this deformation, i.e. the leap between two consecutive macrosteps is relatively small, we do not need a large number of molecular dynamics time steps in order to relax the system. On the contrary, in the case of taking a small number of macrosteps, i.e. if we choose a relative bigger leap between two consecutive macrosteps, we are forced to select a large number of molecular dynamics steps in order to relax the system.

As we have mentioned earlier, the key goal is to study the range where the Cauchy–Born rule is applicable or in others words, find out the state where the deformation becomes inhomogeneous. Therefore, the position of each atom i in the lattice of each macrostep for both types of computations is followed during the ensuing deformation by the molecular dynamics. We compute the standard deviation ², denoted by sd , in each macroscopic deformation step according to the equation

$$sd = \sqrt{\frac{1}{N-1} \sum_{i=1}^N [\mathbf{r}_i^{CB} - \mathbf{r}_i^{MD}]^2}. \quad (2.3.1)$$

The position \mathbf{r}_i^{CB} of the atom i indicates the constrained position in a lattice under the prescription of homogeneous deformation or rather the Cauchy–Born rule. \mathbf{r}_i^{MD} is the position of the same atom i but in a lattice where the unconstrained molecular dynamics are considered after perturbation. N represents the number of constrained and unconstrained atoms in our model. Summarizing, the standard deviation compares the position of each atom i in our system with itself as if it displaces as an ideal Cauchy–Born deformation. That gives us an idea about the behaviour of the system during the deformation process.

2.4 On the Validity of the Cauchy–Born Rule in the Two Dimensional Case. Numerical Results.

In order to investigate the limitations of the Cauchy–Born rule and the transition to non–affine deformation, several types of deformation such as simple shear, uniaxial extension, pure shear and dilatation have been performed. Different lattice orientations adopting the values 0, 15 and 30 degrees were also considered to compare results as visualized in Figure 2.6.

²See details of the standard deviation in Appendix A

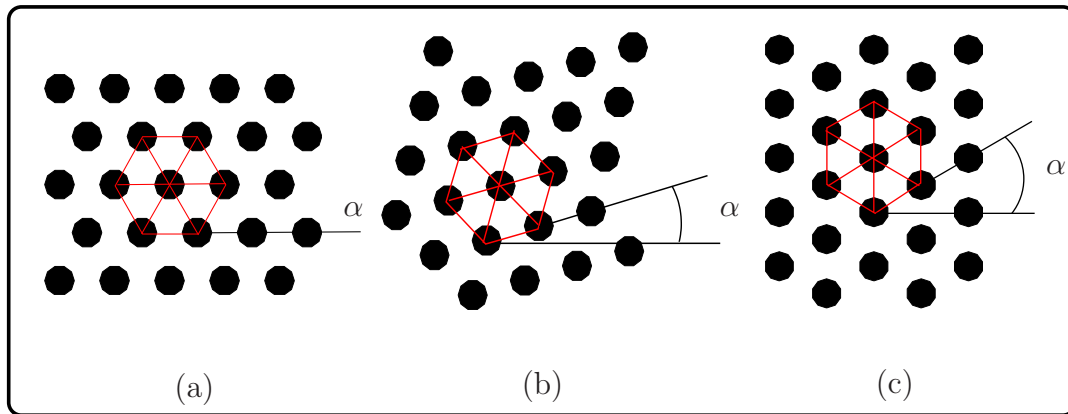


Figure 2.6: Different orientations of the lattice in two dimensional case for a $\langle 111 \rangle$ plane. The lattice orientation $\alpha^o = 0$ is represented in the figure a. The orientations $\alpha^o = 15$ and $\alpha^o = 30$ are shown in figure b and c respectively.

To study convergence (like in the case of mesh refinement) the simulations must be performed with a varying number of unconstrained atoms. The number of atoms which compose the lattice take the values 256, 1024 and 4096 particles, see Figure 2.4. The lattice constant r_0 in the reference configuration has the value $r_0 = 0.286 \text{ nm}$ and the cut-off radius r_c considered is $r_c = nr_0$ with $n = 3$. That means, that we considered the atoms included in a circle with a radius $3r_0$ as we can see in Figure 2.7. This allows us to reduce the computational effort (the reasons to choose this cut-off radius are explained later for each case of deformation).

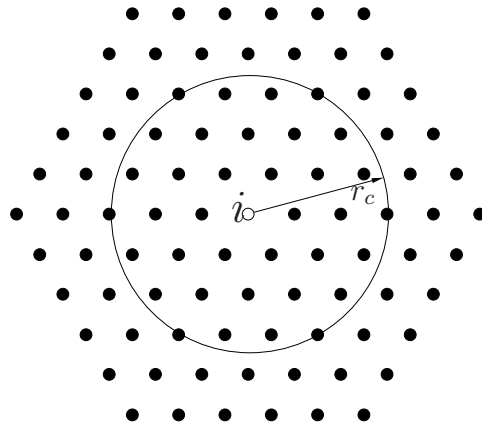


Figure 2.7: Representation of the cut-off radius r_c considered in our simulations that limit the summation range of the interatomic forces to a domain around the atom i .

For the present work, the Lennard–Jones potential, Equation 1.4.3, is considered for the molecular dynamics computations. The parameters σ and ϵ , that are fitted to Aluminium in our computations, are obtained from the table 2.1 of reference [125] for the value $n = 3$ and deduced from the values given in [42]. We reiterate this table here, see Table 2.1.

n	Number atoms	$\varepsilon (nN \cdot nm)$	$\sigma (nm)$
1	6	0.1913	0.2547
2	12	0.1729	0.2569
3	18	0.1706	0.2572
4	24	0.1701	0.2573
5	30	0.1699	0.2573

Table 2.1: Parameters ε and σ of the Lennard – Jones pair potential. The first column represents the number of next neighbours considered in the lattice configuration. The second column indicates the number of atoms included in the corresponding cut–off radius considered.

The equations of motion are solved numerically using the velocity–Verlet algorithm. This yields the trajectories of the particles described by the positions, velocities and accelerations when they change with respect to time. The Verlet neighbour list is used for computing the interactive forces, see Section 1.5. The sphere radius for each atom is $r_{list} = 1.1 r_c$. This r_{list} combined with the cut–off radius, substantially reduces the computational time for the purpose of this work. The molecular dynamics (micro) step is set to $1.0 \times 10^{-15} sec$ in both types of simulations. Finally, the step size between two consecutive macro steps during the molecular dynamics simulation are shown in the table 2.2.

Type of deformation	Cauchy–Born rule & Molecular dynamics	Molecular dynamics
simple shear	$\Delta\alpha = \pi/5000$	$\Delta\alpha = \pi/12000$
uniaxial extension	$\Delta\lambda = 1.002\sigma$	$\Delta\lambda = 1.0004\sigma$
pure shear	$\Delta\lambda = 1.0015\sigma$	$\Delta\lambda = 1.0004\sigma$
dilatation	$\Delta\lambda = 1.0015\sigma$	$\Delta\lambda = 1.0004\sigma$

Table 2.2: The first column shows the type of deformation performed, simple shear, uniaxial extension, pure shear and dilatation. The second column of the table shows the step size between two consecutive macro steps for these cases of considered deformation. Here, the Cauchy–Born rule was applied in the whole system. The third column represents the step size between two consecutive macro steps for the same cases of deformation. But here, the Cauchy–Born rule is only applied on the boundary.

Several cases of deformation are presented in the next section. In the first case, a simple shear deformation has been performed. In the second case an uniaxial extension has been computed. In the end, a pure shear deformation and dilatation deformation have been analysed to complete this study.

2.4.1 Simple Shear Deformation

The simple shear deformation is characterised by the deformation gradient

$$\mathbf{F} = \mathbf{I} + \gamma [\mathbf{e}_1 \otimes \mathbf{e}_2], \quad (2.4.1)$$

where \mathbf{e}_i , $i = 1, 2$ are the Cartesian basis vectors, \mathbf{I} denotes the identity tensor and the factor γ represents the shear number $\gamma = \tan(\alpha)$, see Figure 2.8.

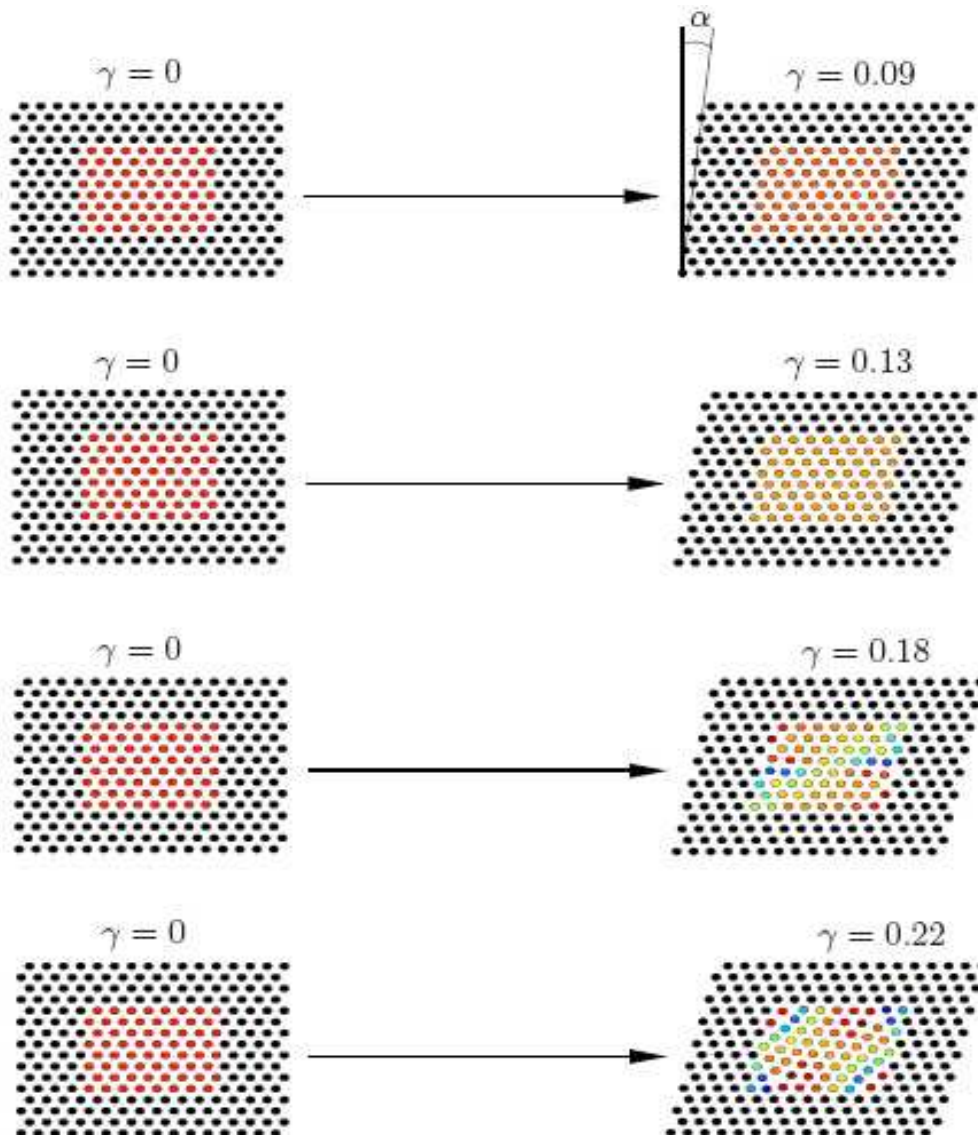


Figure 2.8: Material and spatial crystallite configuration for simple shear deformation. In the top row a homogeneous deformation state of the constrained atoms corresponds to the validity of the Cauchy–Born rule. In the bottom row an inhomogeneous deformation state of the unconstrained atoms indicates the loss of validity of the Cauchy–Born rule. For the sake of representation the results for only 256 atoms and 0 degrees lattice orientation are shown.

Figure 2.8 represents the shear deformation evolution for different values of γ . For simple shear deformation, the atoms are forced to displace tangentially. For sake of representation, the lattice depicted in Figure 2.8 shows a configuration with only 256 atoms with orientation 0 degrees.

Simple Shear Deformation and the Influence of the Cut–Off Radius.

The choice of the cut–off radius is a crucial issue in any atomistic simulation using potential functions, particularly in molecular dynamics due to the influence in the computational demand. Therefore, several simulations were performed in order to determine the proper cut–off radius for our next computations. The characteristics of the lattice are: 5320 atoms, divided in 2997 unconstrained atoms and 2323 constrained atoms with lattice orientation 0 degree, see Figure 2.6 (a). All simulations were computed with the same micro molecular dynamics time step, equal to $1.0 \times 10^{-15} \text{sec}$ and the same number of macro steps. The parameters σ and ϵ of the Lennard–Jones potential (1.4.3) are chosen according to the Table 2.1 of the reference [125] for different values of the cut–off radius (see also Table 2.1).

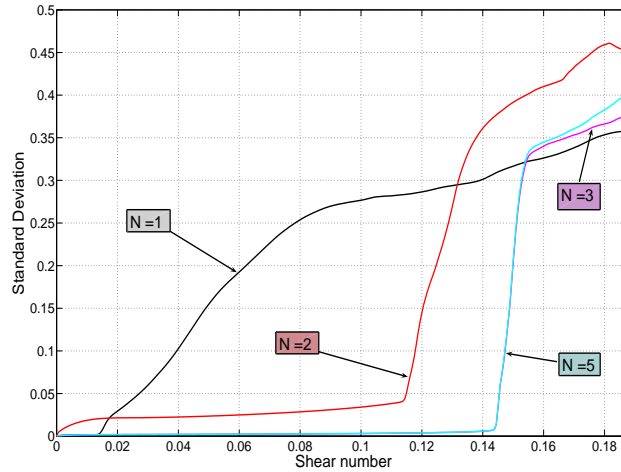


Figure 2.9: Standard deviation for simple shear deformation using Lennard–Jones potential comparing different cut–off radius for 0 degree lattice orientation. The cut–off radius correspond of $n = 3$ seems to be a good approximation to compute the interactive forces.

Figure 2.9 shows the evolution of the standard deviation versus the shear number γ for several values of cut–off radius. It is easy to recognize that the standard deviation converges to a shear number of $\gamma = 0.144$ when the cut–off radius is increased and more atoms are considered for computing the interactive forces. Of course with that the accuracy increases but at the expense of the computational demand. It may also be observed that the difference between $n = 3$ and $n = 5$ is insignificant. Therefore, hereafter the cut–off radius for the simple shear deformation case is chosen to be $n = 3$. That represents the next three neighbours or rather 36 atoms altogether at the beginning of the simulation, see Figure 2.7. That allows us to significantly reduce the computational effort without too much loss of accuracy.

Simple Shear Deformation for Lennard–Jones Potential.

Figure 2.10 shows the evolution of the standard deviation versus the shear number γ . We wish to check the influence of the number of atoms when they are progressively increased in the lattice. The orientations considered were 0, 15 and 30 degrees. In each figure, it can be seen that from a shear number of $\gamma = 0$ to a shear number between $\gamma = 0.14$ and $\gamma = 0.16$, depending on the number of atoms considered in our model, the standard deviation has a value approximately constant and equal to zero.

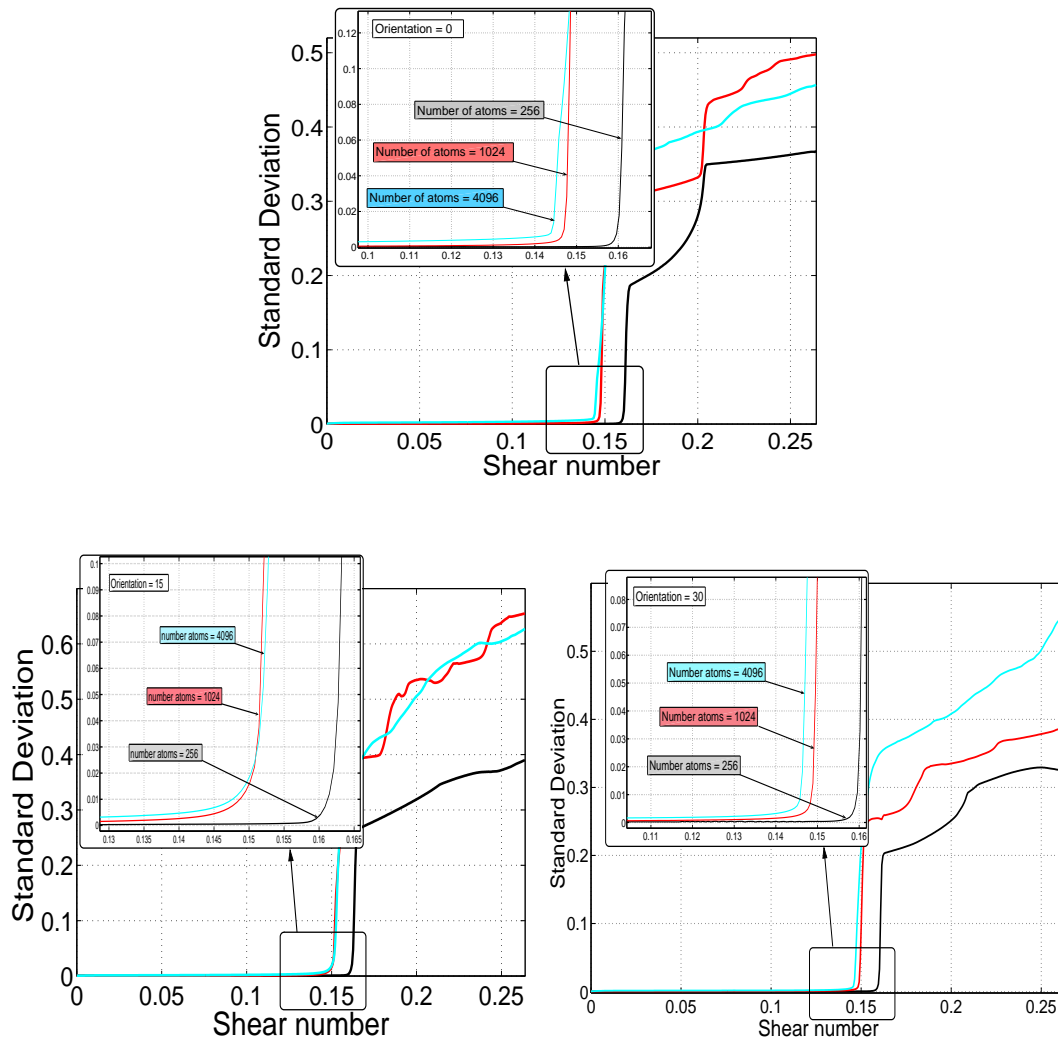


Figure 2.10: Standard deviation versus the shear number γ for simple shear deformation using Lennard–Jones potential comparing 256, 1024, 4096 number of atoms for 0, 15 and 30 degrees lattice orientation. The shear number that marks deviation from the Cauchy–Born rule converges with higher numbers of unconstrained atoms.

Thus, the unconstrained lattice follows essentially the homogeneous deformation, i.e. the Cauchy–Born rule renders stable atomic positions. From this deformation state, the value of the standard deviation increases dramatically, indicating the limit of the Cauchy–Born rule where the deformation starts to be inhomogeneous. In all of them, the shear

number that marks deviation from the Cauchy–Born rule converges with higher number of unconstrained atoms to a value close to $\gamma \approx 0.14$ as can be seen in the detailed figures placed on them.

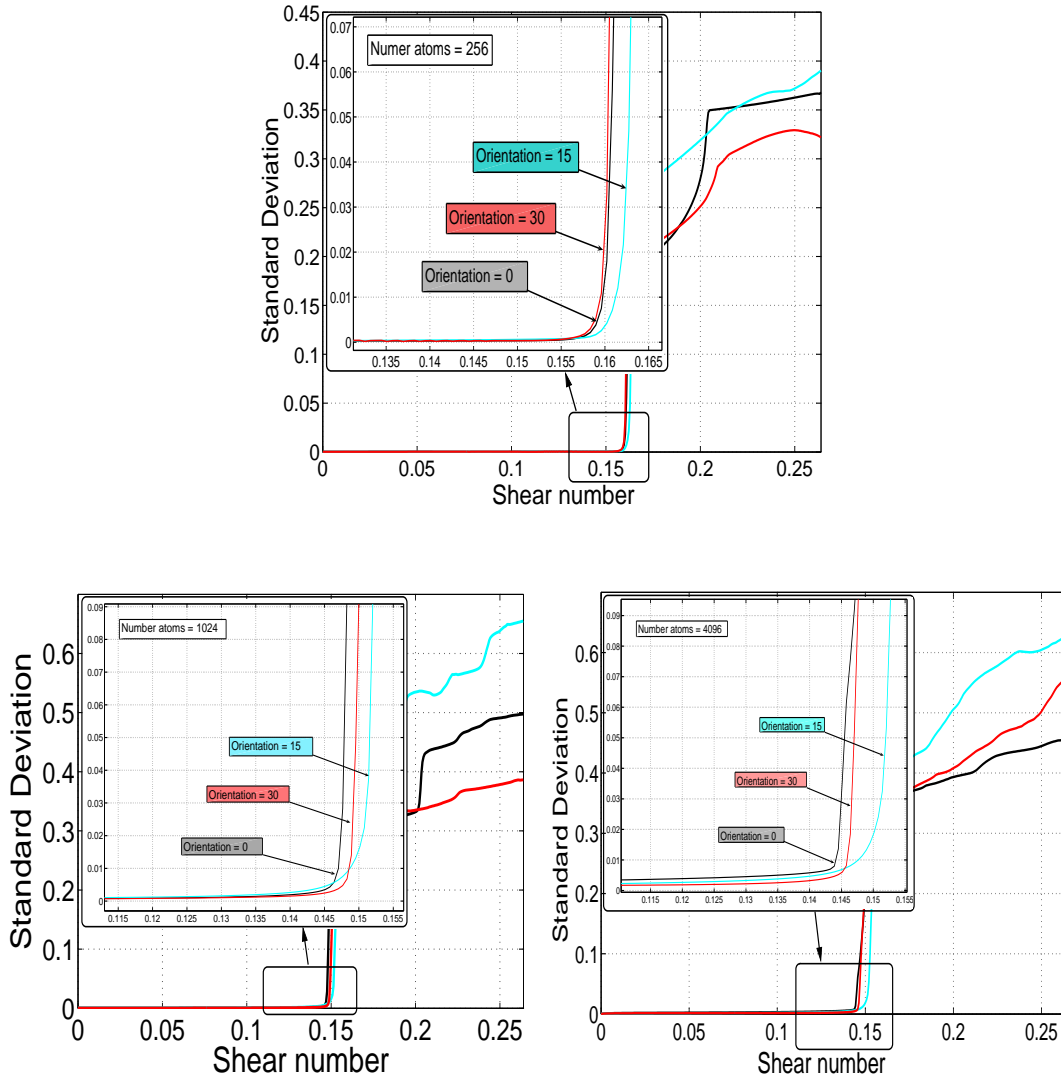


Figure 2.11: Standard deviation versus the shear number γ for simple shear deformation using Lennard–Jones potential comparing 0, 15, 30 degrees lattice orientations for 256, 1024 and 4096 atoms. The shear number that marks deviation from the homogeneous deformation is approximately independent of the orientation considered.

Figure 2.11 depicts the evolution of the standard deviation versus the shear number γ comparing different lattice orientations containing different numbers of atoms. From a shear number of $\gamma = 0$ until a shear number between $\gamma = 0.14$ and $\gamma = 0.16$, depending on the orientation, the standard deviation is approximately equal to zero. Thus, the unconstrained lattice follows the Cauchy–Born rule during this period. From this deformation, the standard deviation indicates divergence and its value increases steeply, displaying the limit of the applicability of the Cauchy–Born rule.

Figures 2.12 and 2.13 show the evolution of the standard deviation versus the shear number γ using in this case the second type of computations, this is where the Cauchy–Born rule is only applied on the boundary in each macro step whereas molecular dynamics is used in the unconstrained atoms.

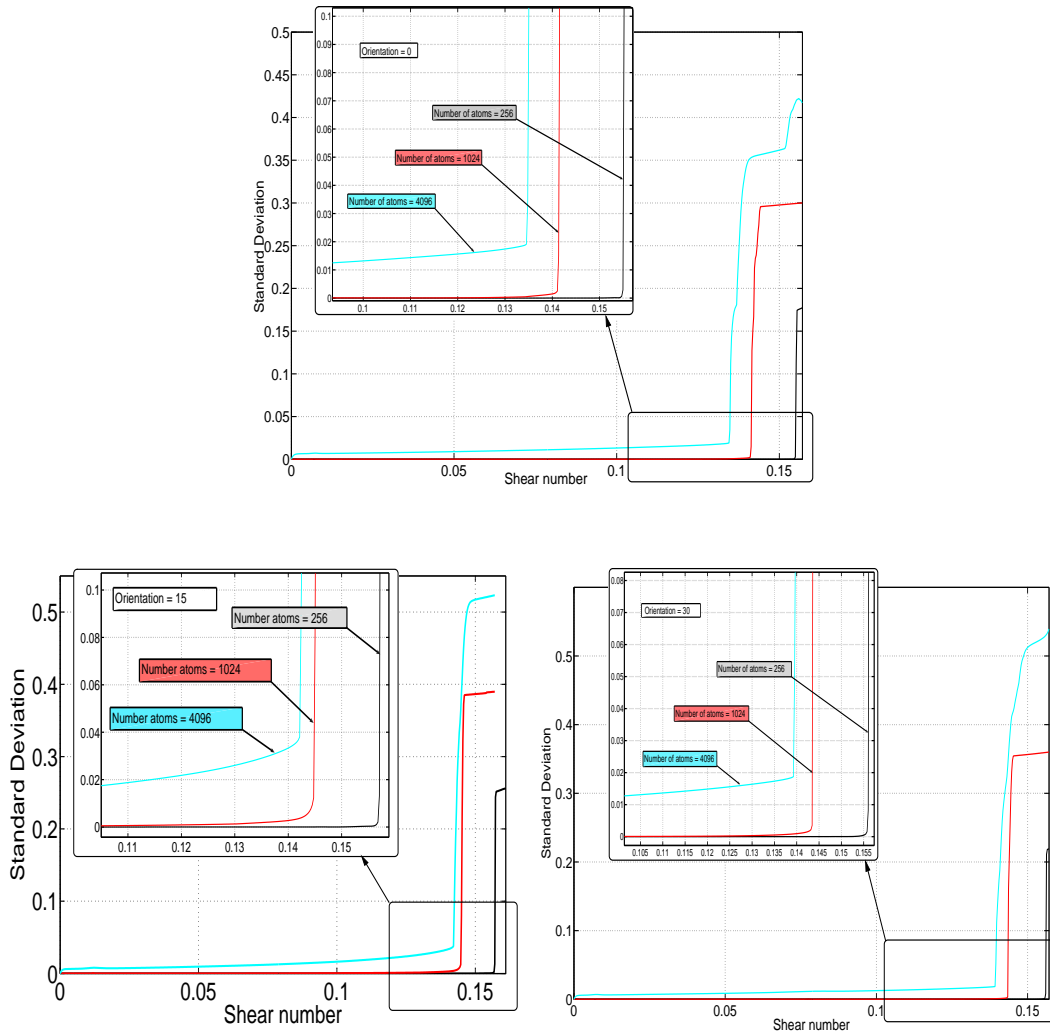


Figure 2.12: Standard deviation for simple shear deformation using Lennard–Jones potential comparing 256, 1024, 4096 number of atoms for 0, 15 and 30 degrees lattice orientation. Here, the second type of simulations is used.

The comparison in Figure 2.12 was performed for a different number of atoms in the model with lattice orientations 0, 15 and 30 degrees as done in Figure 2.10 while figure 2.13 shows the behaviour of the model comparing different number of atoms in three types of lattice orientation (0, 15 and 30 degrees) as in Figure 2.11. The deformation state where the Cauchy–born rule becomes inadequate occurs approximately at the same state as acquired in the simulations performed before, see Figures 2.10 and 2.11. The convergence occurs when we take into account a higher number of unconstrained atoms to a value close to $\gamma \approx 0.135$ which marks the onset of instabilities. It is also possible

to observe that the value of the shear number γ varies from a range of $\gamma \approx 0.135$ to $\gamma \approx 0.155$ depending on the number of atoms considered. Nevertheless, the failure of the Cauchy–Born is almost achieved at the same point independently of the lattice orientation.

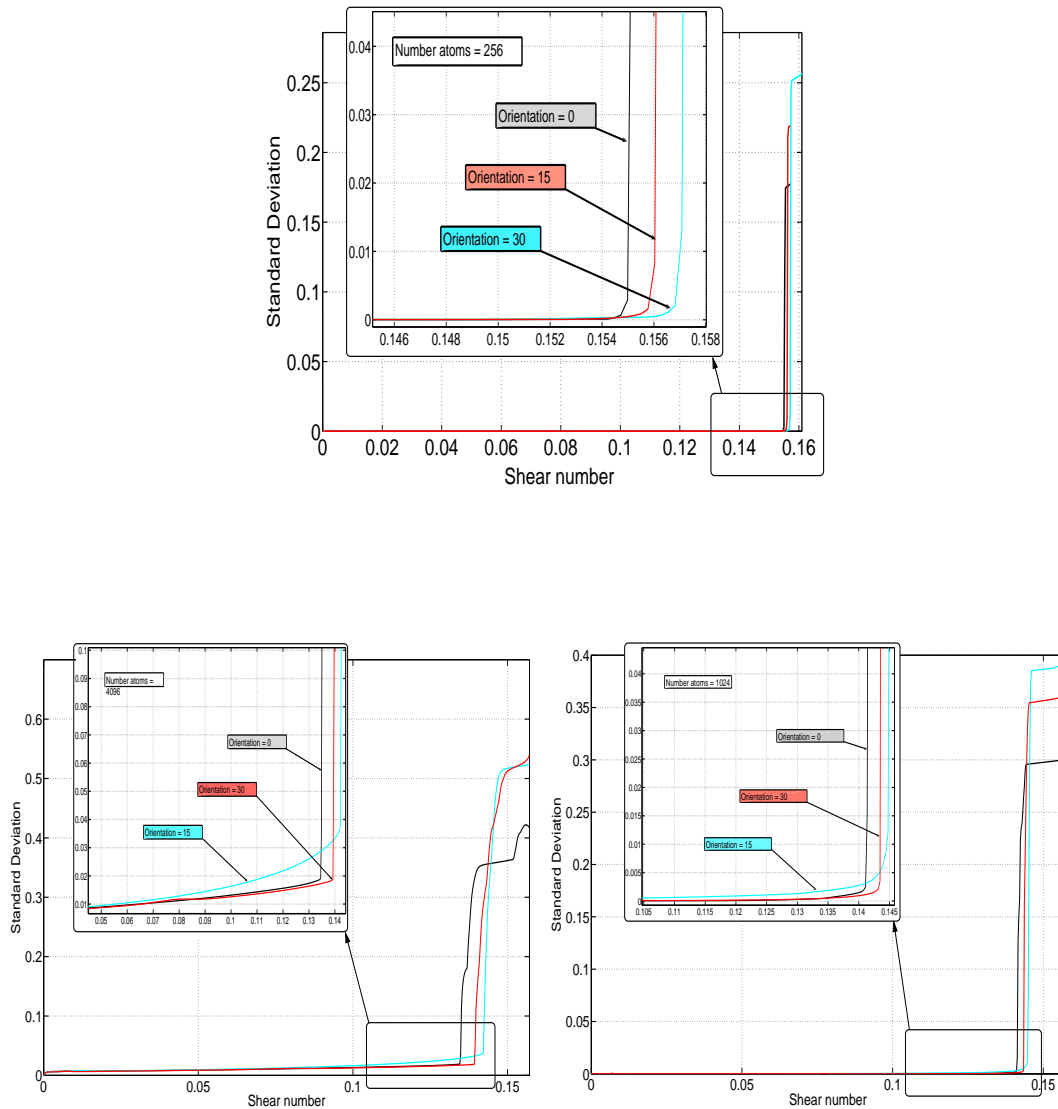


Figure 2.13: Standard deviation versus the shear number γ for simple shear deformation using Lennard–Jones potential comparing 0, 15, 30 degrees lattice orientations for 256, 1024 and 4096 atoms. Here, the second type of simulations is used.

The result using a continuum failure criterion is displayed in Appendix C Figure C.1. The acoustic tensor reveals a $\gamma \approx 0.142$ which corresponds to the limit of the elastic domain. Note that numerical analysis such as molecular dynamics tries to estimate round–off errors using algorithms. That means they use finite digits to represent infinite digits of real numbers. Therefore the results within the molecular dynamics approach render a range of γ to indicate the elastic limit and not an exact value as the result obtained within the continuum mechanics approach.

2.4.2 Uniaxial Extension

The uniaxial extension deformation (without any lateral contraction) is characterized by the deformation gradient

$$\mathbf{F} = \mathbf{I} + [\lambda - 1] \mathbf{e}_1 \otimes \mathbf{e}_1, \quad (2.4.2)$$

where \mathbf{e}_i , $i = 1$ is the Cartesian basis vector, \mathbf{I} is the second order identity and the factor λ represents the stretch.

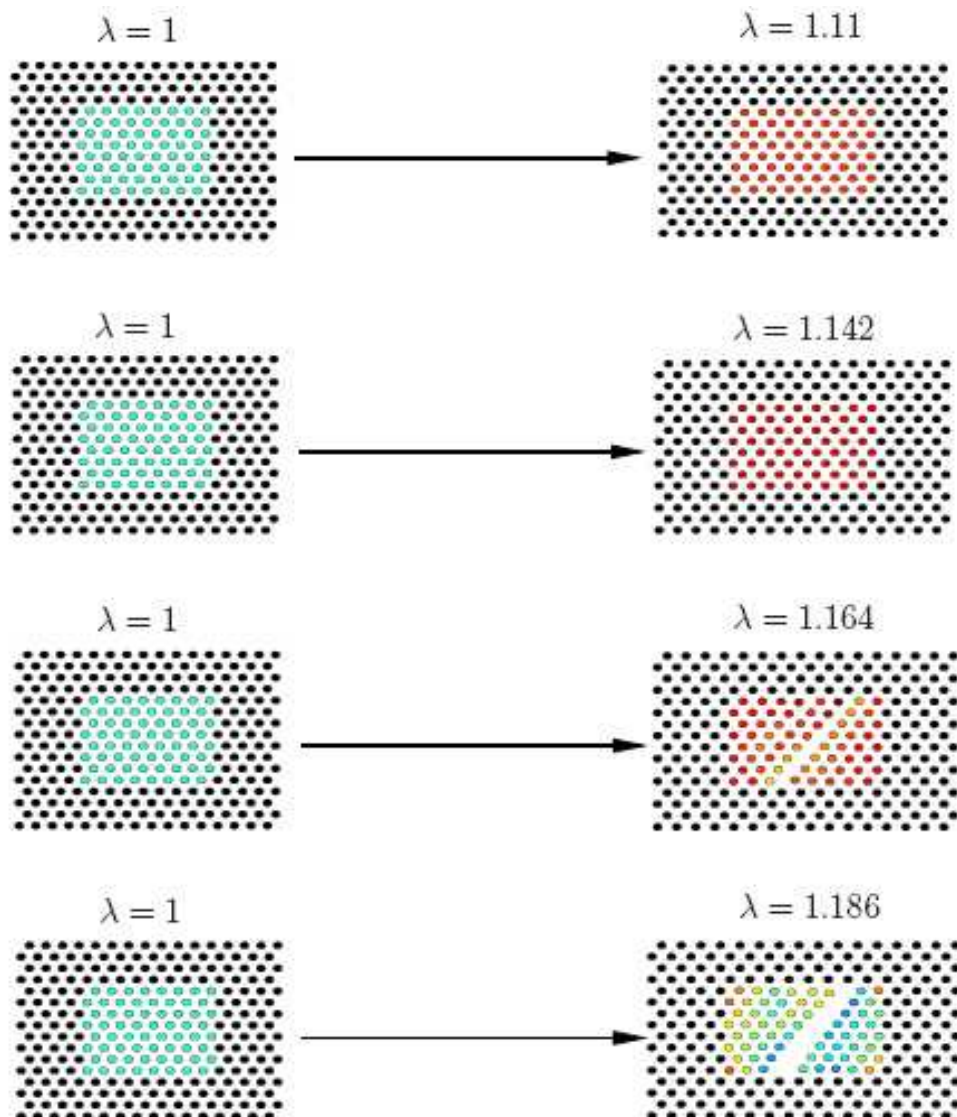


Figure 2.14: Material and spatial crystallite configuration for uniaxial extension deformation. In the top row a homogeneous deformation state of the unconstrained atoms corresponds to the validity of the Cauchy–Born rule. In the bottom row an inhomogeneous deformation state of the unconstrained atoms indicates the loss of validity of the Cauchy–Born rule.

Figure 2.14 represents the uniaxial extension deformation evolution for different values of λ . For the uniaxial extension deformation, the atoms are obliged to move horizontally without vertical contraction. For the sake of representation the results for only 256 atoms with orientation 0 degrees are shown.

Uniaxial Extension Deformation and the Influence of the Cut–off Radius.

To check the influence of the cut–off radius in an uniaxial extension deformation, several simulations containing 5320 atoms in a 0 degree orientation were performed using the values of σ and ϵ of the Lennard–Jones potential function, Equation 1.4.3, exposed in Table 2.1. The computations were performed for the same micro time step and the same number of macro steps. Figure 2.15 depicts the standard deviation versus the stretch λ with different options in the cut–off distance. It can be appreciated that with a higher number of atoms considered in the cut–off radius the accuracy increases being negligible the difference between $n = 3$ and $n = 5$. Therefore, the cut–off radius considered for the next simulations within the uniaxial extension case is $n = 3$ which represents the next three neighbours. That allows us to significantly reduce the computational cost.

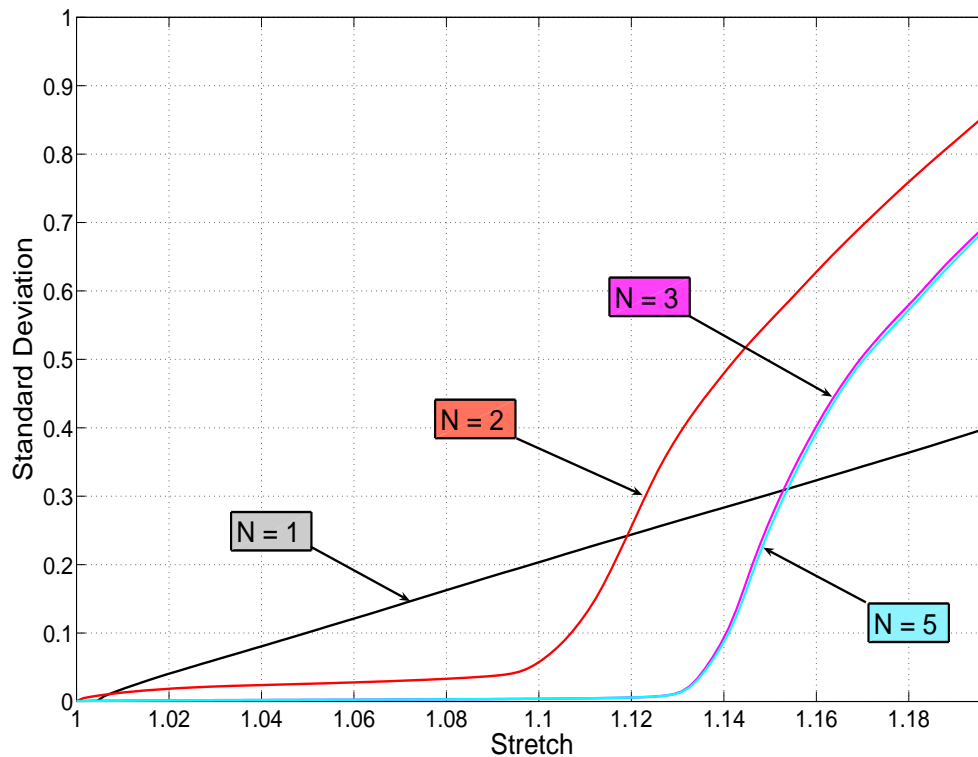


Figure 2.15: Standard deviation versus the stretch λ for uniaxial extension deformation using Lennard–Jones potential while comparing different cut–off radius in a 0 degree lattice orientation. The figure exhibits that for $n = 3$ and $n = 5$ the standard deviation shows no difference. That means that the cut–off radius $n = 3$ is a good approximation for computing the interactive forces.

Uniaxial Extension Deformation for Lennard–Jones.

Figure 2.16 shows the standard deviation versus the stretch λ depicting different lattice orientations in order to see the influence of using different numbers of unconstrained atoms for studying the stability of the Cauchy–Born rule.

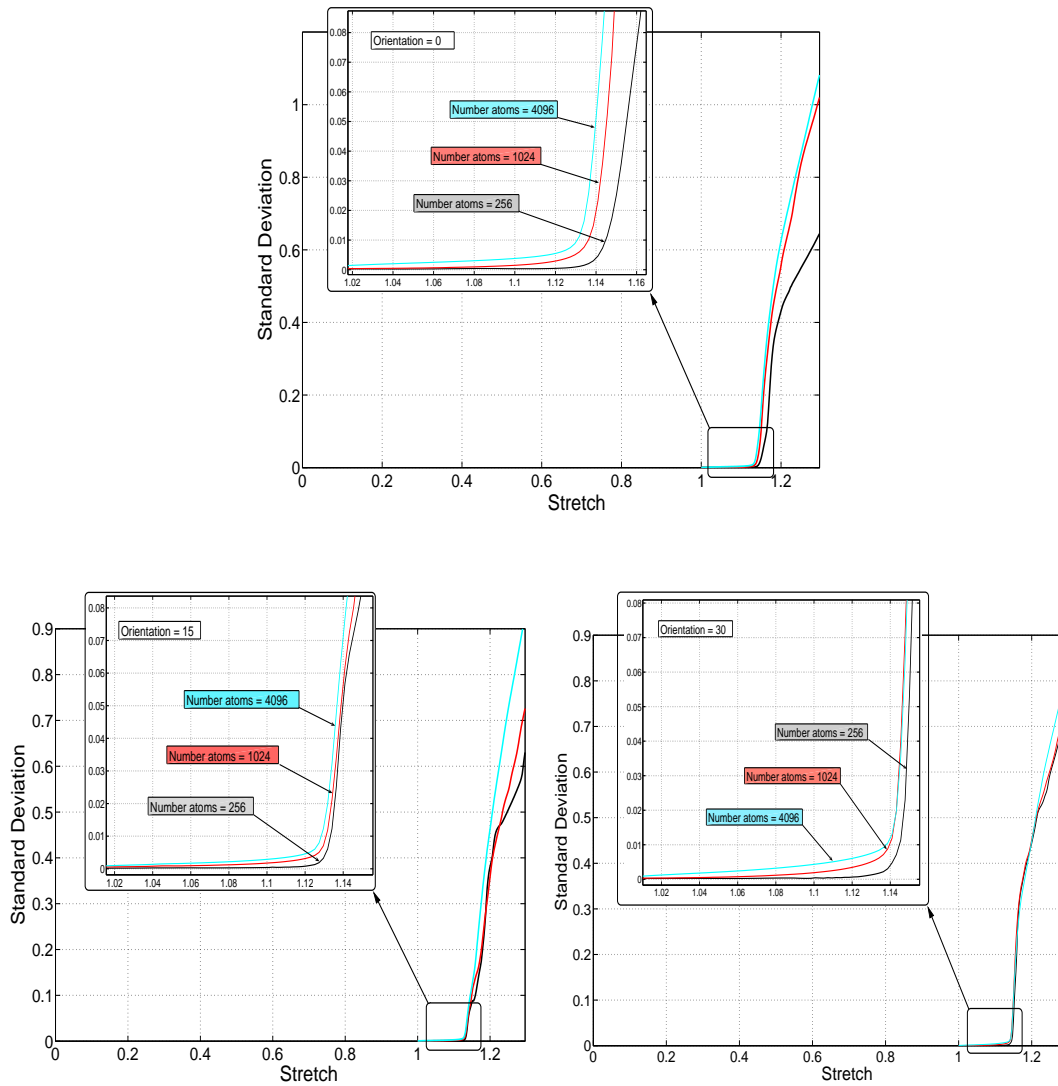


Figure 2.16: Standard deviation versus the stretch λ for uniaxial extension deformation using Lennard–Jones potential comparing 256, 1024, 4096 number of atoms for 0, 15 and 30 degrees lattice orientation. The stretch λ which marks deviation from an affine deformation tends to be $\lambda \approx 1.14$ converging with a higher number of unconstrained atoms.

Obviously, from a $\lambda = 1$ to roughly a stretch value between $\lambda = 1.12$ and $\lambda = 1.14$, the standard deviation estimation is approximately equal to zero and constant. As an interpretation during this period, the deformation remains homogeneous and stable. The particles behave as if they displace homogeneously. From this deformation state, the value of the standard deviation increases drastically. In other words, this value indicates again the limit where the Cauchy–Born rule starts to fail and the deformation becomes inho-

mogeneous due to instabilities. In each figure the stretch number that marks deviation from the ideal homogenous deformation converges with a higher number of unconstrained atoms to a near value of $\lambda \approx 1.14$ as can be distinguished in the detailed figures.

Figure 2.17 represents again the standard deviation versus the stretch λ but for a different number of unconstrained atoms comparing different lattice orientations.

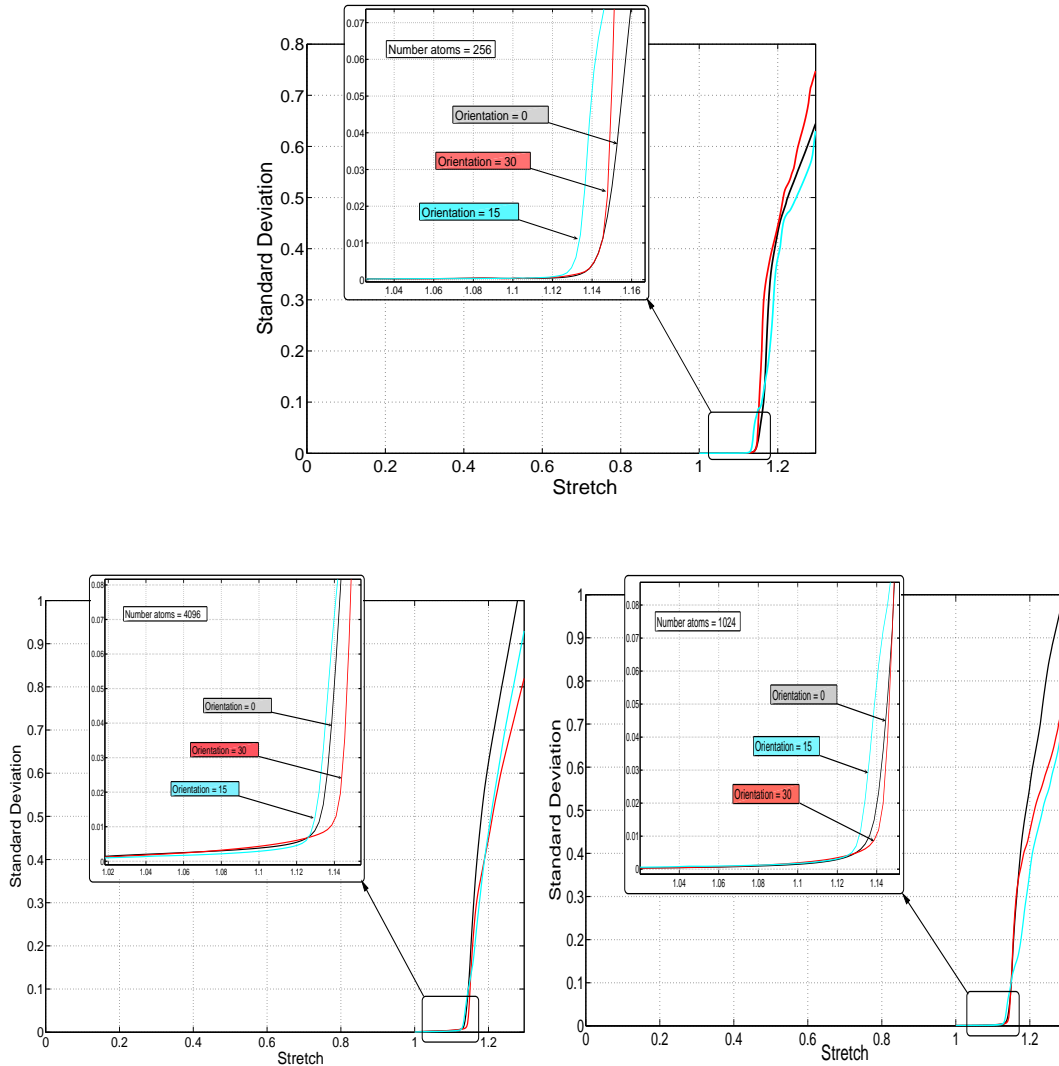


Figure 2.17: Standard deviation for uniaxial extension deformation using Lennard–Jones potential comparing 0, 15, 30 degrees lattice orientation with 256, 1024 and 4096 atoms. The stretch value that marks deviation from homogeneous deformation independently converges from the lattice orientation.

In the range from a $\lambda = 1$ until a stretch value between 1.12 and 1.15, the value of the standard deviation is almost equal to zero. During this period, the deformation remains homogeneous and the usage of the Cauchy–Born rule as a homogenization technique is adequate. From this deformation state, the value of the standard deviation diverges indicating the onset of instabilities.

In order to compare results the same simulations but using the second type of computations are presented in Figures 2.18 and 2.19 . We reiterate, the Cauchy–Born rule is only applied on the boundary in each macro step which act as a rigid wall whereas molecular dynamics is used in the unconstrained atoms with the purpose of capturing instabilities.

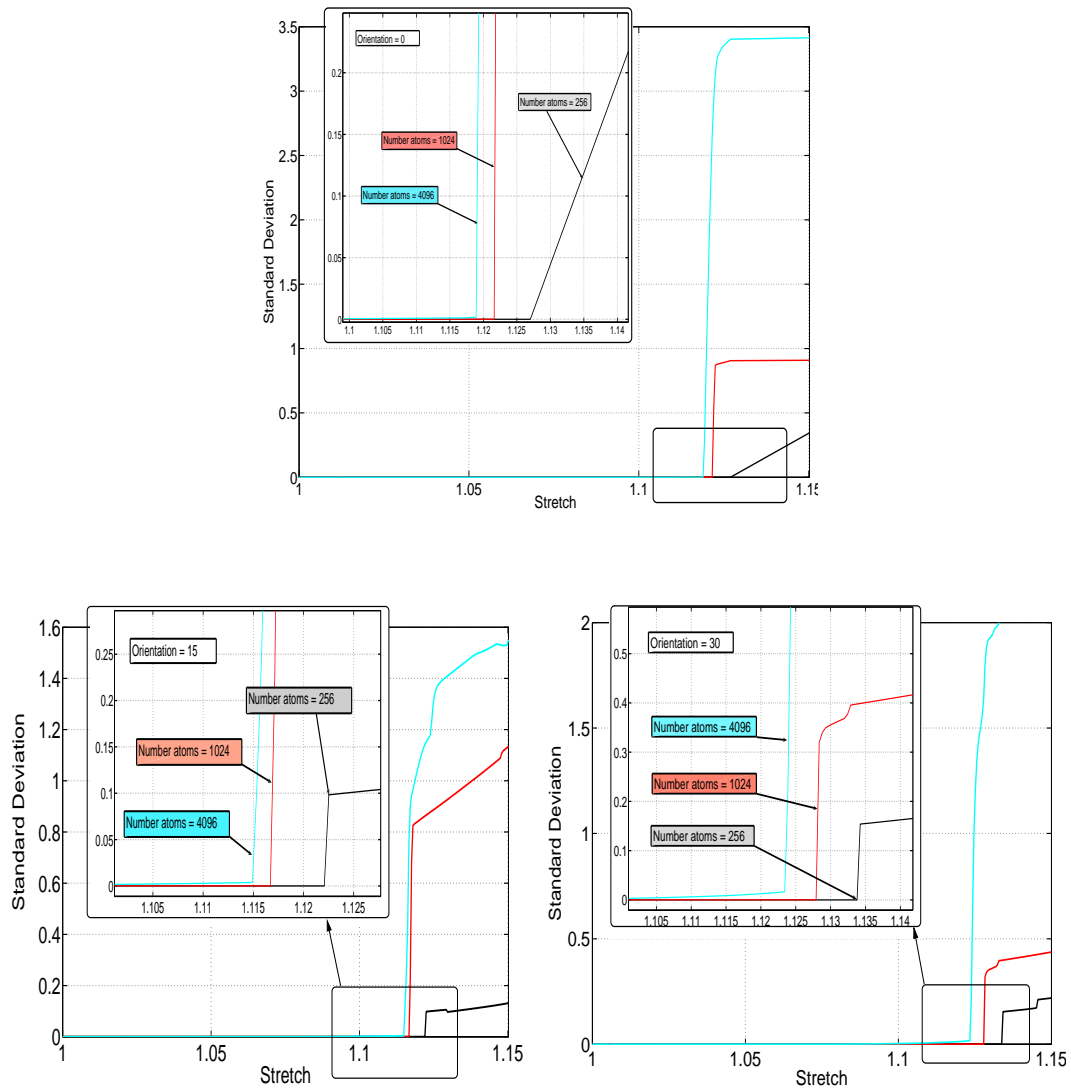


Figure 2.18: Standard deviation versus the stretch λ for uniaxial extension deformation using Lennard–Jones potential comparing 256, 1024, 4096 number of atoms for 0, 15 and 30 degrees lattice orientation. Here the second type of computations is applied in order to compare results.

These figures depict again the evolution of the standard deviation versus the stretch λ . We discovered that a deformation state where the Cauchy–born rule becomes inadequate occurs earlier as before, approximately around the stretch value $\lambda \approx 1.12$ and even for an orientation 15 degrees the value is $\lambda \approx 1.115$. The range of validity is less which mark Figures 2.16 and 2.17. In this context the modelling of material behaviour within a

Cauchy–Born approximation is restricted to this λ .

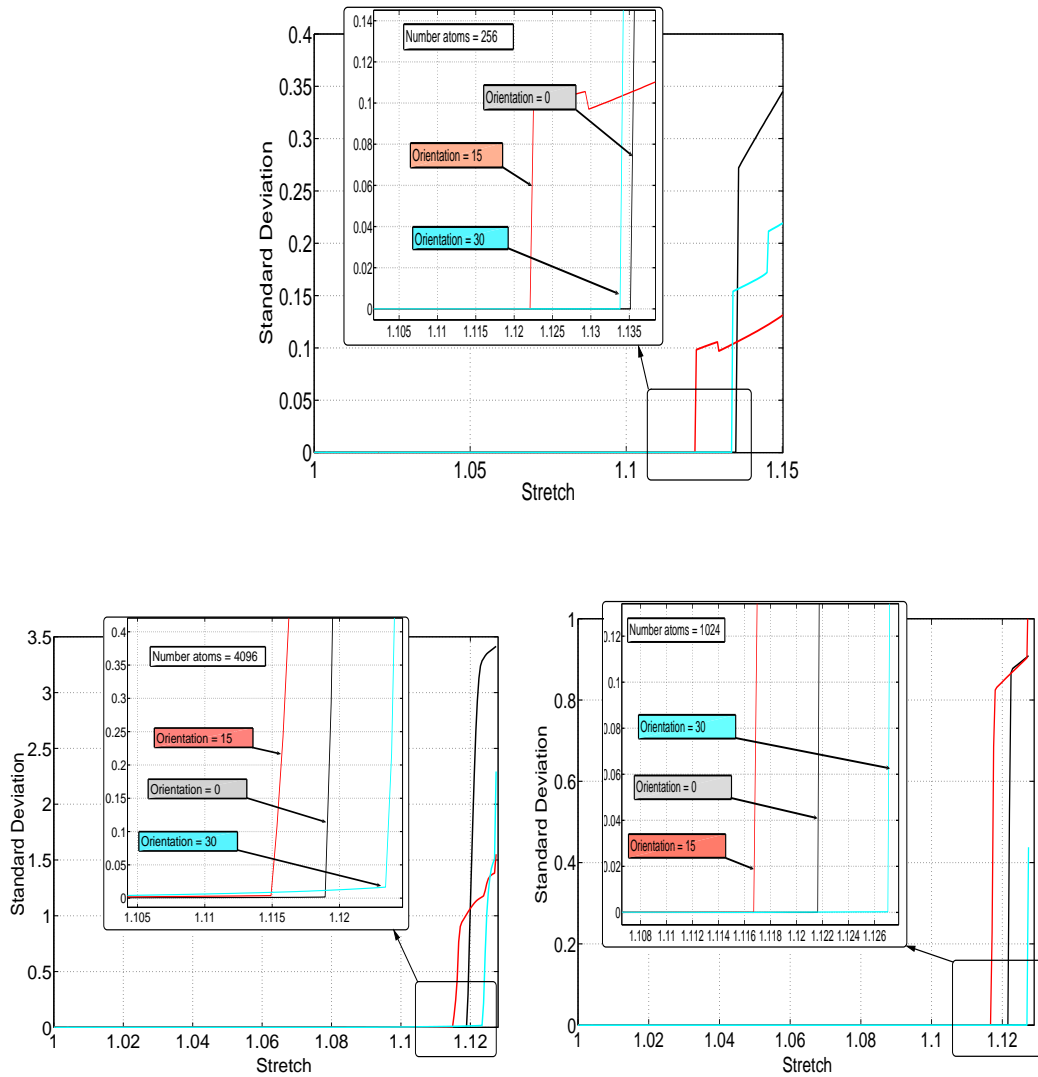


Figure 2.19: Standard deviation for uniaxial extension deformation using Lennard–Jones potential comparing 0, 15, 30 degrees lattice orientation with 256, 1024 and 4096 atoms. Here the second type of computations is applied in order to check if both computations render the same results.

To compare results an Appendix C is placed at the end of this work where the corresponding results using the acoustik tensor are expounded. For uniaxial extension deformation the limit of the elastic domain corresponds to the stretch value $\lambda = 1.12$ for 0 and 15 degrees in the lattice while $\lambda = 1.137$ for orientation 30 which agree with the values acquired before with molecular dynamics. Mention that the molecular dynamics results suffer from round–off errors since numerical algorithms are used. Despite this both approaches reveal similar results.

2.4.3 Pure Shear Deformation

The Pure Shear deformation is characterised by the deformation gradient

$$\mathbf{F} = \mathbf{I} + [\lambda - 1] \mathbf{e}_1 \otimes \mathbf{e}_1 + [\lambda^{-1} - 1] \mathbf{e}_2 \otimes \mathbf{e}_2, \quad (2.4.3)$$

where the factor λ represents the stretch and \mathbf{I} as the identity tensor.

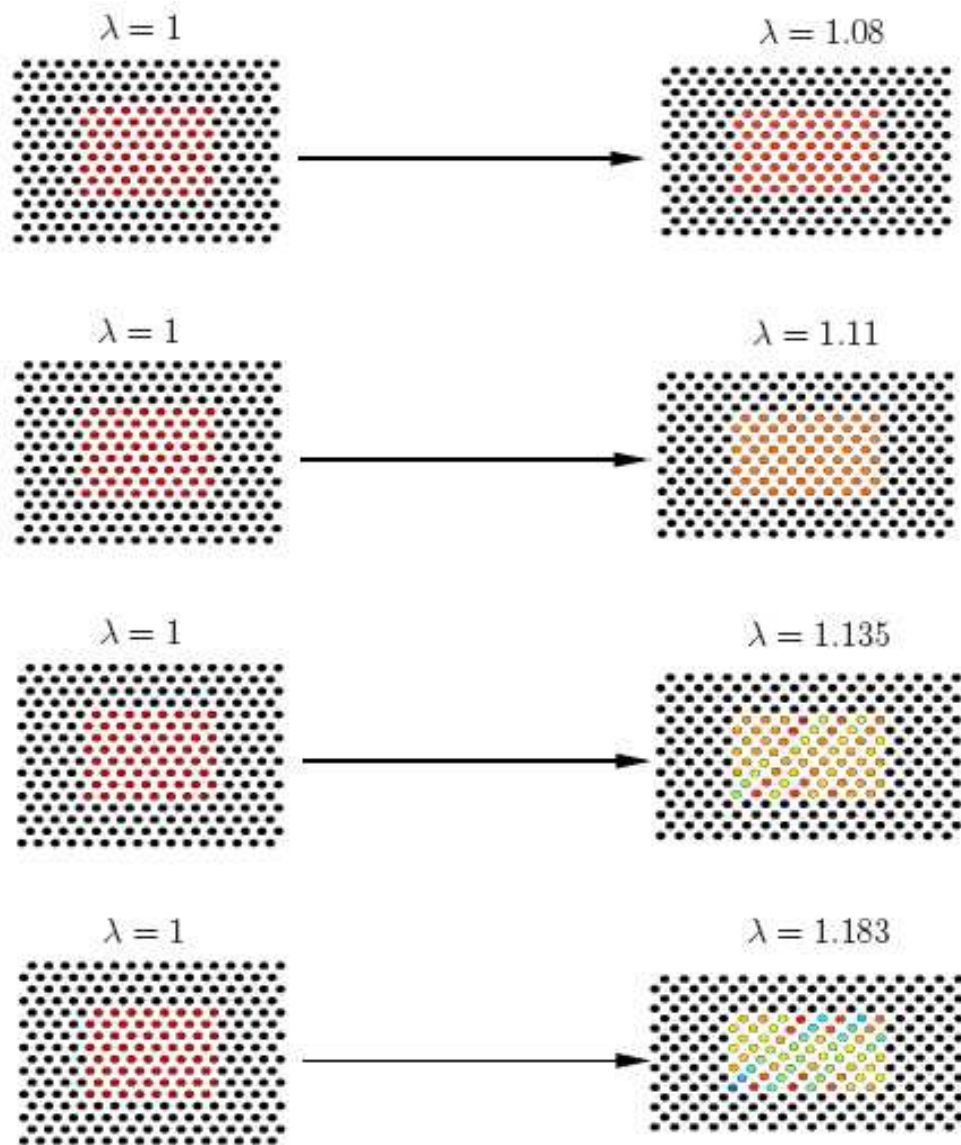


Figure 2.20: Material and spatial crystallite configuration with a lattice orientation $\alpha = 0$ subjected to pure shear deformation. The values $\lambda = 1.08$ and $\lambda = 1.11$, which yield a homogeneous deformation state, verify the Cauchy–Born rule. The values $\lambda = 1.135$ and $\lambda = 1.183$ generate an inhomogeneous deformation state and indicate the loss of stability of the Cauchy–Born rule.

Figure 2.20 represents the positions of the unconstrained and constrained atoms for different values of λ . Here the specimen is forced to move horizontally but with vertical contraction. For the sake of representation the results for only 256 atoms with orientation 0 degrees are shown.

Pure Shear Deformation and the Influence of the Cut–Off Radius.

Again a study of the cut–off radius is needed to strike a balance between accuracy and efficiency in further computations. That means, we need to use an appropriate cut–off radius for computing the interactive forces among the particles without losing effectiveness in studying the Cauchy–Born rule. In order to achieve that, we have performed several simulations displayed in Figure 2.21.

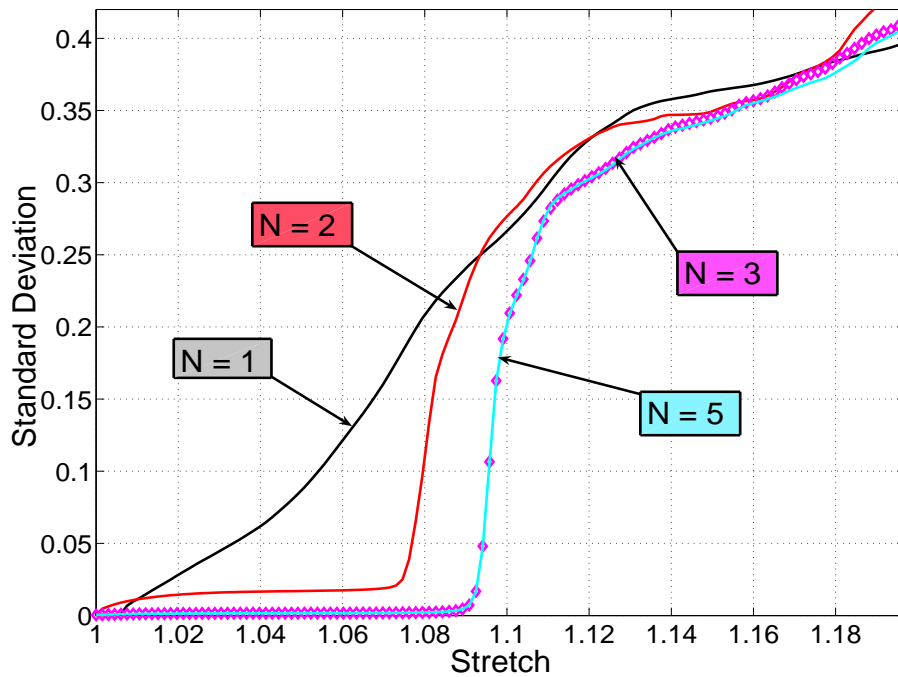


Figure 2.21: Standard deviation for pure shear deformation using Lennard–Jones potential comparing different cut–off radius for 0 degrees of the lattice orientation. The cut–off radius correspond to $n = 3$ has been revealed as a good approximation to compute the interactive forces.

The model contains 5320 atoms in a 0 degree orientation. 2323 of them are used as constrained atoms. They also act as a rigid wall and they are placed around 2997 unconstrained atoms in the remaining interior region where the standard molecular dynamics approach is used. The different values of σ and ϵ in the Lennard–Jones potential function, Equation 1.4.3, are displayed in Table 2.1. The computations were performed for the same micro time step (Δt) and the same number of macro steps. As we increase the number of atoms within the cut–off radius, i.e. when n goes from $n = 1$ to $n = 5$, we find out that the simulations yield the same homogeneous deformation state for $n = 3$ as well as for $n = 5$. In other words, both verify the Cauchy–Born rule for the same range of

validity and diverges nearly at the same value of λ . Therefore, the election of the cut-off radius is clear and renders $n = 3$. With that we tackle our objective without losing much accuracy due to the cut-off radius approximation.

Pure Shear Deformation for Lennard–Jones.

In the Figure 2.22 the standard deviation versus the stretch λ is represented again confronting different number of unconstrained atoms in lattice orientations 0, 15 and 30 degrees. Here, the first type of simulations in the sense of Lyapunov are used.

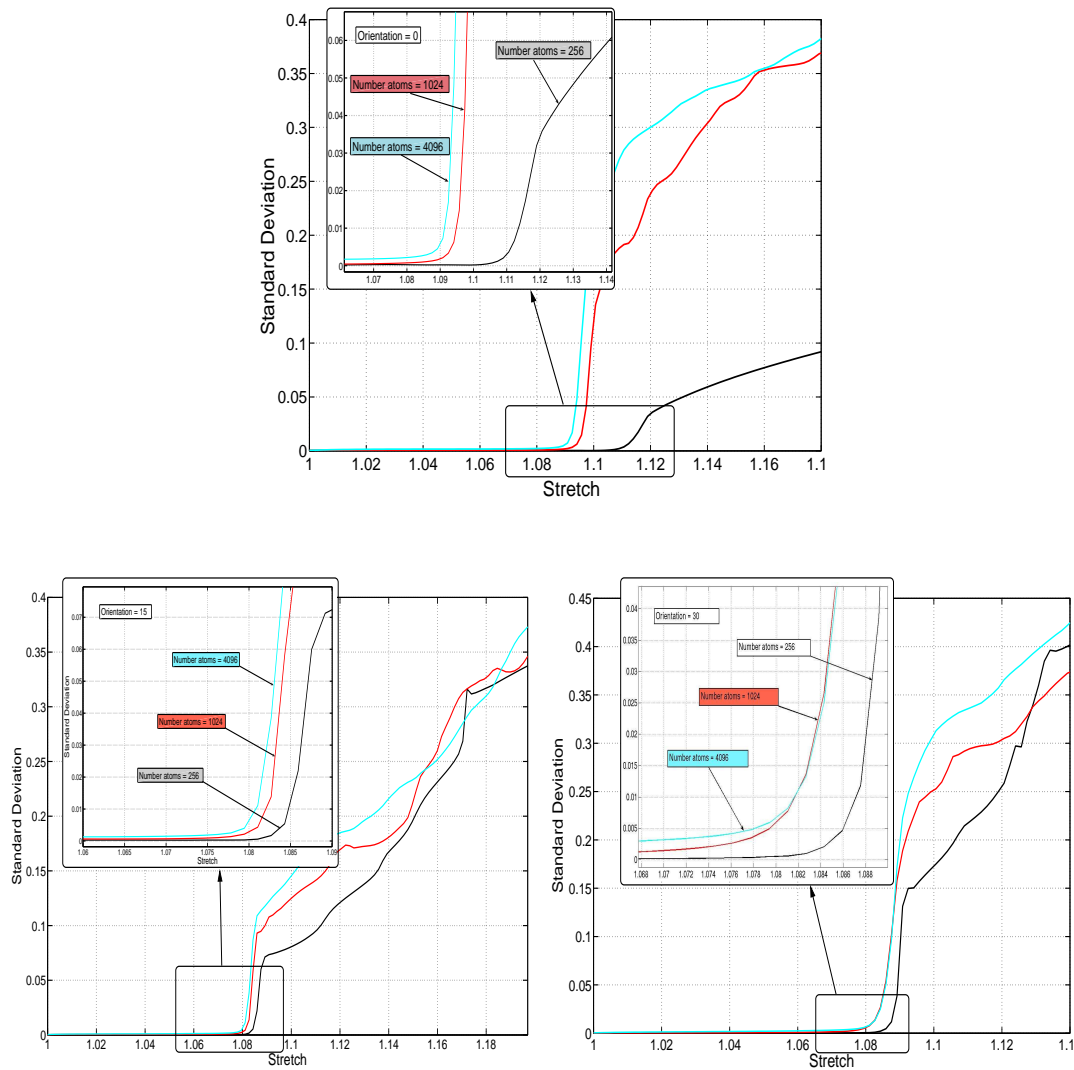


Figure 2.22: Standard deviation versus the stretch λ for pure shear deformation using Lennard–Jones potential comparing 256, 1024, 4096 number of atoms for 0, 15 and 30 degrees lattice orientation. The stretch λ which marks deviation from a homogeneous deformation converges with higher number of atoms.

Clearly, in the range from a $\lambda = 1$ until a stretch value between $\lambda = 1.08$ and $\lambda = 1.11$, the value of the standard deviation is approximately equal to zero. In this period, the

simulation produces homogeneous deformation and the atoms move as predicted by the Cauchy–Born assumption. Constrained and unconstrained atoms render affine displacement fields. Nevertheless, this deformation state marks the onset of complex atomistic behaviour impossible to model within the Cauchy–Born rule. It is easy to recognize that the standard deviation converges to a constant value when a higher number of atoms is increased.

In Figure 2.23 the comparison is done for different orientations using 256, 1024 and 4096 atoms. In this case it may be distinguished that the loss of stability in the Cauchy–Born rule, i.e. the failure point, does not occur at the same state as in the previous deformation cases such as simple shear or uniaxial extension. The range where the Cauchy–Born rule fails due to instabilities varies from $\lambda = 1.075$ to a value of $\lambda = 1.095$.

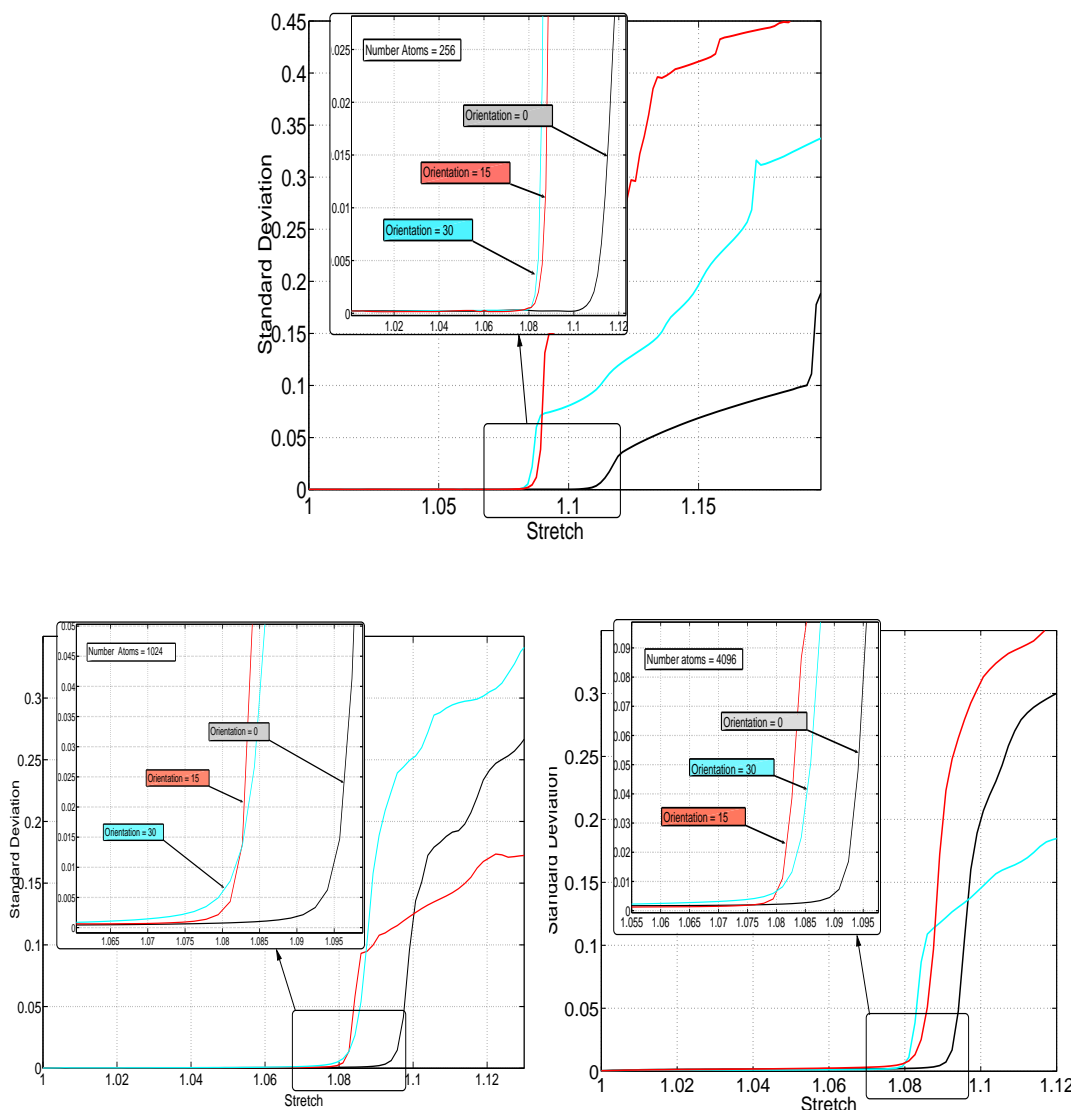


Figure 2.23: Standard deviation for pure shear deformation using Lennard–Jones potential comparing 0, 15, 30 degrees lattice orientation with 256, 1024 and 4096 atoms. The stretch λ which marks deviation is different depending on the orientation considered.

The outcomes using the second type of simulations where the constrained and unconstrained particles are treated independently are exhibited in Figures 2.24 and 2.25. Again, they reveal similar results as in Figures 2.22 and 2.23. The limit of the stretch λ which indicates the range of applicability of the Cauchy–Born rule converges to a value $\lambda \approx 1.085$ for an orientation of 0 degree and $\lambda \approx 1.075$ for an orientation of 30 degrees when the number of atoms were increased.

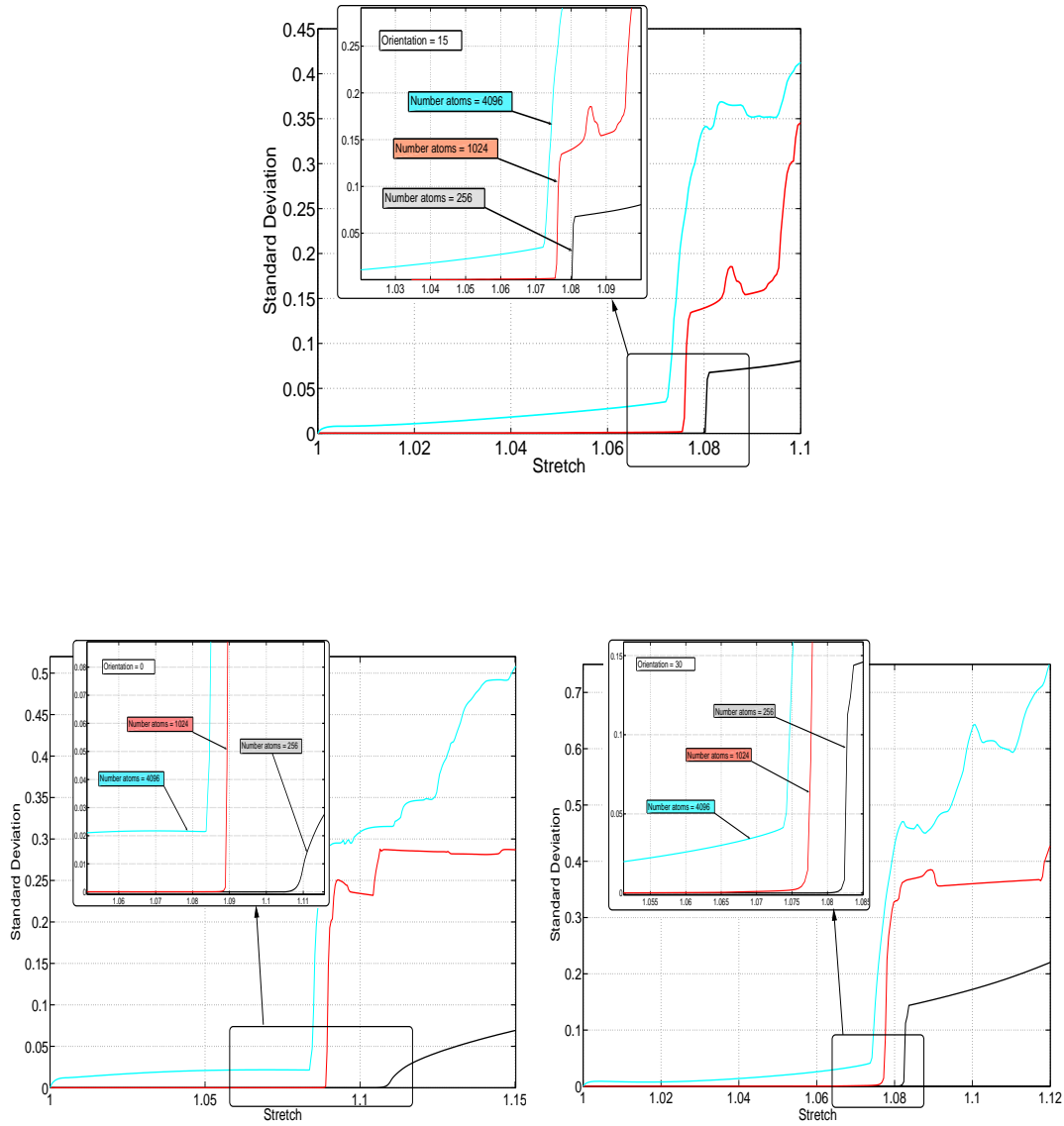


Figure 2.24: Standard deviation versus the stretch λ for pure shear deformation using Lennard–Jones potential comparing 256, 1024, 4096 number of atoms for 0, 15 and 30 degrees lattice orientation. Here the second type of computation is applied.

Figures 2.24 and 2.25 are performed using the second type of simulations using molecular dynamics in order to compare the results displayed in figures 2.22 and 2.23. Again, the limit of the stretch λ , which indicates the range of applicability of the Cauchy–Born rule, tends to a value of $\lambda \approx 1.085$ for a 0 degree orientation, $\lambda \approx 1.075$ for a 30 degrees

orientation and $\lambda \approx 1.07$ considering 15 degrees orientation when the number of atoms were increased. In Figure 2.25 may be appreciated that the starting failure state for orientations 15 and 30 degrees occur at $\lambda \approx 1.075$ whereas for 0 degrees at $\lambda \approx 1.085$ as in the previous figures, i.e. 2.22 and 2.23.

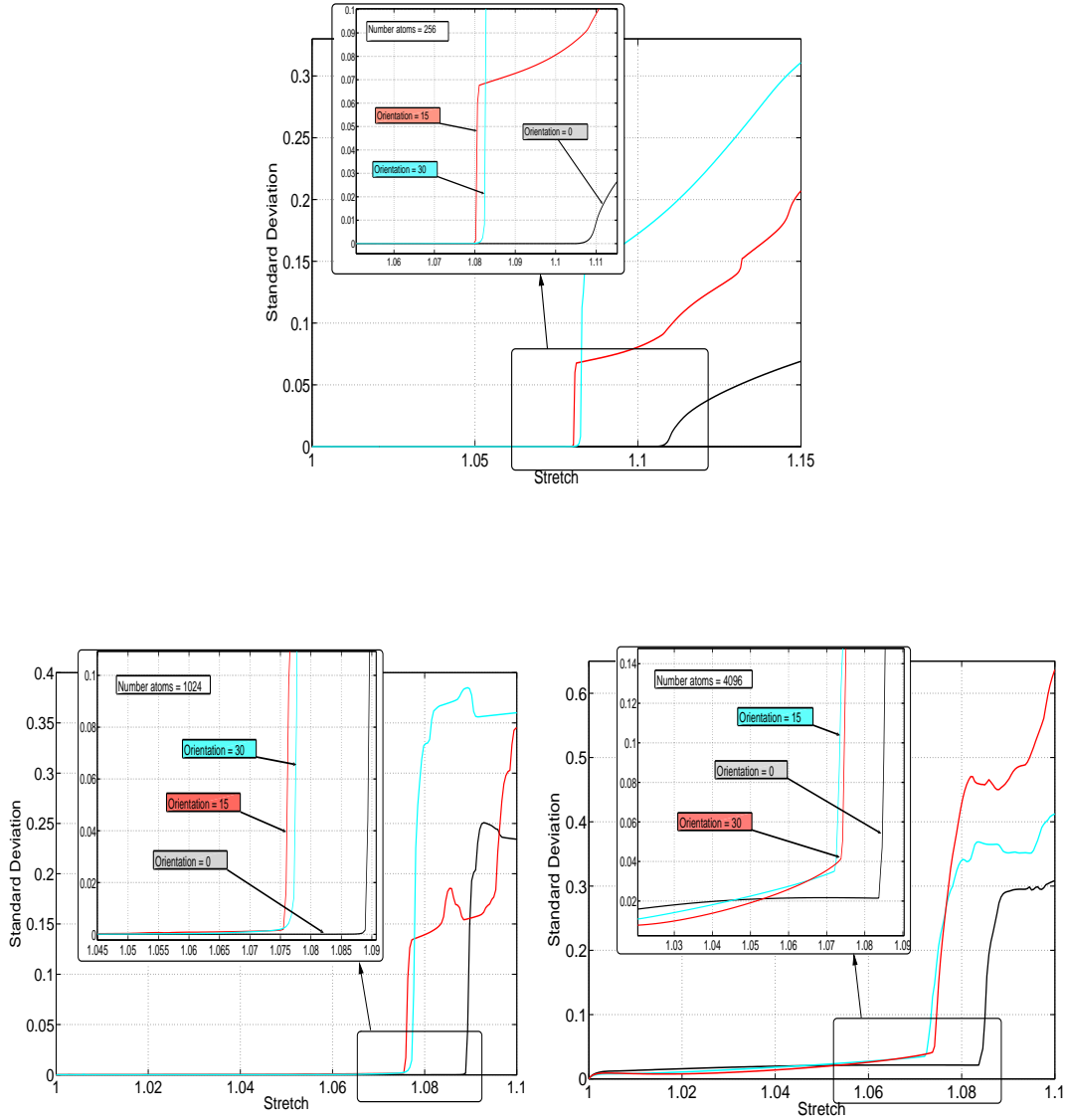


Figure 2.25: Standard deviation for pure shear deformation using Lennard–Jones potential comparing 0, 15, 30 degrees lattice orientation with 256, 1024 and 4096 atoms. Here the second type of computation is applied in order to check if both computations render same results.

The result using the acoustic tensor within the continuum mechanics framework can be found in Appendix C Figure C.3. The acoustic tensor or rather the study of the loss of rank 1 convexity reveals values of the stretch equal to $\lambda = 1.0705$ for lattice orientations 30 and 15 and $\lambda = 1.085$ for lattice orientations 0. They coincide with the beginning of the critical deformation state. They agree with the results obtained with molecular dynamics although round–off errors are involved in these computations.

2.4.4 Dilatation Deformation

The dilatation deformation is characterised by the deformation gradient

$$\mathbf{F} = \mathbf{I} + [\lambda - 1] \mathbf{e}_1 \otimes \mathbf{e}_1 + [\lambda - 1] \mathbf{e}_2 \otimes \mathbf{e}_2, \quad (2.4.4)$$

where \mathbf{e}_i , $i = 1, 2$ are the Cartesian basis vectors, \mathbf{I} denotes again the identity tensor and the factor λ represents the stretch

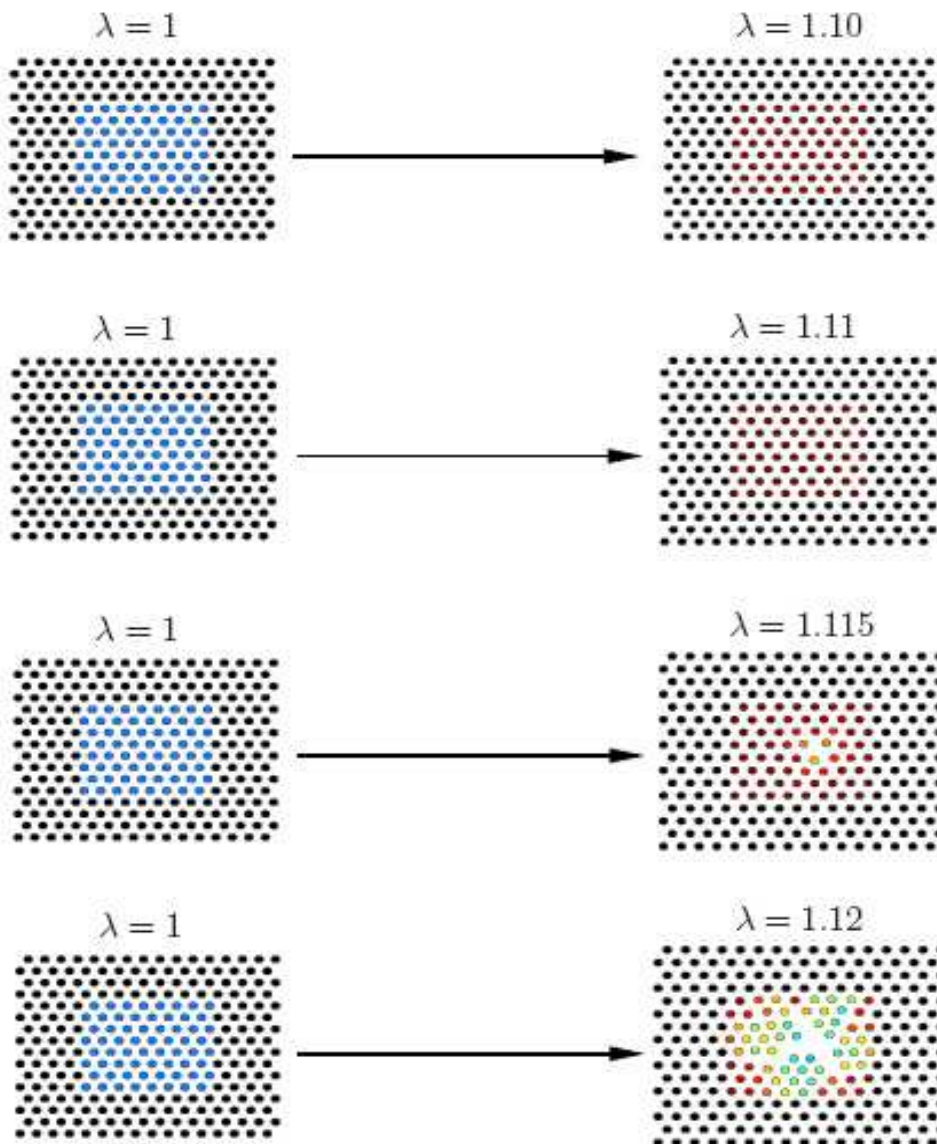


Figure 2.26: Material and spatial crystallite configuration with a lattice orientation $\alpha = 0$ subjected to dilatation. The values $\lambda = 1.10$ and $\lambda = 1.11$, which yield a homogeneous deformation state, verify the Cauchy–Born rule. The values $\lambda = 1.115$ and $\lambda = 1.12$ generate a inhomogeneous deformation state and indicate the loss of stability of the Cauchy–Born rule.

Figure 2.26 depicts the dilatation deformation evolution for different values of λ . The atoms are obliged to move horizontally with vertical extension. For the sake of representation the results for only 256 atoms are illustrated.

Dilatation Deformation and the Influence of the Cut–off Radius.

In practical applications, the interaction radius is chosen to reduce the summation over the interacting atoms to the closest neighbours. Thus, we reduce the computational demand without attaining unstable or unphysical results. In order to select a proper cut–off distance within the dilatation deformation and with the purpose of studying the stability of the Cauchy–Born rule, several simulations were carried out using the Lennard–Jones potential function, Equation 1.4.3. Again the parameters σ and ϵ were taken from the Table 2.1. The computations were performed for the same micro time step and the same number of macro steps. The lattice is configured with 5320 atoms in a 0 degree orientation as in the other cases of deformation.

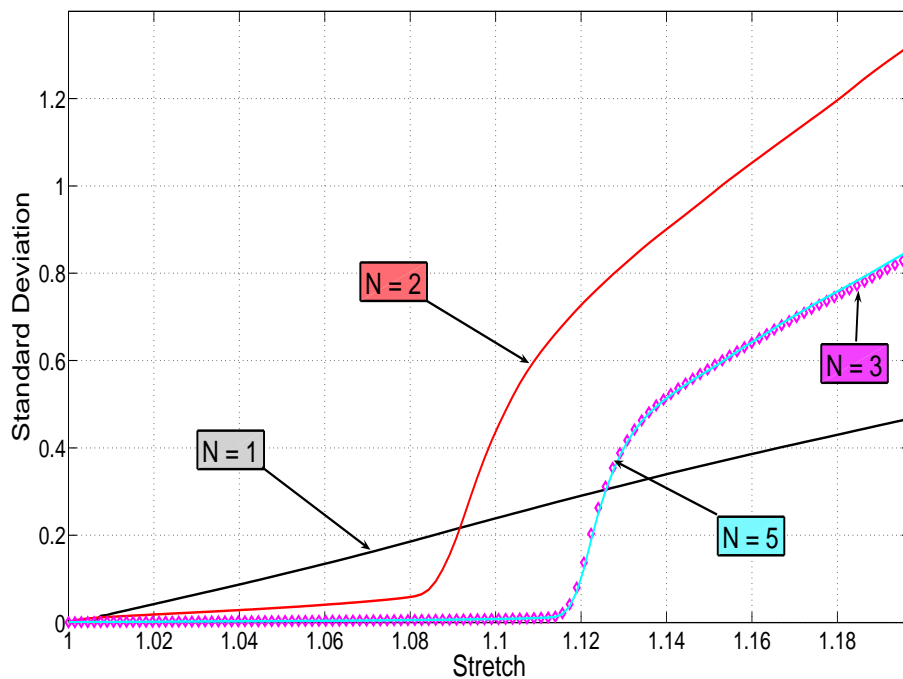


Figure 2.27: Standard deviation for dilatation deformation using Lennard–Jones potential comparing the cut–off radius for 0 degrees of the lattice orientation. The difference between $n = 3$ and $n = 5$ is negligible. Therefore, $n = 3$ seems to be a good election to calculate the interactive forces during the simulation.

Figure 2.27 represents the standard deviation versus the stretch λ with different choices for n , i.e. how many particles are incorporated in the cut–off radius. This figure reveals that as the number of atoms taken into account for computing the interactive forces increases, the stretch λ converges to $\lambda = 1.115$. Consequently, we observe that the difference between $n = 3$ and $n = 5$ is negligible. Therefore, in order to interplay accuracy but at the same time effectiveness the choice of the cut–off radius in the next computations is adopted to be $n = 3$.

Dilatation Deformation for Lennard–Jones.

Figure 2.28 depicts the evolution of the standard deviation versus the stretch λ using a progressively higher number of atoms for different lattice orientations, 0, 15 and 30 degrees.

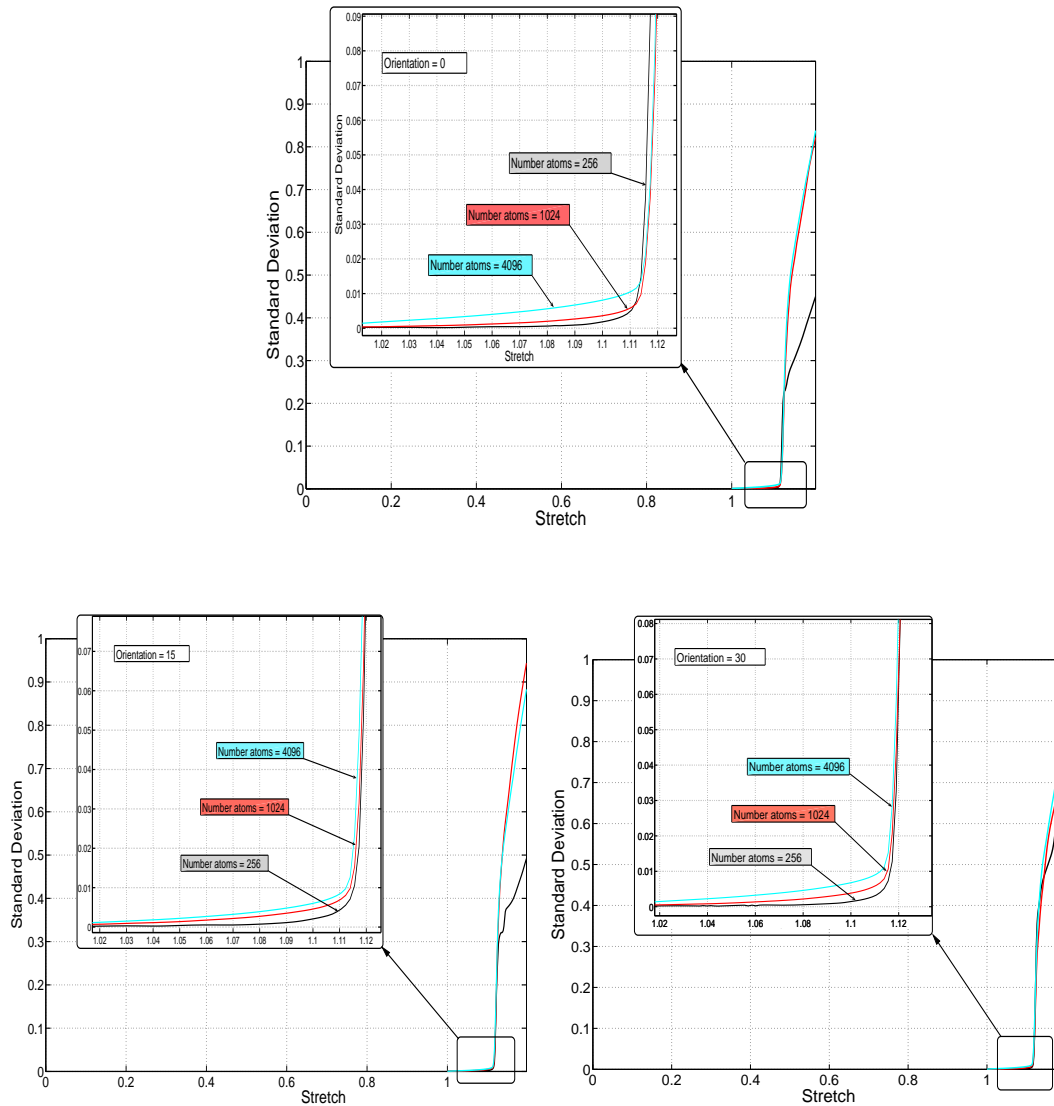


Figure 2.28: Standard deviation for dilatation deformation using Lennard–Jones potential comparing 256, 1024, 4096 number of atoms for 0, 15 and 30 degrees lattice orientation. The stretch value $\lambda \approx 1.11$ marks the onset of instabilities and converges with a higher numbers of atoms.

Obviously, in the range between a shear number value $\lambda = 1$ and a shear number approximately between $\lambda = 1.11$ and $\lambda = 1.12$ the standard deviation renders a value nearly equal to zero. That means that the dilatation deformation process yields homogeneous behaviour verifying the Cauchy–Born rule within this period. From this deformation state, the value of the standard deviation increases abruptly, indicating the state of initial

instabilities or rather the point where the rule starts to fail. In regard to the influence of the number of atoms, this figure reveals insignificant importance of that. This means the starting failure state is almost the same.

Figure 2.29 reproduces the evolution of the standard deviation versus the stretch λ . Here, the main purpose is to examine the possible influence of having different lattice configurations on the stability of the Cauchy–Born rule against perturbations.

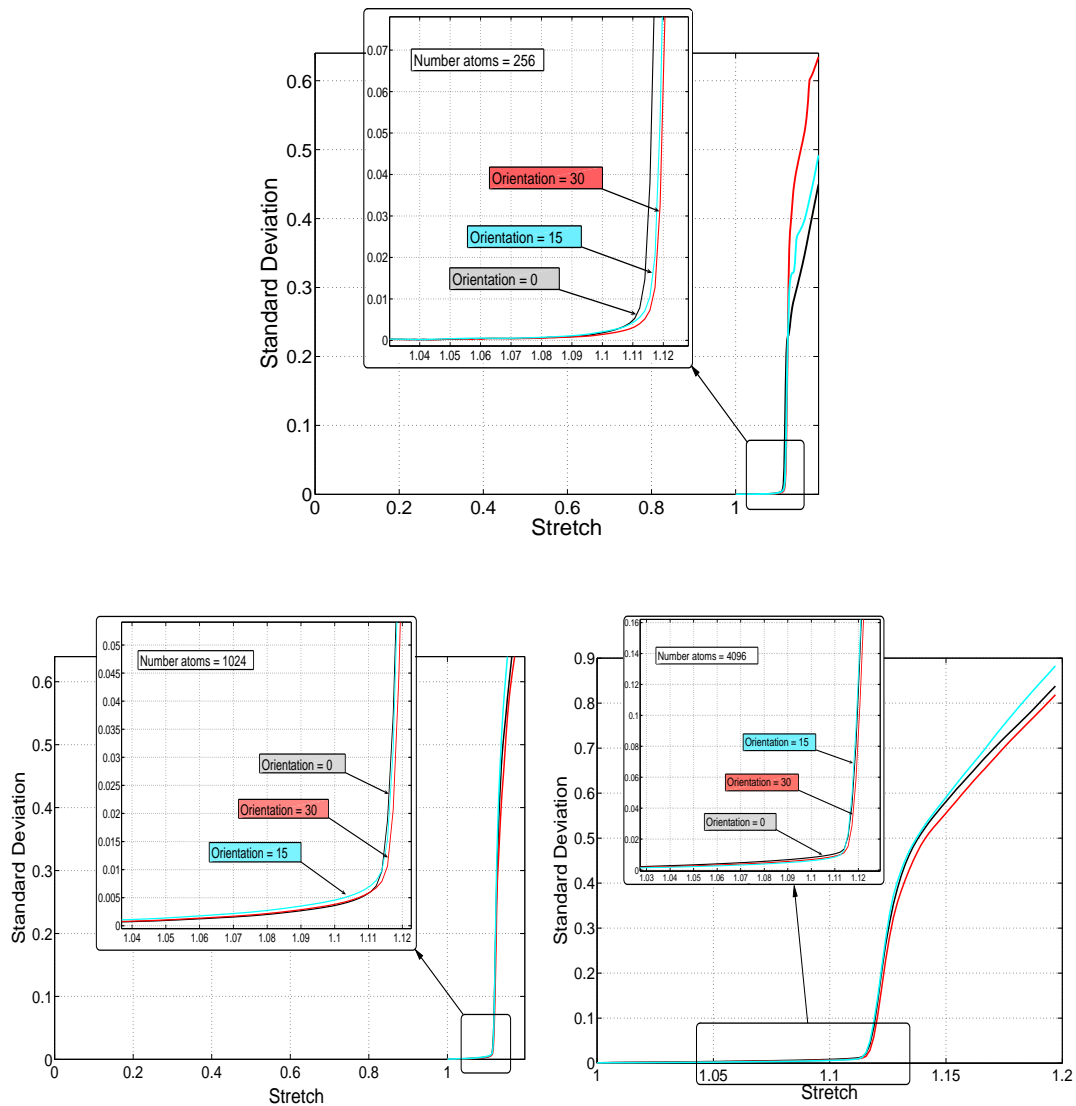


Figure 2.29: Standard deviation for dilatation deformation using Lennard–Jones potential comparing 0, 15, 30 degrees lattice orientation with 256, 1024 and 4096 atoms. The stretch λ which marks deviation is practically the same independent of the orientation considered.

From a stretch of $\lambda = 1$ until a stretch between $\lambda = 1.11$ and $\lambda = 1.12$, depending on the number of atoms considered in our model, the standard deviation gives us a value approximately equal to zero. Thus, this regime corresponds to the period in which the

Cauchy–Born rule is adequate for describing material behaviour, i.e. the unconstrained lattice follows affine homogeneous deformation. From this deformation state, the value of the standard deviation increases steeply, pointing out the boundary of its applicability. Note that the bifurcated regime starts almost at the same deformation state independently of the orientation considered.

Again the results monitored before are compared with the results obtained using the second type of computations in which constrained and unconstrained particles are updated separately. This is done in order to confront whether both types of simulations indicate the same state of transition to an inhomogeneous deformation or to ascertain the range of validity of the Cauchy–born rule for the dilatation deformation case.

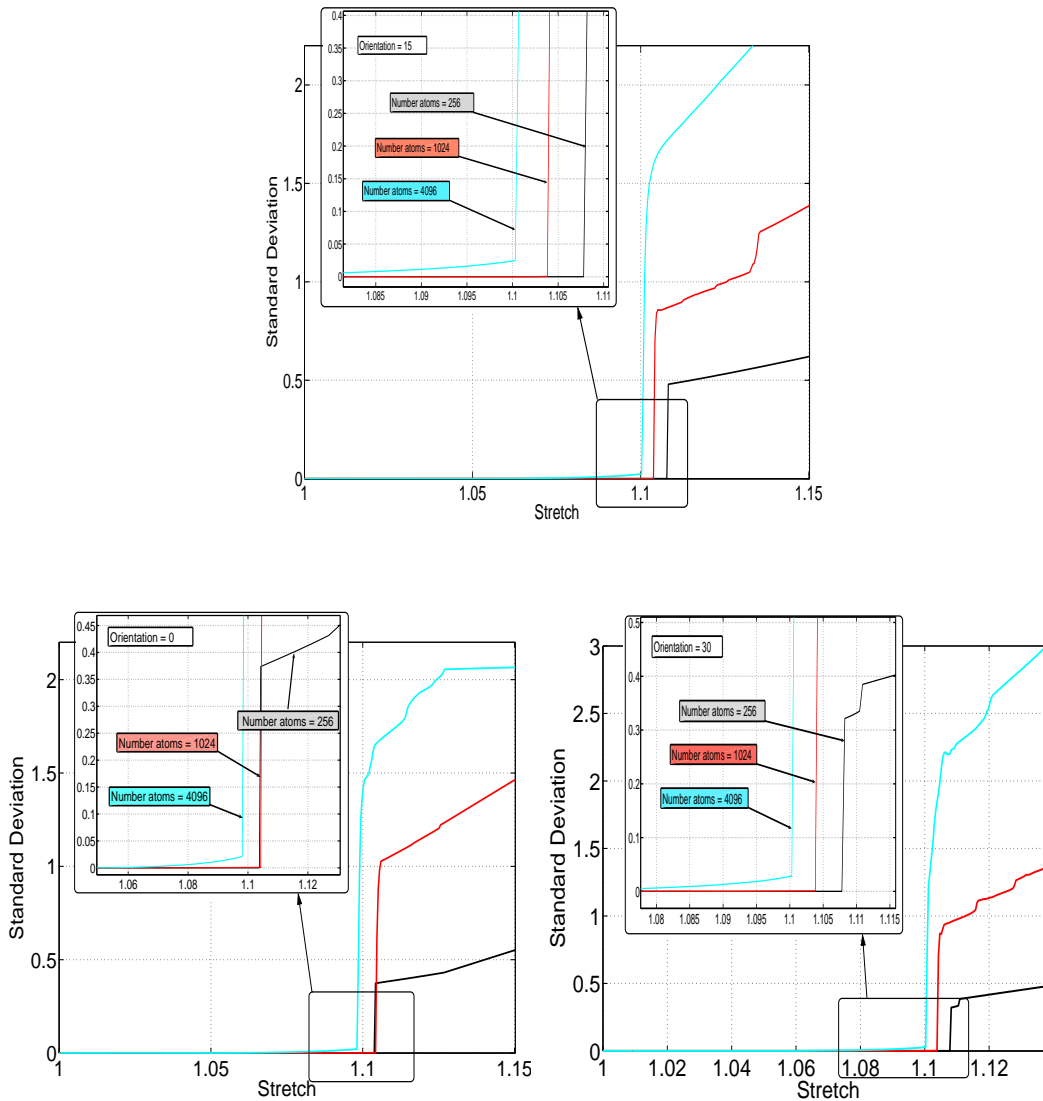


Figure 2.30: Standard deviation for dilatation deformation using Lennard–Jones potential comparing 256, 1024, 4096 number of atoms for 0, 15 and 30 degrees lattice orientation.

We distinguish in Figure 2.30 that from a stretch value of $\lambda = 1$ to $\lambda \approx 1.1$ for 0, 15 and 30 degrees lattice orientations for the standard deviation give us the validity of the Cauchy–Born rule. This result agrees well with the one achieved in the simulation performed before, see Figure 2.28. The same occurs comparing Figures 2.31 and 2.29. It turns out that both computations reveal the onset of instabilities at the same state $\lambda \approx 1.11$. From this point, once again the standard deviation value increases drastically because from this point the system is not stable anymore.

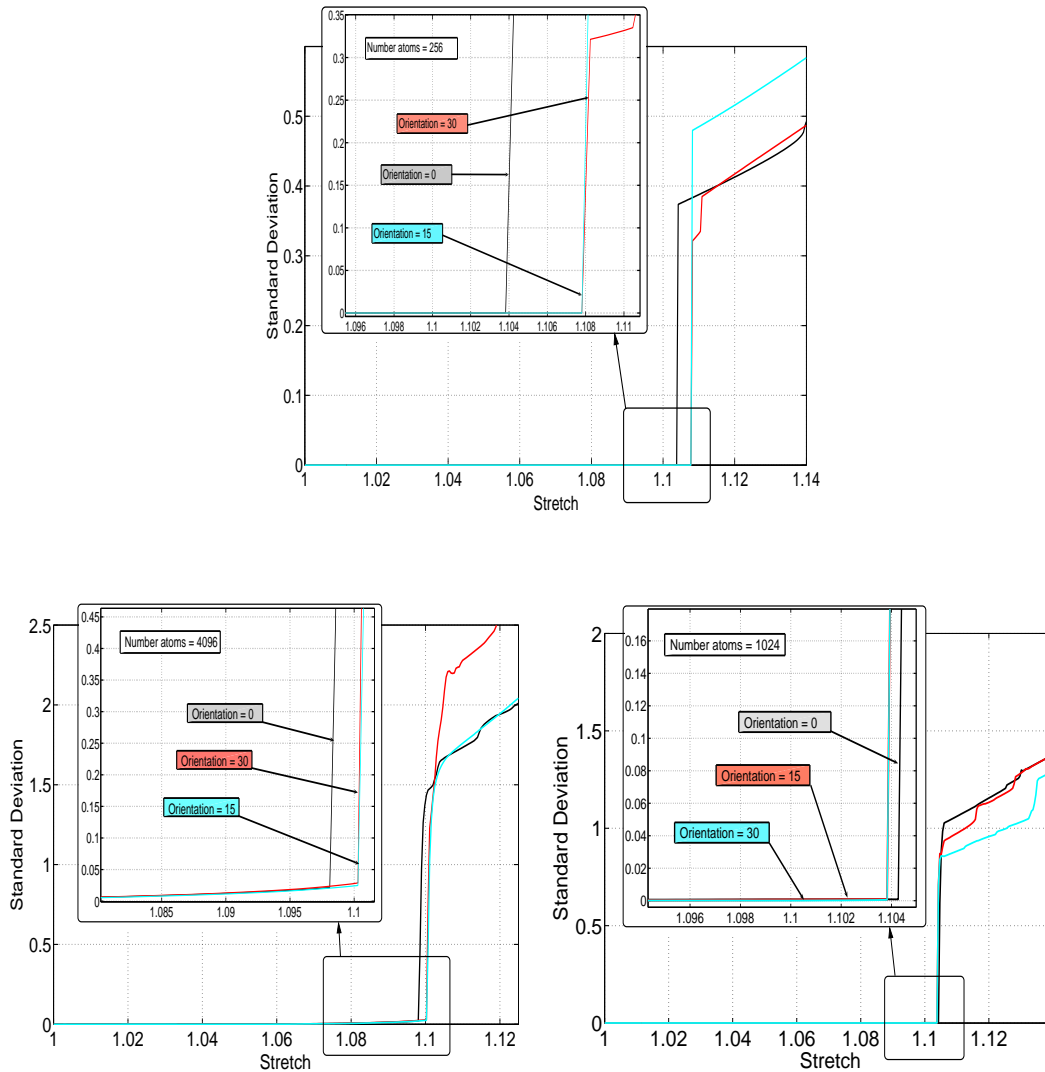


Figure 2.31: Standard deviation for dilatation deformation using Lennard–Jones potential comparing 0, 15, 30 degrees lattice orientation with 256, 1024 and 4096 atoms.

The corresponding result within the continuum mechanics can be seen in Appendix C Figure C.4. The value where the instabilities begin is $\lambda = 1.1131$. This result agrees with the results exhibited above. Note that the simulations performed with molecular dynamics suffer from round–off errors since we use approximation equations and/or algorithms to estimate the trajectories of the atoms.

2.5 Summary

A study on the validity of the Cauchy–Born rule and its transition to an inhomogeneous deformation was undertaken using atomistics in the sense of molecular dynamics which can capture complex nanoscale behaviour as well as atomistic displacement. Parallel to the use of molecular dynamics, the results obtained here can be compared to a classical continuum mechanics approach using the acoustic tensor. This was done by Sunyk and Steinmann [126] and later included in Steinmann et al. [123]. They only provide results for the deformation cases simple shear and uniaxial extension limited for 0 and 30 degrees orientation respectively. Therefore we have included an appendix, see Appendix C, in order to complete the results acquired so far with molecular dynamics. Note that the purpose of this work or rather this appendix is not to delve into the acoustic tensor concept used to study material stability.

In each figure presented here, the state from where the deformation becomes inhomogeneous, the value of the standard deviation increases dramatically. This indicates the limits of the Cauchy–Born rule. That is because from this point the system is no longer stable and the difference among the positions of the unconstrained and constrained atoms increases drastically. Thus, the results in the post–bifurcated regime is an artefact that is heavily influenced by the boundary conditions and thus of no particular relevance in the present context. Furthermore it is worth to comment that the departures from the Cauchy–Born rule occur at different strains in simple shear and in the other modes. Finally, the dependence of the cut–off radius on the form of the interatomic potential plays an important role in these simulations. That is intensely discussed in the work pursued by Sunyk [125]. There, it is studied the choice of the cut–off by comparing the strain energy density, W_0 , for different integer scaling factors. It is recognizable that the energy converges to a constant value with the increasing the scaling factor.

For the dynamic case to be investigated in Chapter 4 the interface between the constrained and unconstrained atoms produces another problem which it relates to the pulses initiated in the dynamic domain and reflected at the interface due to the constrained atoms. This then behaves as a rigid boundary avoiding the smooth absorption of these waves. Such phenomenon was noted by Doll and Adelman [43] and Holmes and Belytschko [69]. It is also interesting to broaden the simulations using several techniques developed recently, e.g. by Cai et al [24], Holian and Ravelo [67], Qu and al [107] in order to avoid or reduce these spurious reflections.

It is important to remark that the atoms in Figures 2.8, 2.14, 2.20 and 2.26 are coloured using the atomic level stress, see details in Appendix B. Specifically, according to the expression, B.2, which provides the average virial stress over an effective volume. Actually, the meaning of the colour in the present context is irrelevant for us since the goal is not to describe the state of the stress of the atoms in the system but to find out the limit of the Cauchy–Born rule validity. Expression B.2 is only used in order to distinguish the constrained and unconstrained atoms during the simulation. Finally, it is worth to comment that the unconstrained atoms are coloured according to the scalar product, i.e.

the trace of Equation B.2, which it is related to the hydrostatic pressure. Nevertheless, it would be possible to colour Figure 2.8 with a shear stress, since we studied a shear deformation case, instead of with the trace (the volumetric stress) for a much more precise description of the different states.

3 Horizontal Coupling in Continuum Atomistics

3.1 Introduction

The phenomenological mechanical behaviour of materials reveals a strong multiscale dependence, at the spatial scale as well as the temporal scale, see Figure 3.1¹. For instance, at the fundamental level, features of crystalline solids may be attributed to electronic interactions which obey first principles such as the Schrödinger equation. However, quantum-mechanics is still limited to short scales in time and length. Ignoring the role of electrons and assuming some empirical interactions allow us to increase the length and time scales until the atomistic level, where molecular dynamics or Monte Carlo simulations may be performed for describing crystal structures. Beyond the atomic scale, we encounter mesoscopic theories (such as crystal plasticity) dealing with grain boundaries or dislocation mechanics. Finally, the continuum mechanics framework dominates at the material scale to model mechanical properties [147]. From now on, we restrict our attention to molecular dynamics and continuum mechanics methods.

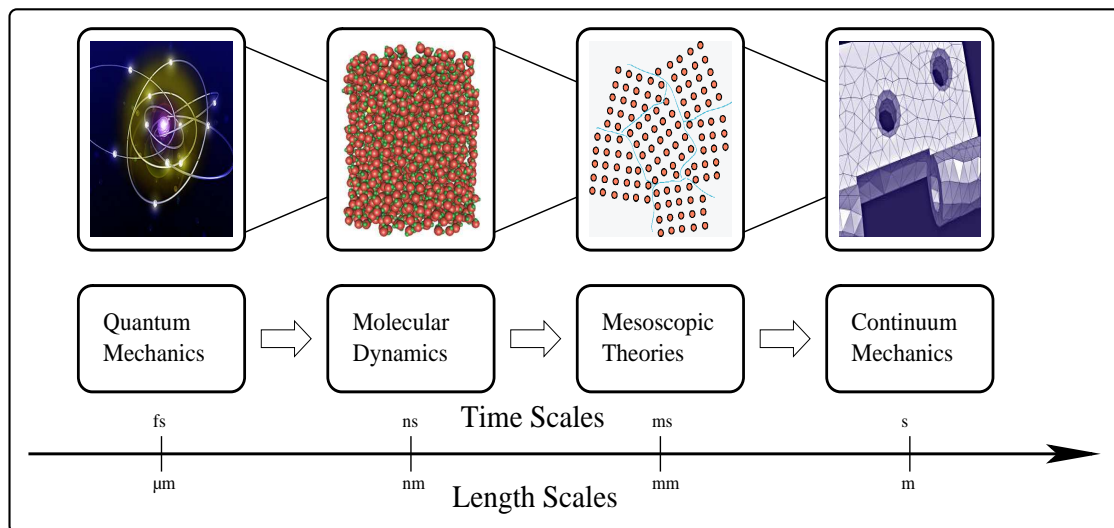


Figure 3.1: Schematic representation giving an overview over the typical length and times scales for different simulations tools. From the quantum mechanics methods at the sub-micronscales, to molecular dynamics and montecarlo, as well as mesoscale methods (crystal plasticity or coarse grains approaches) until classical continuum theories e.g. finite element method (FEM).

¹The idea of this figure was taken from the work pursued by Buehler [21]

Thanks to the ongoing constant advances in computational power and accessibility the range of applications of molecular dynamics approach is rapidly increasing. The earlier works were done by Rahman [109] dealing with only a few hundred atoms whereas several researchers have recently performed large size systems, simulations including up to one billion atoms [2, 3]. It has also become a realistic computational option for simulating a variety of physical problems and analyse of traditionally complex atomic phenomena such as dislocations [26, 118], phase transitions [91, 117], cracks opening and fracture [61, 68], that had been impossible to deal with thus far, see figure 3.2. Furthermore, molecular dynamics with empirical potentials nowadays plays a key role to model large length scale associated to the plastic process in materials [22].

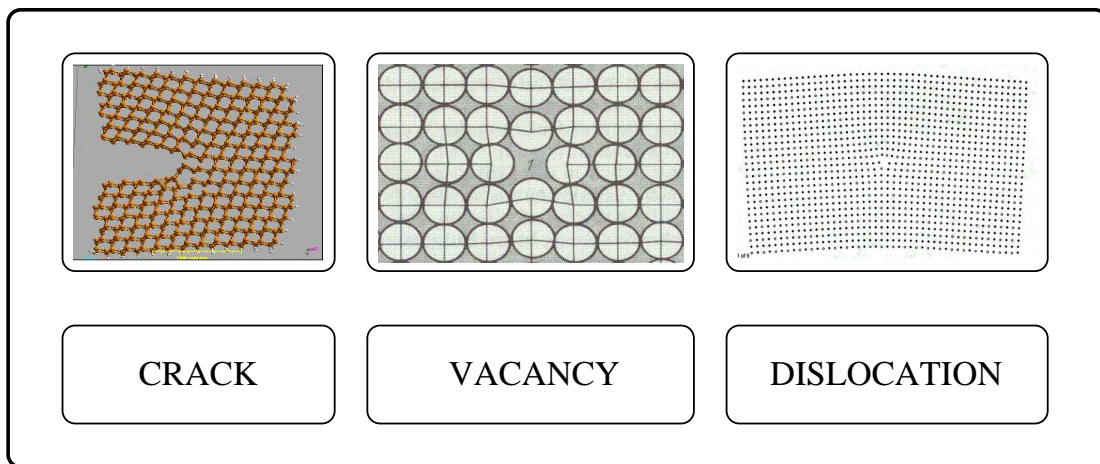


Figure 3.2: Representation of the typical atomic phenomena which occur in materials such as cracks opening, vacancies as well as dislocations.

Nevertheless, the length and time scales are still limited. For example traditional time scales are of order of 10^{-15} seconds which is used for 10 nm length scales. In addition, the relaxation time required varies for each different property. An example would be a model near a phase transition which become slower and therefore need a relaxation time beyond the time achievable by a simulation. Furthermore, the realistic modelling of a macroscopic problem is not yet feasible with a fully atomistic simulation due to the exhaustive computational demand and the excessive and often useless data which results at the end. In large scale atomistic calculations only a small set of atoms does anything interesting. Another problem associated with molecular dynamics is the comparison of results obtained from simulations with real experiments because these are carried out in much longer length and time scales.

On the contrary, the continuum mechanics framework has dominated the research activity of mechanics over the past decades to predict material behaviour in time and space. The range of application of continuum models allows us to efficiently compute large systems of material speaking in terms of stresses and strains but at the expense of suffering lack of accuracy, discretization errors and including a number of uncertainties in the precision of the simulations (how good the constitutive model is).

The purpose of the present work is to introduce a coupling constitutive model for multi-scale analysis combining the traditional molecular dynamics approach as atomistic method and finite element method based on the Cauchy–Born rule as continuum approach. The physical domain is divided in two spatial regions. A schematic representation of the geometry used in this model is depicted in figure 3.3. One is the atomistic domain represented by the white circles. It contains the critical region of study where molecular dynamics is used. This region is embedded in the continuum domain represented by the square elements.

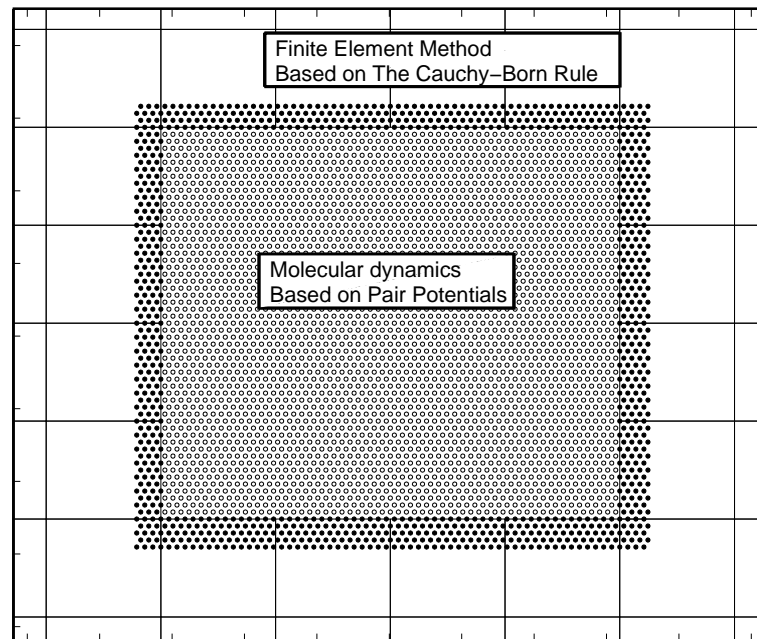


Figure 3.3: Representative coupling model between an atomistic region in the sense of molecular dynamics based on pair-potentials and continuum using finite element method based on the Cauchy–Born rule.

This produces a common difficulty in these hybrid models due to the fundamental incompatibility of the non-local character of the atomistic description and the local continuum description [40]. In the continuum modelling the kinematics are characterized by the so-called Cauchy–Born rule [129], which provides an elegant formulation to bridge information between atomistic and continuum models. The Cauchy–Born rule prescribes atomistic positions in the strained crystal by the application of the local deformation gradient. The application of the Cauchy–Born rule requires sufficiently homogeneous deformation as it was studied in the previous chapter.

Note that the main goal of numerous researchers has also been to provide a computational solution for the analysis of deformation processes at different length and time scales in a unified framework as well as to pursue homogenization approaches. Therefore, we will review some of the strategies proposed so far before introducing the model suggested here.

3.2 Short Overview over the Atomistic/Continuum Coupling Techniques

In the last few years several scale bridging techniques have appeared in order to solve the problem related with the lack of microstructural information in continuum models. They also try to overcome the limitations of the prohibitive computational demand of a fully macroscopic atomistic simulation. Here is where hybrid models come into play. They attempt to provide a computational solution to analyze physical phenomena at different length and time scales in a unified framework.

A very popular approach is the Quasicontinuum method (QC), see e.g. Tadmor [129], Shenoy et al. [118] and Tadmor et al. [131]. The idea is to simulate a macro system under non-linear deformation using molecular mechanics. Some selected atomic degrees of freedom are removed and interpolated from a subset of representative atoms similar to finite element interpolation. The constitutive law is based on these representative atoms governed by the Cauchy–Born rule which force these atoms to deform according to the local continuum deformation gradient. Summarizing, the degrees of freedom are substantially reduced and atomistic resolution is only maintained in domains where defects play a key role. A recent review on the current state of the method is provided in Miller and Tadmor [92]. The classical version of the quasicontinuum was restricted to zero temperature simulations. Recently, however, the method was extended to finite temperatures [44].

An analytical approach developed recently is the tight-binding (FE/MD/TB) method or also called MAAD proposed by Abraham, Broughton, Bernstein and Kaxiras [1,20]. The simulation system is composed of three different parts. A continuum region where linear finite elements are applied. Then, near the crack tip, an atomistic region where molecular dynamics is used and a quantum mechanics region in which the tight-binding model is used to model bond breaking in silicon. In order to couple each domain, the authors introduced handshake regions where they overlap and thereby transmit the information from one domain to the other.

Another effective method is the so called CADD model proposed by Shilkrot et al. [119,120]. The philosophy consists of a continuum region in which an atomistic domain is embedded. This computational method allows to transfer dislocations from atomistics to the continuum domain combining atomistic and discrete dislocation mechanics.

The finite element and atomistic model (FEAT) is historically the earliest method of such models. It was developed by Kohlhoff et al. [78] in order to simulate crack propagation in b.c.c. crystals. Finally, the CLS approach of Rudd and Broughton [114,115] formulated a coarse-grained method which attempt to derive an effective Hamiltonian for a set of coarse-grained variables. This method exhibits good results for one-dimensional models but it is still difficult to compute. A fundamental review comparing the methods mentioned so far was pursued by Curtin and Miller [40].

In the end, we also refer the reader to an alternative hybrid method developed by Liu and co-workers [143, 144] called scale bridging. The idea is that the finite elements exists everywhere, this is in the entire computational domain, even where the molecular dynamics is applied. Other models dealing with this topic are the works done by Weinan et al. [46], Rodney [112], Mortensen et al. [95], Belytschko et al. [12, 151], Rafii-Tabar et al. [108] and more recently Kwon and Jung [80] and Zhennen and Xiurum [153].

The layout of the present chapter is as follows: The main definitions and tools of continuum modelling, applications and limitations of the Cauchy–Born rule are given in Section 3.3. Section 3.4 presents in detail the coupling method. Lastly, numerical examples are displayed in Section 3.5, followed by the conclusions, which close the chapter.

3.3 Essentials of Continuum Mechanics Framework. The First–Order Cauchy–Born Rule.

In order to introduce terminology and notation, a short summary of the governing kinematics aspects corresponding to the spatial motion problem within the continuum mechanics framework is described. An overview of the tools applied in the present work for the continuum–atomistic modelling are also outlined in this section. In this context, the (first–order) Cauchy–Born rule studied in the previous chapter is reiterated as a homogenization technique to bridge atomistic and continuum scales.

3.3.1 Kinematics of Continuum Mechanics

In continuum mechanics a body is considered as a collection of material points. In this context, let $\varphi(\mathbf{X})$ denote the non–linear deformation map which relates material points \mathbf{X} in the material configuration \mathcal{B}_0 of a physical particle to spatial points \mathbf{x} in the spatial configuration \mathcal{B}_t of the same physical particle as

$$\mathbf{x} = \varphi(\mathbf{X}). \quad (3.3.1)$$

Figure 3.4 illustrates a schematic representation of the pointwise kinematics of continuum mechanics.

The linear tangent map associated to the spatial motion is represented by the two–point tensor \mathbf{F} , Equation 3.3.2, known as the local continuum deformation gradient.

$$\mathbf{F} = \nabla_{\mathbf{X}} \varphi = \frac{\partial \varphi}{\partial \mathbf{F}}. \quad (3.3.2)$$

The deformation gradient \mathbf{F} plays a crucial role in continuum mechanics since it serves as a transformation rule [70]. For instance, it transforms infinitesimal line elements of the material tangent space $T\mathcal{B}_0$ to infinitesimal line elements of the spatial tangent space $T\mathcal{B}_t$

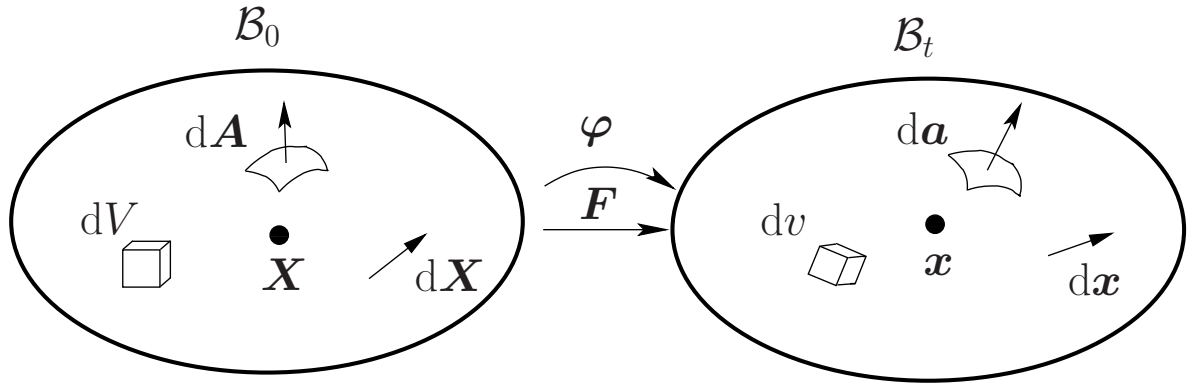


Figure 3.4: Spatial motion nonlinear deformation map and the deformation gradient. Furthermore, the transformations of line, area and volume elements in the material configuration, \mathcal{B}_0 , and spatial configuration, \mathcal{B}_t , are plotted.

$$d\mathbf{x} = \mathbf{F}d\mathbf{X}. \quad (3.3.3)$$

Then, the determinant of the deformation gradient \mathbf{F} , i.e. the spatial motion Jacobian is denoted by $J = \det \mathbf{F}$. Since the deformation gradient is invertible, its determinant is needed to be nonzero $J \neq 0$. The Jacobian relates volume elements dv and dV from the spatial configuration to the material configuration respectively

$$J = \frac{dv}{dV}. \quad (3.3.4)$$

The transformation of the area elements $d\mathbf{a}$ in the spatial configuration to $d\mathbf{A}$ in the material configuration is possible thanks to the Nanson's formula as follows

$$d\mathbf{a} = J\mathbf{F}^{-t}d\mathbf{A}. \quad (3.3.5)$$

\mathbf{F}^{-t} being the transpose of the inverse deformation gradient \mathbf{F} . The area elements are defined by the use of the material and spatial normal vectors \mathbf{N} and \mathbf{n} respectively

$$d\mathbf{A} = \mathbf{N}dA. \quad (3.3.6)$$

$$d\mathbf{a} = \mathbf{n}da. \quad (3.3.7)$$

The deformation gradient can also be used to describe the constitutive response of the continuum. For instance, typical strain measures are defined by the right Cauchy–Green tensor $\mathbf{C} = \mathbf{F}^t \cdot \mathbf{F}$ and the left Cauchy–Green tensor $\mathbf{b} = \mathbf{F} \cdot \mathbf{F}^t$, see [16, 70, 122].

For hyperelastic material response, the stored strain energy density per unit volume W in \mathcal{B}_0 is given by

$$W_0 = W_0(\mathbf{F}; \mathbf{X}) \quad (3.3.8)$$

which is a function of the deformation gradient \mathbf{F} and in general of the reference placement \mathbf{X} .

We now reiterate the familiar quasi–static balance of momentum which reads

$$\text{Div} \mathbf{P} + \mathbf{b}_0 = \mathbf{0} \quad (3.3.9)$$

Equation 3.3.9 involves the spatial motion Piola stress tensor \mathbf{P} . It is a two point tensor generated by the first derivative of the strain energy density $W_0(\mathbf{F}; \mathbf{X})$ with respect to the deformation gradient \mathbf{F}

$$\mathbf{P} = \nabla_{\mathbf{F}} W_0 = \frac{\partial W_0}{\partial \mathbf{F}} \quad (3.3.10)$$

The Piola transformation of \mathbf{P} renders the Cauchy stress $\boldsymbol{\sigma}^t = J^{-1} \mathbf{P} \mathbf{F}^t$ and the Piola–Kirchhoff stress $\mathbf{S} = \mathbf{F}^{-1} \mathbf{P}$.

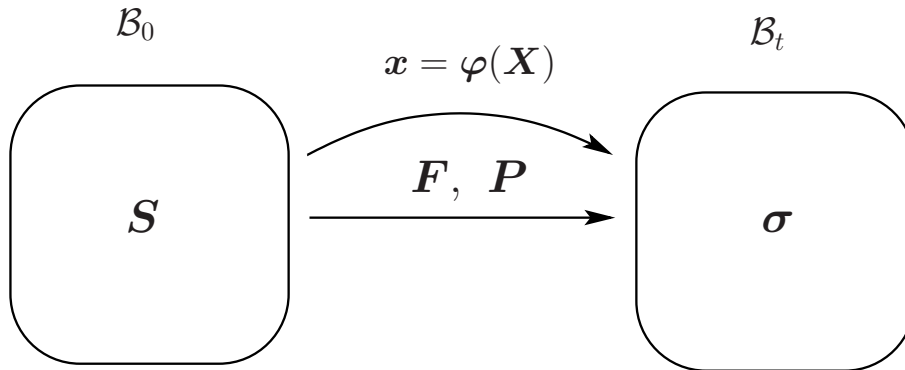


Figure 3.5: Kinematics of the spatial motion problem. \mathcal{B}_0 represents the material configuration whereas \mathcal{B}_t represents the spatial or also known as current configuration.

The fourth order tangent operator \mathbb{L} is a consequence of the linearization of the stress tensor \mathbf{P} . It relates the increment in \mathbf{P} to the increment in the deformation gradient. It is defined as the second derivative of the strain energy with respect to the deformation gradient.

$$\mathbb{L} \doteq \frac{\partial^2 W_0}{\partial \mathbf{F} \otimes \partial \mathbf{F}} \quad (3.3.11)$$

3.3.2 Atomistic Constitutive Modelling

In order to facilitate further discussion, we briefly reiterate the description of the classical lattice statics outlined in the previous chapter 2. We imagine an infinite defect-free crystal consisting of N interacting atoms. The kinematics of this crystallite body is traditionally represented by the distance among the particles included in the system. Let us consider any two atoms labelled i and j . The relative distances \mathbf{R}_{ij} and \mathbf{r}_{ij} between these two atoms in the material configuration \mathcal{C}_0 and in the spatial configuration \mathcal{C}_t respectively, see bottom part of Figure 2.3, are

$$\mathbf{R}_{ij} = \mathbf{R}_i - \mathbf{R}_j \quad \text{with} \quad R_{ij} = |\mathbf{R}_{ij}|, \quad (3.3.12)$$

$$\mathbf{r}_{ij} = \mathbf{r}_i - \mathbf{r}_j \quad \text{with} \quad r_{ij} = |\mathbf{r}_{ij}|, \quad (3.3.13)$$

where $\mathbf{R}_i, \mathbf{R}_j$ are the position vectors of atoms i and j in the material configuration and \mathbf{r}_j and \mathbf{r}_i the position vectors of the same atoms but in the spatial configuration. We assume that the total internal energy E^{int} of the crystal can be defined as the sum of all energy contributions of the atoms which compose the lattice

$$E^{int} = \sum_i E_i, \quad (3.3.14)$$

in which E_i is the i -atom energy contribution which typically depends on the distances among the N atoms $E_i = E_i(r_{i1}, \dots, r_{iN})$. Despite all shortcomings mentioned in chapter 1 and for the sake of efficiency and simplicity, we will restrict the contribution in the energy to two-body interactions. Thus, the energy contribution E_i of the atom i can be characterized as

$$E_i = \frac{1}{2} \sum_{j \neq i} \phi(r_{ij}), \quad (3.3.15)$$

where $\phi(r_{ij})$ represents again the pair potential function which governs the interatomic mechanical behaviour. Typical examples were discussed in chapter 1. Here, we reiterate the well-known Lennard–Jones potential energy function which reads

$$\phi(r_{ij}) = 4\epsilon \left[\left[\frac{\sigma}{r_{ij}} \right]^{12} - \left[\frac{\sigma}{r_{ij}} \right]^6 \right], \quad (3.3.16)$$

with the atomic separation $r_{ij} = |\mathbf{r}_{ij}|$. The symbols σ and ϵ are parameters which must be fitted to the considered material. The energy contribution E_i of the atom i is then given by

$$E_i = \frac{1}{2} \sum_{j \neq i} \phi(r_{ij}) = \sum_{j \neq i} 2\epsilon \left[\left[\frac{\sigma}{r_{ij}} \right]^{12} - \left[\frac{\sigma}{r_{ij}} \right]^6 \right]. \quad (3.3.17)$$

Consequently, the derivative of the total internal energy E^{int} , equation 3.3.14, with respect to the position vector \mathbf{r}_i of the i th atom provides the total force \mathbf{f}_i acting upon this atom due to the interactions with all others atoms. Using the chain rule we may write the force on i in the form

$$\mathbf{f}_i = -E_{,\mathbf{r}_i}^{int} = \sum_{j \neq i} \mathbf{f}_{ij} = - \sum_{j \neq i} \frac{\partial E_i}{\partial \mathbf{r}_i} = -\frac{1}{2} \sum_{j \neq i} \frac{\partial \phi(r_{ij})}{\partial \mathbf{r}_i} \quad (3.3.18)$$

$$= -\frac{1}{2} \sum_{j \neq i} \frac{\phi(r_{ij})}{\partial r_{ij}} \frac{\partial r_{ij}}{\partial \mathbf{r}_{ij}} \frac{\partial \mathbf{r}_{ij}}{\partial \mathbf{r}_i} = \sum_{j \neq i} -\frac{1}{r_{ij}} \frac{\partial \phi(r_{ij})}{\partial r_{ij}} \mathbf{r}_{ij}. \quad (3.3.19)$$

Then, the interactive force \mathbf{f}_{ij} acting on the atom i due to the atom j , see Figure 3.3.2, can be defined for the case of pair potentials as

$$\mathbf{f}_{ij} = -\frac{\phi'_{ij}}{r_{ij}} \mathbf{r}_{ij}. \quad (3.3.20)$$

The prime in ϕ'_{ij} denotes the derivative of the interatomic potential function ϕ_{ij} with respect to the relative distance r_{ij} and \mathbf{r}_{ij}/r_{ij} which represents the unit normal vector [7].

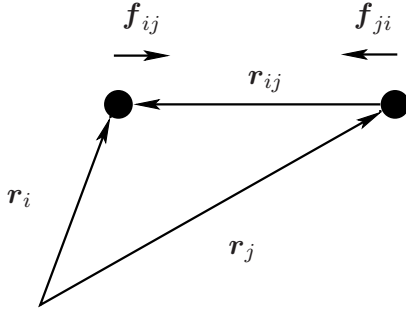


Figure 3.6: The relative distance vectors between i and j is represented by \mathbf{r}_{ij} whereas \mathbf{f}_{ij} denotes the interaction force. Note that $\mathbf{f}_{ij} = -\mathbf{f}_{ji}$.

The second derivative of the total energy with respect to the position vector \mathbf{r}_j yields a second order tensor, this is the atomic stiffness \mathbf{k}_{ij} , which restricted to the considered case of pair potentials takes the format

$$\mathbf{k}_{ij} = -E_{,\mathbf{r}_i \mathbf{r}_j}^{int} = \frac{\phi'_{ij}}{r_{ij}} \mathbf{I} + \left[\frac{\phi''_{ij}}{r_{ij}^2} - \frac{\phi'_{ij}}{r_{ij}^3} \right] \mathbf{r}_{ij} \otimes \mathbf{r}_{ij}, \quad (3.3.21)$$

where \otimes denotes the standard dyadic product. Equation 3.3.21 was discussed by Sunyk and Steinmann [127] and is needed in the solution strategy within the continuum–atomistic modelling. For details see also [125]. Note that a non–linear version of the second order term in Equation 3.3.21 was discussed in connection with gradient elasticity by Triantafyllidis and coworkers starting in 1986 [135].

3.3.3 Continuum–Atomistic Constitutive Modelling

Once the atomistic constitutive modelling is described, the next and main issue is how to relate continuum and atomistic scales in a mixed vertical constitutive model. The central idea to achieve is that the explained continuum quantities such as the stress tensor, Equation 3.3.10, and tangent operator, Equation 3.3.11, can be computed directly from atomistic calculations. The first step relies on replacing the phenomenological macroscopic continuum strain energy density W_0 , Equation 3.3.8, by an appropriate atomistic energy potential function as E_i , Equation 3.3.17. Under the consideration that the energy of each atom i is distributed uniformly over a volume V_i , both energies can be related as

$$W_0 = \frac{E_i(r_{i1}, \dots, r_{iN})}{V_i} = \frac{1}{2V_i} \sum_{j \neq i} \phi_{ij} = W_0(r_{i1}, \dots, r_{iN}), \quad (3.3.22)$$

where V_i is known as the Voronoi polyhedron, see Figure 3.3.3, and r_{i1}, \dots, r_{iN} represent the relative distances between atom i and their neighbours.

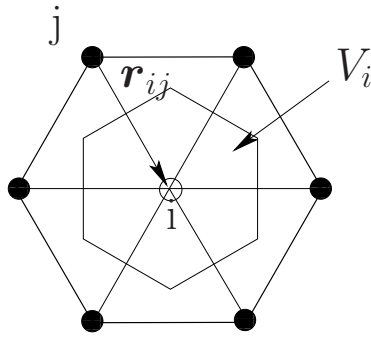


Figure 3.7: The Voronoi polyhedron V_i in the two dimensional case at the initial configuration. Each Voronoi cell is made by connecting the lattice points, in this case atoms, drawing lines. Then, at the midpoint normal lines are drawn. The smallest volume or area enclosed in these lines is the the Voronoi polyhedron.

The remaining problem consists of establishing the underlying kinematic relation between continuum deformation and atomic vectors. That is possible by appealing to the Cauchy–Born rule, which is a standard formulation for linking atomistic and continuum models [129]. Under the condition of an infinite defect-free crystal, the Cauchy–Born rule postulates that when a single crystal volume is subjected to a prescribed displacement of its boundary, all atoms of the volume follow this displacement, as outlined in detail in the previous chapter. In other words, the relative lattice vector \mathbf{r}_{ij} of the spatial configuration \mathcal{C}_t result from the corresponding \mathbf{R}_{ij} in the material configuration \mathcal{C}_0 by the application of the local deformation gradient \mathbf{F} , Equation 3.3.2, i.e. the Cauchy–Born is defined as

$$\mathbf{r}_{ij} = \mathbf{F} \cdot \mathbf{R}_{ij}. \quad (3.3.23)$$

Its major restriction and implication is that this assumption is only valid as long as the perfect infinite representative crystal remains homogeneous [85]. In practical simulations, the computation over all the atoms in the body have been replaced by a computation over a certain number of neighbour atoms included in a cut-off radius ($\mathbf{r}_{\text{cut-off}}$) which limits

the calculation of the interatomic forces.

Consequently, the strain energy density W_0 , equation 3.3.8, can be reformulated in terms of the relative distance vectors in the material configuration \mathcal{C}_0 and the deformation gradient \mathbf{F} as

$$W_0(r_{i1}, \dots, r_{iN}) = W_0(|\mathbf{F} \cdot \mathbf{R}_{i1}|, \dots, |\mathbf{F} \cdot \mathbf{R}_{iN}|). \quad (3.3.24)$$

At this point we reiterate the expression of the constitutive law, i.e. the Piola stress tensor \mathbf{P} , Equation 3.3.10, which takes the following explicit format for pair potentials

$$\mathbf{P} \doteq \frac{\partial W_0(\mathbf{F}, \mathbf{X})}{\partial \mathbf{F}}. \quad (3.3.25)$$

Then

$$\mathbf{P}(\mathbf{X}_i) = \frac{1}{2V_i} \sum_{j \neq i} \mathbf{f}_{ji} \otimes \mathbf{R}_{ij}. \quad (3.3.26)$$

where $\mathbf{f}_{ji} = -\mathbf{f}_{ij}$ is the interatomic force. Analogously to the known formula in continuum mechanics, we obtain the Cauchy stress tensor

$$\boldsymbol{\sigma}^t = J^{-1} \mathbf{P} \mathbf{F}^t = \frac{1}{2v_i} \sum_{j \neq i} \mathbf{f}_{ji} \otimes \mathbf{R}_{ij} \mathbf{F}^t = \frac{1}{2v_i} \sum_{j \neq i} \mathbf{f}_{ji} \otimes \mathbf{r}_{ij}, \quad (3.3.27)$$

where $J = v_i/V_i$ and the Piola–Kirchhoff stress is

$$\mathbf{S} = \mathbf{F}^{-1} \mathbf{P} = \frac{1}{2V_i} \sum_{j \neq i} \mathbf{F}^{-1} \mathbf{f}_{ji} \otimes \mathbf{R}_{ij} = \frac{1}{2V_i} \sum_{j \neq i} \frac{\partial \phi_{ij}}{\partial r_{ij}} \mathbf{R}_{ij} \otimes \mathbf{R}_{ij}. \quad (3.3.28)$$

Likewise, the expression for the tangent operator (3.3.11) is deduced considering (3.3.21) and (3.3.8) and renders the expression

$$\mathbb{L} \doteq \frac{\partial^2 W_0}{\partial \mathbf{F} \otimes \mathbf{F}}. \quad (3.3.29)$$

Then $\mathbb{L}(\mathbf{X}_i)$

$$\mathbb{L}(\mathbf{X}_i) = \frac{\partial \mathbf{P}}{\partial \mathbf{F}} = \frac{1}{2V_i} \sum_{j \neq i} \mathbf{k}_{ij} \bar{\otimes} [\mathbf{R}_{ij} \otimes \mathbf{R}_{ij}]. \quad (3.3.30)$$

where $\bar{\otimes}$ denotes the non–standard dyadic product ($[\mathbf{A} \bar{\otimes} \mathbf{B}] : \mathbf{C} = \mathbf{A} \cdot \mathbf{C} \cdot \mathbf{B}$) and \otimes again denotes the standard dyadic product, see appendix D.

So far, we have displayed the collection of quantities deduced by Sunyk and Steinmann [127] such as the stress tensor and tangent stiffness necessary within the continuum mechanics framework. They serve to link deformation or rather transmit information from the atomistic scale to the continuum scale. Moreover, they allow us the usage of the non–linear finite element method.

3.3.4 The Finite Element Simulation Structure

A numerical example is outlined in this section using the Cauchy–Born rule within the non–linear finite element method (FEM). We wish to reiterate the sequence of explanation exposed by Sunyk in his PhD thesis [125] and summarized in [127]. The main purpose of this extra section is twofold: First to show the applicability of the Cauchy–Born rule as a gateway to bring atomistic information into the realm of continuum mechanics in a vertical way. Secondly, in order to facilitate further understanding of the horizontal coupling between the FE approximation and molecular dynamics or rather between the continuum and atomistic domains. For detailed descriptions of the finite element method, the books written by Hughes [74] and Zienkiewicz [156] are excellent references. For German readers the book by Wriggers [150] is recommended and for examples implemented in Matlab see also [79]. The idea behind the simulation code consists of applying several steps as follows

1. Once the macroscopic body and the representative atomistic structure in each integration point are defined, an external load is applied (for example on the top of the body as in the depicted Figure 3.9).
2. That produces a macroscopic deformation in each element which allows us to compute the deformation gradient \mathbf{F} , equation 3.3.2.
3. The new atomistic placement of the underlying crystal lattice at the nano–scale is then computed by appealing to the Cauchy–Born rule which prescribed these atomic position by the application of the macroscopic deformation gradient \mathbf{F} using the equation 3.3.23.
4. With this new configuration of the representative crystallite we are in the situation of computing the continuum quantities as the Piola stress tensor, Equation 3.3.26, and the tangent operator, Equation 3.3.30, at the Gauss points of each element (e).

$$\mathbf{P}_e \doteq \frac{1}{2V_e} \sum_{j \neq i} \mathbf{f}_{ji} \otimes \mathbf{R}_{ij}.$$

$$\mathbb{L}_e \doteq \frac{1}{2V_e} \sum_{j \neq i} \mathbf{k}_{ij} \overline{\otimes} [\mathbf{R}_{ij} \otimes \mathbf{R}_{ij}].$$

5. This iterative process combining macro deformation and atomistic computations continues until the prescribed deformation is reached.

The basic procedure is summarized in table 3.1. In the following, an example of application is depicted.

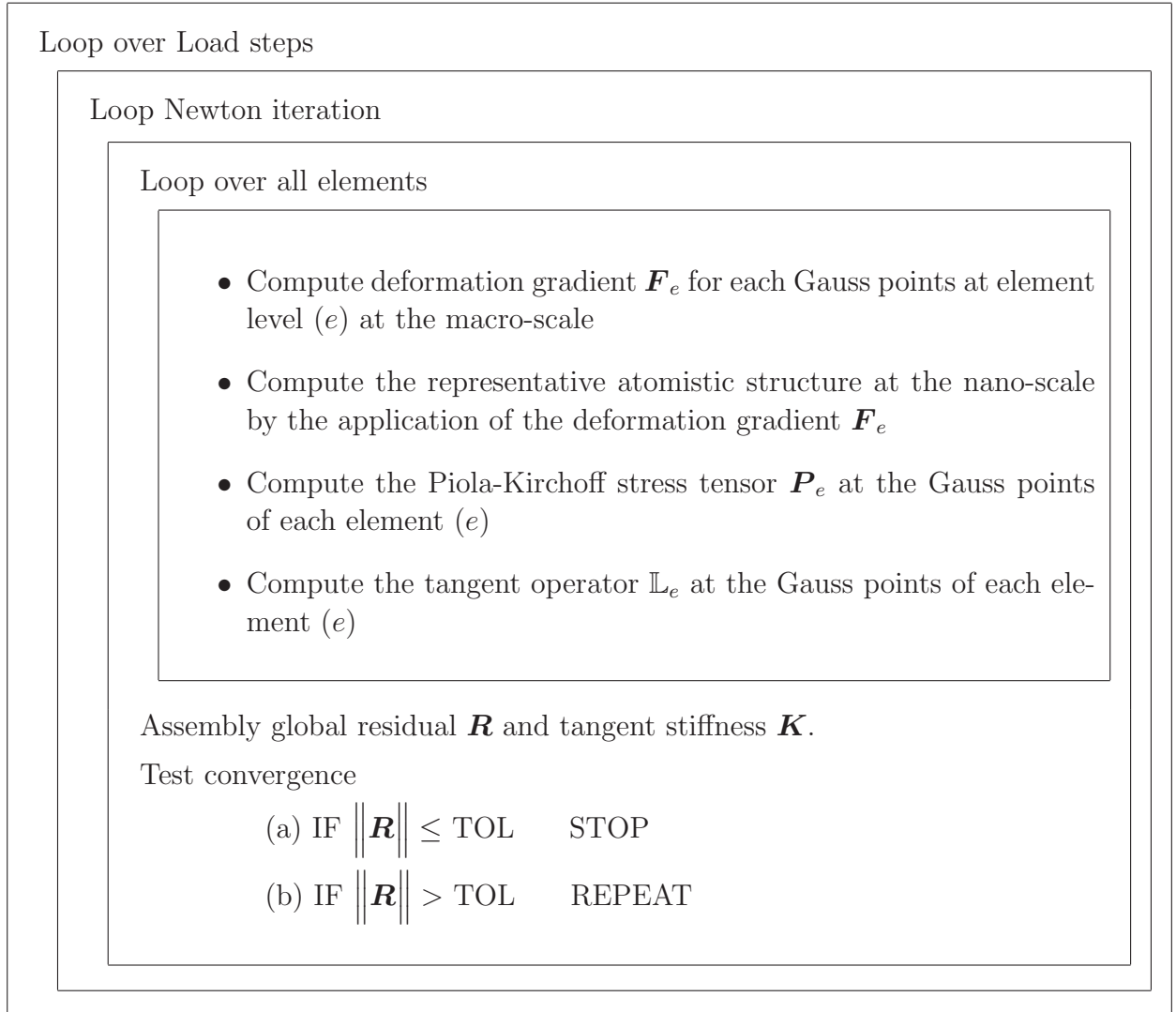


Table 3.1: Illustration of the algorithmic implementation using the Cauchy–Born rule as a gateway to link atomistic and continuum scales within a finite element approximation.

Example

In the present example, we consider a specimen in the three dimensional case. In Figure 3.9 is represented its geometry. We adopted 8–node elements for discretising the model that consists in 18 elements and 56 nodes. The loading conditions imposed for the specimen are plotted in the same Figure 3.9. They are applied on the top of the structure distributed uniformly in order to simulate a shear deformation. Zero displacement boundary conditions are used on the lower boundary. Furthermore, the nodes on the top are constrained and forced to move only horizontally with vertical impedance. The atoms of the representative crystal, i.e. the underlying configuration, are distributed in a *fcc*–type crystalline material. For the sake of representation a two dimensional lattice structure is represented in the detailed figures. We use the Lennard–Jones potential function, Equation (1.4.3), as a prototype model to compute the stress tensor as well as the tangent operator. The parameters σ and ϵ of the Lennard–Jones potential are shown in Table 3.2 for different lengths of the cut–off radius.

n	Number atoms	Length cut–off radius	$\epsilon (nN \cdot nm)$	$\sigma (nm)$
1	12	$a \frac{\sqrt{2}}{2}$	0.0957	0.2548
2	18	a	0.0854	0.2571
3	42	$a \sqrt{\frac{3}{2}}$	0.0748	0.2598
4	54	$a \sqrt{2}$	0.0728	0.2604
4	78	$a \sqrt{\frac{5}{2}}$	0.0709	0.2610
6	86	$a \sqrt{3}$	0.0705	0.2611

Table 3.2: Representation of length of the cut–off radius for different distance as well as the number of atoms within each cut–off radius. The corresponding parameters ϵ and σ of the Lennard–Jones pair potential are also shown. The lattice parameter is denoted by a which takes the value for Aluminium $a = 0.4044nm$.

These parameters are fitted to aluminium and they have been deduced from the values given in [42] under two conditions: First, stress-free in the material lattice configuration \mathcal{C}_0 . Secondly, the energy of an atom in the unloaded lattice is deduced following the Equation (3.3.24). It must yield the sublimation energy which in this case is $E_s = 3.58 eV = 0.574 nN nm$. The lattice parameter of Aluminium is $a = 0.4044 nm$ and the nearest neighbour distance has a value $r_0 = \sqrt{3} a/2 = 0.286 nm$. The cut–off radius considered is $r_c = n a$, with $n = 3$. The Wigner–Sitz cell for *fcc*–structure leads a value $V_i = a^3/4$ in the three dimensional case, see Figure 3.8². Figure 3.9 on the left shows the initial undeformed state whereas on the right a deformation state of the same specimen is displayed.

²This figure was taken from the web–side <http://omnis.if.ufrj.br/rrds/cursos/matcond/cap04/redes-3d.html>

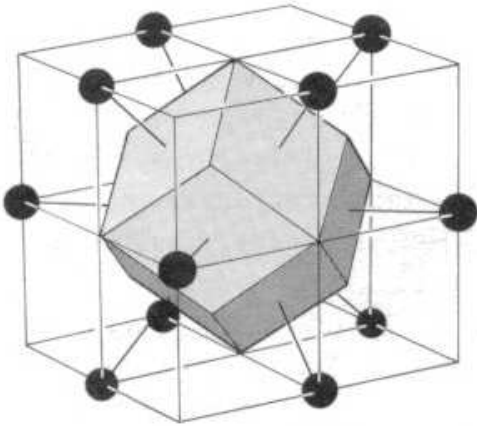


Figure 3.8: The Wigner–Seitz cell of fcc lattice in real space. It is made by taking the lines to the nearest and next neighbour points and bisecting them with planes.

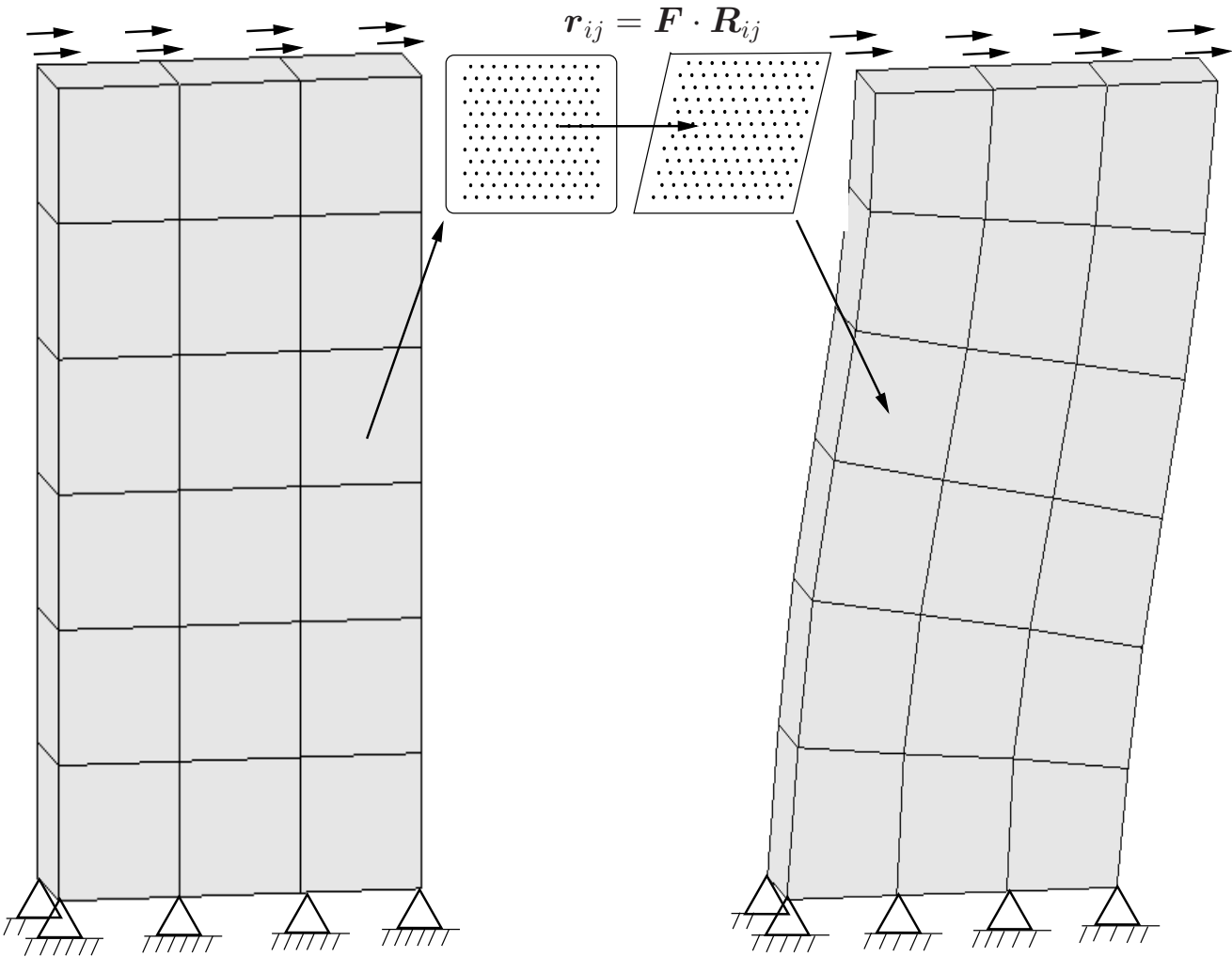


Figure 3.9: Schematic representation of a three dimensional structure with 18 elements using the Cauchy–Born rule within the non-linear finite method.

3.4 Coupling Algorithm in Continuum Atomistics

The central problem with the use of the Cauchy–Born rule is that this assumption is blind to defects and homogeneous deformation is required [129]. Therefore, the introduction of an atomistic method such as molecular dynamics is necessary for exploring the material structure at the sub–microscale. In spite of the ongoing rapid advances in computer power and accessibility a realistic modelling of a macroscopic problem is not yet viable with a fully atomistic simulation due to the exhaustive computational demand necessary for simulations in the sense of molecular dynamics. Simply large atomistic calculations result in excessive and often useless data where only a few set of atoms do anything interesting. The time and length that can be proved by molecular dynamics are still limited as well, even using parallel computers. That is the reason why a hybrid method combining atomistic resolution is necessary in order to capture the complex behaviour at the micron–scale with continuum techniques. These multiscale methods allow us to drastically reduce the number of degrees of freedom that a complete molecular dynamics computation of the same domain would possess. They also focus only on regions where something interesting happens using a resolution adapted to the type of solution considered.

Unfortunately, the coupling between molecular dynamics and the finite element method or rather between the atomistic and continuum regions, is a critical issue of such hybrid models due to the incompatibility between the non–local and local character of these two domains respectively [40]. A schematic illustration of the geometry set–up for the present work (2– dimensional case) is illustrated in Figure 3.10.

The physical problem is divided in two spatial regions as proposed by [78], [115] and [120]. A fully atomistic domain represented by the white circles. These atoms are considered as unconstrained atoms where the molecular dynamics approach is applied. By surrounding the atomistic region the continuum domain can be found where the finite element method is performed and the deformation is obliged to follow the Cauchy–Born rule. For the sake of simplicity only a few number of atoms and elements are represented. Additionally, an artificial set of atoms (black circles) overlap the continuum region. These atoms are considered constrained atoms, i.e. with zero temperature or $\mathbf{v} = \mathbf{0}$. They have several functions. First, they attempt to ensure that the unconstrained atoms close to the interface are properly placed avoiding the non–physical surface which arises in such coupled models as noted by Kohlhoff et al. [78] and Liu and co–workers [88]. Thus, they assure a smooth transition from the atomistic to the continuum, so that the unconstrained atoms have a complete set of interatomic neighbours. They then inform the unconstrained atoms about the deformation resulted in the continuum. They belong to the continuum and their positions are completely determined by the deformation that occurs in it. The minimum width of the constrained atoms region must be at least equal to the cut–off radius used for the interatomic computations in the unconstrained domain [120]. Finally, the atoms located at the interface are placed in order to transmit the deformation from the atomistic to the continuum, see detailed explanation below.

The principal issues for linking the finite element method and molecular dynamics are the definition of the forces and the treatment of the displacement field. In order to achieve

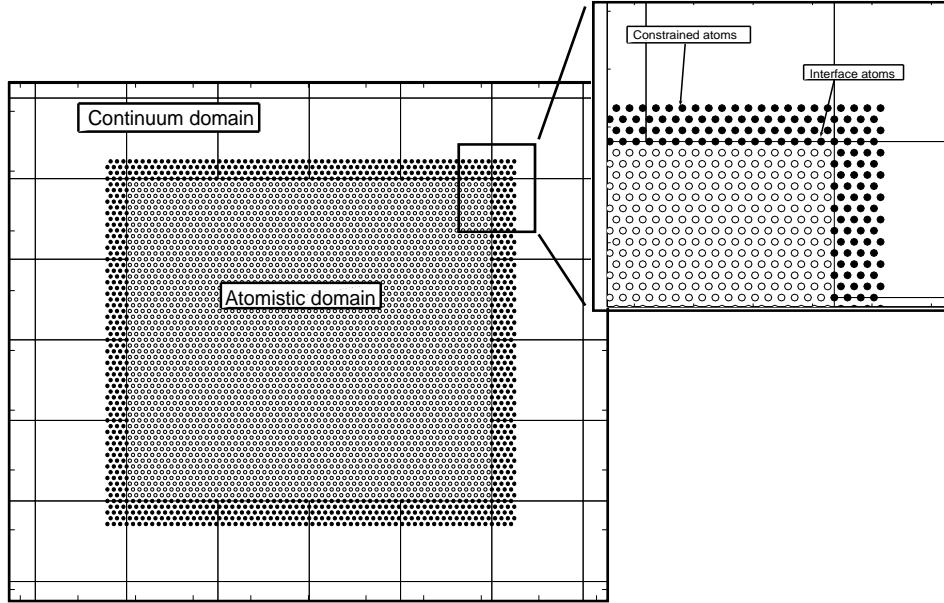


Figure 3.10: The white circles in the middle represent the atomistic domain in two the two dimensional case where the molecular dynamics method is applied. The domain around the atoms represents the continuum where finite elements are used. The coupling between atomistic and continuum is carried out through the black circles or also known as constrained atoms.

that, the coupled model is solved iteratively and independently. The solution procedure is as follows

1. Once the model is constructed and the atoms are placed in an equilibrium position, an external load in the system is applied in order to produce deformation in the system. A finite element solution can now be performed. The process is as follows: The macroscopic deformation gradient \mathbf{F} is computed at the mesoscale for every element in the mesh, which defines the displacement field. By appealing the Cauchy–Born rule the underlying atomistic system is obliged to deform according to the continuum deformation gradient. This allows the calculation of continuum quantities as stress tensor and tangent stiffness at the quadrature points direct from the interatomic potential following the relations (3.3.28) and (3.3.29) developed by Sunyk and Steinmann [127]. That produces a nodal displacement in every element, that means mesoscopic deformation. With that, the new placement of the embedded constrained atoms are linearly interpolated. Thus, they are instantaneously fixed from the positions of the corners using the corresponding shape functions of the finite element in which they reside as follows

$$\mathbf{u}_i^e = \sum_{I=1}^{node} N_I(\boldsymbol{\xi}_i) \mathbf{u}_I^e \quad (3.4.1)$$

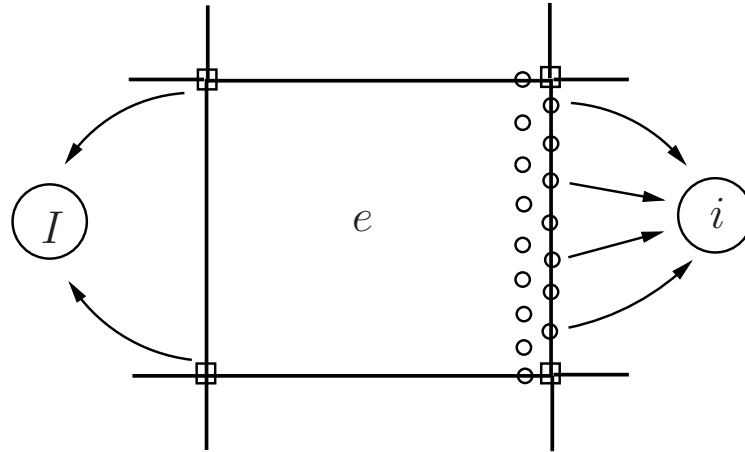


Figure 3.11: This figure represents a finite element called e with the constrained atoms residing on it. It also shows the notation applied within the description for the nodes and atoms.

Here e , i and I symbolize the notation for labelling the corresponding finite element, the unconstrained atoms and the finite nodes, respectively. \mathbf{u}_I^e denote the nodal displacements of the element called e and $N_I(\boldsymbol{\xi}_i)$ are the corresponding shape functions. The displacement field of the constrained atoms is represented by \mathbf{u}_i^e .

2. With the new fixed positions of the constrained atoms on the boundary, a new equilibrium position of the unconstrained atoms can be reached. To run the molecular dynamics simulation, an initial random perturbation is given to the atoms in order to oblige them to move and thus follow the constrained atoms. After that, the velocities (Temperature) of the unconstrained atoms are rescaled in a proportional manner at regular intervals in time during the equilibration period until 0 K temperature by the velocity scaling method. Then, the system is maintained constant at this temperature during the production period and if the instantaneous temperature increases exceeding a certain tolerance limit, the temperature is again rescaled to 0 K. The process takes approximately 4500 micro times steps. The equations of motion are solved numerically using the velocity Verlet algorithm, which yields the phase trajectories of the unconstrained atoms. Note that for consistency the same interatomic potential should be used in the atomistic domain as well as within the continuum framework.
3. Once the unconstrained atoms achieve internal equilibrium, the forces exerted by the unconstrained atoms on the constrained atoms (but only on the atoms placed at the interface) are computed, neglecting the effect of the other constrained particles. For visual clarity, a one dimensional example is presented in Figure 3.12.
4. Then, the equivalent nodal forces of the elements surrounding the atomistic domain are computed by the forces of the constrained atoms placed on the interface as

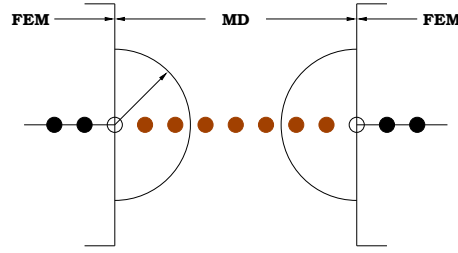


Figure 3.12: Illustrative one dimension coupling algorithm. In the internal region the atoms are unconstrained whereas surrounding this region a FE approximation is applied. The semicircles represent the influence radius to compute the forces on the boundary.

$$\mathbf{F}_I = \sum_{I=1}^{n_{atoms}} N_I(\boldsymbol{\xi}_i) \mathbf{f}_i \quad (3.4.2)$$

Here \mathbf{f}_i represents the interatomic forces and \mathbf{F}_I represents the nodal forces of the element where the atoms i are placed. Again, $N_I(\boldsymbol{\xi}_i)$ are the shape functions of the corresponding elements, see [80].

5. Finally, the simulation continues with these macro finite element steps and micro molecular dynamics iterations until the prescribed sought deformation is achieved. Moreover, for consistency to the coupling algorithm the same interatomic potential as in the atomistic domain should be used.

Summarizing, the sequence of application for transmitting the information from the continuum to the atomistic region is depicted in Figure 3.13. We reiterate the highlights of the basic procedure for the coupling approach in Table 3.3.

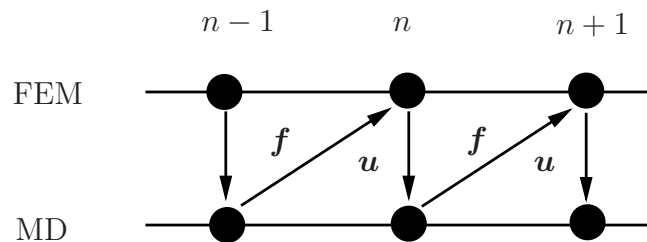


Figure 3.13: Sequence of application in the coupling algorithm. From step $n-1$ to n we transmit the forces. New atomistic positions are then found. From n to $n+1$ the forces are transmitted again. The process continues until the prescribed deformation is encountered.

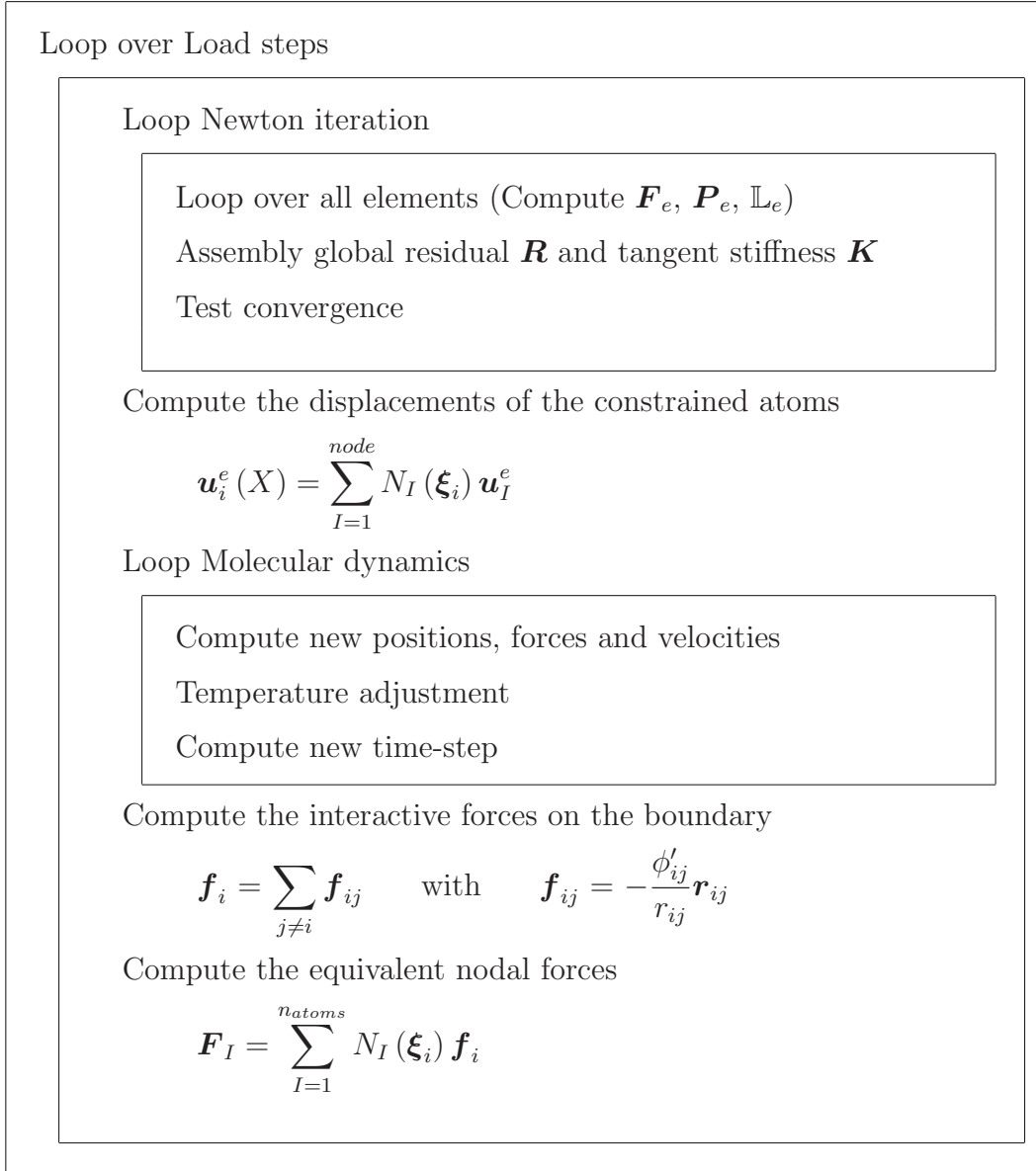


Table 3.3: Algorithm implementation of the coupling atomistic/continuum model. First, the finite element method based on the Cauchy–Born rule is computed. The solution acquired is used for the placement of the unconstrained atoms. That produces an imbalance situation between the constrained and unconstrained atoms. Therefore, a new molecular dynamics solution is needed. This process is repeated several times until the prescribed deformation is attained.

3.5 Some Numerical Results and Analysis

In this section two types of examples are used to illustrate the applicability of the coupled atomic/continuum model. All examples presented here are two dimensional cases for a *fcc*-type crystalline material oriented to $\langle 111 \rangle$ plane using the Lennard-Jones potential function as a prototype model, Equation 1.4.3. The parameters σ and ϵ , fitted to aluminium in our computations, are obtained from the table 2.1 of [125] for the value $n = 3$. These parameters are deduced from the values given in [42] under the conditions of a stress-free material lattice configuration (\mathcal{C}_0) as well as the energy of an atom in the unloaded lattice is deduced following Equation 3.3.24. It must yield the sublimation energy $E_s = 3.58eV = 0.574nNnm$. The lattice constant r_0 has the value $r_0 = 0.286nm$ and the cut-off radius considered is $r_c = nr_0$, which allows us to significantly reduce the computational effort. The molecular dynamics micro step between two consecutive intervals is set to 1.0×10^{-15} seconds and the number of micro iterations are approximately 4500 micro steps, performed in each macro step.

The first example presents a nanolevel crack growth of a rectangular box approximately the size $184.2nm \times 214nm$, see Figure 3.14. This figure shows the initial configuration of the model. For sake of representation and visual clarity only a small atomistic domain near the crack tip is depicted. The boundary conditions imposed are plotted in the same figure where the bottom nodes at both extreme sides are constrained to avoid vertical and horizontal motion. The total number of elements is 656 with 721 nodes. 20 elements are placed around the atomistic domain. The number of atoms in the atomistic region is 15628, divided in 13169 as unconstrained atoms and 2459 as constrained atoms with 326 being used at the interface. The model is loaded on the top in both directions at constant increments in order to produce crack driving. In order to create a discontinuity, i.e. a initial crack situation, some atoms at the initial configuration in the atomistic domain were removed. The detailed figure on Figure 3.16 shows the initiation of the crack. Here it is possible to distinguish an initial void that forms ahead of the crack tip before the fracture is completed. Another three Figures 3.17, 3.18 and 3.19 are plotted in different deformed configurations to illustrate the crack opening. For the purpose of visual facilities in order to follow the fracture detailed figures are placed on them. The atoms there are coloured according to the atomic level stress. It is important to note that the bottom interface between atomistic and continuum exerts a negative influence on the crack propagation. This interface acts as a rigid boundary impinging the normal evolution of the crack or rather when the crack encounters the interface, it cannot leap into the continuum due to the fundamental incompatibility between both approaches. That disturbs the computation process and therefore it is necessary to stop it at this deformation state.

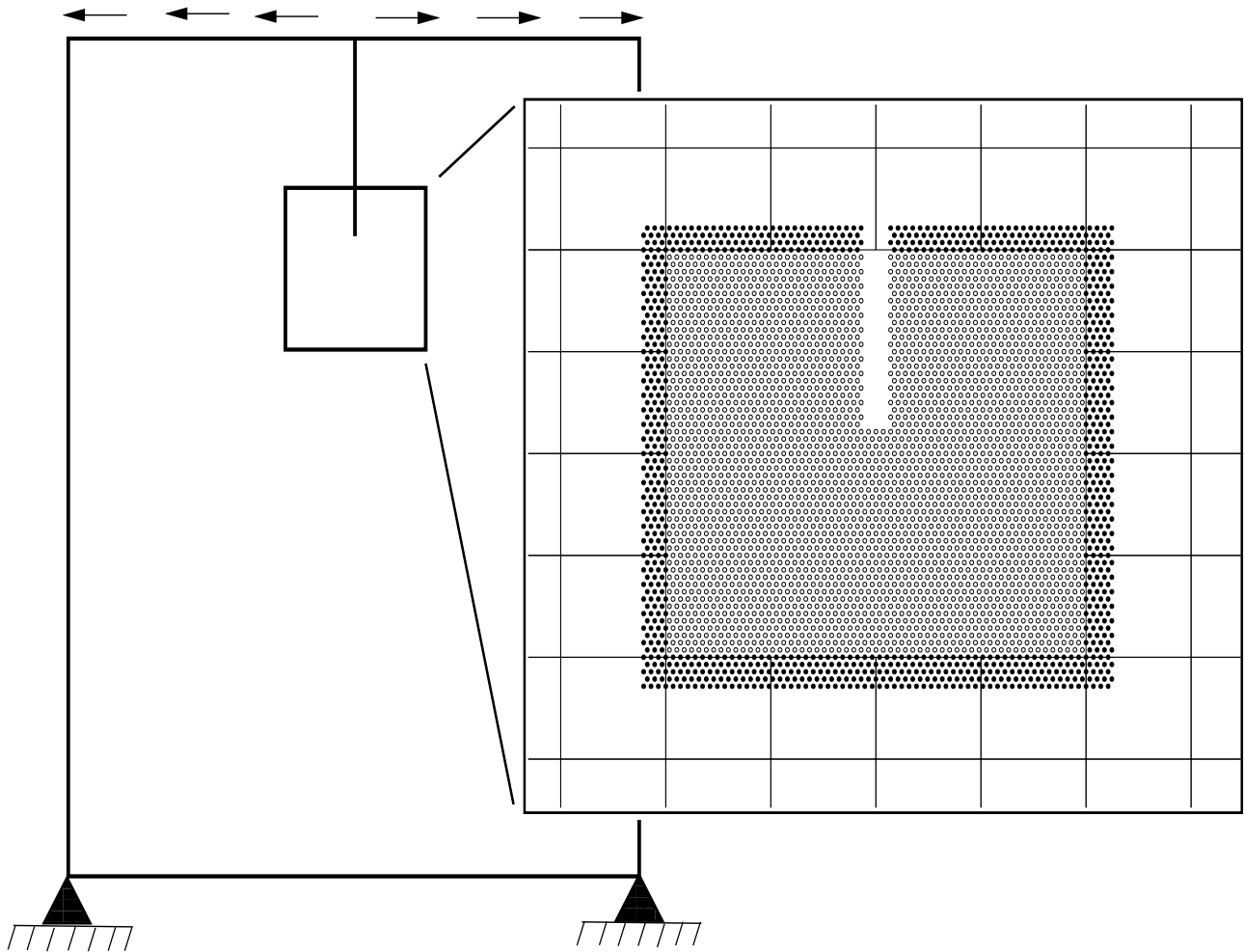


Figure 3.14: Crack model with 656 elements in the continuum domain and 15628 atoms in the atomistic region. The atoms are distributed in 13169 unconstrained atoms and 2459 constrained atoms of which 326 are used at the interface. For the sake of representation only a few number of atoms are pictured in the detailed figure.

The second example deals with a rectangular plate that has a rounded nanovoid in the central part of the simulated domain, see Figure 3.15. The geometry and loading conditions are represented in the same figure. The size of the box is approximately $92.1 \text{ nm} \times 136.7 \text{ nm}$. The total number of elements are 320 with 366 nodes. The number of atoms at the atomistic domain embedded in the finite element mesh is in this case 10391, distributed as follow: 8314 atoms are used as unconstrained particles where molecular dynamics is applied, 2077 as constrained atoms with 276 being placed at the interface. The forces are applied in both directions simultaneously in constant increments in order to produce deformation and crack opening. Figures 3.20 and 3.21 show several intermediate states of deformation to illustrate crack driving. During the deformation process or rather the crack opening some dislocations emerge coming from the central hole and migrate through the atomistic domain until encountering the interface. As in the previous case, this exerts damaging influence on the simulation process because the dislocations cannot come into the continuum domain crossing the boundary, see Figures

3.22 and 3.23. This is the reason why in these Figures some voids appear at the corners in the atomistic domain. Therefore, this is a good point for extending the investigation focusing on the avoidance of the pulses initiated in the dynamic domain and reflected at the interface due to the constrained atoms. They act as a rigid boundary avoiding the smooth absorption of these waves. One approach dealing with these problems is the multiscale method developed by Shilkrot et al. [120] and Qu et al. [107].

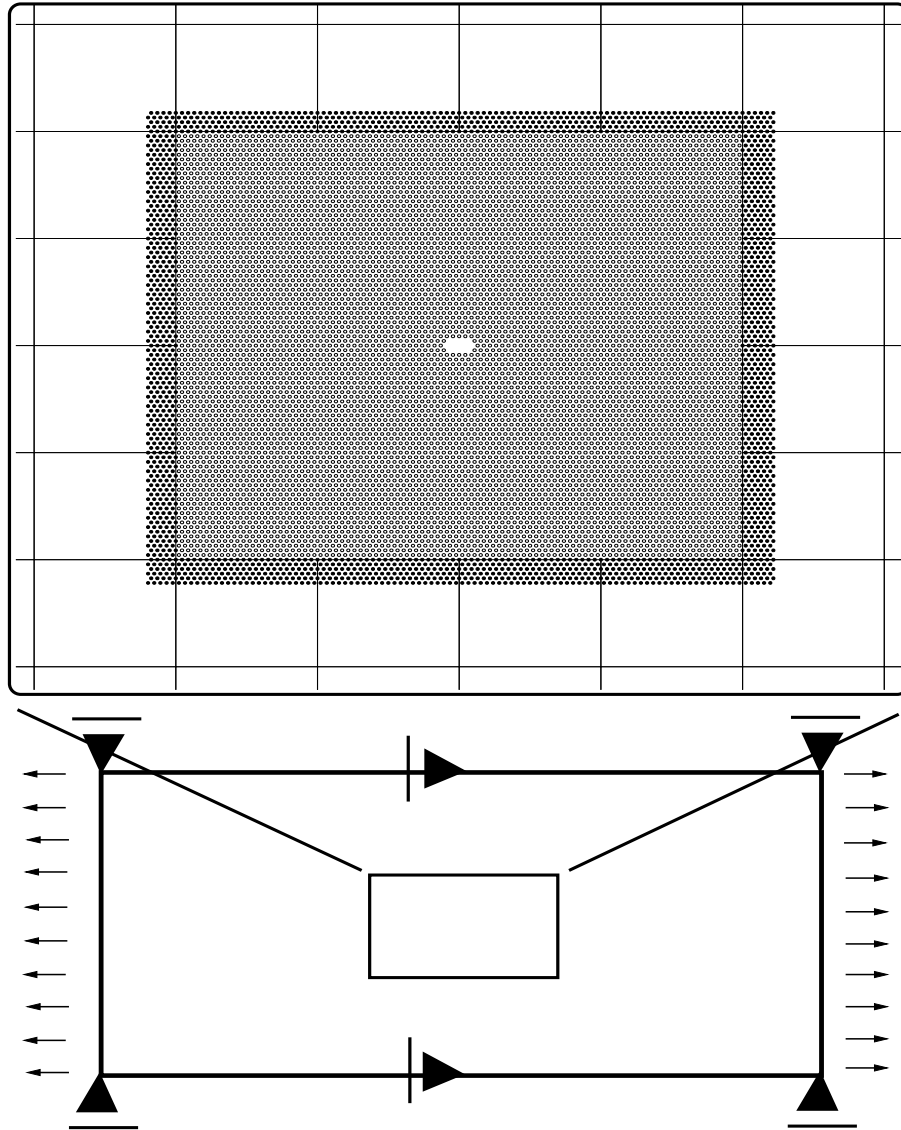


Figure 3.15: Crack model with 320 elements in the continuum domain and 10391 atoms in the atomistic region. The atoms are distributed in 8314 unconstrained atoms and 2077 constrained atoms with 276 being used at the interface.

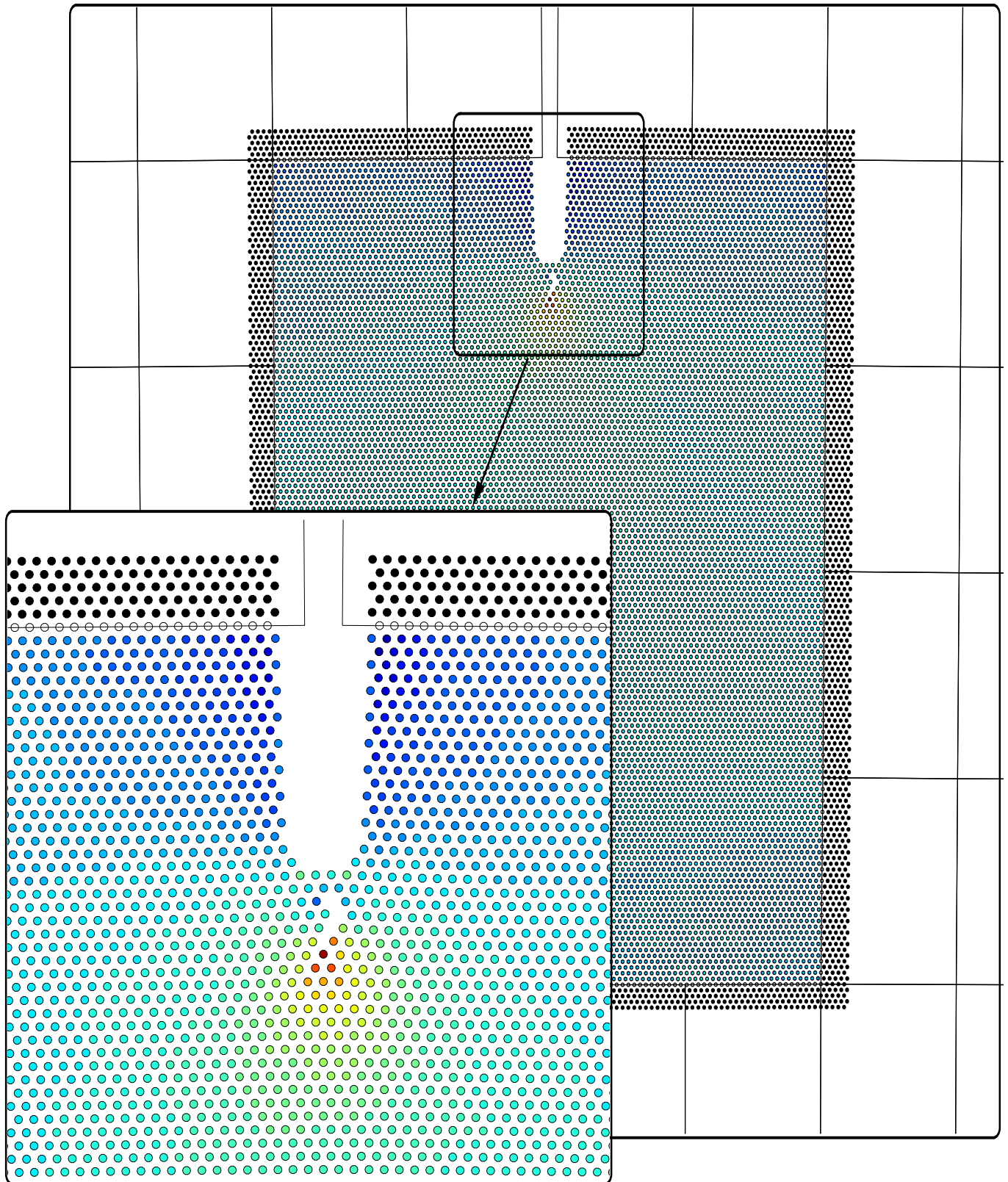


Figure 3.16: Initiation of the crack opening in the coupling model. In the detailed figure it is possible to observe an initial void that forms ahead of the crack tip before the separation among the atoms is completed

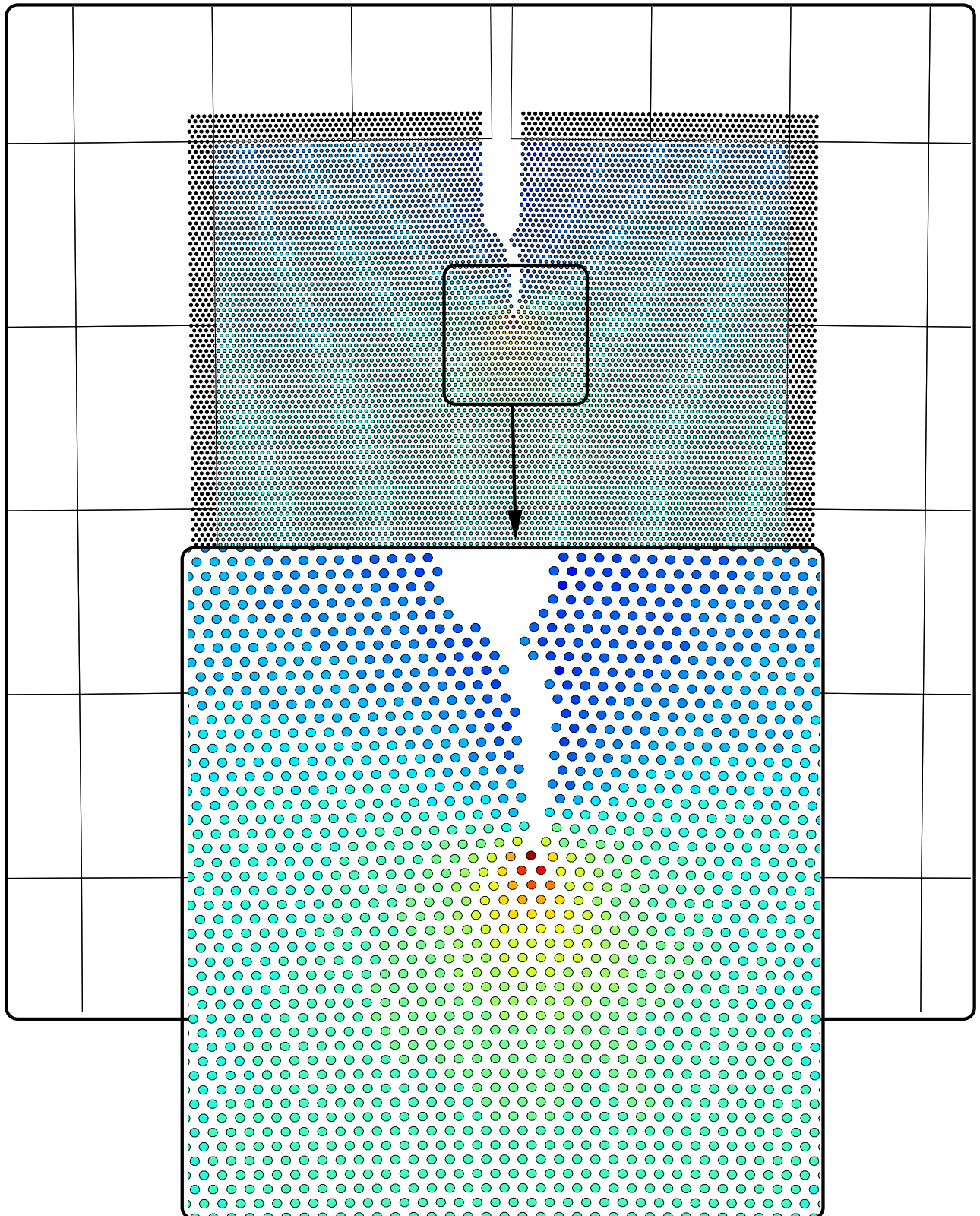


Figure 3.17: Crack opening in the coupling model in an intermediate state of deformation.

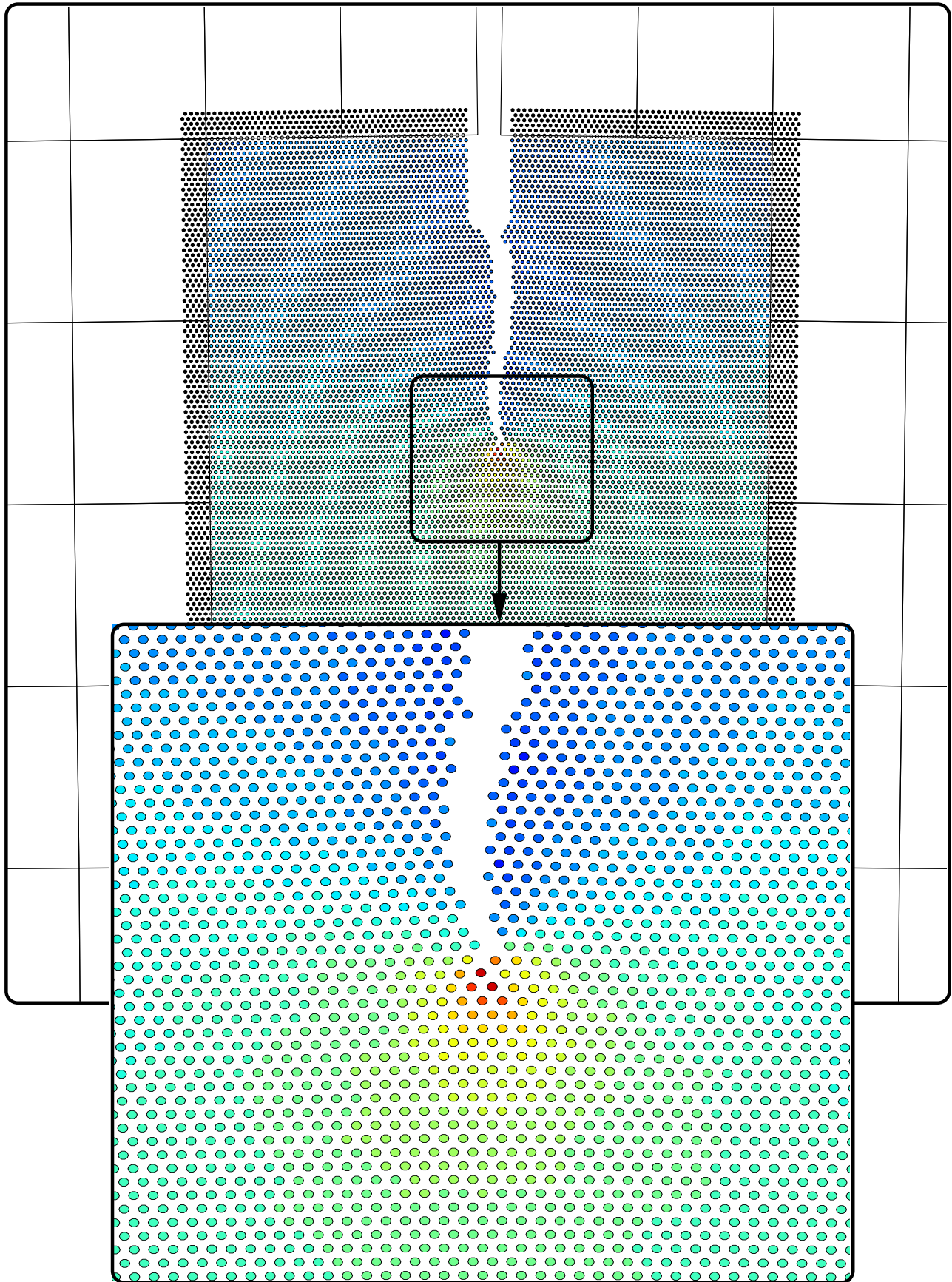


Figure 3.18: Crack opening in the coupling model in a intermediate state of deformation.

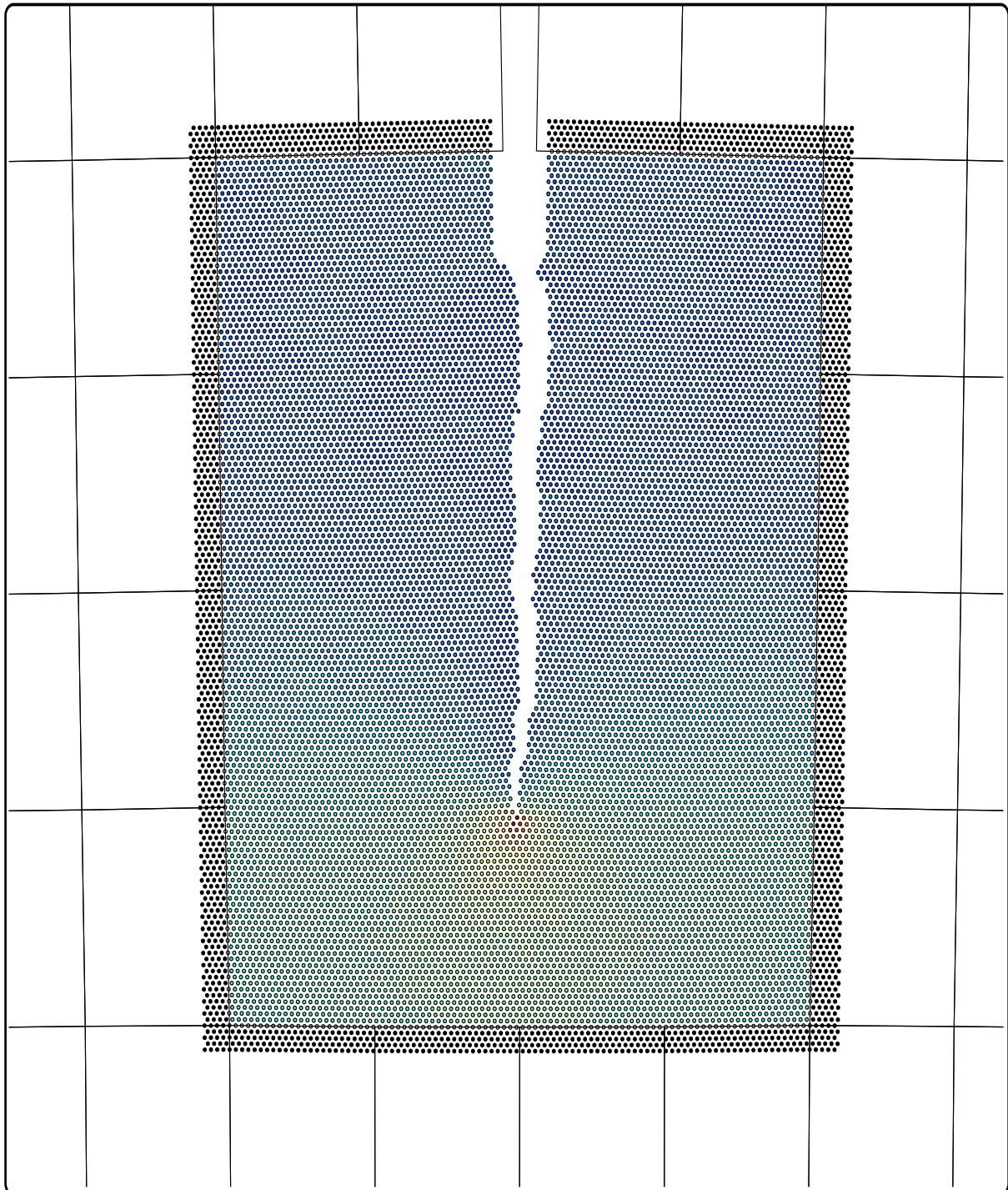


Figure 3.19: Crack opening in the coupling model in a intermediate state of deformation.

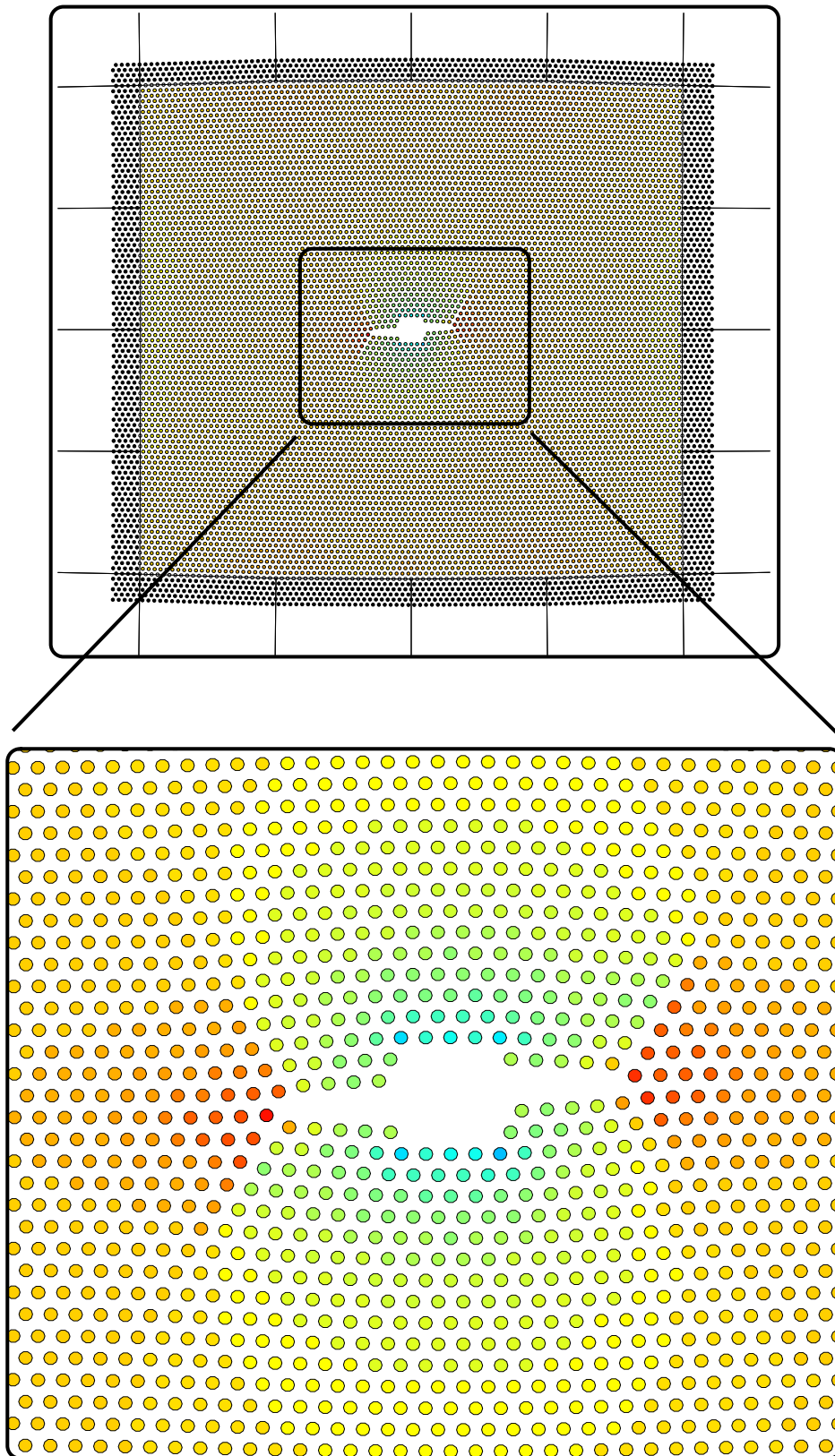


Figure 3.20: Crack opening in the coupling model in an intermediate state of deformation.

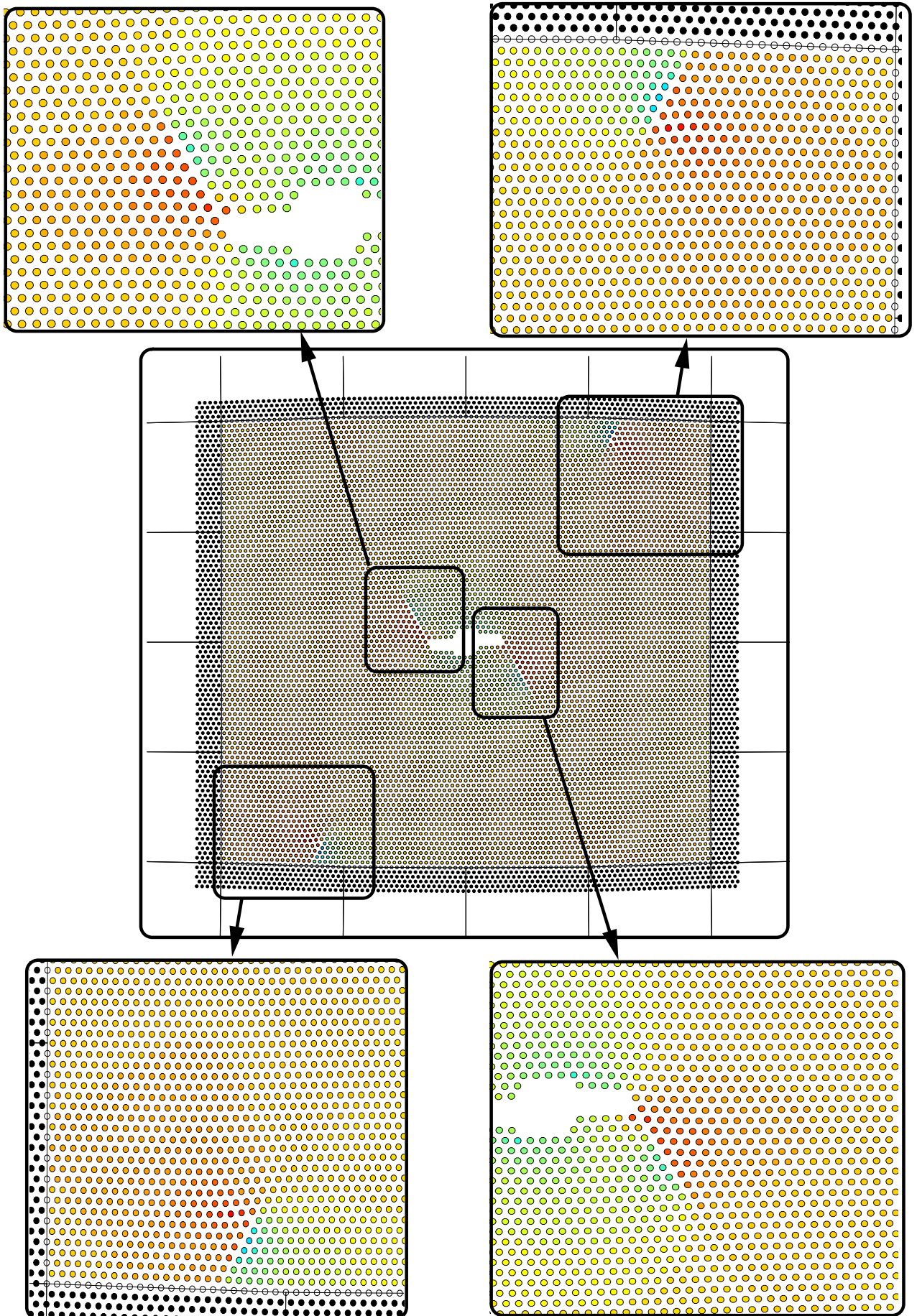


Figure 3.21: Crack opening in the coupling model in an intermediate state of deformation. 101

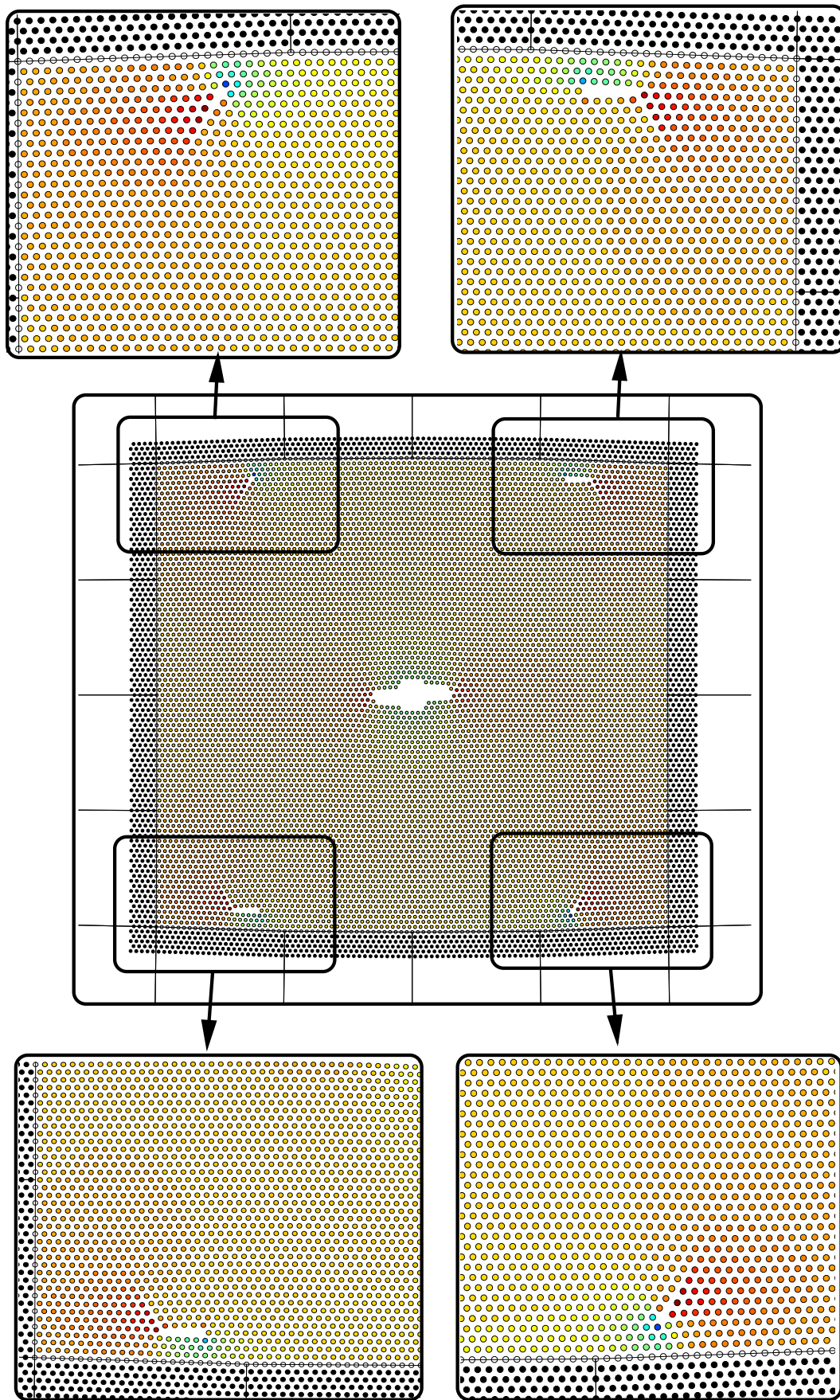


Figure 3.22: Crack opening in the coupling model in a intermediate state of deformation.

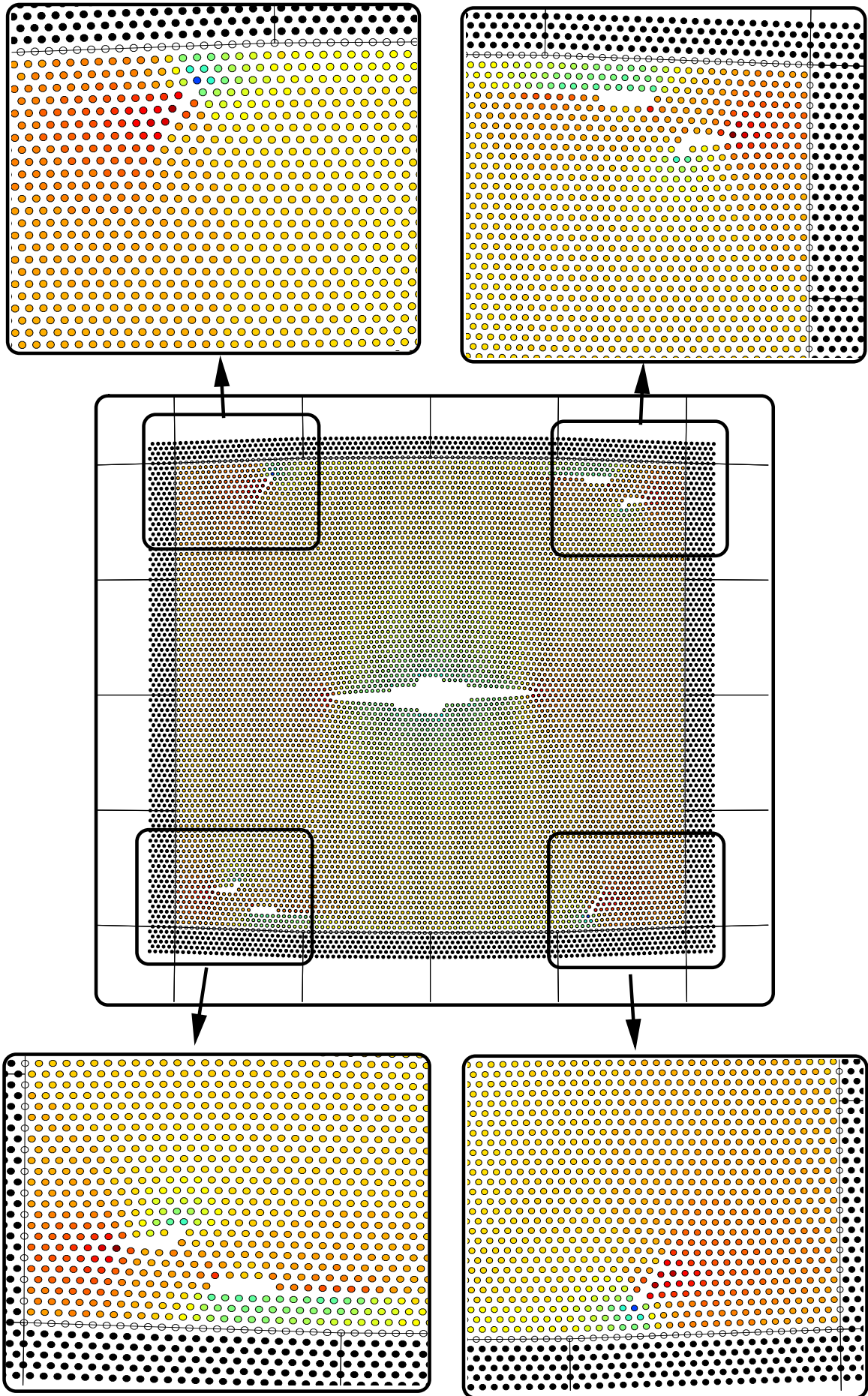


Figure 3.23: Crack opening in the coupling model in a intermediate state of deformation.¹⁰³

3.6 Summary

The purpose of this chapter was to present the methodology used to develop a hybrid model for studying several cases of nano-deformation. We combined atomistics simulations in the sense of molecular dynamics with the finite element method within the continuum framework. The resolution was adapted according to the type of solution considered, i.e. an atomistic domain to capture the material behaviour complexity with a finite mesh to capture the smooth parts of the solution with the objective of interplaying accuracy and efficiently. This computational model present some difficulties due to pulses initiated in the dynamic domain which are reflected at the interface because the constrained atoms, i.e. the continuum domain acts as a rigid boundary avoiding the normal transition through the whole domain. This will be treated in Chapter 4. Finally note that the atoms in the figures are coloured according to the atomic level stress, see Appendix B.

4 Wave Reflections at the Atomistic/Continuum Interface

4.1 Introduction

For the dynamic model the interface between the constrained and unconstrained atoms used to study the validity of the Cauchy–Born rule, Chapter 2, and the atomistic/continuum boundary within the coupling algorithm, Chapter 3, produces an additional problem related to the pulses initiated in the dynamic domain. The origin of these pulses is due to the lattice vibrations. They are reflected at the interface due to the constrained atoms because they act as a rigid boundary avoiding the smooth absorption of these waves, i.e. they impinge the normal propagation into the continuum domain. Thus, they return to the atomistic region and produce a growth of energy in the lattice disturbing the correct behaviour of the material as can be seen in Figures 3.20 and 3.21. Such phenomena was noted by Doll and Adelman [43], Holmes and Belytschko [69], Ohsawa and Kuramoto [101].

The main purpose here is devoted to broaden the simulations carried out in the two previous chapters applying an approach which allows us to deal with the pulses mentioned above. In order to achieve this, the chapter is organized as follows: The first section contains a brief explanation of some current research activities which have been treated with these spurious reflections. Afterwards, we put our attention towards the method suggested by Holian and Ravelo [67] and implemented by Qu, Shastry, Curtin and Miller [107]. This method is intended to be applied to the study of the Cauchy–Born rule. Finally, we extend the application of this technique to the coupling algorithm presented in Chapter 3.

4.2 Current State of Research

This section points out several techniques which have been developed recently in order to avoid or reduce the wave reflections generated at the atomistic domain. These waves need a special treatment using an efficient atomistic/continuum transition as proposed by Cai et al. [24]. They introduce an approach to minimize wave reflections at the interface imposing a time–dependent boundary condition. This reduces the influence of such boundary in the results. The strategy is efficient for one–dimensional linear problems, but the idea is too expensive in practice since the exact boundary tend to be non–local [86].

In order to obtain balance between efficiency and accuracy, Weinan and Huang [145,146]

suggested a coupled method using a new class of matching conditions between atomistic and continuum. The idea is to minimize the phonon reflections at the interface and ensure the transmission of the information between these regions. They reported examples limited also for one-dimensional linear models and at zero temperature.

Following this line of research, Wagner and Liu [143] and Wagner et al. [144] have developed a hybrid method combining molecular dynamics and a continuum mechanics framework. Molecular dynamics is used in a localized region while the continuum is computed covering the entire domain including the atomistic region. At the interface, they introduce a form of the Langevin equation to minimize the wave reflections.

Based on the spatial decomposition strategy, Abraham et al. [1] and Broughton et al. [20] coupled together three different approaches in a unified algorithm for illustrating silicon fracture. These three approaches are quantum descriptions, molecular dynamics and continuum mechanics. To reduce the pulses generated at the atomistic scale, a damping was introduced into the handshake region between the continuum and atomistic regions.

Xiao and Belytschko developed a bridging method for coupling molecular and continuum models where the Hamiltonian is a linear combination of the continuum and molecular Hamiltonians [151]. This allows the proper transfer of energy between both domains without using any filtering procedure near the overlapping zone. In addition this can avoid the common wave reflections which appears in these multiscale approaches at the molecular/continuum interface.

Another popular idea was proposed by Holian and Ravelo [67]. They efficiently prevent the waves generated by a propagating crack by inserting a “viscous damping” at the atomistic domain, this is an energy absorbing region. This idea was implemented in a series of works. An incomplete list includes Gumbsch and coworkers [61], Zhou et al. [155], To and Li [134], Collino and Tsogka [37], Holland and Marder [68]. In the next section, we will introduce the notion of “viscous damping” with the twofold purpose to apply to the Cauchy–Born rule and to the atomistic/continuum coupling model introduced in Chapter 3. Finally, we refer the reader to the works [114,115], [47], [103,104] and [75] for a deeper discussion on the topic.

4.3 Theoretical Foundations of the Damping Zone

In this section our attention will be focused on the approach suggested by Holian and Ravelo [67] and employed by Qu, Shastry, Curtin and Miller [107] in the atomistic/discrete dislocation method. We will touch only a few aspects of the theory. We will then display several examples following the ideas applied by these authors [107] to the study the validity of the Cauchy–Born rule carried out in Chapter 2 and the coupling algorithm of Chapter 3.

The method consists of inserting an artificial damping zone, i.e. a filter using a Langevin–

type thermostat near the interface (constrained atoms) in order to deal efficiently with the reflection effects. Restricted to the atomistic domain, this is divided in three different regions, see Figure 4.1. The outside region, coloured in black, acts as a rigid boundary where the constrained atoms are placed. These atoms are forced to follow the homogeneous deformation or the deformation which occurs within each element in the case of the coupling algorithm. They assure that the unconstrained atoms have a complete set of interatomic neighbours. The region coloured in green is where molecular dynamics with a damping term is used. Finally the remaining internal domain (red zone) is simulated without damping by using the standard molecular dynamics method in the same way as in Chapters 2 and 3.

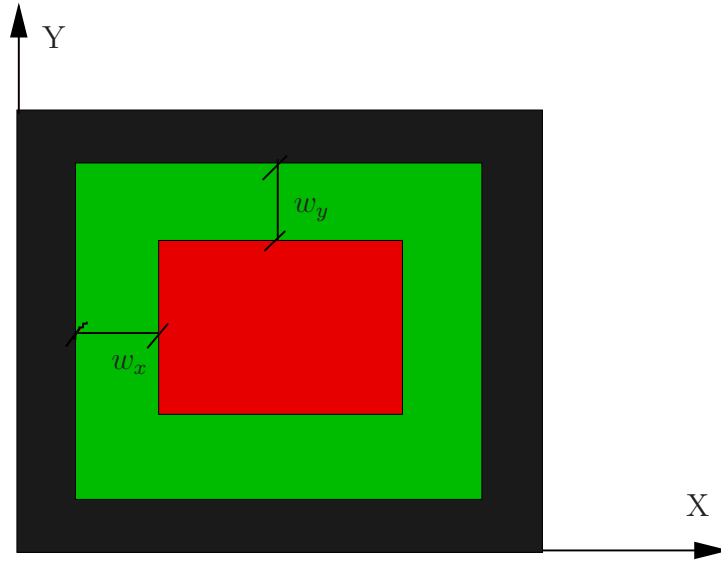


Figure 4.1: The black region represents the constrained atoms under the Cauchy–Born rule. The damping atoms are placed in the green area and the red region indicates the unconstrained atoms without damping. w_x and w_y are the widths of the damping zone.

The idea of a damping zone is to include a damping term, i.e. a friction parameter proportional to the velocity \mathbf{v} , and a random force term into the equations of motion for the atoms in the damped strip. This implies that the damping term depends indirectly on the empirical potential used for the simulated system. We follow the same notation as in [107]. Thus, we can rewrite Newton’s equations in the form

$$\ddot{\mathbf{r}} = \frac{\mathbf{F}}{m} - \gamma \mathbf{v} + \chi \frac{\mathbf{F}_A}{m}, \quad (4.3.1)$$

where γ is the damping coefficient, χ represents a random number ($-1 \leq \chi \leq 1$) and \mathbf{F}_A is the random acceleration component for each dimension which takes the format

$$F_{A_i} = \sqrt{\frac{6\gamma k_B T_0}{m\Delta t}}, \quad i = x, y, z \quad (4.3.2)$$

Here, k_B is the Boltzmann constant, m is the mass of a particle, γ represents the damping coefficient, T_0 is the desired equilibrium temperature and Δt is the micro molecular dynamics time step used in order to numerically solve Newton's equations. In our case, we wish to reach a zero temperature $T_0 = 0$, and therefore the random acceleration term $\frac{\mathbf{F}_A}{m}$ is also zero. Thereby, the above expression 4.3.1 may be written as

$$\ddot{\mathbf{r}} = \frac{\mathbf{F}}{m} - \gamma \mathbf{v} \quad (4.3.3)$$

Following what Qu et al. proposed in [107], we define the damping coefficient γ to vary linearly over the width of the damping zone as follows

$$\gamma = \gamma_0[1 - \eta]. \quad (4.3.4)$$

Here γ_0 is the maximum damping, approximately 1/2 of the Debye frequency ω_D , which is the theoretical maximum frequency of vibration of the atoms in a crystal and η is the minimum of the division among the distance from the atom position to each boundary by the respective width of the damping region [107].

$$\eta = \min \left(\frac{x - x_{min}}{w_x}, \frac{x_{max} - x}{w_x}, \frac{y - y_{min}}{w_y}, \frac{y_{max} - y}{w_y} \right). \quad (4.3.5)$$

Thereby the damping coefficient changes linearly from zero at the no damping boundary area of the unconstrained atoms to γ_0 at the constrained boundary atoms, see figure 4.2.

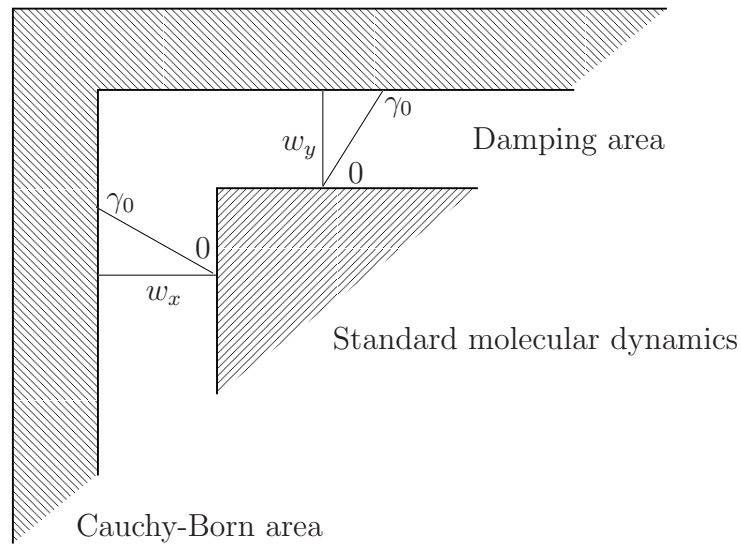


Figure 4.2: The damping coefficient γ varies linearly over the damping zone width. At the constrained boundary atoms $\gamma = \gamma_0$ and at the no damping boundary area of unconstrained atoms $\gamma = 0$.

In contrast to the method developed by Qu, Shastry, Curtin and Miller in [107], our system is subjected to a certain deformation in each macrostep, see figures 2.8, 2.14, 2.20 and 2.26. This applied deformation causes variations in the damping zone widths. In order to maintain a constant number of atoms in each area so that the damping coefficient γ_0 varies linearly, both widths must be updated in each macrostep .

4.4 The Cauchy–Born Rule. Numerical Results Using a Damping Zone.

Restricting our study to the influence of the damping zone on the stability of the Cauchy–Born rule we proceed as follows: We limited ourselves to a system with 4096 atoms and a lattice orientation of 0 degree. This system is simulated with two different damping zones for simple shear, pure shear, uniaxial extension and dilatation. On the one hand, we take a damping zone with the widths $w_x = 2.2897 \text{ nm}$ and $w_y = 2.2559 \text{ nm}$. This simulation is constituted by three different areas, see Figure 4.1. The internal region where the molecular dynamics method and the Cauchy–Born rule are used, is formed by 2997 atoms, of which 1575 are placed in the damping zone and 1422 are computed without artificial damping. The outside region is formed by 1099 constrained atoms. On the other hand, we apply the damping in the whole unconstrained domain in order to compare results.

The maximum damping is $\gamma_0 = 0.45\omega_D$, where the Deybe frequency for Aluminium is $\omega_D = 5.6 \times 10^{13} \text{ s}^{-1}$ [107]. The rest of the parameters such as the Lennard–Jones parameters, the initial position, the time step, etc... that are used in these simulations are the same as the ones used in Chapter 2. The size step between two consecutive steps is also the same as before. The results obtained in these simulations are compared with the results for 4096 atoms and lattice orientation 0 degree achieved in the simulations without artificial damping of the Chapter 2. Again the velocity–Verlet algorithm is used to update the particle positions, velocities and accelerations in time with the only difference of taking into account where it is applied, i.e. if the damping coefficient must be added or not. We used the first type of simulations. That means that the Cauchy–Born rule is applied in the whole domain in each macro deformation step. Afterwards a small random perturbation of the velocities with a Maxwell distribution to the unconstrained atoms is applied. Then the trajectories of the atoms are followed using the molecular dynamics method until reaching a new equilibrium state. These macro and micro iterative steps continue until the prescribes macro deformation is acquired. The standard deviation is computed in each macroscopic time step to detect the onset of instabilities. This procedure was explained in detail in Chapter 2.

For the sake of a clear interpretation for the next figures, we have to mention that "No damping" represents the no damping simulation obtained in the Chapter 2, "Partial damping" describes the simulation with the damping zone explained before and "Total damping" shows the simulation with all unconstrained atoms damped in order to see the influence of the damped region when the number of damped atoms are increased.

4.4.1 Simple Shear Deformation

We briefly review that the simple shear deformation is characterised by $\mathbf{F} = \mathbf{I} + \gamma [\mathbf{e}_1 \otimes \mathbf{e}_2]$ called the deformation gradient where \mathbf{e}_i , $i = 1, 2$ are the Cartesian basis vectors. \mathbf{I} denotes the identity tensor and the factor γ represents the shear number $\gamma = \tan(\theta)$, see Figure 2.8. In this case the atoms are forced to displace tangentially along the boundary. This movement allows the widths of the damping zone to remain constant and therefore, we do not need to update them, see the undergraduate final thesis [140].

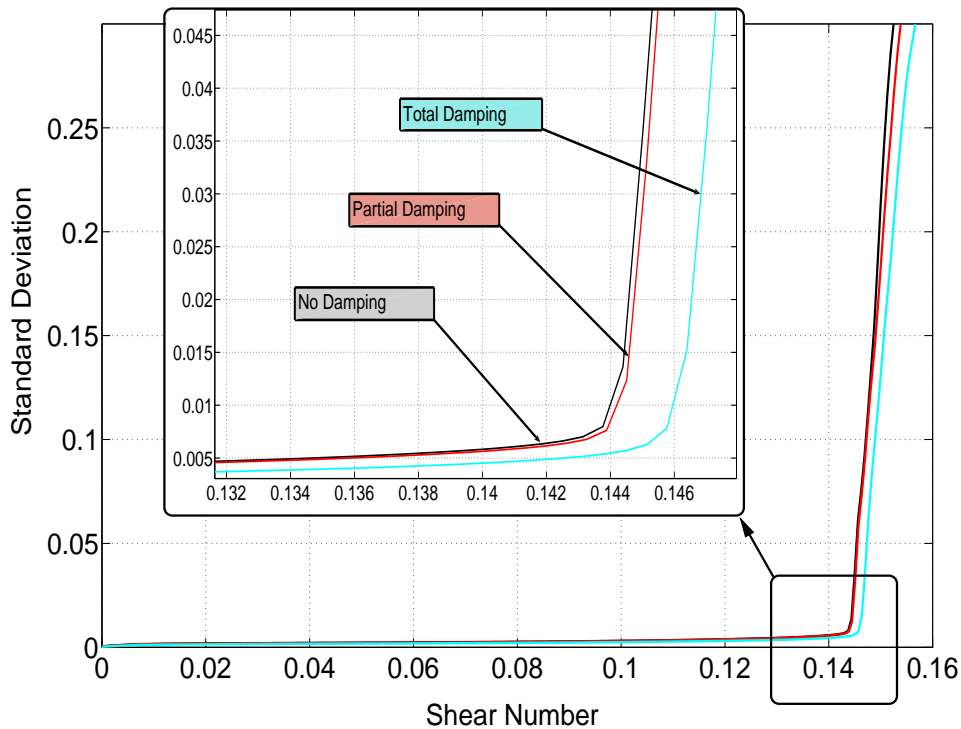


Figure 4.3: Evolution of the standard deviation versus the shear number γ for simple shear deformation with 4096 atoms and 0 degrees, where "No damping" describes the no damping simulation, "Partial damping" represents the simulation with the widths $w_x = 2.2897 \text{ nm}$ and $w_y = 2.2559 \text{ nm}$ and "Total damping" shows the simulation with all the internal atoms damped.

In figure 4.3 we can observe the evolution of the standard deviation versus the shear number γ . Note how the limit of the Cauchy–Born rule is larger, between $\gamma = 0.1455$ and $\gamma = 0.146$, when the damping is applied in all the unconstrained atoms. This is due to some of the spurious reflections being absorbed. However, although the standard deviation is smaller in the no damping area than in the partial damping zone, the deformation becomes inhomogeneous for approximately the same shear number, between $\gamma = 0.1465$ and $\gamma = 0.147$.

4.4.2 Uniaxial Extension Deformation

The uniaxial extension deformation is characterized by $\mathbf{F} = \mathbf{I} + [\lambda - 1] \mathbf{e}_1 \otimes \mathbf{e}_1$ known as the deformation gradient where \mathbf{e}_i , $i = 1, 2$ are the Cartesian basis vectors, \mathbf{I} is the second order identity and the factor λ represents the stretch. For the uniaxial extension the atoms are subjected to move horizontally without vertical deformation. This displacement obliges to update the width w_x in each macrostep with a variation proportional to λ , see the diplom thesis [140].

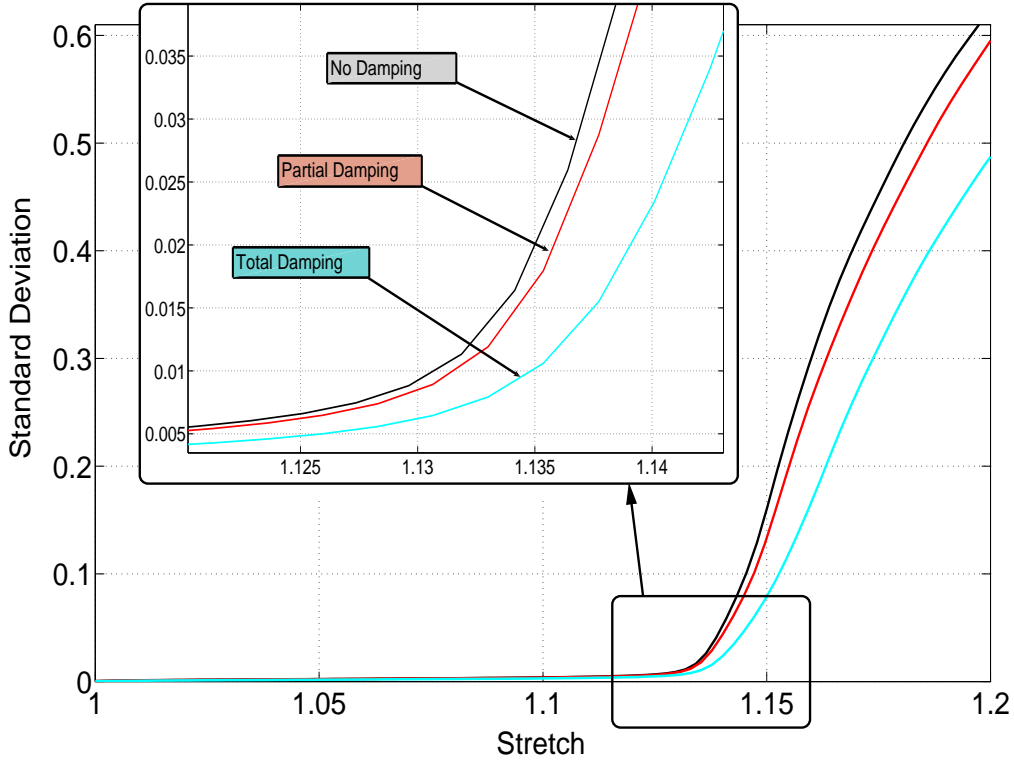


Figure 4.4: Evolution of the standard deviation versus the stretch λ for uniaxial extension with 4096 atoms and 0 degrees, where "No damping" describes the no damping simulation, "Partial damping" represents the simulation with the widths $w_x = 2.2897 \text{ nm}$ and $w_y = 2.2559 \text{ nm}$ and "Total damping" shows the simulation with all the internal atoms damped.

In figure 4.4 the limit of the Cauchy–Born rule for the uniaxial extension case can be observed. Notice that it is larger when damping is used in all the unconstrained atoms, between $\lambda = 1.133$ and $\lambda = 1.135$ due to some spurious reflections being removed. For the same stretch λ the limit of the Cauchy–Born rule is approximately the same, between $\lambda = 1.131$ and $\lambda = 1.133$. Despite this, the standard deviation is smaller in the no damping area than in the partial damping region.

4.4.3 Pure Shear Deformation

In Pure Shear deformation case the deformation gradient is denoted by $\mathbf{F} = \mathbf{I} + [\lambda - 1] \mathbf{e}_1 \otimes \mathbf{e}_1 + [\lambda^{-1} - 1] \mathbf{e}_2 \otimes \mathbf{e}_2$ where the factor λ represents the stretch and \mathbf{I} again the identity tensor. For the uniaxial extension the atoms are subjected to move horizontally without vertical deformation. This displacement obligates us to update the width w_x and w_y in each macrostep with a variation proportional to λ , see the diplom thesis [140].

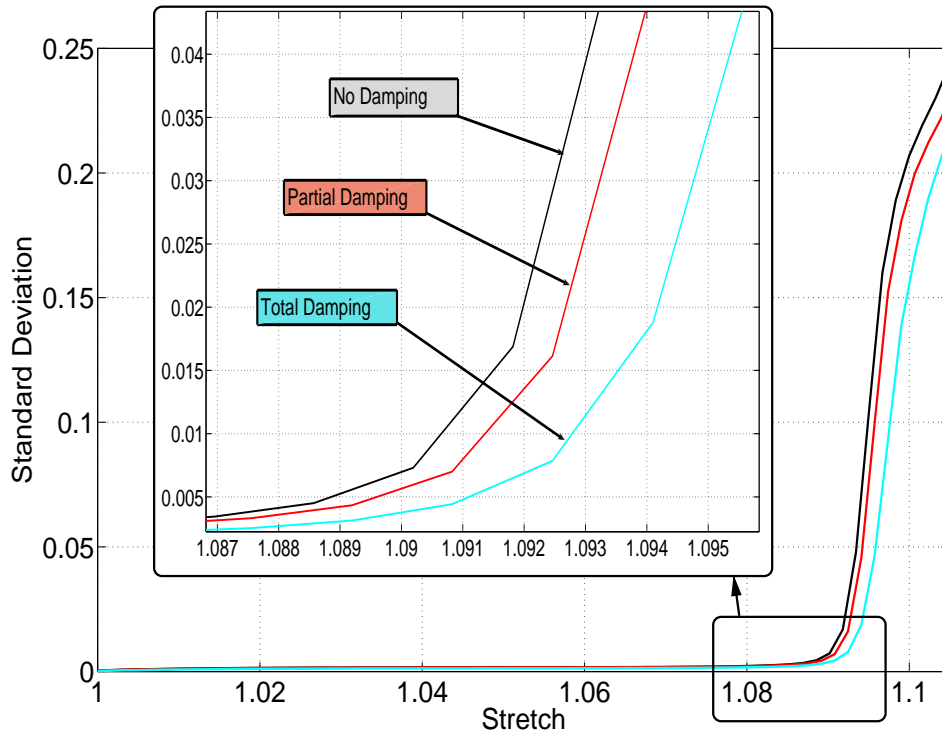


Figure 4.5: Evolution of the standard deviation versus the stretch λ for uniaxial extension with 4096 atoms and 0 degrees, where "No damping" describes the no damping simulation, "Partial damping" represents the simulation with the widths $w_x = 2.2897 \text{ nm}$ and $w_y = 2.2559 \text{ nm}$ and "Total damping" shows the simulation with all the internal atoms damped.

In figure 4.5 the limit of the Cauchy–Born rule for the uniaxial extension case can be observed. Notice that it is larger when damping is used in all the unconstrained atoms, between $\lambda = 1.133$ and $\lambda = 1.135$ due to some spurious reflections being removed. For the same stretch λ the limit of the Cauchy–Born rule is approximately the same, between $\lambda = 1.131$ and $\lambda = 1.133$. Despite this, the standard deviation is smaller in the no damping area than in the partial damping region.

4.4.4 Dilatation Deformation

The deformation gradient $\mathbf{F} = \mathbf{I} + [\lambda - 1] \mathbf{e}_1 \otimes \mathbf{e}_1 + [\lambda - 1] \mathbf{e}_2 \otimes \mathbf{e}_2$ characterizes the dilatation deformation case where \mathbf{e}_i , $i = 1, 2$ are the Cartesian basis vectors, \mathbf{I} denotes the identity tensor and the factor λ represents the stretch. The dilatation case atoms are obliged to move horizontally and vertically in a proportional manner. The widths of the damping zone change in each macrostep. The variation is proportional to λ for both w_x (horizontal extension) and w_y (vertical extension), see the diplom thesis [140].

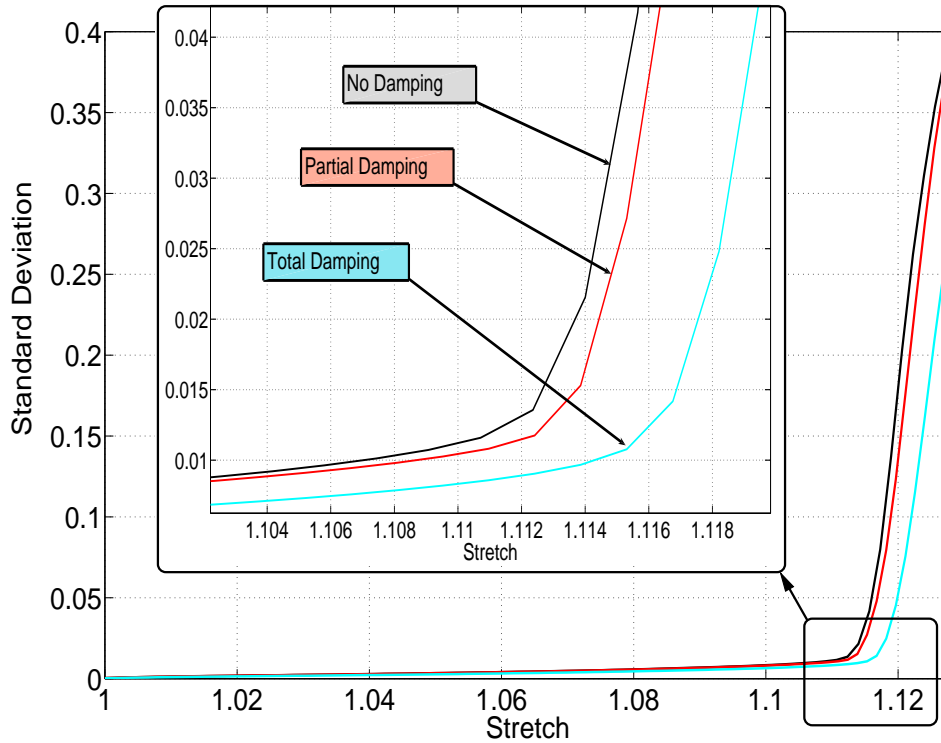


Figure 4.6: Evolution of the standard deviation versus the stretch λ for dilatation deformation with 4096 atoms and 0 degrees, where "No damping" describes the no damping simulation, "Partial damping" represents the simulation with the widths $w_x = 2.2897 \text{ nm}$ and $w_y = 2.2559 \text{ nm}$ and "Total damping" shows the simulation with all the internal atoms damped.

As in the previous figures, figure 4.6 shows that the limit of the Cauchy-Born rule for the total damping zone is the largest of all, approximately between $\lambda = 1.116$ and $\lambda = 1.117$. Although no damping and partial damping have a similar limit for the Cauchy-Born rule, between $\lambda = 1.113$ and $\lambda = 1.114$, the standard deviation is smaller in the no damping area than in the partial damping zone because some spurious waves are eliminated.

4.5 The Horizontal Coupling Algorithm. Numerical Results Using a Damping Zone

In this section, we wish to extend the application of the damping zone to the horizontal coupling approach introduced in the previous Chapter. The motivation is to avoid or insofar as we can reduce, the spurious energetic pulses initiated in the dynamic domain impinging the atomistic/continuum model as can be seen in Figure 3.21. To this end, we again insert a damping zone near the interface, i.e. close to the boundary between the unconstrained atoms and the constrained atoms. The equations of motion within the molecular dynamics framework in the damping zone are modified including a friction term proportional to the velocity in the same way as done before on the study of the Cauchy–Born rule. Summarizing the philosophy is the same as in the previous Section. Hereafter we will mention the relevant parameters implemented to the coupled atomistic/continuum model with the damping domain. It is worth to mention that the damping zone may not depend only on viscous motion of the atomistic regime but also on internal inertia of the continuum regime.

The example deals with the same rectangular plate with a round hole in the central part of the simulated domain as represented in Figure 3.5. The geometry and loading conditions are the same as depicted there. The total number of elements are 320 with 366 nodes. The number of atoms at the atomistic domain embedded in the finite element mesh are 10391, distributed as follows: 8314 atoms are used as unconstrained particles and 2077 as constrained atoms with 276 being placed at the interface. From these 8314 unconstrained atoms, 2514 are placed in the damping zone while the remaining atoms, i.e. 5800 atoms are put in the interior domain where a standard molecular dynamics algorithm without any artificial damping is applied. This means the widths of the damped region are $w_x = 2.14 \text{ nm}$ and $w_y = 2.23 \text{ nm}$ at the unloaded initial configuration. There, the damping coefficient changes linearly from zero at the no damping boundary of the unconstrained atoms to γ_0 at the constrained boundary atoms within the finite elements. The Lennard–Jones parameters σ and ϵ are the same as before taken the same value $n = 3$. The lattice constant r_0 again represents the value of $r_0 = 0.286 \text{ nm}$ and the cut–off radius considered is $r_c = n r_0$. The molecular dynamics micro step between two consecutives intervals is set to 1.0×10^{-15} seconds and we reiterate that number of micro iterations are roughly 4500 micro steps, performed in each macro step. Figures 4.7 and 4.8 illustrate the same intermediate states as in Figures 3.22 and 3.23. In this case, thanks to the damping term inserted, we attain to remove some spurious reflections. However, at the end of the simulation the holes at the corners appear again to be perturbing the computation because of the inherent incompatibility between the atomistic/continuum interface, i.e. the constrained and constrained atoms. This atomistic phenomena, such as dislocations, cannot cross into the finite element mesh anyhow. Therefore, it is necessary to incorporate a better strategy to overcome this setback.

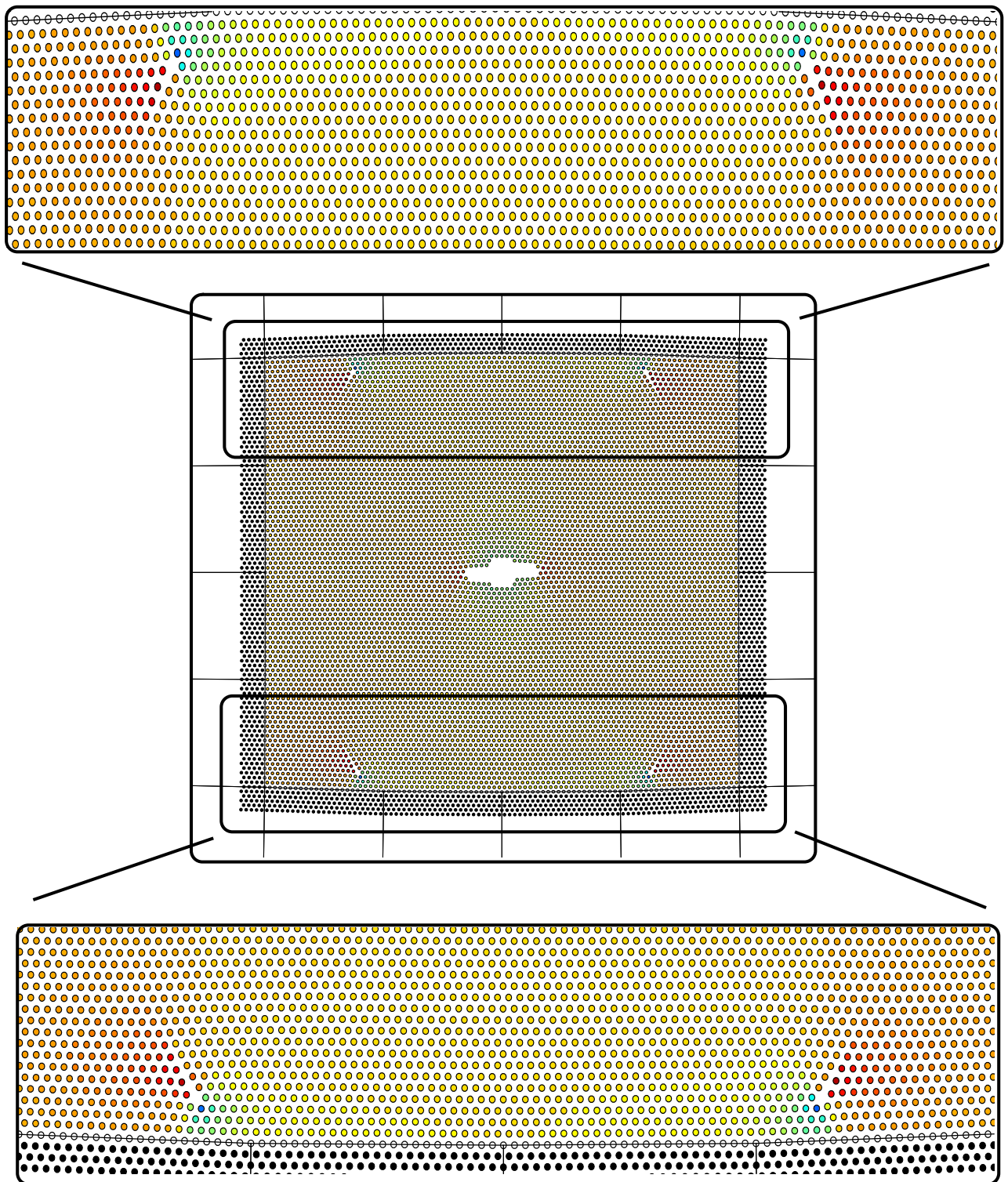


Figure 4.7: Crack opening in the coupling model with damping zone. They represent the same intermediate state of deformation as in Figure 3.20

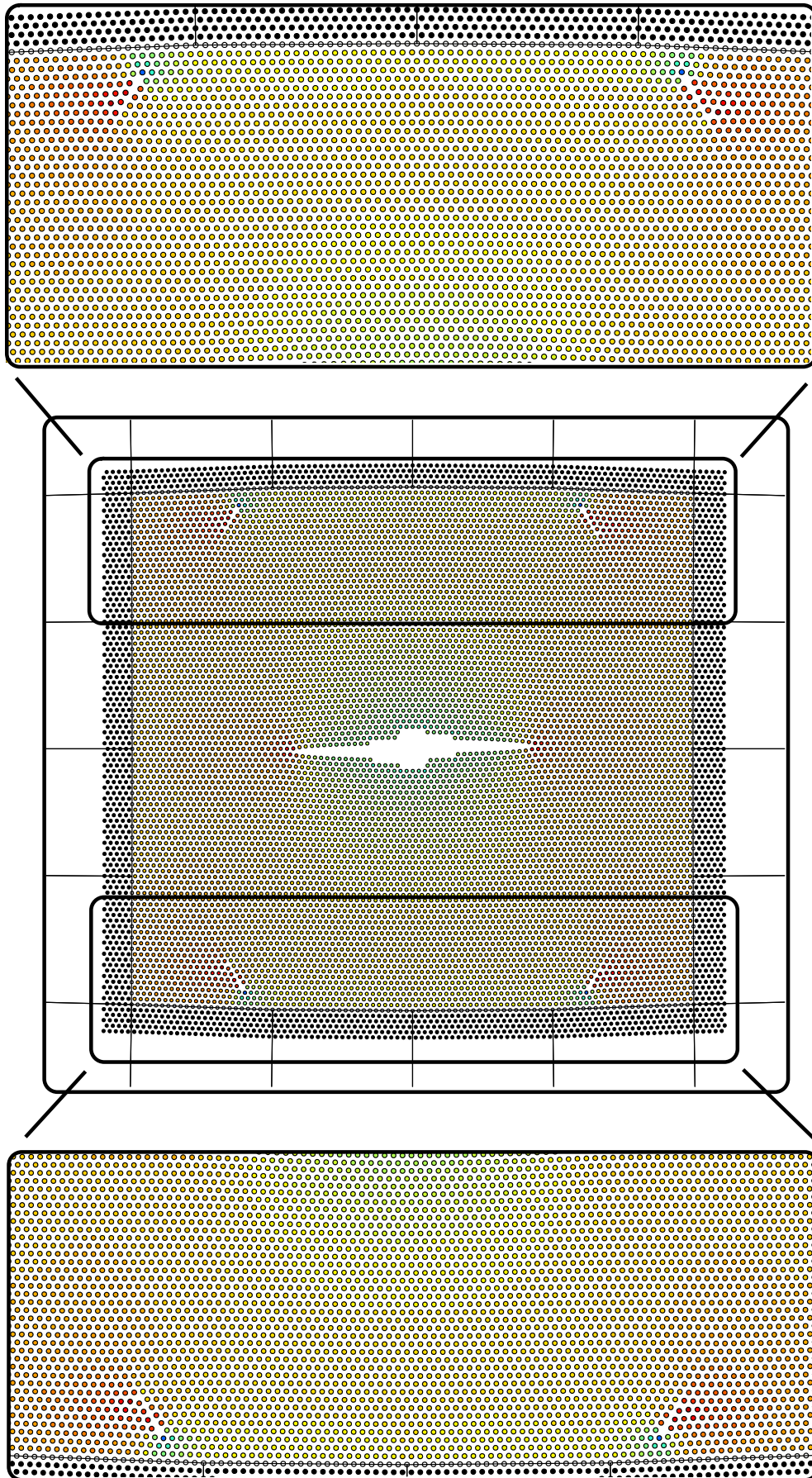


Figure 4.8: Crack opening in the coupling model with damping zone. They represent the same intermediate state of deformation as in Figure 3.21

5 Conclusions and Outlook

In the present work the main purpose was to present a continuum–atomistic multiscale algorithm for the analysis of crystalline deformation. To this end we combined the classical homogenization technique Cauchy–Born rule within a finite element approximation with a molecular dynamics resolution of the atomistic region. The aim was twofold.

- On the one hand the Cauchy–Born rule plays a central role in continuum–atomistic modelling and hence in the present contribution since it serves as a gateway linking the micronscale and the macroscale, i.e. atomistic simulations and the continuum mechanics. Therefore, the first part of this thesis deals with this atomistic informed model for capturing fine–scale features. The major application but at the same time limitation of the Cauchy–Born rule is that it is restricted to sufficiently homogeneous deformations. This rule cannot capture nanolevel defects, i.e. inhomogeneous deformation of the crystal. A study on the validity of the Cauchy–Born rule and its transition to non–affine deformations was then developed for different cases of deformation. To this end, an atomistic failure criteria was introduced in the sense of molecular dynamics which can capture complex nanoscale behavior as well as to simulate atomistic displacement. The standard deviation statistical measure was also introduced in this context as nothing more than a numerical tool for this purpose. Note that, the basic theoretical background of molecular dynamics approach had previously been outlined with special regard to potential energy functions and algorithms.
- To cope with the latter, the second part of the work covers the methodology used to develop a horizontal FEM/MD hybrid model for multi–scale analysis and the study of several representative cases of crystalline defects. To do this we began by reviewing the formulation of the continuum mechanics framework needed for this contribution. Then, we reiterated the vertical coupling within the continuum modelling which kinematics are characterized by the mentioned Cauchy–Born rule. This rule facilitates the incorporation of atomistic level information to the continuum model in an elegant way. Afterwards we combined the Cauchy–Born rule within a finite element approximation with an atomistic domain where the molecular dynamics approach was applied. The resolution was adapted according to the type of solution considered, i.e. an atomistic domain to capture the material behaviour complexity with a finite mesh to capture the smooth parts of the solution with the objective of interplaying accuracy and efficiently. Eventually, some numerical results were presented closing the chapter.

- In the end, the interface between the constrained and unconstrained atoms, i.e. the transition between the atomistic and continuum domain, unfortunately produces an additional problem related to the dynamic case. The pulses initiated in the dynamic domain ended up being reflected at the interface due to the constrained atoms, which then acted as a rigid boundary avoiding the smooth absorption of these waves. Therefore, both studies (the investigation of the range of validity of the Cauchy–Born rule and the horizontal coupling model) served as a good point of departure for extending the simulations to the dynamic case using the technique suggested by Holian and Ravelo [67] and implemented following the steps exhibit in Qu, Shastry, Curtin and Miller [107].

In regard to the outlook, several problems seem to be attractive for discussion in the future.

- The study of the Cauchy–Born rule may be also broadened to the three dimensional case using not only pair potentials but also introducing other types of potentials such as the proposed by Daw and Basques [42] or Finnis and Sinclair [54]. The study to other lattice configurations, such as b.c.c. structure, could complete the serie of works done in this area. The same study using the determinant of the acoustic tensor, or rather the loss of rank 1 convexity can be introduced. That would allow us to verify if the possible results acquired with both approaches would indicate the loss of the validity of the Cauchy–Born rule for the same state of deformation.
- Contrary to the study of the Cauchy–Born rule, the results achieved regarding the horizontal multiscale model were not able to be compared to other methods. Therefore, it is important to do it in order to check if the model renders similar results. In addition, the considerations in this work are restricted to pair–potentials for the sake of simplicity and also to the two dimensional case of a $\langle 111 \rangle$ –plane of a *fcc* type crystal due to the computational demand required. Therefore, a proposal for the future is to extend the computations to the three dimensional case introducing a more realistic energy function, i.e. an EAM potential function to capture atomistic phenomena. Moreover, other applications such as a nano–indentation test may be applied since it is an important method for determining material properties.
- Note that several problems arised during this work. One being in regards to the Figure ??, depicting the crack opening, the atomistic/continuum interface impedes the normal develop of the crack growth into the continuum domain. As a result this produces a disturbance in the simulation and the computation must be stopped. Therefore, it is of interest to develop a model to overcome this setback. One possibility would be to follow the evolution of the crack beyond the atomistic domain when the crack cross the interface. Other possibility would be allowance to move the atomistic region in conjunction with the crack itself. That means, use a resolution

adapted to the crack situation. We can add a set of atoms where a high degree of detail is required such as the crack tip whereas several atoms placed away from the complex material behaviour are removed and replaced with finite elements. With that, the model focuses only on regions, where the material contains interesting information and not only restricted to the initial atomistic/continuum configuration.

- Moreover, the treatment of the dislocations found out in the second example may be a field of interest in terms of how to allow the transition to the continuum without perturbing the atomistic domain. One approach dealing with this topic is the model proposed by Curtin et al. [119,120]. It would be great to introduce these ideas here for obtaining accurate results.

A The Standard Deviation

This appendix is devoted to give a brief exposition of the concept of the standard deviation quantity used in chapter 2, Equation 2.3.1. To achieve this aim, we will previously summarize some relevant statistical definitions and notations. In the end, we will restrict our attention to showing the difference between using a denominator $N - 1$ instead of N in Equation 2.3.1, which is the main purpose of this appendix. A more complete theory and detailed proofs may be obtained in a variety of books listed here [9], [14], [52], [64], [87] and [113].

Population

A population is a collection of reference elements (animals, people or things) in which we are interested and we wish to describe a certain phenomenon. Typical examples of phenomena studied on populations are for instance the choice of the voters in an election, the number of defects involved in a factory on a given day, all possible outcomes in successive tosses of a coin or the average temperatures for cities.

Population can be finite or infinite. The problem dealing with large finite populations arises due to size, time, cost, and other resource constrain in order to extract the important information, i.e. the features of the set of data in its entirety. In addition, dealing with infinite populations is generally impossible. Therefore, a representative sample taken from a population is necessary to yield some knowledge about the population.

Sample

A sample is a selected group of units, i.e. a reduced set of data from a population with the objective of drawing valid conclusions about the population, i.e. attempt to describe accurately a certain general phenomenon.

Sampling is the process of collecting and selecting a number of subjects from the subjects of a population. The sample must be representative of the general population and large enough to avoid errors, i.e. divergence between the phenomenon observed on a sample and the real population value.

Estimator

A statistic is a function applied to a sample data where the function itself does not depend on the distribution of the sample. An estimator is a statistic which is chosen to calculate a parameter of interest in the sample and then, used to give information about an unknown parameter in the population. Some typical estimators are for instance the

sample mean value and the sample variance, which are explained in detail later. To be a good estimator it is necessary to have the following characteristic: unbiased, consistency, high quality, efficiency and robustness. Next, we will mention these features although the most important for us is the unbiased characteristic because it allows us to explain the standard deviation equation used in the current work.

1. **Unbiased.** Bias occurs when the estimator has a tendency to yield results that differ from the values on the population. Suppose we want to estimate the population parameter θ using an estimator $\hat{\theta}$. Then, the bias of $\hat{\theta}$, i.e. the random error, is defined as the expected value of the estimator $\hat{\theta}$ minus the population value θ

$$bias(\hat{\theta}) := E(\hat{\theta} - \theta). \quad (\text{A.1})$$

In other words, using basic properties of expected value (see properties A.7 and A.10 of expectation) and knowing that $\hat{\theta}$ is a function and θ is a parameter, Equation A.1 may be rewritten as follows

$$bias(\hat{\theta}) := E(\hat{\theta}) - \theta. \quad (\text{A.2})$$

Thus, the estimator $\hat{\theta}$ is said to be an unbiased estimator of θ if the bias is 0, i.e. if $E(\hat{\theta}) = \theta$.

2. **Consistency.** An estimator is consistent, although it can be biased, if the bias reduces as the sample size grows. That means, an estimator $\hat{\theta}$ (where n is the sample size) is a consistent estimator for parameter θ if

$$\lim_{n \rightarrow \infty} bias(\hat{\theta}) = 0. \quad (\text{A.3})$$

3. **Mean square error (MSE)** The quality of an estimator is usually measured by computing the mean square error.

$$MSE(\hat{\theta}) = E[(\hat{\theta} - \theta)^2] = \left(bias(\hat{\theta})\right)^2 + VAR(\hat{\theta}). \quad (\text{A.4})$$

It can be seen that the mean square error is the sum of the variance and the square bias of the estimator. The lower the mean square error the better estimator.

4. **Efficiency.** The efficiency of an estimator is generally judged by the inverse of the variance of the estimator.
5. **Robustness** An estimator is robust when it maintains good properties against small variations in the model.

Expectation

A random variable is a function that associates a unique numerical value with every outcome of an experiment. An important quantity associated with random variables is the term expectation, symbolised by $E[X]$ or also called mathematical expectation. Let X be a discrete random variable. Thus, let us take a finite set of data $\{x_1, x_2, \dots, x_N\}$, such that $P[X = x_i] > 0$ for all $i = 1, \dots, N$. Let us denote $p_i = P[X = x_i]$, then the expectation of X is defined as

$$E[X] := \sum_i^N x_i P[X = x_i] = \sum_i^N x_i p_i. \quad (\text{A.5})$$

If each data x_i for all $i = 1, \dots, N$, has the same probability, i.e. $p_i = p_j$ for all $i = 1, \dots, N$, the expected value of X is also denoted by \bar{X} which is called the arithmetic average or arithmetic mean

$$\bar{X} = \frac{x_1 + x_2 + \dots + x_N}{N}. \quad (\text{A.6})$$

The mean is a common average measure used to report central tendency, i.e. to locate the centre of the distribution of a random variable. Sometimes, it may not be appropriate for describing distributions where the presence in the set is affected and influenced by a few extreme values (large or small). These distortions can occur when the mean is different from the median, i.e. the data set is skewed with one or more extreme values. When this happens the median may be a better representative measure of central tendency than the mean. Another measure to indicate central tendency is the mode, which represents the most frequent value in the set of data.

Here, we review some of the main properties of the expectation

1. Expected value of a constant a is equal to that constant

$$E[a] = a. \quad (\text{A.7})$$

2. If X and Y are random variables such that $X \leq Y$ and $E[X]$ and $E[Y]$ exist, then

$$E[X] \leq E[Y]. \quad (\text{A.8})$$

3. If a and b are two real numbers, X a random variable and $E[X]$ exists, then, the expectation of $E[aX + b]$ also exists and verified

$$E[aX + b] = a E[X] + b. \quad (\text{A.9})$$

4. If X and Y are random variables and $E[X]$ and $E[Y]$ exist, then

$$E[X + Y] = E[X] + E[Y]. \quad (\text{A.10})$$

5. If X and Y are two independent random variables and their expectations exist, then

$$E[XY] = E[X]E[Y]. \quad (\text{A.11})$$

Variance

The mean, median and mode are very useful to estimate a frequency distribution, but they do not give us an idea about the degree of spread of values. Therefore, the introduction of a measure for describing the scatter of observations around the expected value, i.e. its statistical dispersion is necessary. This measure is called variance and is defined as

$$\text{VAR}(X) := E[(X - E[X])^2]. \quad (\text{A.12})$$

The term variance was first introduced by Ronald Fisher in 1918 [55]. The variance of a random variable X is typically denoted by $\text{VAR}(X)$, σ_X^2 or simply σ^2 when there is no doubt about which is the random variable.

Using the described features of the expectation explained above, we can rewrite the variance in the form

$$\begin{aligned} \text{VAR}(X) &= E[(X - E[X])^2] = E[X^2] + E[(E[X])^2] - E[2XE[X]] \\ &= E[X^2] + (E[X])^2 - 2E[X]E[X] = E[X^2] - (E[X])^2. \end{aligned} \quad (\text{A.13})$$

This is often used to calculate the variance in practice, although it suffers from numerical approximation error if the two components of the equation, $E[X^2]$ and $(E[X])^2$, are similar in magnitude.

Restricted to a discrete random variable and considering that $p_1 = \dots = p_N$, i.e. $E[X] = \bar{X}$, the population variance is given by

$$\sigma^2 = \frac{1}{N} \sum_{i=1}^N (x_i - \bar{X})^2. \quad (\text{A.14})$$

where \bar{X} is the population mean, see Equation A.6. σ^2 gives us an idea about how much variation there is away from the average (mean). This is merely a special case of the

general definition of variance introduced above.

In many practical situations such as in large populations, the true variance of a population is not known a priori. The method is to use a sample in order to estimate the variance of these populations. We take a simple random sample, i.e. a set of independent random variables $\{Y_1, \dots, Y_n\}$ equally distributed as X . Remark, that the purpose of this appendix is to estimate the variance population, which from now on is denoted by σ^2 . It happens that a good estimator of the expectation of the population is the mean sample which is defined as¹

$$\bar{Y}_n = \frac{1}{n} \sum_{i=1}^n Y_i. \quad (\text{A.15})$$

Then, it would not be strange to think that a good estimator of the population variance, σ^2 , would be the sample variance defined by

$$S^2 = \frac{1}{n} \sum_{i=1}^n (Y_i - \bar{Y}_n)^2. \quad (\text{A.16})$$

However, we will see in the following proof that S^2 is not a good estimator of σ^2 , i.e. the population variance. The problem of Equation A.16 is that it is a biased estimator of the population variance (see property 1 of estimators), i.e. the expected value of the sample variance, $\text{E}[S^2]$, is not the population variance σ^2 .

$$\text{E}[S^2] = \frac{n-1}{n} \sigma^2 \neq \sigma^2 \quad (\text{A.17})$$

Proof of statement A.17

$$\begin{aligned} \text{E}[S^2] &= \text{E} \left[\frac{1}{n} \sum_{i=1}^n (Y_i - \bar{Y}_n)^2 \right] \\ &= \text{E} \left[\frac{1}{n} \sum_{i=1}^n \left((Y_i - \text{E}[Y_1])^2 + (\text{E}[Y_1] - \bar{Y}_n)^2 + 2(Y_i - \text{E}[Y_1])(\text{E}[Y_1] - \bar{Y}_n) \right) \right] \\ &= \sigma^2 + \text{VAR}(\bar{Y}_n) + \text{E} \left[\frac{2(\text{E}[Y_1] - \bar{Y}_n)}{n} \sum_{i=1}^n (Y_i - \text{E}[Y_1]) \right] \\ &= \frac{n+1}{n} \sigma^2 - 2\text{VAR}(\bar{Y}_n) = \frac{n-1}{n} \sigma^2. \end{aligned} \quad (\text{A.18})$$

Therefore, the sample variance is not the best estimator of the population variance. In order to avoid the bias of the variance sample, the (quasi)variance is defined as

¹We omit the proof of this assumption and refer the reader to the references listed at the beginning of the appendix.

$$\widehat{S}^2 = \frac{n}{n-1} S^2 = \frac{1}{n-1} \sum_{i=1}^n (Y_i - \bar{Y}_n)^2 \quad (\text{A.19})$$

which is an unbiased estimator of the population variance, i.e. $E[\widehat{S}^2] = \sigma^2$. That is the reason why the (quasi)variance sample and not the variance sample is used for our computations. In addition, when we measure one time, i.e. $n = 1$, the result of Equation A.19 gives an indetermination $0/0$. That means, that the result is an uncertain number, i.e. we cannot say anything about the divergence from the mean value. On the contrary, if we use the Equation A.16 to evaluate the divergence from the mean value, the result is 0 and that is not necessarily true. However, note that in practice, if the size of the sample increases, i.e. n is reasonably large, the difference between the variance and the (quasi)variance decreases tending to the variance of the population.

Standard Deviation

The unit of variance is the square of the unit of observation. For example, the variance of a set of heights measured in centimetres will be given in square centimetres. This fact has motivated that instead of using the (quasi)variance, we use its square root, known as the (quasi)standard deviation. The (quasi)standard deviation is applied as a measure of the dispersion of a set of data from its mean. Therefore, the (quasi)standard deviation can be expressed as:

$$sd = \sqrt{\frac{1}{n-1} \sum_{i=1}^n (Y_i - \bar{Y}_n)^2} \quad (\text{A.20})$$

A large (quasi)standard deviation indicates that the data points are far from the mean and a small (quasi)standard deviation indicates that they are closely around the mean.

In our simulations the Equation A.20 is applied. Since we study convergence, i.e. we increase the number of atoms to study the range of applicability of the Cauchy–Born rule, the lattices used are interpreted as a sample of a large crystal configuration (population) and therefore the Equation A.20 with $n - 1$ is a better approximation to compute the standard deviation instead of using n .

B Atomistic Stress

The pressure P at the boundary of a system may be calculated from the virial theorem of Clausius [35]

$$PV = Nk_B T - \frac{1}{3} \left\langle \sum_{i,j < i} \mathbf{r}_{ij} \cdot \mathbf{f}_{ij} \right\rangle. \quad (\text{B.1})$$

Here, the symbol V denotes the volume, N the total number of particles in the system, T the temperature and k_B is the Boltzmann's constant. The angular brackets mean average over time and the term within it refers to the internal virial where \mathbf{r}_{ij} is the separation of atoms i and j and \mathbf{f}_{ij} is the force on atom i due to atom j . In summary, the first term refers to the kinetic pressure and the second one to the potential pressure. A general reference here is [7] and for a deeper discussion of the theory see also [136].

The atomic level stress $\boldsymbol{\sigma}_i$ is based on a generalization of the above-mentioned theorem, see Nielsen et al. [97], which renders ¹

$$\boldsymbol{\sigma}_i = -\frac{1}{\Omega_i} \left(\frac{1}{2} \sum_{j \neq i} \mathbf{f}_{ij} \otimes \mathbf{r}_{ij} + m_i \mathbf{v}_i \otimes \mathbf{v}_i \right) \quad (\text{B.2})$$

where Ω_i is the local atomic volume around atom i , \mathbf{v}_i is the velocity of this atom i , \mathbf{r}_{ij} is the vector joining particles i and j and \mathbf{f}_{ij} is the force upon atom i due to the neighbour j . As can be seen in the formula B.2 the atomic level stress consists of two terms. The first part depends on interatomic forces and the second contribution on the mass and velocity of atomic particles. Restricted to lattice statics, i.e. the stationary case, the contribution of the kinetic term is identical to zero and hence the expression B.2 is reduced to the force part. Some other works dealing with the topic are for instance [141,157].

In the general case the virial stress tensor has been served to describe the current state of stress in an atomic crystal as well as to the characterisation of defects [45], determination of elastic constants [89] and used in molecular dynamics simulations [36,57]. Some other authors also dealt with this topic include Yip et al. [33] and Delph et al. [38]. However, recent works show that the virial stress including the kinetic term is not equivalent to the classical Cauchy stress, see Zhou [154]. In addition, The total virial stress needs to be average over the time and space to be identified with the Cauchy stress. Therefore the correct link of quantities such as the virial stress between atomistic scale and continuum scale still remains an important subject in research.

¹This expression is a simplification for the case in which the energy function depends only on the separations between the atoms, see Egami and Vitek [141] for details.

C Continuum Failure Criteria

We have included this appendix with the simple purpose of comparing the accuracy of the results obtained in Chapter 2. To this end, the acoustic tensor or rather the study of the loss of rank 1 convexity was applied as continuum failure criteria. This tool was also used in the work carried out by Sunyk and Steinmann [126]. They focused on studying the stability of the Cauchy–Born rule for a shear deformation with 0 degree lattice orientation and uniaxial extension deformation with 30 degrees lattice orientation. These results are reiterated here and broaden to other deformation cases such as pure shear and dilatation as well as to different lattice orientations in order to complete this work and of course to compare to the results obtained in Chapter 2. As a result it turns out that both approaches, i.e. the acoustic tensor and the atomistic failure criteria in the sense of molecular dynamics, indicate the loss of the validity of the Cauchy–Born rule for the same state of deformation. Note that the objective is not to delve into this continuum stability theory but only report an extension of the results pursued in [123,126].

Failure Criteria

Based on the stored energy density the analysis of the loss of infinitesimal rank 1 convexity at the continuum level is given by

$$[\mathbf{m} \otimes \mathbf{N}] : \partial_{\mathbf{F}\mathbf{F}}^2 W_0 : [\mathbf{m} \otimes \mathbf{N}] \geq 0., \quad (\text{C.1})$$

where W_0 is again the phenomenological macroscopic energy. Loss of rank 1 convexity coincides with the possible onset of the (local) transition from an homogeneous deformation state to an inhomogeneous state of the continuum. It can be analysed thanks to the acoustic tensor \mathbf{q} which, for the case of pair potentials, takes the intriguing format in terms of a weighted sum of atomic stiffness tensors

$$\mathbf{q} = \frac{1}{2V_i} \sum_{j \neq i} \mathbf{q}_{ij} \quad \text{with} \quad \mathbf{q}_{ij} = [\mathbf{R}_{ij} \cdot \mathbf{N}]^2 \mathbf{k}_{ij}. \quad (\text{C.2})$$

Here \mathbf{m} denotes the jump or rather polarization vector in the deformed configuration, \mathbf{N} represents the normal to the failure surface in the material configuration and \mathbf{k}_{ij} denotes the atomistic level stiffness, which for the pair potential case takes the format outlined in Equation 3.3.21. Here, the singularity of \mathbf{q} , i.e. $\min \{\det \mathbf{q}\} = 0$, marks the loss of rank 1 convexity and thus the onset of possible non–homogeneous deformation. See the Phd Thesis of Sunyk and Lambrecht [81,125] for a complete explanation related to the loss of rank 1 convexity analysis.

Numerical Results

Simple Shear Deformation

The corresponding result for simple shear deformation within the realm of continuum mechanics can be seen in Figure C.1 where the determinant of the acoustic tensor \mathbf{q} versus the shear number is depicted. They show the shear number where the sign-change of the \mathbf{q} occurs. These values are at $\gamma \approx 0.14$ for lattice orientations 30 and 15 and $\gamma \approx 0.142$ for lattice orientations 0 which could be considered to correspond to the critical deformation state. Since the Cauchy–Born model is essentially an elastic model, loss of rank 1 convexity can also be interpreted to indicate the limit of the elastic domain. These results agree well with the results achieved in the simulations performed with molecular dynamics.

Uniaxial Extension Deformation

Figure C.2 depicts the determinant of the acoustic tensor \mathbf{q} versus the stretch λ for different orientations (0, 15 and 30). In this case the sign-change of the $\min\{\det \mathbf{q}\}$ corresponds to the stretch value $\lambda = 1.12$ for 0 and 15 degrees in the lattice while $\lambda = 1.137$ for orientation 30. These results are in a good agreement with the results obtained from the standard deviation based on molecular dynamics.

Pure Shear Deformation

Loss of rank 1 convexity performed in terms of the acoustic tensor indicates essentially the state of losing the elastic behaviour of the model. To find out this state, the determinant of the acoustic tensor \mathbf{q} versus the stretch for pure shear deformation with different orientations was depicted in Figure C.3. They show the value of the stretch where the sign-change of the \mathbf{q} occurs. They could be considered to coincide to the critical deformation state. These values are at $\lambda = 1.0705$ for lattice orientations 30 and 15 and $\lambda = 1.085$ for lattice orientations 0, which correspond to the values achieved with the atomistic criteria.

Dilatation Deformation

Finally Figure C.4 displays the determinant of the acoustic tensor \mathbf{q} versus the stretch for dilatation case with different orientations. We discovered that the state of sign-change of $\min\{\det \mathbf{q}\}$, i.e. the possible onset of the transition to an inhomogeneous configuration in the lattice, corresponds approximately to the value $\lambda = 1.1131$ independently of the orientation considered. These results agree well with the results achieved in the simulations performed with molecular dynamics as can be seen in the figures shown before.

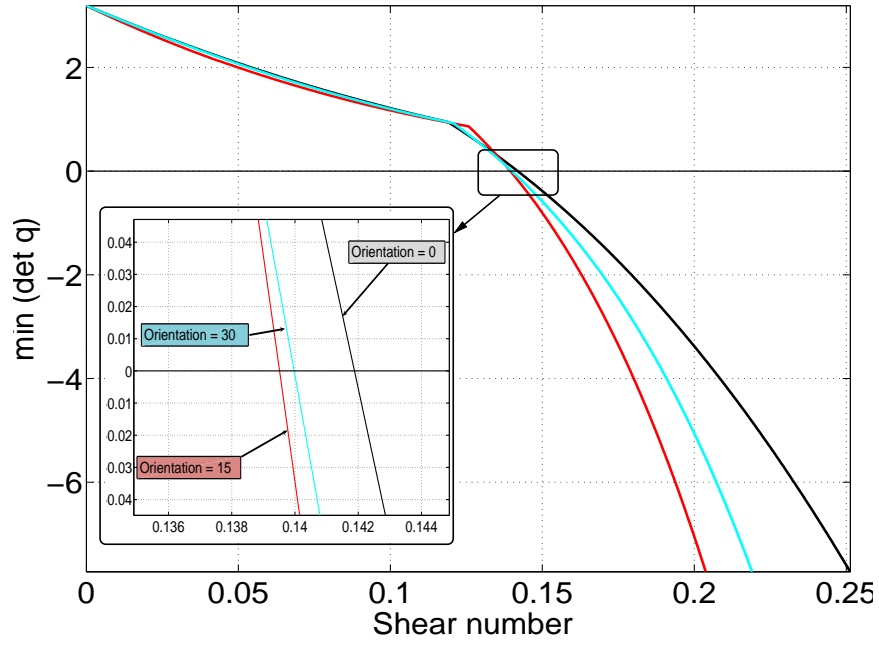


Figure C.1: The minimum of acoustic tensor determinant q as a function of the shear number γ for the case of simple shear deformation performed for different orientations in the lattice.

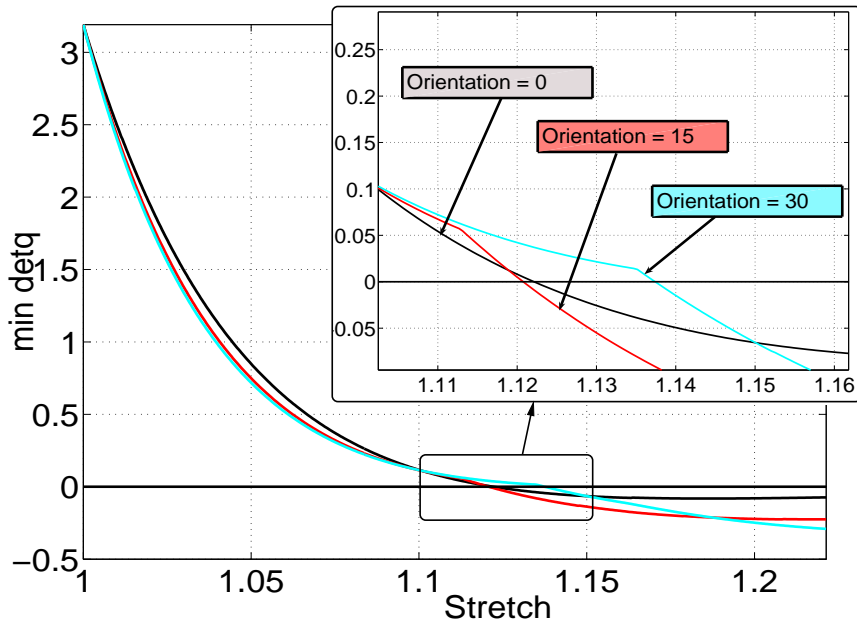


Figure C.2: The minimum of acoustic tensor determinant q as a function of the stretch λ for the case of uniaxial extension deformation performed for different orientations in the lattice.

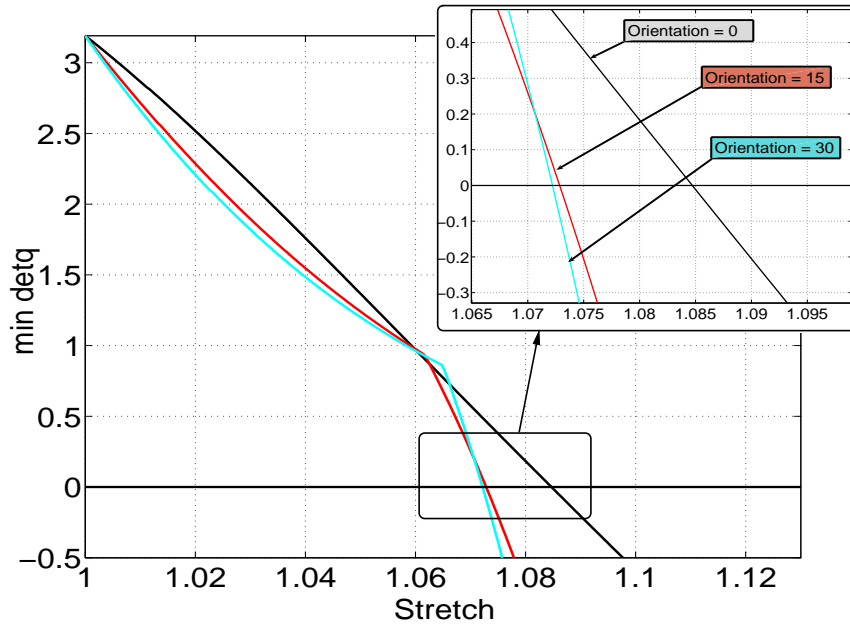


Figure C.3: The minimum of acoustic tensor determinant q as a function of the stretch λ for the case of pure shear deformation performed for different orientations in the lattice.

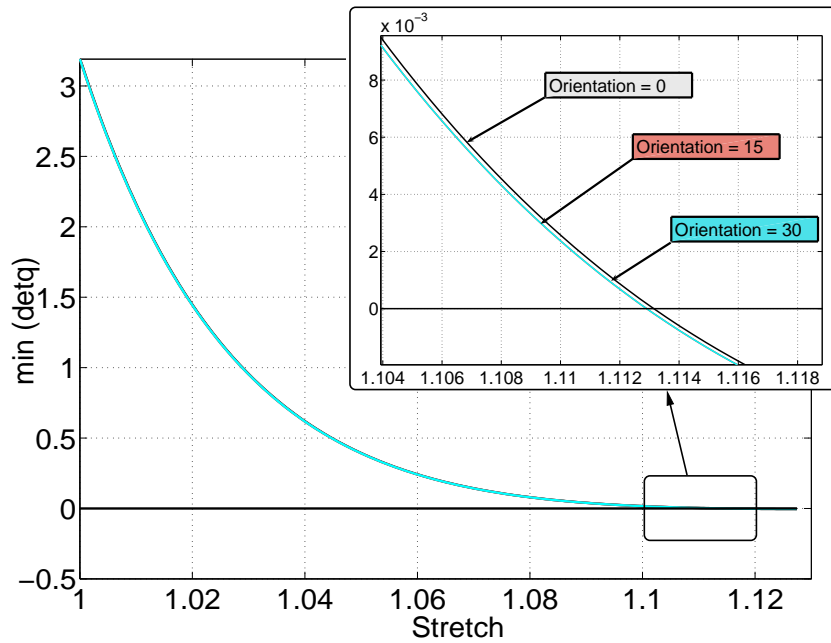


Figure C.4: The minimum of acoustic tensor determinant q as a function of the stretch λ for the case of dilatation deformation performed for different orientations in the lattice.

D Miscellaneous

A Note on Unit Conversions and Reduced Units

An important issue that remains is the choice of the units in molecular dynamics computations. Several real quantities within the molecular dynamics framework and also in nano- or micro mechanics may produce accuracy problems if they must be computed in real units or rather in SI units. These quantities are normally very small at this level. See Table below which gives an overview of some common unit conversions used in molecular dynamics.

Quantity	Unit name	Symbol	Conversion
Force	Newton	N	1 N = 1 kg m/s ²
Length	Angstrom	Å	1 Å = 10 ⁻¹⁰ m
Time	Femtosecond	fs	1 fs = 10 ⁻¹⁵ sec.
Work, Energy	Joule	J	1 J = 1 Nm · nm = 1 kg m ² /s ²
Energy	Electron volt	eVol	1 eVol = 1.602177733 × 10 ⁻¹⁹ J
Mass	Atomic mass unit	amu	1 amu = 1.67 × 10 ⁻²⁷ kg

In case the particles in the system interact via pair-potentials such as Lennard-Jones energy function, they are defined by a few parameters such as ϵ and σ which are specified in fundamental units of energy and length. That allows us to reduce the units of these quantities as well as to save computational cost. We summarize in the next table some of these variables in reduced units which were used during this work, see [7, 137] for more details.

Density	$\rho^* = \rho\sigma^3$
Temperature	$T^* = k_B \frac{T}{\epsilon}$
Energy	$E^* = \frac{E}{\epsilon}$
Pressure	$P^* = P \frac{\sigma^3}{\epsilon}$
Time	$t^* = \left(\frac{\epsilon}{m\sigma^2}\right)^{\frac{1}{2}} t$
Force	$f^* = f \frac{\sigma}{\epsilon}$
Surface tension	$\gamma^* = \gamma \frac{\sigma^2}{\epsilon}$

Notation

Dyadic product

$$\begin{aligned} \mathbf{A} &= \mathbf{a} \otimes \mathbf{b} & A_{ij} &= a_i b_j \\ \mathbf{C} &= \mathbf{A} \otimes \mathbf{B} & C_{ijkl} &= A_{ij} B_{kl} \end{aligned}$$

Nonstandard dyadic products

$$\begin{aligned} \mathbf{C} &= \mathbf{A} \overline{\otimes} \mathbf{B} & C_{ijkl} &= A_{ik} B_{jl} \\ \mathbf{C} &= \underline{\mathbf{A}} \otimes \mathbf{B} & C_{ijkl} &= A_{il} B_{jk} \end{aligned}$$

Bibliography

- [1] F.F. Abraham, J. Broughton, N. Bernstein, and E. Kaxiras. Spanning the continuum to quantum length scales in a dynamic simulation of brittle fracture. *Europhys. Lett.*, 44:783–787, 1998.
- [2] F.F. Abraham, R. Walkup, H. Gao, M. Duchaineau, T. Diaz de la Rubia, and M. Seager. Simulating materials failure by using up to one billion atoms and the world’s fastest computer: Brittle fracture. *PNAS*, 99(9):5777–5782, 2002.
- [3] F.F. Abraham, R. Walkup, H. Gao, M. Duchaineau, T. Diaz de la Rubia, and M. Seager. Simulating materials failure by using up to one billion atoms and the world’s fastest computer: Work-hardening. *PNAS*, 99(9):5783–5787, 2002.
- [4] B.J. Alder and T.E. Wainwright. Phase transition for a hard sphere system. *J. Chem. Phys.*, 27(5):1208–1209, 1957.
- [5] B.J. Alder and T.E. Wainwright. Studies in molecular dynamics. i. general method. *J. Chem. Phys.*, 31(2):459–466, 1959.
- [6] M.P. Allen. Introduction to molecular dynamics simulation. *NIC Series*, 23(23):1–28, 2004.
- [7] M.P. Allen and P.J. Tildesley. *Computer Simulation of Liquids*. Clarendon Press Oxford, 1987.
- [8] H.C. Andersen. Molecular dynamics at constant pressure and/or temperature. *J. Chem. Phys.*, 72(72):2384–2393, 1980.
- [9] R. B. Ash. *Real analysis and Probability*. Academic Press, 1972.
- [10] M.I. Baskes. Modified Embedded–Atom potential for cubic materials and impurities. *Phys. Rev.*, B46(5):2727, 1991.
- [11] M.I. Baskes and M.S. Daw. Embedded–Atom Method: derivation and application to impurities, surfaces and other defects in metals. *Phys. Rev.*, B29:6443, 1984.
- [12] T. Belytschko and S.P. Xiao. Coupling methods for continuum model with molecular model. *International Journal for Multiscale Computational Engineering*, 1(4):1543–1649, 2003.
- [13] H.J.C. Berendsen, W.F. Postma, W.F. van Gunsteren, A. DiNola, and J.R. Haak. Molecular dynamics with coupling to an external bath. *J. Chem. Phys.*, 81(8):3684–3690, 1984.
- [14] P. Billingsley. *Probability and Measure, 3rd Edition*. John Wiley and Sons, 1995.
- [15] M. Bishop, M.H. Kalos, and H.L. Frisch. Molecular dynamics of polymeric systems. *J. Chem. Phys.*, 70(03):1299–1304, 1979.

- [16] J. Bonet and D. Wood. *Nonlinear continuum mechanics for finite element analysis*. Cambridge University Press, 1997.
- [17] M. Born. *Dynamik der Kristallgitter*. Teubner, 1915.
- [18] M. Born and K. Huang. *Dynamical theory of crystal lattices*. Oxford, Clarendon Press, 1954.
- [19] W. Brostow, J. P. Dussault, and B. L. Fox. Construction of Voronoi polyhedra. *J. Comput. Phys.*, 29:81–92, 1978.
- [20] J. Q. Broughton, Farid F. Abraham, Noam Bernstein, and Efthimios Kaxiras. Concurrent coupling of length scales: Methodology and application. *Phys. Rev. B*, 60(4):2391–2403, 1999.
- [21] J.M. Buehler. Atomistic and continuum studies of deformation and failure in brittle solids and thin film systems. 2004.
- [22] J.M. Buehler and H. Gao. Ultra large scale simulations of dynamic materials failure. *Handbook of Theoretical and Computational*, 2004.
- [23] J.M. Buehler, A. Hartmaier, M. A. Duchaineau, Abraham F.F., and H. Gao. The dynamical complexity of work-hardening: a large-scale molecular dynamics simulation. *Acta Mechanica Sinica*, 21(2):103–111, 2004.
- [24] W. Cai, V.V. de Koenig, M. Bulatov, and S. Yip. Minimizing boundary reflections in coupled-domain simulations. *Phys. Rev. Lett.*, 85(15):3213–3216, 2000.
- [25] A. E. Carlsson. *Advances in Research and Applications*, volume 43. Edited by H. Ehrenreich and D. Turnbull (Academic, New York, 1990), 1990.
- [26] A. Carpio and L.L. Bonilla. Discrete models for dislocations and thier motion in cubic crystals. *Phys. Rev. B*, 12:1087–1097, 2005.
- [27] R. Carr and M. Parrinello. Unified approach for molecular dynamics and density functional theory. *Phys. Rev. Lett.*, 55(22):2471–2474, 1985.
- [28] A. L. Cauchy. De la pression ou tension dans un système de points matériels. *Exercices De Mathematiques, 1828*. Available in Cauchy, Augustin Louis Oeuvres Complétées, Tome 20, 253-277.
- [29] A. L. Cauchy. Sur l'équilibre et le mouvement d'un système de points matériels sollicités par des forces d'attraction ou de répulsion ou de répulsion mutuelle. *Exercices De Mathematiques, 1828*. Available in Cauchy, Augustin Louis Oeuvres Complétées, Tome 20, 227-252.
- [30] A. L. Cauchy. Sur l'équilibre et le mouvement intérieur des corps considérés comme des masses continues. *Exercices De Mathematiques, 1829*. Available in Cauchy, Augustin Louis Oeuvres Complétées, Tome 21, 162-173.
- [31] A. L. Cauchy. Sur les équations différentielles d'équilibre ou de mouvement pour un système de points matériels sollicités par de forces d'attraction ou de répulsion mutuelle. *Exercices De Mathematiques, 1829*. Available in Cauchy, Augustin Louis Oeuvres Complétées, Tome 21, 162-173.

-
- [32] S.P. Chen, T. Egami, and V. Vitek. Local fluctuations and ordering in liquid and amorphous metals. *Phys. Rev. B*, 37(5):2440–2448, 1988.
- [33] K.S. Cheung and S. Yip. Atomic-level stress in an inhomogeneous system. *J. Appl. Phys.*, 70(10):5688–5690, 1991.
- [34] Christophe Chipot. *Metodos numericos para dinamica molecular*. 2003.
- [35] R. Clausius. The dynamical theory of gases. *Philos. Mag*, 40(122):130, 1870.
- [36] F. Cleri. Representation of mechanical loads in molecular dynamic simulations. *Phys. Rev. B*, 65(65):014107–1 – 014107–6, 2001.
- [37] F. Collino and C. Tsogka. Application of the perfectly matched absorbing layer model to the linear elastodynamic in anisotropic heterogeneous media. *Geophysics*, 66(27):294–307, 2001.
- [38] J. Cormier, J.M. Rickman, and T.J. Delph. Stress calculation in atomistic simulations of perfect and imperfect solids. *J. Appl. Phys.*, 89(1):99–104, 2001.
- [39] S.A. Cote, B. Smith, and P.J.D. Lindan. *Democritus tutorial*. Daresbury Laboratory, 2001.
- [40] W. A. Curtin and Ronald E. Miller. Atomistic/continuum coupling in computational materials science. *Modelling and Simulation in Materials Science and Engineering*, 11(11):33–68, 2003.
- [41] Yu Da-Qi, Min Chen, and Xiu-Jun Han. Structure analysis methods for crystalline solids and supercooled liquids. *Phys. Rev. E*, 72(5):051202, 2005.
- [42] M. S. Daw, M.I. Daw Foiles, J., and M.I Baskes. The Embedded-Atom Method: A review theory and applications. *Mater. Sci. Rep.*, 9:251–310, 1993.
- [43] J.D. Doll and D.R. Dion. Generalized langevin equation approach for atom/solid-surface scattering: Numerical techniques for gaussian generalized langevin dynamics. *J. Chem. Phys.*, 65(9):3762–3766, 1976.
- [44] L. Dupuy, E.B. Tadmor, R.E. Miller, and R. Phillips. Finite temperature quasicontinuum: Molecular dynamics without all the atoms. *Phys. Rev. Lett.*, 95(060202):1–4, 2005.
- [45] K. Egami, T. Maeda and V. Vitek. Structural defects in amorphous solids: A computer simulation study. *Phil. Mag. A*, 41:883, 1980.
- [46] B. Engquist and W. E. The heterogeneous multi-scale methods. *Comm. Math. Sci.*, 1(3):423–436, 2003.
- [47] B. Engquist and A. Majda. Absorbing boundary conditions for numerical simulation of wave. *Applied Mathematical Sciences*, 74(5):1765–1766, 1977.
- [48] F. Ercolessi. A molecular dynamics primer. *International School for Advanced Studies. Spring College in Computational Physics, ICTP, Trieste*, 1997.
- [49] J.L. Ericksen. The Cauchy and Born hypotheses for crystals, Phase Transformations and Material Instabilities in Solids. *Academic Press*, 23(23):61–78, 1984.

- [50] D.J. Evans. The frequency dependent shear viscosity of methane. *Molecular Physics*, 37(6):1745–1754, 1979.
- [51] D.J. Evans and Gary P. Morriss. *Statistical mechanics of Nonequilibrium Liquids*. Academic Press, 1990.
- [52] T. S. Ferguson. *Mathematical Statistics*. Academic Press, 1967.
- [53] M.W. Finnis, P. Agnew, and A.J.E. Foreman. Thermal excitation of electrons in energetic displacement cascades. *Phys. Rev. B*, 44(2):567–574, 1991.
- [54] M.W. Finnis and J.E. Sinclair. A simple empirical n-body potential for transition metals. *Phil. Mag. A*, 50:45–55, 1984.
- [55] R.A. Fisher. The correlation between relatives on the supposition of mendelian inheritance. *Philosophical Transactions of the Royal Society of Edinburgh*, 52:399–433, 1918.
- [56] S.M. Foiles, M.I. Baskes, and M.S. Daw. Embedded atom method. *Phys. Rev. B*, 33(33):7983, 1986.
- [57] S.J.V. Frankland, G.M. Harik, V.M. and Odegard, and T.S. Gates. Stress-Strain Behavior of Polymer Carbon-Nanotube Composites: Molecular Dynamics S Simulation Results, journal = Composites Science and Technology, year = 2003, volume = 63, number = 11, pages = 1655–1661.
- [58] D. Frenkel and B. Smith. *Understanding Molecular Simulation: From algorithms to applications*. Academic Press, 1996.
- [59] G. Friesecke and F. Theil. Validity and failure of the Cauchy–Born hypothesis in a Two-Dimensional Mass–Spring Lattice. *J. Nonlinear Sci.*, 12:445–478, 2002.
- [60] J.B. Gibson, A.N. Goland, M. Milgram, and G.H. Vineyard. Dynamics of Radiation Damage. *Phys. Rev.*, 120(4):1229–1252, 1960.
- [61] P. Gumbsch, S.J. Zhou, and B.L. Holian. Molecular dynamics investigation of dynamic crack stability. *Phys. Rev. B*, 55(6):3445–3455, 1997.
- [62] Gonzalo Gutierrez. Elementos de simulation computational. Dinamica molecular y metodo de Monte Carlo. 2001.
- [63] R.S. Haberlandt, G. Frizsche, G. Peinel, and K. Heinzinger. *Molekulardynamik*. Springer, 1995.
- [64] J.M. Haile. *Molecular Dynamics Simulation*. Wiley, 1991.
- [65] J. Hannes and Hans C. Andersen. Icosahedral Ordering in the Lennard–Jones Liquid and Glass. *Phys. Rev. Lett.*, 60(22):2295–2298, 1988.
- [66] D.W. Heermann. *Computer Molecular Methods in Theoretical Physics*. Springer, 1989.
- [67] B.L. Holian and R. Ravelo. Fracture simulation using large-scale molecular dynamics. *Phys. Rev. B*, 51(17):275–288, 1995.
- [68] D. Holland and M. Marder. Ideal brittle fracture of silicon studied with molecular dynamics. *Phys. Rev. Lett.*, 80(4):746–749, 1998.

-
- [69] N. Holmes and Belytschko T. Postprocessing of finite element transient response calculations by digital filters. *Computers and Structures*, 6:211–216, 1976.
- [70] G.A. Holzapfel. *Nonlinear Solid Mechanics*. 2001.
- [71] J.D. Honeycutt and H. C. Andersen. Molecular dynamics study of melting and freezing of small Lennard–Jones clusters. *J. Phys. Chem.*, 91(19):4950–4963, 1987.
- [72] W.G. Hoover. Canonical dynamics: Equilibrium phase–space distribution. *Phys. Rev. A*, 31(31):1695–1697, 1985.
- [73] W.G. Hoover. *Computational Statistical Mechanics*. Elsevier Science Pub C, 1991.
- [74] T.J.R. Hughes. *The Finite Element Method*. Dover Publications, 1987.
- [75] E.G. Karpov, G.J. Wagner, and W.K. Liu. A Green’s function approach to deriving non–reflecting boundary conditions in molecular dynamics simulations. *International Journal for Numerical Methods in Engineering*, 62(62):1250–1262, 2005.
- [76] L. Kelchner, C., J. Plimpton, S., and J.C. Hamilton. Dislocation nucleation and defect structure during surface indentation. *Phys. Rev. B*, 58(17):11085–11088, 1998.
- [77] C. Kittel. *Einführung in die Festkörperphysik*. Oldenburg Wissensch. Vlg, 1983.
- [78] S. Kohlhoff, P. Gumbsch, and H.F. Fischmeister. Crack propagation in b.c.c. crystals studied with a combined finite–element and atomistic model. *Philos. Mag A*, 64(4):851–878, 1991.
- [79] Y.W. Kwon and Hyochoong Bang. *The Finite Element Method using Matlab*. CEC Mechanical Engineering series, 2000.
- [80] Y.W. Kwon and S.H. Jung. Atomic model and coupling with continuum model for static equilibrium problems. *Computers and Structures*, 82(82):1993–2000, 2004.
- [81] M. Lambrecht. Theorie und Numerik von Materialinstabilitäten elastoplastischer Festkörper auf der Grundlage inkrementeller Variationsformulierungen. *Ph.D. Thesis*, 2002.
- [82] J.E Lennard-Jones. *Proc. R. Soc. London A*, 106(106):463, 1924.
- [83] J. Li. Atomeye: An efficient atomistic configuration viewer. *Model. Simul. Mater. Sci. Engrg.*, 11:173–177, 2003.
- [84] J. Li. Atomistic visualization. *Handbook of Materials Modeling*, 192(192):1051–1068, 2005.
- [85] S. Li and W.K. Liu. *Meshfree Particle Methods*. Springer, 2004.
- [86] X. Li and E. Weinan. Multiscale modeling of dynamics of solids at finite temperature. *Journal of the Mechanics and Physics of Solids*, 53:1650–1685, 2005.
- [87] B.W. Lindgren. *Statistical Theory*. Chapman and Hall. New York, 1993.
- [88] W.K. Liu, E.G. Karpov, S. Zhang, and H.S. Park. An introduction to computational nanomechanics and materials. *Computer Methods in Applied Mechanics and Engineering*, 193(193):1529–1578, 2004.

- [89] J.F. Lutsko. Stress and elastic constants in anisotropic solids: Molecular dynamics techniques. *J. Appl. Phys.*, 64(3):1152–1154, 1988.
- [90] D.A. MacDuarrie. *Statistical mechanics*. Harper and Row, 1976.
- [91] R. Meyer and P. Entel. Martensite–austenite transition and phonon dispersion curves of feni studied by molecular dynamics simulations. *Phys. Rev. B*, 57(9):5140–5147, 1998.
- [92] R.E. Miller and E.B. Tadmor. The quasicontinuum method: Overview, applications and current directions. *Journal of Computer-Aided Materials Design*, 9(9):203–239, 2002.
- [93] F. Milstein. *Mechanics of Solids*. Oxford, Pergamon Press, 1982.
- [94] P.M. Morse. *Phys. Rev.*, 34(57), 1929.
- [95] J. Mortensen, J. Schiotz, and W. Jacobsen. The quasicontinuum method revisited. *SIMU Newsletter*, (Issue 4):119, 2002.
- [96] H.P. Myers. *Introductory Solid State Physics*. CRC Press, 1990.
- [97] O.H. Nielsen and R.M. Martin. Quantum–Mechanical Theory of Stress and Force. *Phys. Rev. B*, 32(6):3780–3791, 1985.
- [98] K. Nishimura and N. Miyazaki. Molecular dynamics simulation of crack growth under cyclic loading. *Computational Materials Science*, 31(3–4):269–278, 2004.
- [99] M. Nomura, S. Lee, and J.B. Adams. Vacancy diffusion along twist grain boundaries in copper. *J. Mat. Res.*, 6(1):1–4, 1991.
- [100] S. Nose. A molecular dynamics method for simulation in the canonical ensemble. *Mol. Phys.*, 52(42):255–268, 1984.
- [101] K. Ohsawa and E. Kuramoto. Flexible boundary condition for a moving dislocation. *J. Appl. Phys.*, 86(1):179–185, 1999.
- [102] M. Ortiz and R. Phillips. Nanomechanics of Defects in Solids. *Advances in Applied Mechanics*, 36(36):1–79, 1999.
- [103] H.S. Park, E.G. Karpov, and W.K. Liu. A temperature equation for coupled atomistic/continuum simulations. *Computer Methods in Applied Mechanics and Engineering*, 193(193):1713–1732, 2004.
- [104] H.S. Park, E.G. Karpov, and W.K. Liu. Non–reflecting boundary conditions for atomistic, continuum and coupled atomistic/continuum simulations. *International Journal for Numerical Methods in Engineering*, 64(64):237–259, 2005.
- [105] M. C. Payne, M. P. Teter, D. C. Allan, T. A. Arias, and J. D. Joannopoulos. Iterative minimization techniques for ab initio total–energy calculations: Molecular dynamics and conjugate gradients. *Rev. Mod. Phys.*, 64(4):1045–1097, 1992.
- [106] William H. Press, Brian P. Flannery, Saul A. Teukolsky, and William T. Vetterling. *Numerical recipes: The art of scientific computing*. Cambridge University Press, 1986.
- [107] S. Qu, W.A. Curtin, and R.E. Miller. A finite–temperature dynamic coupled atomistic/discrete dislocation method. *Modelling and Simulation in Materials Science and Engineering*, 13(13):1101–1118, 2005.

-
- [108] H. Rafii-Tabar, L. Hua, and M. Cross. A multi-scale atomistic-continuum modelling of crack propagation in a two-dimensional macroscopic plate. *J. Phys.: Condens. Matter*, 10(10):2375–2387, 1998.
- [109] A. Rahman. Correlations in the motion of atoms in liquid Argon. *Phys. Rev.*, 136(2A):A405–A411, 1964.
- [110] A. Rahman and F.H. Stlinger. Improved simulation of liquid water by molecular dynamics. *J. Chem. Phys.*, 60(4):1545–1557, 1974.
- [111] D. Rapaport. *The art of molecular dynamics simulation*. Cambridge University Press, 1995.
- [112] D. Rodney. Mixed atomistic/continuum methods: Static and dynamic quasicontinuum methods. *Proceedings of the NATO Conference "Thermodynamics, Microstructures and Plasticity"*, Eds A. Finel, D. Maziere, M. Veron, 2003.
- [113] V. K. Rohatgi. *An Introduction to Probability Theory and Mathematical Statistics*. Wiley, Nueva Cork, 1976.
- [114] R.E. Rudd and J.Q. Broughton. Coarse-gradient molecular dynamics and the atomic limit of finite elements. *Phys. Rev. B*, 58(58):5893–5896, 1998.
- [115] R.E. Rudd and J.Q. Broughton. Concurrent coupling of length scales in solid state systems. *Phys. Stat. Sol.*, 217(1):251–291, 2000.
- [116] A.A. Selezenev, A.Y. Aleynikov, N.S. Gantchuk, P.V. Yermakov, J.K. Labanowski, and A.A. Korkin. Sage md: molecular dynamic software package to study properties of materials with different models for interatomic interactions. *Computational Materials Science*, 28(28):107–124, 2003.
- [117] Y. Shao, P.C. Clapp, and J.A. Rifin. Molecular dynamics simulation of martensitic transformations in NiAl. *Metallurgical and Materials Transactions*, 27(A):1477–1489, 1996.
- [118] V. B. Shenoy, R. Miller, E. B. Tadmor, D. Rodney, R. Phillips, and M. Ortiz. An adaptive finite element approach to atomic-scale mechanics - The quasicontinuum method. *ArXiv Condensed Matter e-prints*, October 1997.
- [119] L.E. Shilkrot, W.A. Curtin, and R.E. Miller. A coupled atomistic/continuum model of defects in solids. *Journal of the Mechanics and Physics of Solids*, 50(50):2085–2106, 2002.
- [120] L.E. Shilkrot, R.E. Miller, and W.A. Curtin. Multiscale plasticity modeling: coupled atomistics and discrete dislocation mechanics. *Journal of the Mechanics and Physics of Solids*, 52(52):755–787, 2004.
- [121] M. Springborg. *Density functional methods in chemistry and materials science*. Wiley, 1997.
- [122] P. Steinmann. Application of material forces to hyperelastostatic fracture mechanics. i. continuum mechanical setting. *International Journal of Solids and Structures*, 37:7371–7391, 2000.
- [123] P. Steinmann, A. Elizondo, and R. Sunyk. Studies of validity of the Cauchy–Born rule by direct comparison of the continuum and atomistic modelling. *Modelling and Simulation in Material Science and Engineering*, 14:1–11, 2006.

- [124] F. H. Stillinger and Thomas A. Weber. Computer simulation of local order in condensed phases of silicon. *Phys. Rev. B*, 31(8):5262–5271, 1985.
- [125] R. Sunyk. On aspects of mixed continuum–atomistic material modelling. *Ph.D. Thesis*, 2004.
- [126] R. Sunyk and P. Steinmann. Localization analysis of mixed continuum–atomistic models. *J. Phys. IV France*, 11(11):251–258, 2001.
- [127] R. Sunyk and P. Steinmann. On higher gradients in continuum–atomistic modelling. *International Journal of Solids and Structures*, 40(40):6877–6896, 2003.
- [128] W.C. Swope and H.C. Andersen. Computer simulation method for the calculation of equilibrium constants for the formation of physical clusters of molecules: Application o small water clusters. *J. Chem. Phys.*, 76(76):637–649, 1992.
- [129] E.B. Tadmor. The quasicontinuum method. *Ph.D. Thesis*, 1996.
- [130] E.B. Tadmor, R. Phillips, and M. Ortiz. Mixed atomistic and continuum models of deformation in solids. *Langmuir*, 12(12):4529–4534, 1996.
- [131] E.B. Tadmor, R. Phillips, and M. Ortiz. Quasicontinuum analysis of defects in crystals. *Phil. Mag.*, A(73):1529–1563, 1996.
- [132] J. Tersoff. Empirical interatomic potential for silicon with improved elastic properties. *Phys. Rev. B*, 38(14):9902–9905, 1988.
- [133] J. Tersoff. New empirical–approach for the structure and energy of covalent systems. *Phys. Rev. B*, 37(12):6991–7000, 1988.
- [134] A. C. To and S. Li. Perfectly matched method for multiscale simulations. *Phys. Rev. B*, 71(1):1–8, 2005.
- [135] N. Triantafyllidis and E.C. Aifantis. A gradient approach to localization of deformation. i. hyperelastic materials. *Journal of Elasticity*, 16(13):225–237, 1886.
- [136] D.H. Tsai. The virial theorem and stress calculation in molecular dynamics. *J. Chem. Phys.*, 70(3):1375–1382, 1979.
- [137] H.M. Urbassek. *Computersimulation in den Materialwissenschaften*. Kaiserslautern, 1988.
- [138] L. Verlet. Computer ”experiments” on classical fluids i. thermodynamical properties of Lennard–Jones molecules. *Phys. Rev.*, 159(1):98, 1967.
- [139] L. Verlet. Computer experiments on classical fluids ii. equilibrium correlation functions. *Phys. Rev.*, 165(1):201–214, 1968.
- [140] J. Villanueva. On the validity of the Cauchy–Born rule in continuum/atomistics modelling. *Diploma Thesis, University of Kaiserslautern*, 2006.
- [141] V. Vitek and T. Egami. Atomic level stresses in solids and liquids. *Phys. Stat. Sol. (b)*, 144(157):145–156, 1987.
- [142] Igor Volkov, Marek Cieplak, Joel Koplik, and Jayanth R. Banavar. Molecular dynamics simulations of crystallization of hard spheres. *Phys. Rev. E*, 66(6):061401, 2002.

-
- [143] G. J. Wagner and W. K. Liu. Coupling of atomistic and continuum simulations using a bridging scale decomposition. *J. Comput. Phys.*, 190(1):249–274, 2003.
- [144] Gregory J. Wagner, Karpov Eduard G., and Wing Kam Liu. Molecular dynamics boundary conditions for regular crystal lattices. *Computer Methods in Applied Mechanics and Engineering*, 193(17–20):1579–1601, 2004.
- [145] E. Weinan and Z. Huang. Matching conditions in atomistic-continuum modeling of materials. *Phys. Rev. Lett.*, 87(13):135501–1–4, 2001.
- [146] E. Weinan and Z. Huang. A dynamic atomistic–continuum method for the simulation of crystalline materials. *J. Comput. Phys.*, 182:234–261, 2002.
- [147] E. Weinan and X.T. Li. Multiscale modeling of crystalline solids. *submitted to the Handbook of Computational Material Science*.
- [148] M. Wen, S. Fukuyama, and K. Yokogawa. Visualisation of deformation in atomistic simulation. *Computational Materials Science*, 30(30):217–222, 2004.
- [149] L.V. Woodcock. Isothermal molecular dynamics calculations for liquid salts. *Chem. Phys. Lett.*, 10(3):257–261, 1971.
- [150] P. Wriggers. *Nichtlineare Finite-Element-Methoden*. Springer, 2001.
- [151] S.P. Xiao and T. Belytschko. A bridging domain method for coupling continua with molecular dynamics. *Computer Methods in Applied Mechanics and Engineering*, 193(193):1645–1669, 2004.
- [152] G. Zanzotto. The Cauchy–Born hypothesis, nonlinear elasticity and mechanical twinning in crystals. *Acta Cryst.*, A(52):839–849, 1996.
- [153] Z. Zhennan and G. Xiurun. A new quasi-continuum constitutive model for crack growth in an isotropic solid. *European Journal of Mechanics and Solids*, 24(24):243–252, 2005.
- [154] M. Zhou. A new look at the atomic level virial stress: on continuum–molecular system equivalence. *Royal Society of London Proceedings Series A*, 459:2347–2392, September 2003.
- [155] S.J. Zhou, P.S. Lomdhal, R. Thomson, and B.L. Holian. Dynamic crack processes via molecular dynamics. *Phys. Rev. Lett.*, 76(13):2318–2321, 1996.
- [156] O. C. Zienkiewicz. *The Finite Element Method*. McGRAW–HILL, 1982.
- [157] J.A. Zimmermann, C.L. Kelchner, J.C. Klein, J.C. Hamilton, and Foiles S.M. Surface step effects on nanoindentation. *Phys. Rev. Lett.*, 87(16):1–4, 2001.

Curriculum Vitae

Name: Aitor Elizondo Sanchis
Adress: Paseo de Estrasburgo n° 12 2A
Vitoria (Spain)
Date and place of birth: 14.07.1975, Stuttgart (Germany)

Schools and Universities:

1981 – 1989 General education school in Vitoria(Spain)
1989 – 1993 Instituto Los Herran in Vitoria (Spain)
1993 – 2001 University of Bilbao (Spain)
2001–2002 University of Kaiserslatern(Germany)
(Diplom Ingenieur)

Professional experience:

12/2002 - 4/2003 Internship at Chair of Applied Mechanics
(University of Kaiserslautern).
4/2003 - 9/2003 Internship at Company Joh. Heines–Wuppertal GmbH Nachf.
Since 10/2003 Ph.D. Student, University of Kaiserslautern,
Chair of Applied Mechanics.
Prof. Dr.-Ing. Habil. Paul Steinmann